CATALYSTS DEVELOPMENT AND MECHANISTIC STUDY OF ETHANOL STEAM REFORMING FOR LOW TEMPERATURE H_2 PRODUCTION

CATHERINE CHOONG KAI SHIN

NATIONAL UNIVERSITY OF SINGAPORE

2013

CATALYSTS DEVELOPMENT AND MECHANISTIC STUDY OF ETHANOL STEAM REFORMING FOR LOW TEMPERATURE H_2 PRODUCTION

CATHERINE CHOONG KAI SHIN

(B.Eng. & M.Eng. National University of Singapore, Singapore)

A THESIS SUBMITTED

FOR THE DEGREE OF DOCTOR OF PHILOSOPHY

DEPARTMENT OF CHEMICAL & BIOMOLECULAR ENGINEERING

NATIONAL UNIVERSITY OF SINGAPORE

2013

DECLARATION

I hereby declare that this thesis is my original work and it has been written by me in its entirety. I have duly acknowledged all the sources of information which have been used in the thesis.

This thesis has also not been submitted for any degree in any university previously.

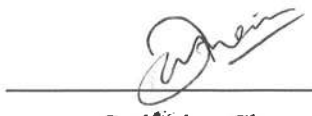

Catherine Choong Kai Shin

22nd December 2012

ACKNOWLEDGEMENTS

I would like to take this opportunity to express my sincere gratitude and appreciation to my supervisor, Dr Chen Luwei from Institute of Chemical and Engineering Sciences (ICES), for her invaluable advice and guidance throughout my PhD candidature. I have benefitted from her expertise in heterogeneous catalysis and reactor system, of which form the basis of this thesis. The knowledge and experimental skills which she has patiently imparted on me, prepares me for the challenges ahead. The journey towards the completion of this thesis would not be that enjoyable and rewarding if not for her unconditional support, optimism and friendship. I am also indebted to my supervisor, A/P Hong Liang from NUS. His commitment to student's success is unparalleled. His insightful suggestions and comments have guided me through my doctoral study.

I would also like to thank Professor Lin Jianyi from ICES. He has encouraged me to pursue this degree and provided help in every possible way. His advice on results interpretation and analysis has contributed tremendously to the completion of this thesis.

I am extremely thankful to Professor Lioubov Kiwi and Dr. Fernando Cárdenas-Lizana at Ecole Polytechnique Fédérale de Lausanne (EPFL), Switzerland, who have given me the opportunity to work in their research laboratory during my stay as an exchange student. They allowed me to explore other research areas in heterogonous catalysis, particularly in hydrogenation of chloronitrobenzene. I would not have adapted fast enough if not for their kind hospitality and guidance.

Special thanks go to my colleagues from ICES who have rendered me incredible assistance during my PhD candidature: Dr. Armando Borgna, Dr. Zhong Ziyi, Dr. Huang Lin, Dr Chang Jie, Dr. Lim San Hua, Dr. Poernomo Gunawan, Poh Chee Kok and Wang Zhan, Lee Koon Yong. I am also extremely grateful to Dr. Ang Thiam Peng, Dr. Teh Siew Pheng, Jaclyn Teo and Tay Hui Huang, who have since departed from ICES, for their unconditional support and encouragement during the course of the study. Their friendships remain fondly at heart.

Finally, I would like to thank my parents who have provided me with an all round education and imparted me with sound values, which allow me to venture courageously in all aspects of life. This journey would not have completed without their nurture for the past 30 years. Special thanks to my husband, for his continuous support and understanding at each turn of the road.

TABLE OF CONTENTS

SUMMARY

Low temperature ethanol steam reforming (ESR) provides an economical way to produce hydrogen for fuel cells application. At low temperature ($T \leq 673$ K), less energy is required and a faster start-up time is anticipated. Furthermore, water-gas shift reaction (WGSR) — an intermediate reaction pathway during ESR, converts CO, a poison to Pt anode of fuel cell, to CO_2 and H_2 in the presence of steam is thermodynamically more favorable at low temperature. WGSR removes CO from the product affluent and thus minimize the use of down-stream reactor units such as WGS reactors and preferential CO oxidation unit. Therefore, it is plausible to enhance WGS during ESR. However, low temperature ESR poses several challenges in catalyst formulation. Low temperature ESR often leads to sluggish catalytic activity as it is an endothermic reaction. Deactivation by carbon formation is also common, especially over Ni-based catalysts at low temperature reaction conditions. In this study, catalytic studies were performed under realistic ESR conditions using various active metals (Ni, Pt, Rh and Pd) supported on calcium-modified alumina support. Promoter such as iron was also introduced during catalyst formulation. Reaction and deactivation mechanisms were studied over these catalysts, providing useful information. Through a detailed study, an effective catalyst, Rh-Fe/Ca-Al_2O_3, which has high ESR activity, low CO selectivity and good stability was unearthed.

The catalytic activity and stability of Ni catalysts supported on calcium-modified Al_2O_3 of various Ca loading (0-7 wt. %) were examined at different

temperature using a 5-channel micro-reactor. Among the catalysts tested, nickel catalyst supported on 3 wt. % Ca-Al_2O_3 shows high ethanol conversion and long catalytic stability. The presence of Ca reduces the acidity and increases the basicity of the alumina support, promoting the formation of CH_3CHO and depressing the formation of coke precursors C_2H_4. In addition, the surfaces of Ca-modified alumina supports are enriched with surface hydroxyls which assist in the removal of coke deposits. The addition of higher loading of calcium (i.e. Ni/7 wt. % Ca-Al_2O_3), however, deteriorates the stability of the catalyst and it performs even worse than the Ca-free nickel catalyst (Ni/Al_2O_3). This is attributed the deposition of carboneous species. Deactivation study shows that the coking rate is enhanced over catalyst with higher Ca loading. The weaker nickel and support interaction due to the incorporation of Ca increases the availability of surface Ni which enhances the formation of coke via dissociation of CH_4. Furthermore, the addition of Ca also influences the particle size of Ni which in turn has an effect on the type of carbon deposited. High Ca loading on Ni/Al_2O_3 catalyst leads to large Ni particle size which facilitates the formation of encapsulating coke.

Examination of the ESR reaction mechanism of noble metals (Pt, Rh and Pd) supported on optimized Ca-Al_2O_3 support was conducted. A new ESR reaction mechanism denoted as *formate-driven* mechanism over noble metal catalysts supported on Ca-Al_2O_3 was proposed. This is unlike the traditionally reported ESR *acetate-driven* reaction mechanism which is also observed over noble metal catalysts supported on Ca-free Al_2O_3. The shift from *acetate-driven* to *formate-driven* reaction mechanism in the presence of Ca is due to the

availability of surface oxygen. Since Ca-modified alumina surface is enriched with surface hydroxyls and adsorbed water, the presence of Ca depletes the surface of free oxygen to produce acetate intermediates. Instead, formate species which are responsible for the *formate-driven* mechanism are produced. Formate species are intermediates for WSGR. It is found that the activity of the catalysts in WGSR during ethanol steam reforming decreases in the following order Pt > Rh > Pd. The roles of noble metals were also investigated.

The catalytic performance of Rh/Ca-Al_2O_3 catalyst leaves room for possible improvement in the catalyst formulation, particularly targeting at lowering the CO selectivity during low temperature ESR. A series of Rh-Fe/Ca-Al_2O_3 catalysts with various Fe loading was synthesized and tested under low temperature ESR conditions. A comparative study with Rh/Ca-Al_2O_3 shows that the addition of Fe can significantly reduce CO selectivity during ESR. A 10 wt. % of Fe loading to Rh/Ca-Al_2O_3 gives high hydrogen yield, low CO selectivity and good catalytic stability for at least 280 h. Iron helps in converting CO to CO_2 and H_2 in the presence of steam via WGSR. Further catalytic testing and characterization show that intimate interaction between Rh and Fe is required. Formate species which are WGSR intermediates are observed over Rh-Fe/Ca-Al_2O_3 via infrared spectroscopy upon CO adsorption. The formation of coordinatively unsaturated ferrous (CUF) could be responsible for the synergistic effect.

The catalytic performances of Rh-Fe catalysts supported on various metal oxides (Ca-Al_2O_3, MgO and ZrO_2) were studied under same ESR conditions. The

WGSR effect in ESR is achieved best with Rh-Fe catalyst supported on Ca-Al_2O_3 followed by MgO and then ZrO_2. The roles of the supports were elucidated. From various characterization results, it is determined that the metal-support interaction influences the chemical states of iron. MgO interacts closely with iron oxide, forming a solid solution and thus reduction of iron oxides to lower valency (i.e. Fe_3O_4) may be hindered. On the other hand, the poor iron oxide and ZrO_2 interaction may lead to the formation Rh-Fe alloy as iron oxide can be reduced to metallic iron. Hence, the metal-support interaction on both MgO and ZrO_2 supports may hinder the formation of Fe_xO_y which are related to production of CUF sites. Over Rh-Fe/Ca-Al_2O_3 catalyst, the favorable metal-support interaction encourages the formation of CUF sites. CUF sites may also serve as water activation sites for the dissociation of steam to surface hydroxyls.

In conclusion, an optimized loading of Ca on alumina has shown to be beneficial to improving the stability of ESR. The catalytic performances and roles of different active metals were studied using Ca-modified Al_2O_3 as support. Many unexpected discoveries such as the *formate-driven* ESR mechanism using noble metal catalysts supported on Ca-Al_2O_3 and the role of Rh-Fe catalyst in reducing CO selectivity during ESR were first reported. Not only does this work identify a potentially good catalyst, Rh-Fe/Ca-Al_2O_3, in maintaining good catalytic stability, high activity and low CO selectivity, it also serves to provide useful insights in designing of catalyst formulation for low temperature ESR using Ca-modified Al_2O_3 as support.

LIST OF TABLES

LIST OF FIGURES

SYMBOLS AND ABBREVIATIONS

Symbols

$d = dp = d_{TEM}$ Surface area-weighted metal diameter (using TEM); (nm)

d_{hkl} Metal particle size (using Scherrer equation); (nm)

E_b Binding Energy

S_{H2} Selectivity of compound H_2

S_{CO2} Selectivity of compound CO_2

S_{CO} Selectivity of compound CO

S_{CH4} Selectivity of compound CH_4

S_{C2H4} Selectivity of compound C_2H_4

S_{CH3CHO} Selectivity of compound CH_3CHO

T_{max} Temperature associated with maximum H_2 consumption/desorption (in temperature programmed reduction/desorption)

Y_{H2} Yield of compound H_2

Abbreviations

BET Brunauer Emmett Teller

CUF Coordinatively Unsaturated Ferrous

DFT Density Functional Theory

DRIFTS Diffused Reflectance Infrared Fourier Transform Spectroscopy

ESR Ethanol Steam Reforming

EXAFS Extended X-ray Absorption

FID Flame Ionization Detector

FTIR Fourier Transform Infra-Red spectroscopy

GC	Gas Chromatography
GHSV	Gas Hourly Space Velocity
SEM	Scanning Electron Microscopy
SR	Steam Reforming
S/E	Steam to ethanol ratio
TCD	Thermal Conductivity Detector
TEM	Transmission Electron Microscopy
TEOM	Tapered Element Oscillating Microbalance
TGA	Thermo-Gravimetric Analysis
TOF	Turnover Frequency
TPD	Temperature Programmed Desorption
TPH	Temperature Programmed Hydrogenation
TPR	Temperature Programmed Reduction
TPO	Temperature Programmed Oxidation
UHV	Ultra High Vacuum
WGSR	Water Gas Shift Reaction
XANES	X-ray Absorption Near Edge Spectroscopy
XRD	X-Ray Diffraction
XPS	X-ray Photoelectron Spectroscopy

PUBLICATIONS

1. Luwei Chen, **Catherine K.S. Choong**, Ziyi Zhong, Lin Huang, Thiam Peng Ang, Liang Hong, Jianyi Lin, "Carbon monoxide-free hydrogen production via low-temperature steam reforming of ethanol over iron-promoted Rh catalyst", *Journal of Catalysis*, 276 (2010), 197-200.

2. **Catherine K.S. Choong**, Ziyi Zhong, Lin Huang, Zhan Wang, Thiam Peng Ang, Armando Borgna, Jianyi Lin, Liang Hong, Luwei Chen, "Effect of calcium addition on catalytic ethanol steam reforming of Ni/Al_2O_3: I. Catalytic stability, electronic properties and coking mechanism", *Applied Catalysis A: General*, 407 (2011), 145-154.

3. **Catherine K.S. Choong**, Lin Huang, Ziyi Zhong, Jianyi Lin, Liang Hong, Luwei Chen, "Effect of calcium addition on catalytic ethanol steam reforming of Ni/Al_2O_3: II. Acidity/basicity, water adsorption and catalytic activity", *Applied Catalysis A: General*, 407 (2011), 155-162.

4. Cárdenas-Lizana Fernando, Bridier Blaise; **Catherine K.S. Choong**, Pérez-Ramírez Javier, Kiwi-Minsker Lioubov, "Promotional Effect of Ni in the Selective Gas-Phase Hydrogenation of Chloronitrobenzene over Cu-based Catalysts", *ChemCatChem*, 4 (2012) 668–673.

Chapter 1

Introduction

1.1. Motivation and Approaches

Hydrogen is an attractive energy carrier which holds great promise of meeting concerns over security of supply and environmental problems. Its energy density is three times higher than that of fossil fuels and can be produced cleanly and renewably. Hydrogen can be utilized in fuel cell to generate electricity for powering stationary or automotive applications. Today, approximately 90% of all hydrogen is produced by steam reforming of natural gas with CO_2 as a by-product [1].

An alternative method of hydrogen production is via ethanol steam reforming (ESR) which converts ethanol and steam into H_2 and CO_2. Ethanol is easy to store, handle and transport due to its low toxicity. Bio-ethanol can be obtained from corn and there is significant improvement in cellulose conversion technology whereby ethanol can also be renewably produced via lignocellulosic biomass such as wood chips and grasses. As such, the CO_2 produced during ESR can be consumed by this agriculture during photosynthesis, ensuring a net-zero emission of CO_2. Low temperature ESR is desirable due to lower energy demand. It is also extremely useful for hydrogen fuel cells such as phosphoric acid fuel cells (PAFCs) and proton exchange membrane fuel cells (PEMFCs) which operate at around 373 K - 473 K. Furthermore, water-gas shift reaction which

converts CO and steam to CO_2 and H_2 is thermodynamically more favorable at low temperature. This will reduce CO poisoning on the Pt anodes of the fuel cells. However, lower hydrogen yield and higher coke deposition are some of the challenges for low temperature ESR.

The main objective of this thesis is to develop active, stable and coke resistance catalysts for the production of CO-free hydrogen during low temperature ESR (573 K -673 K) using Al_2O_3 as support. In order to formulate a good catalyst and to address the problems of low temperature ESR such as CO production and coke formation, catalytic evaluation of the catalysts are complimented with deactivation study and mechanistic derivation In this thesis, several approaches were carried out:

(i) Modification of Al_2O_3 support using Calcium.

Promoters with alkaline properties, such as Li, Na, Mg and La, have been added to the catalysts with the primary purpose of inhibiting the deposition of coke during the reforming process. Alkali earth metals such as Ca can also exert similar effect by reducing the acidic sites of the support and decreases coke formation [2]. Ca has also been used as a catalyst promoter by various research groups in different kinds of reactions, such as methane dry reforming [3], Fischer-Tropsch synthesis [4], propane dehydrogenation [5] and dehydrosulfurization of petroleum feedstocks [6]. However, the effect of CaO modification on Al_2O_3 and its use as a catalyst support for ESR has not been reported. Hence, the effect of Ca

modification of Al_2O_3 based catalysts on low temperature ESR will then be one of the focuses in this thesis.

(ii) Investigation of the role of active metals (Ni, Rh, Pt, Pd) supported on Ca-modified Al_2O_3 at low temperature ESR.

Studies have shown that Ni and Rh are active catalysts for C-C bond cleavage. However, they are not active catalysts for WGSR [7, 8]. Pt metal is excellent catalyst for WGSR but not as active as Rh as an ESR catalyst. These results show that different active metals exhibit different properties in a catalytic system. Furthermore, the catalytic roles of active metals vary on different support material. In this thesis, we seek to identify the roles of the active metals supported on Ca-modified Al_2O_3 through a series catalytic testings and surface mechanism studies.

(iii) Modification of Rh catalyst with different loading of Fe to enhance WGS activity.

Among the active metals examined, Rh demonstrated better performance in terms of ethanol conversion and hydrogen selectivity. However, CO selectivity remains substantial at low temperature ESR and it will poison the anode of the fuel cell, if not otherwise remove from the reformate stream to < 10 ppm. Iron oxide is a well known material for WGSR. With particular interest in reducing

CO concentration in the reformate stream, the effect of Fe loading and modification on Rh/Ca-Al_2O_3 is studied. Rh-Fe catalysts supported on various supports are also investigated.

(v) Study of deactivation mechanism over catalysts.

Deactivation of catalyst appears to be an unavoidable issue during low temperature ESR. It is thus important to understand the deactivation mechanism over our synthesized catalysts such as Ni/Ca-Al_2O_3. The information obtained would be useful for the design of an active, stable and coke resistant catalyst for low temperature CO free hydrogen production.

1.2. Organization of Thesis

This thesis is divided into nine chapters. Chapter 2 of this thesis presents a literature review, providing an overview of the current state-of-art and problems for this ESR. Chapter 3 details the experimental techniques used in this research. Background theory of selected characterization techniques are provided in greater details.

Chapter 4 focuses on the study of Ca modification on Al_2O_3 support using different Ca loading. Changes in the surface properties such as acidity and basicity of the modified supports were probed. Electronic properties of the

modified support were studied using X-ray photoemission spectroscopy (XPS). Catalytic performances of the supports were evaluated using a 5 channel micro reactor.

In Chapter 5, Ca-modified Al_2O_3 supports of various Ca loading were impregnated with Ni. The catalytic activities and stabilities were investigated and compared at low temperature ESR. The deactivation mechanism of the Ni-based catalysts was examined in detail, taking into considerations of Ni particle size, acidity/basicity, electronic properties and steam gasification. Reaction mechanism was derived using infrared spectroscopy and thermal desorption techniques.

Chapter 6 studies the reaction mechanism of noble metal catalysts (Pt, Rh and Pd) on Ca-modified Al_2O_3 support in comparison to the catalysts supported on Ca-free Al_2O_3 support. A new reaction pathway was unraveled.

Chapter 7 builds upon the good performance of Rh catalysts and studies the effect of Fe promotion on the stability and activity of Rh catalyst during low temperature ESR. In Chapter 8, Rh-Fe catalysts synthesized over a few commercial metal oxides as catalysts supports are presented. Catalytic activities were investigated at low temperature ESR.

Chapter 9 summarizes the principal findings in this thesis. Future outlook and directions are provided.

1.3. References

[1] D. Das, T.N. Veziroglu, Int. J. Hydrogen Energy. 26 (2001) 13-28.

[2] A.J. Vizcaíno, A. Carrero, J.A. Calles, Catal. Today 146 (2009) 63-70.

[3] Z.L. Zhang, X.E. Verykios, Catal. Today 21 (1994) 589-595.

[4] A. Bao, K. Liew, J. Li, J. Mol. Catal. A: Chem. 304 (2009) 47-51.

[5] L. Bai, Y. Zhou, Y. Zhang, H. Liu, M. Tang, Catal. Lett. 129 (2009) 449-456.

[6] S. Andonova, C. Vladov, B. Pawelec, I. Shtereva, G. Tyuliev, S. Damyanova, L. Petrov, Appl. Catal. A: Gen. 328 (2007) 201-209.

[7] J. Comas, F. Mariño, M. Laborde, N. Amadeo, Chem. Eng. J. 98 (2004) 61-68.

[8] F. Auprêtre, C. Descorme, D. Duprez, Catal. Commun. 3 (2002) 263-267.

Chapter 2

Literature Survey

2.1. Importance and Challenges of H_2 Production from Ethanol Steam Reforming

According to BP's annual Statistical Review of World Energy, global energy consumption grew by 2.5% on the year before in 2011, indicating a continuous demand for energy [1]. Fossil fuels have been the dominant energy resources which our global framework relies on for energy and power. Robust growth was seen in the consumption of oil, coal and natural gas, which constitutes 87% of the market share. With the increasing usage of fossil fuels for power generation, concerns over environmental pollutions and non-renewability are constantly raised. Hence, there is an urgent need to look for alternative renewable and clean energy such as hydrogen.

Hydrogen is an attractive energy carrier which holds great promise of meeting concerns over security of supply and environmental problems. Its energy density is three times higher than that of fossil fuels and is in large abundance in nature. Table 2.1 shows that 1 kg of H_2 contains the same amount of energy as 2.6 kg of natural gas/methane (CH_4) or 3.1 kg of gasoline. Hydrogen is used in fuel cells to generate electricity in stationary power stations or to power automobiles. The only product from the fuel cell is pure water, therefore eliminating the emission of pollutants. Hydrogen can be produced from various sources such as

fossil fuels, nuclear energy as well as renewable energy sources such as biomass, wind and solar. This encourages diversity in the primary supply for fuels and hence increases energy security. Hydrogen production via renewable resources, nuclear reactors and even fossil fuels with sequestration of carbon reduces greenhouse gas emission and is considered environmental friendly.

Table 2.1. Energy density of various hydrocarbons and alcohol fuels [2].

Fuel	Major Chemical Compound	Energy Density (MJ/kg)
Hydrogen	H_2	142.0
Natural gas	CH_4	55.5
LPG	C_3-C_4	50.0
Methanol	CH_3OH	22.5
Ethanol	CH_3CH_2OH	29.7
Gasoline	C_4-C_{12}	45.8
Diesel	C_9-C_{24}	46.3

Steam reforming of natural gas is one of the traditional methods used for production of hydrogen. However, there is increasing interest in ethanol steam reforming (ESR, Eqn. 2.1). This is because ethanol is easy to store, handle and transport due to its low toxicity. In Fig. 2.1 shows that the production of ethanol has been steadily increasing over the past decade, with United States dominating

the market [3]. Production of ethanol from corn is a mature technology. However, issues such as rising food prices as staple food crops are diverted to produce fuel and commodity speculations threaten the corn ethanol production [4]. Recently, there is significant improvement in cellulose conversion technology whereby ethanol can also be renewably produced via lignocellulosic biomass such as wood chips and grasses. The abundance and widely distributed cellulosic biomass sources lower the cost of ethanol production as well avoid any competition with traditional food crops. All of these increase the feasibility of commercializing ethanol-based on-board reformers for stationary or automotive applications.

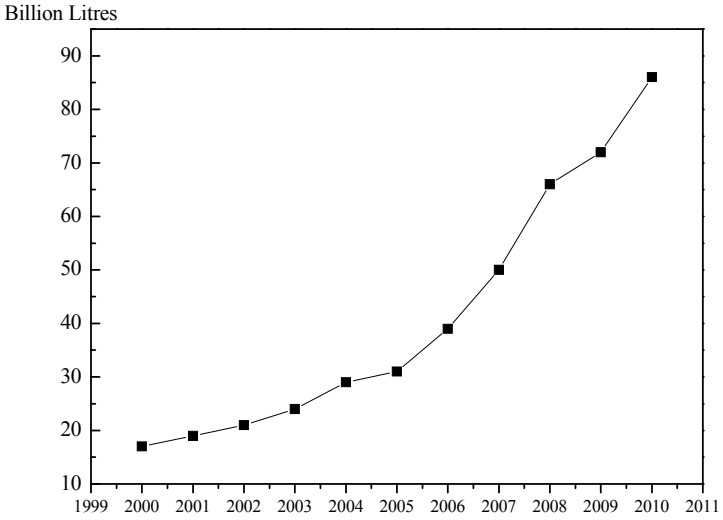

Figure 2.1. Ethanol Production, 2000-2010 [3].

Ethanol steam reforming is thermodynamically favorable at high temperature, producing high hydrogen yield. However, high temperature ESR is not practical in reality due to high operating cost and long start-up time. In

addition, water-gas shift reaction (WGSR) (Eqn. 2.7) is a reversible reaction whereby the equilibrium shifts to the left at high temperature and limits CO conversion to H_2. Since CO will poison the Pt anode of the fuel cells and reduce cell voltage, low temperature ESR has been proposed. The production of H_2 typically takes place in a fuel processor which consists of reformers, compressors/expanders, heat exchangers and a series of CO removal units such as low and high temperature WGS reactors and preferential oxidation unit (PROX) where oxygen is used to oxidize the carbon monoxide (Fig. 2.2.). The favorable WGS equilibrium during low temperature ESR eliminates the need of the additional WGS units downstream. Low temperature ESR is also extremely useful for hydrogen fuel cells such as phosphoric acid fuel cells (PAFCs) and proton exchange membrane fuel cells (PEMFCs) which operate at around 373 K - 473 K. ESR at low temperature also demands less energy, resulting in lower cost of production. However, one of the problems that arise during low temperature ESR is the favored formation of CH_4 and undesirable side reactions leading to coke formation [5-7]. This reduces H_2 selectivity and is detrimental to catalytic lifespan. Therefore, the goal here is to develop a highly active and stable catalyst which inhibits coke formation and CO production for low temperature ESR.

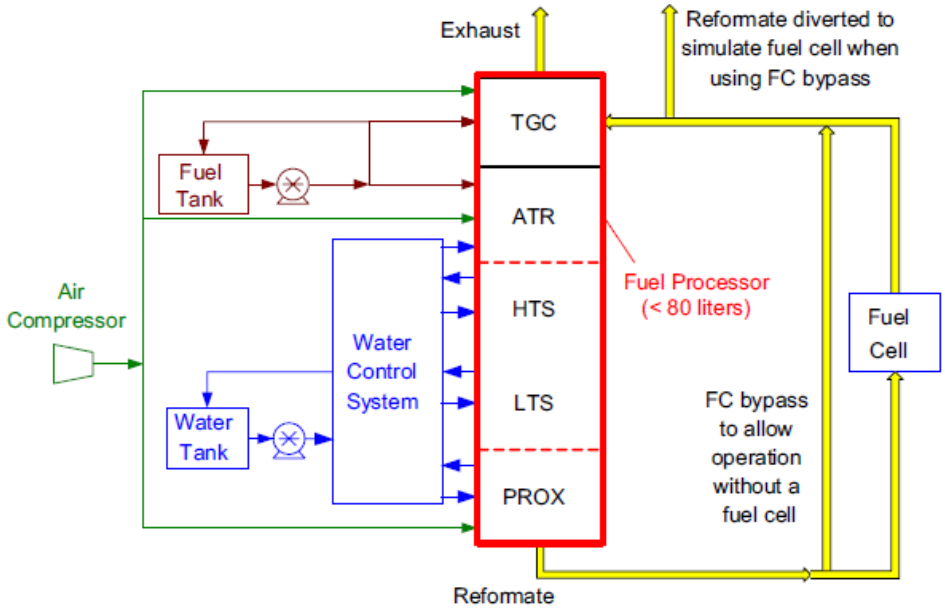

Figure 2.2. Schematic of a fuel processor system [8].

2.2. Reaction Network of Ethanol Steam Reforming

Ethanol steam reforming is an endothermic reaction which produces CO_2 and H_2 from CH_3CH_2OH and steam (Eqn. 2.1)

$$C_2H_5OH + 3H_2O \rightarrow 2CO_2 + 6H_2 \quad (2.1)$$

Due to its thermodynamics, the reaction occurs at higher temperature ranging between 573 K- 1023 K. Typically, a steam to ethanol (S/E) molar ratio of 3 is stoichiometrically sufficient for the reaction. However, higher S/E of as high as 20 have been used, corresponding to that of the S/E of bioethanol or crude ethanol. The excess water also favors WGSR (Eqn. 2.7) and ethanol decomposition (Eqn. 2.2). A drawback on the heavy use of steam would be the high energy cost required for steam generation.

Depending on the catalyst formulation and the reaction conditions such as reaction temperature, pressure, steam/ethanol and gas hour space velocity (GHSV), a variety of reaction intermediates may be present. For example, acidic supports promote ethanol dehydration (Eqn. 2.3) to produce ethylene while dehydrogenation of ethanol to acetaldehyde is promoted on basic support (Eqn. 2.4). Acetaldehyde undergoes decarbonylation to produce CO and CH_4 (Eqn. 2.5). At high temperature, methane steam reforming is thermodynamically favored producing CO and H_2 (Eqn. 2.6). Carbon monoxide can be converted to CO_2 and H_2 via WGSR (Eqn 2.7). These reactions are described in Eqns 2.2-2.7.

Ethanol decomposition

$$C_2H_5OH \rightarrow CH_4 + CO + H_2 \quad (2.2)$$

Ethanol dehydration

$$C_2H_5OH \rightarrow C_2H_4 + H_2O \quad (2.3)$$

Ethanol dehydrogenation

$$C_2H_5OH \rightarrow C_2H_4O + H_2 \quad (2.4)$$

Decarbonylation

$$C_2H_4O \rightarrow CO + CH_4 \quad (2.5)$$

Methane steam reforming

$$CH_4 + H_2O \rightarrow 3H_2 + CO \quad (2.6)$$

Water-gas shift reaction

$$CO + H_2O \rightarrow H_2 + CO_2 \quad (2.7)$$

2.3. Deactivation

Catalyst deactivation refers to the loss of catalytic activity and/or selectivity over time. This is a problem of great concern in most of the industrial catalytic processes. Table 2.2 lists six deactivation mechanisms which occur during heterogeneous catalysis. They are (1) poisoning, (2) fouling, (3) thermal degradation, (4) vapor compound formation and/or leaching accompanied by transport from the catalyst surface or particle, (5) vapor–solid and/or solid–solid reactions, and (6) attrition/crushing. Their mechanisms are defined in brief in Table 2.2. Detailed reading can be found in ref. [9]. In this study, we will focus on the deactivation due to fouling and thermal degradation with relevance to coking and sintering.

Table 2.2. Mechanisms of Catalyst Deactivation [9].

Mechanism	Type	Brief definition/description
Poisoning	Chemical	Strong chemisorption of species on catalytic sites which block the sites for catalytic reaction.
Fouling	Mechanical	Physical deposition of species from fluid phase onto the catalytic surface and in catalyst pores.
Thermal degradation	Thermal	Thermally induced loss of catalytic surface area, support area, and active phase-support

		reactions.
Vapor formation	Chemical	Reaction of gas with catalyst phase to produce volatile compound.
Vapor–solid and solid–solid reactions	Chemical	Reaction of vapor, support, or promoter with catalytic phase to produce inactive phase.
Attrition/crushing	Mechanical	Loss of catalytic material due to abrasion loss of internal surface area due to mechanical-induced crushing of the catalyst particle.

2.3.1. Carbon formation

During ESR, several undesirable reactions resulting in coke deposition often take place simultaneously. Reaction products or intermediates such as CO, CH_4, C_2H_4, CH_3CHO and their fragments may react via various pathways and form coke deposition [10]. Polymerization of unsaturated hydrocarbons C_2H_4 (Eqn. (2.8)) leads to gummy carbonaceous deposits which may contain certain amount of hydrogen and oxygen. Methane undergoes decomposition, producing carbon and hydrogen (Eqn. 2.9). At relatively low temperatures CO disproportionate reaction (Eqn. 2.10), also known as Bourdard reaction, and CO de-oxygenation reaction (Eqn. 2.11) may occur, both forming carbon.

$$\gamma C_nH_{2m} \rightarrow C_{n\gamma} + m\gamma H_2 \quad (2.8)$$

$$CH_4 \rightarrow C + 2H_2 \quad (2.9)$$

$$2CO \rightarrow C + CO_2 \quad (2.10)$$

$$CO + H_2 \rightarrow C + H_2O \quad (2.11)$$

Various forms of carbon were observed depending on the reaction conditions and type of catalysts. Table 2.3. shows the various forms of carbon such as adsorbed atomic carbon (C_α), amorphous carbon (C_β), vermicular carbon (C_v), bulk Ni carbide (C_γ), and crystalline, graphitic carbon (C_c) deposited during CO dissociation [11]. The more reactive, amorphous forms of carbon formed at low temperatures (such as C_α and C_β) are converted at high temperatures over a period of time to less reactive, graphitic forms.

The morphologies of the carbon, typically observed on Ni catalysts, include pyrolitic, encapsulated carbon and carbon filaments. Encapsulated carbon leads to loss of catalytic sites as the active sites are covered by carbon layer while carbon filaments deactivate the catalyst by plugging the pore of the catalyst, and reducing reactant accessibility. This results in mechanical deformation of the catalyst due the high mechanical strength of carbon filaments. Typically carbon filament formation occurs when the adsorbed hydrocarbon species break into adsorbed carbon atoms which dissolve into the metal particle such as Ni. At the point of saturation, carbon will nucleate and carbon filaments will grow with nickel crystal at the top. Many experimental and theoretical studies confirmed that the size of Ni particle has a significant effect on the coke formation [12-16]. Smaller Ni particles have higher carbon resistance as the driving force for carbon diffusion through the small Ni crystals is small and hence are ideal as coke

resistance catalyst [16]. Bengaard et al. demonstrated that the stability of C* is highly sensitive to the superficial structure of Ni using density functional theory (DFT) calculation [15]. It was concluded that a certain minimum nucleus of graphene at Ni step is needed to activate graphitic formation. Nucleation of graphene islands cannot proceed if the step edges are too small. The C* species were found to be more reactive at step sites. Promoters such as potassium, sulfur and gold binds preferentially to these sites, and suppress graphite formation.

In steam reforming, the steam to carbon ratio can influence the rate of coke deposition during the reaction. Thermodynamics calculations showed that coke formation would be inhibited if S/E molar ratio is greater than 2 [17]. This is because steam can assist in the removal of carboneous deposits through gasification. Therefore, the rate at which deactivation occurs for a particular catalyst during steam reforming is related to the difference in the rate of coke formation and rate of carbon gasification. If rate of coke formation is slower than rate of steam gasification, coke formation will be negligible. Since, both carbon formation and gasification is temperature and catalyst dependent, an optimization of the reaction conditions and catalyst formulation is required to attain the state of minimal carbon formation.

Table 2.3. Forms and Reactivities of Carbon Species Formed by Decomposition of CO on Nickel [11].

Type	Designation	Temperature Formed (K)	T_{max} for temperature-programmed hydrogenation (K)
Adsorbed, atomic (surface carbide)	C_α	473-673	473
Polymeric, amorphous films or filaments	C_β	523-773	673
Vermicular filaments	C_v	573-1273	673-873
Nickel carbide (bulk)	C_γ	423-523	548
Graphite (crystalline) platelets or films	C_c	773-823	823-1123

2.3.2. Sintering

Sintering occurs when particles grow in size at the expense of smaller particles, leading to the reduction of the active surface area. In general, small particles have higher surface energy than larger particles. Once sufficient activation energy is supplied, there is a tendency for smaller particles to agglomerate into larger ones in order to decrease surface free energy. Sehested proposed three mechanisms for the metal particle growth: (i) particle migration, where entire crystallites migrate over the support followed by coalescence; (ii) Ostwald ripening (atom migration), where metal atoms emitted from one crystallite migrate over the support and are captured by another crystallite; and (iii) vapor transport between particles (at high temperatures) [18]. Sintering is

influenced by temperature, composition of the gas over the catalyst, structure and composition of the catalyst support as well as metal-support interactions. Increasing temperature and the presence of steam accelerates the sintering process [19, 20].

2.4. Catalytic Systems

2.4.1. Non-noble metal catalysts

Non-noble metals based catalysts have been widely investigated for ESR, with particular attention on nickel-based catalysts. This is because nickel is less expensive and it is highly active towards rupturing of C-C bond. Its ability to rupture the C-C bond is demonstrated by Gates et al. through the decomposition of ethanol on nickel surface [21]. The dissociation of ethanol proceeds via (i) the scission of O-H in an ethoxide intermediate; (ii) the cleavage of –C-H bond of the methylene group, resulting in the formation of acetaldehyde intermediate; and finally (iii) the breaking of C-C bond on the acetaldehyde intermediate, giving rise to adsorbed –CO and -CH_3. Freni et al. reported that Ni/MgO of 19 wt% Ni loading catalyst is highly selective and stable towards H_2 and CO_2 during high temperature ESR (923 K) with a GHSV of 10,000 h^{-1}. It was proposed that the Ni/MgO does not favor CO methanation and ethanol decomposition reactions due to an electronic effect induced on Ni due to the basic nature of MgO [22]. Fatsikostas et al. studied the catalytic activity of Ni catalysts on γ-Al_2O_3, La_2O_3 and La_2O_3/γ-Al_2O_3 supports [23]. At low temperature (< 823 K), rapid

accumulation of coke deposits due to ethylene formation on the acidic γ-Al_2O_3, deactivated the Ni/γ-Al_2O_3 at a faster rate than Ni/La_2O_3. The rate of coke deposition of Ni/La_2O_3/γ-Al_2O_3 was the lowest among the three catalysts and its beneficial effect was due to the formation of lanthanum oxycarbonate species which constrains the adsorbed C and prevents the formation of deactivating carbon islands. It was also reported that Ni participated in WGSR and methanation reaction. Sun et al. evaluated the low temperature H_2 production of Ni catalysts on various supports and the following results were obtained in decreasing activity: Ni/La_2O_3 > Ni/Y_2O_3 > Ni/Al_2O_3 [24]. The results corresponded to the crystal grain sizes of Ni with smaller Ni crystal grain on La_2O_3 being more active. As previously mentioned, sintering and coking are some issues associated with the use of Ni-based catalysts [18]. Agglomeration of nickel-based catalysts occurs at high temperature and in the presence of water. This results in the loss of active sites for catalytic activity. Frusteri et al. reported a decrease in ethanol conversion from 80% to 45% as the nickel crystallite size of Ni/MgO increased from 72.2 Å to 197 Å over 20 h of ESR reaction at 923 K [25]. Coke formation is related to Ni particle size, with smaller Ni particles having higher carbon resistance as the driving force for carbon diffusion through the small Ni crystals is small [16]. Hence, it is desirable to maintain the small nickel particle size during the reaction. Various efforts made by different research groups to optimize the catalyst formulation for healthy and stable H_2 production during ESR are detailed in 2.5.3.

There is increasing number of reports on the use of cobalt catalysts. Haga et al. evaluated the ESR activity of Al_2O_3 supported transition metal catalysts at 673 K and the hydrogen selectivity increased in the following order Co≫ Ni > Rh > Pt, Ru, Cu [26]. Karim et al. compared the activities of Rh and Co-based catalysts under industrial conditions and Co was found to be more selective to CO_2 and H_2 than Rh at high reaction pressures [27]. However, coking rate was found to be higher on Co than Rh. Song et al. investigated the effect of impregnation medium (either ethanol or de-ionized water) on the activity of Co/CeO_2 and found that Co/CeO_2 prepared using ethanol medium showed better ESR catalytic performance [28]. It was postulated that the oxygenated carbon species will prevent sintering and suppress unwanted side reactions, thus promoting ESR. Cobalt can be supported on different support carrier such as Al_2O_3, MgO, ZnO, SiO_2, CeO_2, La_2O_3, Sm_2O_3 and ZrO_2 [29]. It was reported that CO-free hydrogen was produced from ESR at 723 K over Co catalysts supported on ZnO, La_2O_3, Sm_2O_3 and CeO_2 carriers. Cavallaro et al. compared the activity of Co/MgO with Co/Al_2O_3 and concluded that Co/MgO has higher coking resistance [30].

2.4.2. Noble metal catalysts

Noble metal catalysts such as Rh, Pt, Pd and Ru have been reported to be effective catalysts for ESR. Aupretre et al. compared the catalytic activities of Rh, Pt versus those of the non-noble metal catalysts such as Cu, Ni, Zn, and Fe

catalysts for ESR at 973 K [31]. It was concluded that Rh and Ni catalysts are active and selective towards H_2 production. Liguras et al. evaluated the performance of Rh, Pt, Pd and Ru catalysts on various supports and found that Rh is the most active catalyst at low loading [32]. Indeed, Rh, among other noble metals, has shown to be more active in ESR as it has the greatest activity towards C-C bond cleavage [33]. However, coking also occurs over Rh catalysts despite lower carbon solubility in Rh. Cavallaro et al. demonstrated that, on Rh/Al_2O_3 systems, catalyst deactivation occurs by coke deposition and sintering at H_2O/ethanol ratio of 8.4 at 923 K [34]. Roh et al. also reported deactivation by carbon formation on $Rh/CeO_2–ZrO_2$, but total regeneration was possible at low temperatures [35]. Rhodium demonstrated little WGS activity [31]. The use of Rh catalyst on ceria-zirconia based support sees a decrease in the amount of CO produced during ESR, thus suggesting that ceria based supports facilitate WGSR [36].

Pt is also a suitable catalyst for both ESR and WGSR. Breen et al. has reported that at higher temperatures (> 773 K), the ESR activity of ceria-zirconia supported Pt catalyst is better than Rh and Pd, with no formation of ethylene [37]. Pt/CeO_2 catalyst was also found to be active, selective and stable at low temperature between 673 K and 723 K, in comparison to Pt/Al_2O_3 [38]. Increasing Pt loading enhances the WGS conversion from CO to CO_2, thus removing CO from the reformate stream. Pt modified with V, Nb and Mo metals on SiO_2 support were also studied for low temperature ESR (393 K- 513 K) [39]. The results showed that Nb-oxide promoted Pt/SiO_2 is most active for ethanol

conversion among the rest. The high activity was attributed to a strong metal-oxide interaction in Pt-NbOx.

Other noble metals such as Pd and Ru have been tested for ESR. However, interest level for these noble metals is lower due to poorer catalytic properties than Rh and Pt. Casanovas et al. evaluated ESR performance of Pd catalysts on ZnO and SiO_2. The formation of PdZn alloy through co-deposition of Pd and Zn on ZnO support favored dehydrogenation and hydrogen production [40]. Liguras et al. found that Ru was not active at low loading [32]. However, 5 wt% Ru/Al_2O_3 showed comparable catalytic activity with 1 wt% Rh/Al_2O_3, demonstrating a complete conversion of ethanol with hydrogen selectivity above 95%. The comparable performance of Ru was attributed to its high dispersion of catalyst atom at the support surface.

2.4.3. Catalyst supports

Al_2O_3 is one of the most frequently used supports for industrial applications due to its high surface area, good thermal and mechanical strength. Thermal treatment of hydroxylated oxides leads to partial dehydroxylation, revealing the coordinatively unsaturated O^{2-} ion (basic sites) and an adjacent anion vacancy which exposes 3- or 5- coordinated Al 3p cations (Lewis acid sites). A variety of surface hydroxyl groups can be observed from infrared spectroscopy. Due to its complexity, alumina possesses unique catalytic properties. In ESR, its acidic nature catalyzes the dehydration of ethanol to

ethylene. Freni et al. studied the catalytic activity of Al_2O_3 and found that the production of ethylene and water began at 620 K and eventually reached equilibrium at 873 K [41]. Rh supported Al_2O_3 catalyst showed 100% ethanol conversion above 733 K with no traces of C_2H_4 or CH_3CHO.

Basic support such as MgO reduces coke formation. Ni/MgO catalyst has shown better activity for ESR and deactivation rate is much slower than γ-Al_2O_3 supported catalysts [42]. Frusteri et al. showed that both Rh and Ni catalysts supported on MgO displayed promising catalytic results such as good ethanol conversion, stability and the high hydrogen selectivity [43]. Coke formation rate on Rh/MgO was very low due to its basicity.

Ceria (CeO_2) is a basic and reducible oxide. It has oxygen storage capacity and the oxygen present in the lattice can react with surface carbon to form CO_2. Hence, its presence can improve coke resistance. Ciambelli et al. compared the activity of Pt/CeO_2 and Pt/Al_2O_3 at a low temperature [38, 44]. It was found that more stable carbonaceous species were found on Pt/Al_2O_3 than Pt/CeO_2. This resulted in faster deactivation of Pt/Al_2O_3. Furthermore, the catalytic data revealed that there was negligible CO production at low temperature over Pt/CeO_2, hence demonstrating the WGS ability of CeO_2. Zhang et al. showed that Ir/CeO_2 was the most stable catalyst among Co and Ni, with no appreciable deactivation for 300 h time-on-stream [45]. The strong interaction between Ir and CeO_2 increased metal dispersion and reduced sintering. ZrO_2 is often added to CeO_2 in order to increase oxygen storage ability and improve thermal stability.

2.4.4. Optimization of Catalysts

We have previously discussed that issues such as poor catalytic ESR activity at low temperature, presence of CO in the reformate stream, coke formation and sintering result in poor hydrogen production and quick catalyst deactivation. Optimization of catalysts is therefore carried out in order to resolve these issues. Coking is one of the major problems, especially on metal supported Al_2O_3 catalysts. Al_2O_3 is an acidic support where significant amount of coke can be produced via dehydration of ethanol, resulting in the formation ethylene. Promoters with such as Mg, Ca, K, Na, Li. La and Ce have been added to inhibit coke deposition. Depositing Rh on $MgAl_2O_4$ exhibited higher basicity than alumina-supported Rh, resulted in improved catalyst stability [46]. Vizcaíno et al. introduced Mg to Ni/Al_2O_3 and it was demonstrated that when Mg/Ni ratio is above 0.1, there is a significant reduction in the amount of coke deposition by 25 wt% [47]. Besides, the neutralization of acidic sites of the support, Mg could possibly promote steam-carbon reaction, which removes the carbon deposits. Indeed, basic promoters favor water adsorption and increases OH surface mobility which participate in the coke removal process via steam gasification. The effect of La addition is somewhat different. Coke deposition was prevented through the formation of lanthanum oxycarbonate [48]. The addition of promoters may also improve other properties such as increasing metal dispersion and reducing reduction temperature. For example, Vizcaíno et al. reported a higher dispersion of Ni species with smaller Ni particle size over hydrotalcite-type NiCaAl catalyst

prepared co-precipitation [49]. This led to a higher hydrogen production from ESR at 873 K while maintaining a moderate coking rate.

As previously mentioned, sintering is a serious problem, especially on Ni catalysts. Nickel loading can be optimized in order to achieve the highest metal dispersion and while avoiding agglomeration of nearby metal atoms during thermal treatment. Biswas et al. studied the effect of metal loading on cerium-zicronium support and concluded that high Ni loading of 40 wt% led to lower dispersion and agglomeration of nickel particles [50]. Chen et al. synthesized perovskite-type oxide supported nickel catalysts, $NiO/LaFe_yNi_{1-y}O_3$, which also showed good anti-sintering stability [51]. Devianto et al. modified Ni/MgO catalyst with the addition of Al through a low temperature solid-gas-solid reaction to produce a Ni-Al solid solution. It was report that the particle sizes of Ni-Al were maintained between 15-20 nm under accelerated sintering conditions of 1173 K for 24 h [52]. The sintering effect can also be mitigated through the addition of modifiers. Frusteri et al. has found success in depressing Ni sintering and preventing deactivation by the addition of alkali metals such as Li and K to Ni/MgO [25]. On Rh catalysts, Montini et al. synthesized $Rh/Ce_xZr_{1-x}O_2/Al_2O_3$ nanocomposites whereby Rh nanoparticles were protected from sintering/deactivation by a porous layer of nanocomposite oxides [53].

The addition of a second metal to Ni, Rh and Pt has been studied, with the objective of increasing ESR activity, promoting H_2 selectivity, reducing CO selectivity and/or reducing carbon formation. For example, mixing Cu with Ni shows high steam reforming activity and high selectivity to hydrogen at 573 K

with Cu as the active agent and Ni as a hydrogenating/dehydrogenating site [54, 55]. Örücü et al. studied the effect of Pt-Ni bimetallic catalyst on ESR and it was demonstrated that 0.2 wt%Pt–15 wt%Ni/δ-Al_2O_3 showed resistance to carbon formation at 673–823 K and at water-to-ethanol ratios as low as 3.0 [56]. Baltacıoğlu et al. toyed with different Pt/Ni composites on δ-Al_2O_3 and reported that 0.3wt%Pt-15wt%Ni/δ-Al_2O_3 showed better ESR conversion and increased H_2 selectivity [57]. This was probably due to the better dispersion of Pt and Ni. Le Valent et al. showed that the catalytic activity of Rh/Y_2O_3-Al_2O_3 catalyst was promoted by the addition of Ni which helps to increase Rh accessibility and stability [58]. Similar improvement in metal dispersion of Rh particles was found using Ni–Rh bimetallic catalyst supported on CeO_2 [59]. Bimetallics consisting of Rh-Pt, Rh-Pd and Rh-Ru supported on CeO_2-ZrO_2 supports were reported to have higher activity than their respective monometallic catalysts [33, 60]. While there have been improvements in ESR activity and stability with the use of bimetallic catalysts, reports on reducing CO selectivity with the use of bimetallic catalysts are scare.

2.5. References

[1] BP Statistical Review of World Energy June 2012 (2012) Retrieved October 3rd, 2012, from bp.com/statisticalreview.

[2] V. Subramani, P. Sharma, L. Zhang, K. Liu, Hydrogen and Syngas Production and Purification Technologies, John Wiley & Sons, Inc., 2009, pp. 14-126.

[3] Renewables 2011 Global Status Report (2011) Retrieved October 3rd, 2012, from http://www.ren21.net/.

[4] Biofueling Hunger: How uS Corn ethanol Policy Drives up food Prices in Mexico (2012) Retrieved October 3rd, 2012, from http://actionaidusa.org/assets/pdfs/food_rights/Biofueling_Hunger.pdf

[5] García, E. Y., M.A. Laborde, Int. J. Hydrogen Energy. 16 (1991) 307-312.

[6] K. Vasudeva, N. Mitra, P. Umasankar, S.C. Dhingra, Int. J. Hydrogen Energy. 21 (1996) 13-18.

[7] V. Mas, R. Kipreos, N. Amadeo, M. Laborde, Int. J. Hydrogen Energy. 31 (2006) 21-28.

[8] B.J. Bowers, J.L. Zhao, M. Ruffo, R. Khan, D. Dattatraya, N. Dushman, J.-C. Beziat, F. Boudjemaa, Int. J. Hydrogen Energy. 32 (2007) 1437-1442.

[9] C. Bartholomew, Encyclopedia of Catalysis, John Wiley & Sons, Inc., 2002.

[10] D.L. Trimm, Catal. Today 49 (1999) 3-10.

[11] C.H. Bartholomew, Catalysis Reviews. 24 (1982) 67-112.

[12] D.L. Trimm, Catal. Today 37 (1997) 233-238.

[13] Y.H. Hu, E. Ruckenstein, Advances in Catalysis, Academic Press, 2004, pp. 297-345.

[14] M. García-Diéguez, I.S. Pieta, M.C. Herrera, M.A. Larrubia, L.J. Alemany, J. Catal. 270 (2010) 136-145.

[15] H.S. Bengaard, J.K. NÃ¸rskov, J. Sehested, B.S. Clausen, L.P. Nielsen, A.M. Molenbroek, J.R. Rostrup-Nielsen, J. Catal. 209 (2002) 365-384.

[16] D. Chen, K.O. Christensen, E. Ochoa-Fernández, Z. Yu, B. Tøtdal, N. Latorre, A. Monzón, A. Holmen, J. Catal. 229 (2005) 82-96.

[17] A.L. Alberton, M.M.V.M. Souza, M. Schmal, Catal. Today 123 (2007) 257-264.

[18] J. Sehested, Catal. Today 111 (2006) 103-110.

[19] C.H. Bartholomew, Appl. Catal. A: Gen. 107 (1993) 1-57.

[20] D.H. Prasad, S.Y. Park, H. Ji, H.R. Kim, J.W. Son, B.K. Kim, H.W. Lee, J.H. Lee, Appl. Catal. A: Gen. 411-412 (2012) 160-169.

[21] S.M. Gates, J.N. Russell Jr, J.T. Yates Jr, Surf. Sci. 171 (1986) 111-134.

[22] S. Freni, S. Cavallaro, N. Mondello, L. Spadaro, F. Frusteri, J. Power Sources. 108 (2002) 53-57.

[23] A. Fatsikostas, X. Verykios, J. Catal. 225 (2004) 439-452.

[24] J. Sun, X.-P. Qiu, F. Wu, W. Zhu, Int. J. Hydrogen Energy. 30 (2005) 437-445.

[25] F. Frusteri, S. Freni, V. Chiodo, L. Spadaro, O. Di Blasi, G. Bonura, S. Cavallaro, Appl. Catal. A: Gen. 270 (2004) 1-7.

[26] F.Haga, T. Nakajima, K. Yamashita, S. Mishima, S. Suzuki, Nippon Kagaku Kaishi (1997) 33-36.

[27] A. Karim, Y. Su, J. Sun, C. Yang, J. Strohm, D. King, Y. Wang, Appl. Catal. B: Environ. 96 441-448.

[28] H. Song, U.S. Ozkan, J. Mol. Catal. A: Chem. 318 (2010) 21-29.

[29] J. Llorca, N.Homs, J. Sales, P. de la Piscina, J. Catal. 209 (2002) 306-317.

[30] S. Cavallaro, N. Mondello, S. Freni, J. Power Sources. 102 (2001) 198-204.

[31] F. Auprêtre, C. Descorme, D. Duprez, Catal. Commun. 3 (2002) 263-267.

[32] D. Liguras, D. Kondarides, X. Verykios, Appl. Catal. B: Environ. 43 (2003) 345-354.

[33] P. Sheng, A. Yee, G. Bowmaker, H. Idriss, J. Catal. 208 (2002) 393-403.

[34] S. Cavallaro, V. Chiodo, S. Freni, N. Mondello, F. Frusteri, Appl. Catal. A: Gen. 249 (2003) 119-128.

[35] H. Roh, A. Platon, Y. Wang, D. King, Catal. Lett. 110 (2006) 1-6.

[36] A. Birot, F. Epron, C. Descorme, D. Duprez, Appl. Catal. B: Environ. 79 (2008) 17-25.

[37] J. Breen, R. Burch, H. Coleman, Appl. Catal. B: Environ. 39 (2002) 65-74.

[38] P. Ciambelli, V. Palma, A. Ruggiero, Appl. Catal. B: Environ. 96 (2010) 18-27.

[39] S. Ito, K. Tomishige, Catal. Commun. 12 (2010) 157-160.

[40] A. Casanovas, J. Llorca, N. Homs, J. Fierro, P. de la Piscina, J. Mol. Catal. A: Chem. 250 (2006) 44-49.

[41] S. Freni, J. Power Sources. 94 (2001) 14-19.

[42] A. Fatsikostas, D. Kondarides, X. Verykios, Catal. Today 75 (2002) 145-155.

[43] F. Frusteri, S. Freni, L. Spadaro, V. Chiodo, G. Bonura, S. Donato, S. Cavallaro, Catal. Commun. 5 (2004) 611-615.

[44] P. Ciambelli, V. Palma, A. Ruggiero, Appl. Catal. B: Environ. 96 (2010

) 190-197.

[45] B. Zhang, X. Tang, Y. Li, W. Cai, Y. Xu, W. Shen, Catal. Commun. 7 (2006) 367-372.

[46] F. Aupretre, C. Descorme, D. Duprez, D. Casanave, D. Uzio, J. Catal. 233 (2005) 464-477.

[47] A. Vizcaíno, P. Arena, G. Baronetti, A. Carrero, J.A. Calles, M.A. Laborde, N. Amadeo, Int. J. Hydrogen Energy. 33 (2008) 3489-3492.

[48] M. Sánchez-Sánchez, R. Navarro, J. Fierro, Int. J. Hydrogen Energy. 32 (2007) 1462-1471.

[49] A. Vizcaíno, M. Lindo, A. Carrero, J. Calles, Int. J. Hydrogen Energy. 37 (2012) 1985-1992.

[50] P. Biswas, D. Kunzru, Int. J. Hydrogen Energy. 32 (2007) 969-980.

[51] S. Chen, Y. Liu, Int. J. Hydrogen Energy. 34 (2009) 4735-4746.

[52] H. Devianto, Z. Li, S. Yoon, J. Han, S. Nam, T. Lim, H.. Lee, Int. J. Hydrogen Energy. 35 (2010) 2591-2596.

[53] T. Montini, L. De Rogatis, V. Gombac, P. Fornasiero, M. Graziani, Appl. Catal. B: Environ. 71 (2007) 125-134.

[54] F. Mariño, G. Baronetti, M. Jobbagy, M. Laborde, Appl. Catal. A: Gen. 238 (2003) 41-54.

[55] F. Mariño, M. Boveri, G. Baronetti, M. Laborde, Int. J. Hydrogen Energy. 26 (2001) 665-668.

[56] E. Örücü, F. Gökaliler, A. Aksoylu, Z. Önsan, Catal. Lett. 120 (2008) 198-203.

[57] F. Soyal-Baltacıoğlu, A. Aksoylu, Z. Önsan, Catal. Today 138 (2008) 183-186.

[58] A. Le Valant, N. Bion, F. Can, D. Duprez, F. Epron, Appl. Catal. B: Environ. 97 (2010) 72-81.

[59] J. Kugai, V. Subramani, C. Song, M.H. Engelhard, Y.-H. Chin, J. Catal. 238 (2006) 430-440.

[60] H. Idriss, Platinum Met. Rev. 48 (2004) 105-115.

[61] A. Vizcaíno, A. Carrero, J. Calles, Catal. Today 146 (2009) 63-70.

[62] Z. Zhang, X. Verykios, Catal. Today 21 (1994) 589-595.

[63] A. Bao, K. Liew, J. Li, J. Mol. Catal. A: Chem. 304 (2009) 47-51.

[64] L. Bai, Y. Zhou, Y. Zhang, H. Liu, M. Tang, Catal. Lett. 129 (2009) 449-456.

[65] S. Andonova, C. Vladov, B. Pawelec, I. Shtereva, G. Tyuliev, S. Damyanova, L. Petrov, Appl. Catal. A: Gen. 328 (2007) 201-209.

[66] J. Comas, F. Mariño, M. Laborde, N. Amadeo, Chem. Eng. J. 98 (2004) 61-68.

Chapter 3

Experimental Techniques

3.1. Catalyst Synthesis

Calcium modified Al_2O_3 supports, denoted as *x* Ca-Al_2O_3 where *x* varies between 0 and 7 wt% for Ca, were prepared. The activated, basic γ-Al_2O_3 (Arcōs Organics) support has a specific surface area of 116 m^2/g, specific pore volume of 0.30 cm^3/g and average pore size of 6.60 nm as measured by BET. $Ca(NO_3)_2 \cdot 4H_2O$ (Riedel-deHaën) dissolved in deionised water was introduced onto γ-Al_2O_3 support using incipient wetness impregnation technique to obtain a paste-like mixture. The resulting mixture was calcined in stationary furnace (Carbolite RWF 1200) with the following temperature profile: (1) heat in air to 373 K at 10 K min^{-1} and dwell for 2 h to remove moisture; (2) heat in air to 1123 K at 10 K min^{-1} and dwell for 8 h.

Supported nickel and noble metal (Pt, Rh, Pd) catalysts were impregnated on calcined Ca modified Al_2O_3 supports using aqueous solution of their respective precursors. The precursors used during the synthesis were nickel ($Ni(NO_3)_2 \cdot 6H_2O$ (Arcōs Organics), $Rh(NO_3)_3$ (Aldrich), $H_2PtCl_6.6H_2O$ (Alfa Aesar) and $Pd(NO_3)_2.xH_2O$ (Aldrich)). The loadings of Ni and the noble metals are 10 wt. % and 1 wt. % respectively, unless otherwise stated. The samples were placed in crucibles and calcined with the following heating profile: (1) heat in air to 373 K at 10 K min^{-1} and dwell for 2 h to remove moisture; (2) heat in air to 723 K at 10 K min^{-1} and dwell for 5 h.

To produce iron promoted Rh/Ca-Al_2O_3 catalysts, a two-step wet incipient impregnation was adopted. First, an appropriate amount of $Fe(NO_3)_3$ solution corresponding to a Fe loading of 10 wt. % was impregnated on Ca-Al_2O_3 support. The precursor was: (1) heated in air at 373 K at 10 K min^{-1} and dwelled for 2 h to remove moisture and (2) heated in air to 723 K at 10 K min^{-1} and dwelled for 5 h. This process is known as the first impregnation step. Subsequently, Rh precursors were impregnated on the resulting mixture from the first impregnation step, following closely to the method previously stated. The catalyst is denoted as Rh-Fe/Ca-Al_2O_3.

3.2. Catalyst Characterization

3.2.1. X-ray Diffraction (XRD)

The crystal structures and particle sizes of the synthesized catalysts were studied using a Bruker D8 Advance Diffractometer system equipped with Cu Kα radiation ($\lambda = 0.154$ nm). The profiles were collected at a step width of 0.02° in the (2θ) range from 20° to 90°.

To estimate the particle size of Ni catalysts, Scherrer's formula given in Eqn. 3.1 was employed.

$$d(NiO) = \frac{k\lambda}{B\cos\theta}\frac{180^o}{\pi} \tag{3.1}$$

where *d(NiO)* is the average particle diameter for NiO particles, k = 0.89 is the Scherrer constant, λ is the X-ray wavelength (0.154 nm for CuKα radiation) and

B is the full width half maximum (FWHM) of NiO diffraction peak. Herein, the particle size was calculated based on NiO XRD peak at 43.1^{o}.

3.2.2. Brunauer-Emmett-Teller (BET)

BET specific surface areas were measured by nitrogen adsorption at 77 K using Autosorb-IC, Quantachrome Instruments. Prior to the measurement, the catalysts of approximately 200 mg were outgassed and heated at 473 K overnight. The average pore diameters and the volume of pores were calculated from the desorption data using the Barret–Joyner–Halenda (BJH) method.

3.2.3. Scanning electron microscopy (SEM), Transmission Electron Microscopy (TEM) and Raman Spectroscopy

The morphology of the carbon deposition on spent Ni catalysts was investigated using scanning electron microscopy (SEM) (JEOL JSM-6700F). Transmission electron microscopy (TEM) images of Ni and Rh catalysts were taken using Tecnai G^2 TF20 S-twin microscopt (FEI Company). Samples were dispersed on carbon grids after sonicating the samples in ethanol for 0.5 h. Raman analysis was conducted using LabRAM HR Raman spectrometer at an excitation wavelength of 514.5 nm at a power of approximately 1 mW, using a 50× objective.

3.2.4. Metal Dispersion Measurements

The catalyst dispersion and H_2 uptake were determined by H_2 chemisorption in Thermo Scientific TPROD 1100. 500 mg of the catalyst was first reduced for 2 h at 873 K. After purging in flowing Ar (30 ml min^{-1}) at room temperature, the sample was exposed to flowing H_2 at a constant rate of 50 ml min^{-1} for 45 min. The catalyst was then purged with 30 ml min^{-1} of Ar for another 30 min, heated from 303 K to 873 K with a ramp rate of 20 K min^{-1} in 50 ml min^{-1} of Ar, and held at 873 K for 30 min. The hydrogen desorbed from the sample was detected by a TCD. In order to determine the fraction of nickel reduced to metallic state, O_2 pulse chemisorption was performed at 723 K. The metal dispersion can be calculated using Eqn. 3.2 employed by Bartholomew et al., assuming adsorption stoichiometry of H/Ni = 1 [1].

$$\%D = \frac{1.17X}{Wf} \tag{3.2}$$

where X refers to hydrogen uptake in μmol $g.cat^{-1}$, W refers to the weight percentage of the nickel and f is the fraction of nickel reduced to metal.

3.2.5. Temperature-programmed reduction (TPR)

Temperature-programmed reduction (TPR) measurements were carried out on Thermo Scientific TPROD 1100 to determine the reduction profiles of the catalysts. 50-100 mg of calcined catalysts was loaded into the reactor cell. The sample was thermally treated under Ar stream at 773 K to remove water and other contaminants. After cooling to 303 K, the sample was heated from 303 K to

1123 K at a rate of 10 K min^{-1} in 50 ml min^{-1} of 5% H_2/Ar and maintained at 1123 K for 15 min while the hydrogen consumption was monitored using a TCD.

3.2.6. Temperature-programmed oxidation (TPO)

The type and the quantity of the carbon deposition on spent catalysts were determined by temperature-programmed oxidation (TPO) in which the sample was heated in 50 ml min^{-1} of 5% O_2/He at a rate of 15 K min^{-1} up to 1023 K and held at this temperature for 15 min. CO_2 emission versus the sample temperature was recorded using mass spectroscopy.

3.2.7. Temperature-programmed desorption (TPD)

Temperature-programmed desorption (TPD) measurements were carried using different probe molecules such as NH_3, CO_2, H_2O, CH_3CH_2OH in a quartz reactor packed with 50-100 mg of catalysts from 303 K to 1023 K, with a linear heating rate of 15 K min^{-1}.

NH_3-TPD profiles were collected using Thermo Scientific TPROD 1100 instrument. 100 mg of ***x***Ca-Al_2O_3 support (***x*** varies between 0 and 7) without Ni was loaded in a quartz tube and pretreated in Ar. After cooling, 30 ml min^{-1} of 10% NH_3/He was passed through the sample for 1 h at a constant temperature of 303 K. Finally, the gaseous and weakly adsorbed ammonia were removed by a steady flow of He for another 1 h. The sample was then heated in 50 ml min^{-1} of He with a heating rate of 20 K min^{-1} up to 873 K. The amount of NH_3 desorbed was

measured by the TCD which was previously calibrated. CO_2-TPD profiles were analyzed using mass spectroscopy (HIDEN Analytical). 150 mg of ***x***Ca-Al_2O_3 support was used in the adsorption of CO_2 at 323 K for 30 min. The samples were purged in Ar for 30 min. Desorption of CO_2 took place while heating the sample from 298 K to 1023 K with a ramp rate of 15 K min^{-1}.

H_2O-TPD was performed to evaluate the water adsorption capacity of bare Al_2O_3 and Ca-modified Al_2O_3. After pretreatment, steam was introduced into the system via a bubbler saturator at 333 K for 40 min. After adsorption, the system was purged with Ar for 1.5 h. The H_2O-TPD profiles were continuously analyzed using mass spectroscopy as it was heated from 303 K to 1023 K with a rate of 15 K min^{-1}.

EtOH-TPD profiles were collected for mechanism study over supports, Ni and noble metal catalysts. Prior to adsorption, the supports were pretreated in Ar at 773 K for 1 h. For the catalysts, they were reduced at 837 K or 473 K for 2 h in flowing H_2 for Ni and noble metal catalysts, respectively. Subsequently, 50 ml min^{-1} of flowing Ar was introduced for 15 min to remove residual H_2 before the adsorption of ethanol/He through a bubbler for 20 min at 303 K. Flowing Ar is used to remove physically adsorbed ethanol for another 30 min. The sample was heated up with a ramp rate of 15 K min^{-1} and the desorbed species were detected using mass spectroscopy. The species were characterized using ***m***/***z*** values = 2, 15, 18, 27, 28, 29, 31 and 44 for H_2, CH_4, H_2O, C_2H_4, CO, CH_3CHO, C_2H_5OH and CO_2, respectively.

3.2.8. *In situ* Diffuse Reflectance Infrared Fourier Transform Spectroscopy (DRIFTS)

Infrared (IR) spectroscopy has been used for many years in heterogeneous catalysis to identify the adsorbed species of the catalyst surface or to identify the active sites on the catalyst surface using probe molecules such as CO, CO_2 or pyridine [2]. It is based on the vibrational techniques whereby vibrational excitations of molecules occur by absorbing infrared light. IR radiation covers a wide frequency range between 10-10000 cm^{-1} and can be classified into far-, mid- and near- IR. For heterogeneous catalysis, mid-IR region, ranging from 200 to 4000 cm^{-1} provides valuable information during adsorbate study.

For an observation of a band in IR spectroscopy, a change in the dipole moment of the molecule during the vibration is necessary for the molecule to be "infrared active". A permanent dipole is not necessary as long as there is a change in dipole moment which is proportional to the intensity of the infrared band. When infrared radiation is absorbed, the energy is converted into two major types of molecular vibrations known as stretching and bending as shown in Fig. 3.1. In Fig. 3.2, some bond can stretch in-phase (symmetrical) or out-of-phase (asymmetric stretching). There are various modes of bending various and are illustrated in Fig. 3.3. Considering the $-CH_2$ molecule, the hydrogen can move in the same direction or in opposition direction, giving one deformation and rocking bending vibrations, respectively. There is also possibility of out-of-plane bending and in-plane bending (Fig. 3.4.) which occur in more complex molecules where

hydrogen is isolated from the more rigid parts of the molecules. The infrared absorption involves discrete, quantized energy levels. However, due to the presence of other rotational motions that accompany the individual vibration motion, continuous absorption bands are observed.

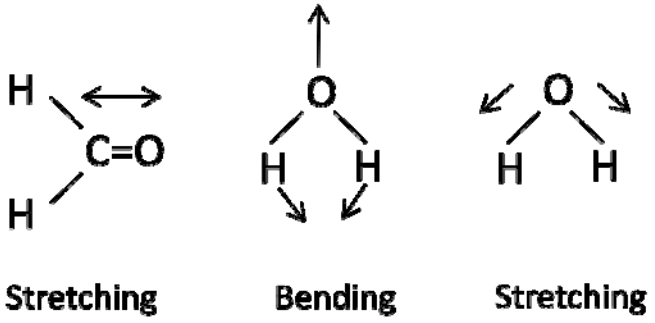

Figure 3.1. Stretching and bending vibrations.

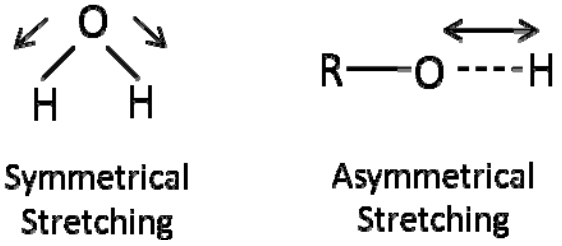

Figure 3.2. Symmetric and asymmetric stretching vibrations.

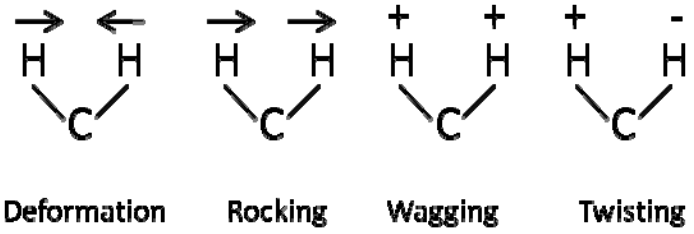

Figure 3.3. Different types of bending vibrations.

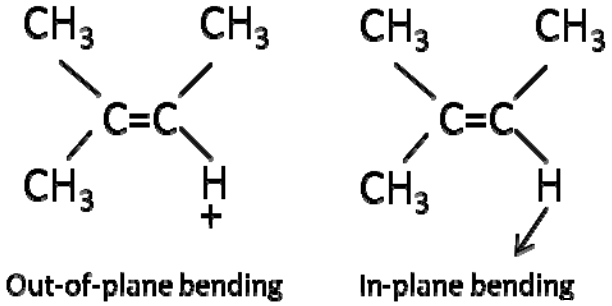

Figure 3.4. Out-of-plane and in-plane bending vibrations.

Fourier-transform infrared (FTIR) spectroscopy enables very faster measurements by measuring all the infrared frequencies simultaneously through the use of a simple optical device known as an interferometer. The interferometer produces a measured signal related to the infrared frequencies in an order of one second. A beamsplitter is employed by most interferometers to split the incroming infrared beam into two optical beams. One fixed, flat mirror is used to reflect off one of the beam while another movable mirror which is within a few millimeters of the beamsplitter is used to reflect off the other beam. The two beams reflect from the mirror and combine at the back of the beamsplitter. The interference of

the two beams yields an interferogram which contains unique information about every infrared frequency that comes from the source. A typical IR setup using an interferometer is as shown in Fig. 3.5. The mathematical method called the Fourier transformation is used to convert the measured interferogram signal into useful frequency spectrum.

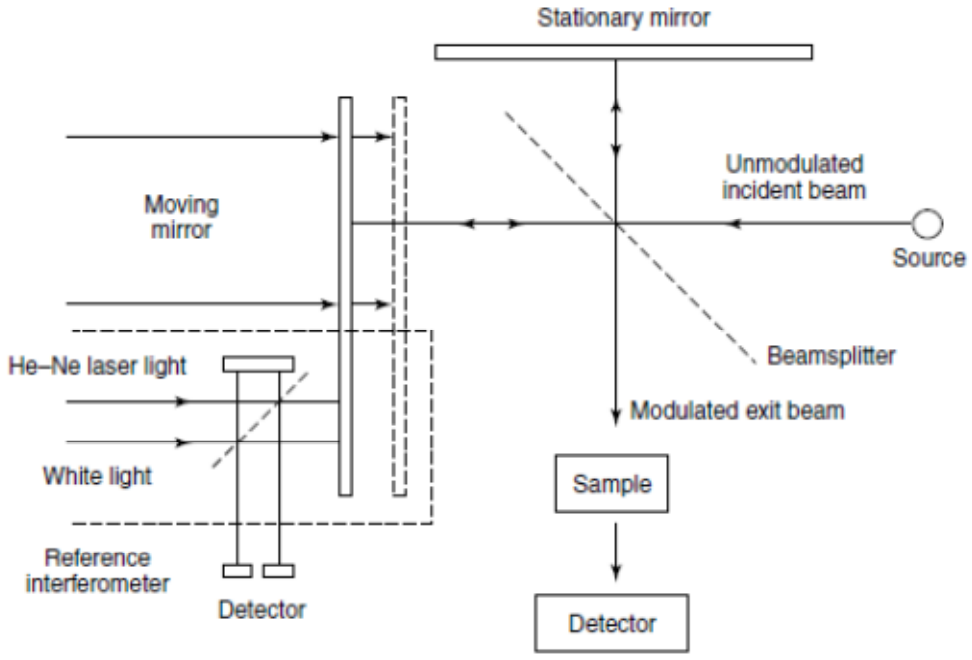

Figure 3.5. Schematic of an interferometer [4].

Diffuse reflectance infrared Fourier transform spectroscopy (DRIFTS) can be used for acquiring IR spectra of rough surface and opaque materials and therefore particularly useful in the field of catalysis to identify adsorbed species. In DRIFTS, the IR beam is directed at an angle on the sample and the incident radiation is scattered in all directions. Large ellipsoidal mirrors are designed to

collect and refocus the diffused scattered light to the detector. A typical DRIFTS setup consists on the focusing mirrors and a dome-shaped stainless steel chamber which is airtight. The interior of the chamber sits a sample cup which can be heated and acts as a small reactor. Gases can be introduced via the gas ports. Fig. 2 illustrates a typical DRIFTS assembly.

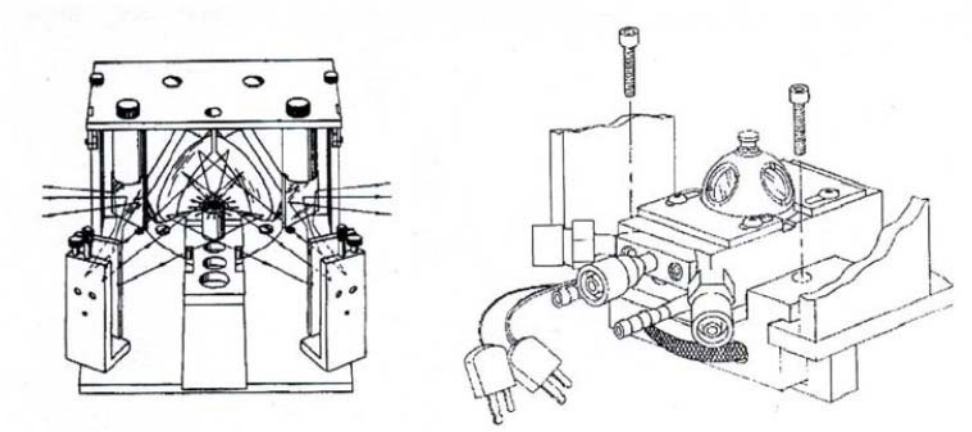

Figure 3.6. *In situ* DRIFTS cell: (a) diffuse reflection assembly and (b) stainless steel reaction chamber with gas ports [5].

In situ DRIFTS was used to evaluate the type of surface hydroxyl groups present on the Al_2O_3, Ca-Al_2O_3 supports and metal supported catalysts. All spectra were recorded at 303 K, based on 256 scans of measurements at a point resolution of 4 cm^{-1} on a Bio-Rad FT-IR 3000 MX using mercury–cadmium–telluride (MCT) detector. The DRIFTS spectrum from powder KBr was used as a reference background. The support sample was placed in a temperature controlled Harrick "Praying Mantis" DRIFTS cell (Harricks HV-DR2) and pretreated at 673 K in He to remove surface moisture and contaminants while the catalyst

sample was first reduced based on standard reduction procedures. The sample was then cooled to 303 K in flowing He.

Probe molecules such as CO and ethanol were used to study the active sites and reaction mechanism of the catalysts. 1% CO/He (20 ml min^{-1}) was introduced at room temperature after the sample has been reduced following standard reduction conditions. CO was adsorbed for 0.1 h and purged for 1 h in flowing He. The spectra were recorded at 303 K, based on 256 scans of measurements at a point resolution of 4 cm^{-1}. The spectrum of the sample taken after reduction was used as reference. The catalysts were heated and IR spectra were taken at variable temperatures between 303 K and 673 K. Similarly, ethanol vapor was introduced via a bubbler and a thermally insulated tube using He carrier. The adsorption took place at 303 K for 20 min on the reduced catalysts and IR spectra were taken after purging the sample for 30 min. The catalysts were heated and IR spectra were taken at variable temperatures between 303 K and 673 K. The spectrum of the sample taken after reduction was used as reference.

3.2.9. X-ray Photoelectron Spectroscopy (XPS)

Photoelectron spectroscopy (PES) is used to investigate the elemental composition, chemical and electronic state of the material, particularly at surface level. The working principle is based on the photoelectric effect whereby when a photon with certain energy hits an atom, the atom releases a photoelectron. A photoelectron will escape from the atom if the energy of the photon is higher than

the binding energy of the electrons in the atom (Fig. 3.7) The kinetic energy is measured by a spectrometer. To calculate the binding energy of the electrons from the measured kinetic energy, one can use the following equation (Eqn. 3.3.)

$$BE = hv - KE - Fspec \quad (3.3)$$

where KE is the electron kinetic energy, BE refers to the binding energy of the atom, F_{spec} refers to the spectrometer work function and hv is the energy of the incoming photon.

This PES technique can be divided into ultraviolet photoelectron spectroscopy (UPS) and X-ray photoelectron spectroscopy (XPS) depending on the source of excitation radiation and energy of the excited electrons. In UPS, only photoelectrons emitted from the valence band or shallow core levels (E < 40 eV) can be accessed by using ultraviolet light from helium lamp source (He I radiation of 21.2 eV and He II radiation of 40.8 eV). In XPS, photoelectrons are emitted from the core level (E > 40eV) by applying soft X-ray radiation such as AlKα ($h\upsilon$ = 1486.6 eV) and MgKα ($h\upsilon$ = 1253.6 eV). It is also possible to initiate the release of Auger electrons through X-ray induced auger electron spectroscopy (XAES). The Auger electrons which are produced as consequence of the XPS primary process are emitted as the ionized atom returns to its ground state. For example, a hole on the K level is produced after the initial removal of the core state electron. The hole is filled with an electron coming from an outer level such as L_1 as the atom relaxes. This results in the availability of excess energy (E_K-E_{L1}) which is transferred to another electron to be ejected as an Auger electron. Each Auger transistion is labelled according to the shell that (1) the core electron is

ejected from, (2) the shell from which an electron relaxes into the core hole and (3) the shell from which the Auger electron is emitted. Based on the illustration in Fig. 3.7(b), the process is denoted as $KL_1L_{2,3}$. The Auger peaks provide valuable chemical information about an atom.

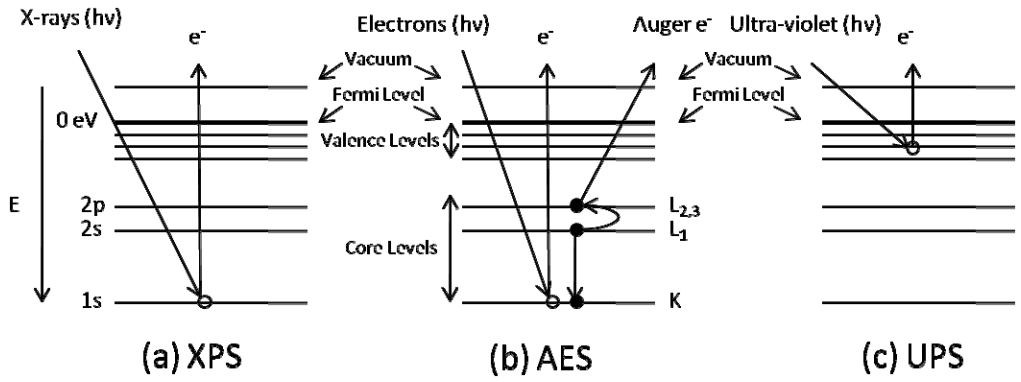

Figure 3.7. Schematic diagram of (a) X-ray photoelectron emission; (b) Auger emission and (c) ultraviolet photoelectron emission.

A typical XPS instrument consists of the following parts: (1) an X-ray source, (2) an electron energy analyzer combined with a detection system and (3) a sample stage in a vacuum chamber (Fig. 3.3). The X-ray source depends on the choice of anode. The most common configuration is the use of twin anode which supplies AlKα and MgKα photons. A quartz monochromator is utilized to adjust the X-ray line width in order to achieve the best energy resolution obtained in a XPS spectrum. A hemispherical sector analyzer is commonly used for the detection of electrons. An ultra high vacuum system of typically in the range of 10^{-8} to 10^{-10} torr is required to prevent the loss of electron energy and to minimize the formation of monolayer of residual gas adsorbed on the sample.

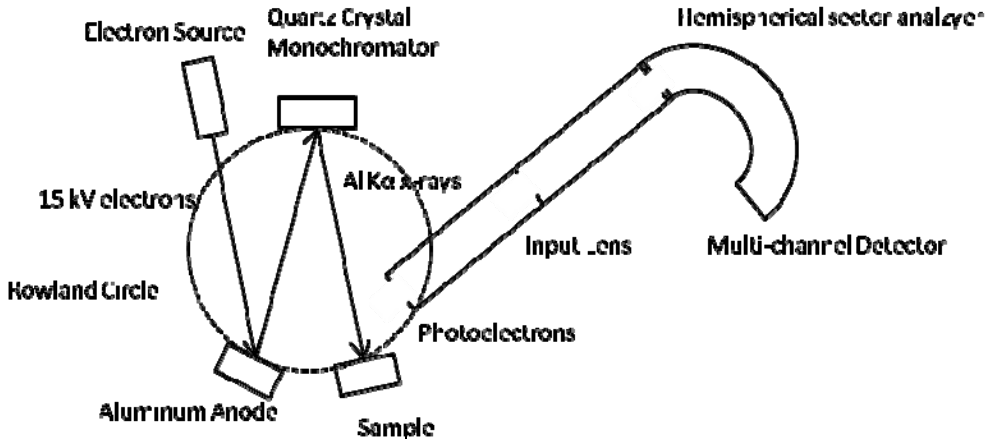

Figure 3.8. Schematic diagram of a typical XPS set-up.

In this study, XPS spectra were obtained on Themo ESCALAB 250, using MgKα ($h\upsilon = 1253.6$ eV) as photon source. To study the reduced catalysts, samples were reduced ex situ (unless otherwise stated) using the standard reduction conditions and transferred into the XPS chamber under Ar protection. Fig. 3.9 shows an example of the wide energy scan of as calcined Ni/Al_2O_3. In the spectrum, a number of peaks were observed and can be grouped into three types with peaks originating from photoemission (1) from core levels, (2) from valence level at low binding energies (0 to 20 eV) and (30 from X-ray excited Auger emission. Detailed XPS scans of the main photoelectron peaks such as Ni 2p, Al 2p, O 1s and valence band were obtained for detailed analysis. In deriving the binding energies of the concerned elements, the binding energies were first adjusted relative to C1s at 284.5 eV. The spectrum was fitted with a Shirley background

using XPS Peak 4.1. The peaks were deconvoluted using with Gaussian–Lorentzian peak shape to obtain an optimum fit.

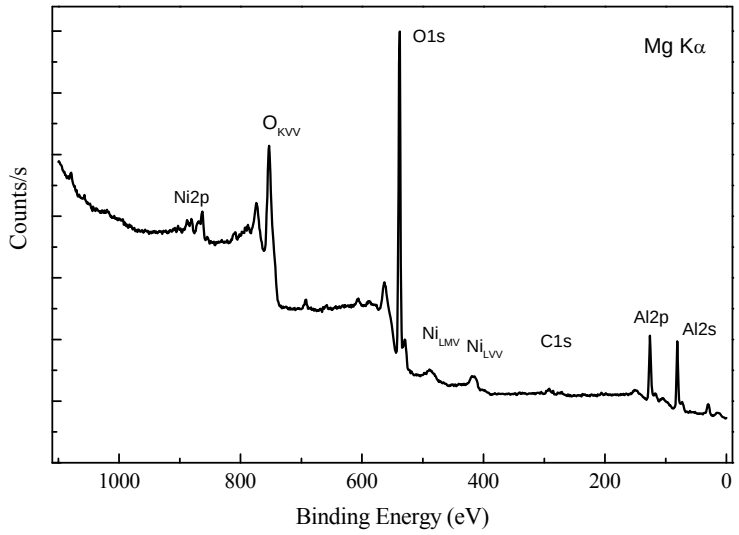

Figure 3.9. Wide energy scan of as calcined Ni/Al_2O_3 catalyst.

3.2.10. X-ray Absorption Near Edge Spectroscopy (XANES)

X-ray absorption spectroscopy (XAS) is commonly used to determine the electronic and geometric structure of a material using tunable high intensity X-ray radiation. A synchrotron light source consists of a circuit of accelerated electrons that give off X-ray phonons, which can excite an electron from a core level to a continuum state through the absorption of a photon. The kinetic energy of this photoelectron is equal to the difference in energy of the incoming X-ray and the binding energy of the electron to the atom. When the energy of the incoming X-ray exceeds the binding energy of the electron, a sharp increase in the absorption signal corresponding to the emission of a photoelectron is observed. This is

known as the absorption edge. The absorption energy is unique for each element as each element has individual binding energies of its electrons in different shells of the absorbing elements for example the K, L and M shells. They are represented by K, L_I, L_{II}, L_{III}, M_I which corresponds to the excitation of an electron from 1s, 2s, $2p_{1/2}$, $2p_{3/2}$, 3s orbitals respectively (Fig. 3.10(a)). Hence, XAS is an element-specific technique. The XAS spectrum has 3 regions (Fig. 3.10(b)): the pre-edge, the X-ray absorption near edge structure (XANES) and the extended X-ray fine structure (EXAFS).

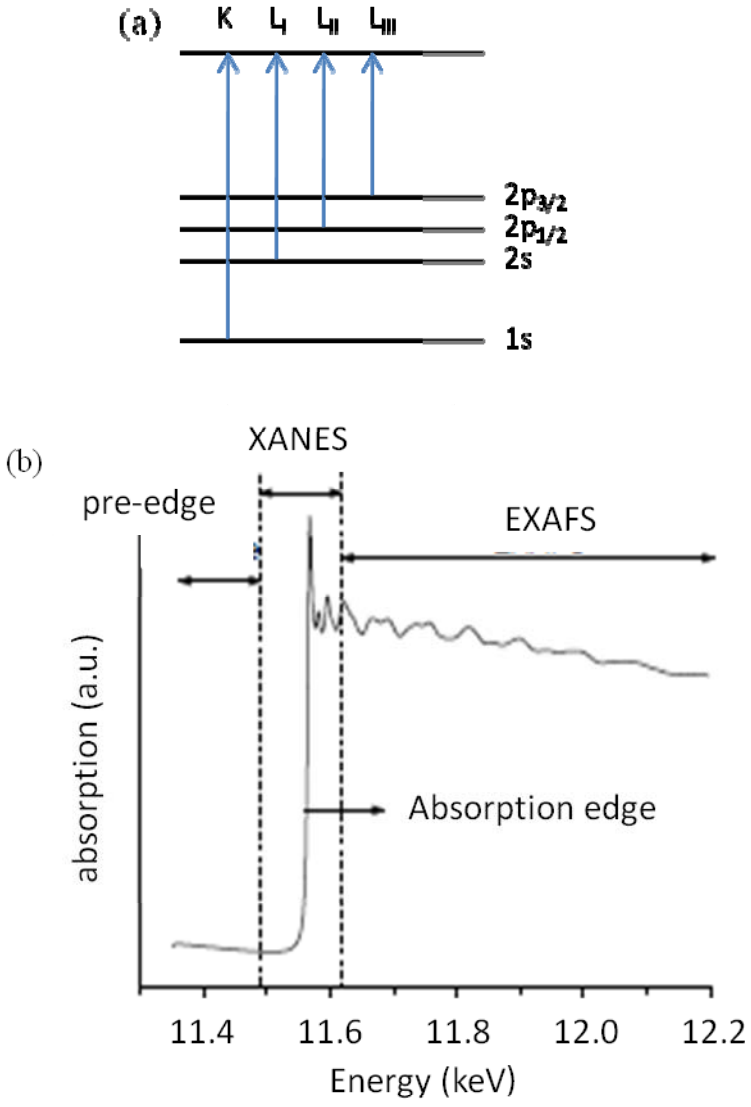

Figure 3.10. (a) Excitation of core electrons by X-ray and (b) regions of an XAS spectrum.

In the pre-edge region, quadrupole transition takes place from 1s core state to an empty 3d state. This transition is weak and only small pre-edge features are observed. In XANES region, important information such as the oxidation state and the local structure of the material can be extracted from the energy position of the absorption edge, intensity of the whiteline and shape of the XANES spectra. The first intense feature after the absorption edge is known as the whiteline. This feature is extremely useful in determining the oxidation state of the material. When a material is oxidized, the whiteline is expected to be more intense as more energetic X-ray is require to eject a core electron from its fully oxidized state. EXAFS region is generally recognized in the XAS spectrum with ~ 30 eV above the edge. This part of the spectrum results from the scattering of free electron on neighboring atoms in the matrix. The scattering and backscattering of photoelectrons create constructive and destructive interferences which influence the electron wave function as a function of the photon energy, thereby producing EXAFS oscillations. Hence, EXAFS investigates the structural information of the material, providing useful characterization of atomic distances and coordination numbers.

In this study, XANES spectra were measured on references and catalyst samples at Shanghai Synchrotron Radiation Facility (SSRF) using BL14W1 beamline. The X-ray ring has a flux of 2 x 1e12 photons per second at 200 mA and 3.5 GeV, and the energy range capability is 4-22.5 keV. Si(111) double crystals

were used as monochromator. The energy resolution is about 2 x 10e-4 at 10 keV. The catalysts were reduced under reaction conditions before collection of spectra at room temperature.

3.2.11. Tapered Element Oscillating Microbalance (TEOM)

Coke formation is an important field of study in many heterogeneous catalytic processes. In order to determine the rate of coke formation, conventional microbalance is often used to study the coke content of the catalysts with large part of the feed bypassing the catalyst sample. This prevents gradientless differential operation which would be useful to obtain uniform coke deposits. In tapered element oscillating microbalance (TEOM), the catalyst is placed at the tip of an oscillating tapered quartz element. The tapered element oscillates in a clamped-free mode as a cantilever beam. In the design, the gases are made to flow through the bed of catalyst, such that it can be considered as a differential operation in an ideal plug flow fixed bed reactor. As the gases interact with the catalyst, any change in mass is detected as a change in its vibrational frequency and is recorded by optics. At the outlet of the TEOM, a mass spectrometer (MS) or gas chromatograph (GC) can be connected for online analysis. A purge gas is passed through the external of the hollow quartz reactor tube to sweep the affluent at the rear end of the system. The systematic diagram of TEOM is as shown in Fig. 3.11.

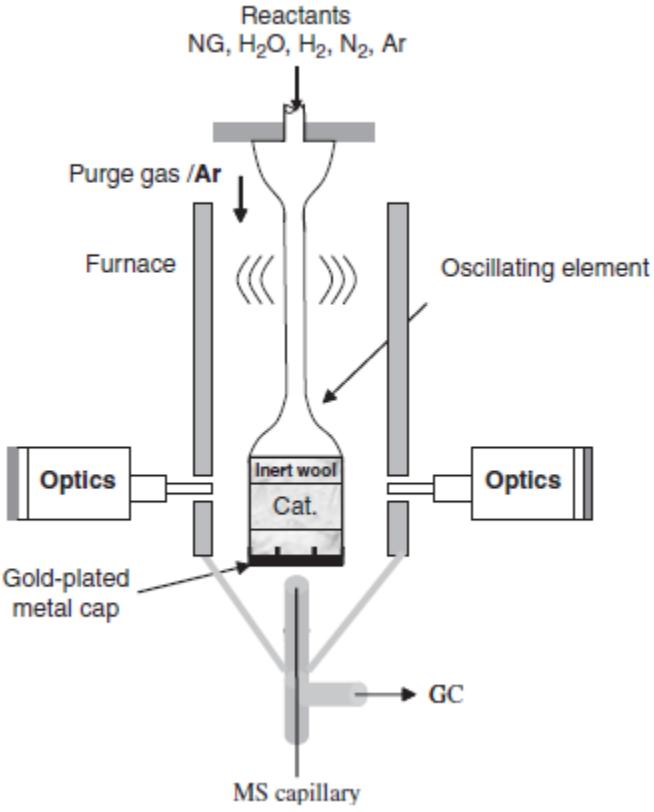

Figure 3.11. An illustration of TEOM [6].

Since the working principle of TEOM is based on the change in vibrational frequency, the change in mass change is given by Eqn. 3.4.

$$\Delta m = m_2 - m_1 = K_0(\frac{1}{f_2^2} - \frac{1}{f_1^2}) \quad (3.4)$$

where Δm is the change of mass with time, K_0 is the spring constant and f_1 and f_2 are the vibrational frequencies at the beginning of the experiment and during the experiment, respectively. An excellent review of the principles and applications of TEOM is detailed in reference [6].

In this thesis, methane decomposition study was conducted in TEOM (Rupprecht and Patashnick Co., Albany NY) to study the rate of coke deposition on Ni-based catalysts. 50 mg of the Ni catalyst was carefully loaded between two layers of quartz wool at the tip of the quartz oscillating element. The catalyst was reduced by H_2 at 873 K for at least 2 h. The sample was purged with flowing He after reduction. 50 ml min^{-1} of 10% CH_4/Ar was introduced into TEOM, passing through the reduced nickel catalyst at 773 K for 20 min. The mass change as a result of methane decomposition was monitored.

To study the steam gasification of the coke deposition, the coke-deposited catalyst was cooled to 423 K in TEOM and steam in flowing Ar at a rate of 0.002 ml min^{-1}. The catalyst was heated to 1023 K in the presence of steam with a ramp rate of 10 K min^{-1}. The steam gasification products such H_2, CO and CO_2 were detected versus temperature, using mass spectroscopy.

3.3. Catalytic Evaluation

The catalytic evaluation experiments were performed using a fully automated, customized 5-channel quartz micro-reactor (BEL-REA-5, Japan). The process flow diagram is illustrated in Fig. 3.12. Each of the quartz reactor tube was loaded with 100 mg of the catalyst. Temperatures of the samples were individually monitored with thermocouples located just on top of the catalyst samples. The catalysts were reduced by hydrogen at 873 K for 2 h via the common reactors gas inlet. During reaction, 40 ml min^{-1} of Ar was flown into one of the selected reactor tube, along with 0.005 ml min^{-1} of ethanol–water mixture

(1:10 molar ratio) which was injected by a Shimadzu Liquid Pump and vaporized at 443 K within the reactor. The total gas hourly space velocity was kept constant at 27,000 ml (g-cat h)$^{-1}$, monitored by mass flow controller. In the meantime, the remaining catalysts in three other quartz tubes are protected under flowing Ar from the common reactors gas inlet.

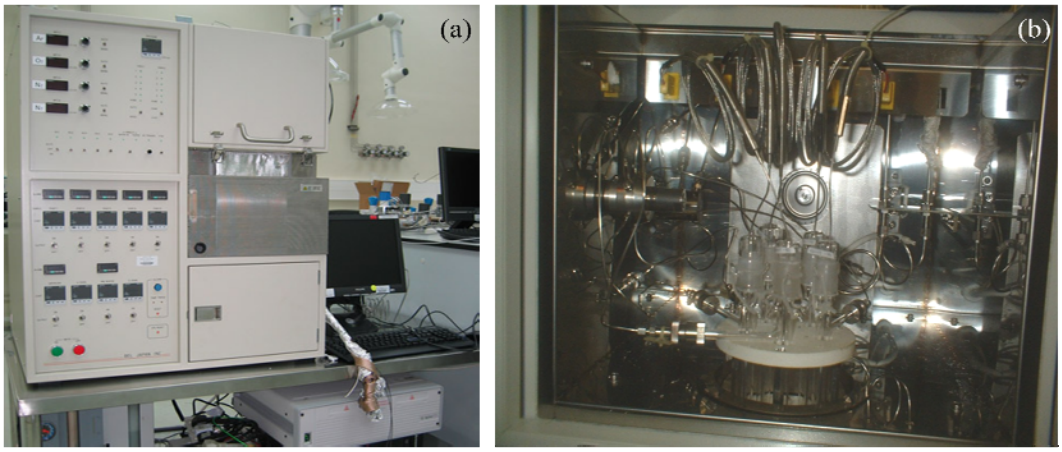

Figure 3.12. (a) Fully automated 5-channel quartz micro-reactor; (b) interior of reactor and (c) simplified process flow diagram for ESR.

The reaction products were analyzed online using a gas chromatograph (GC) (Varian CP-3800) with three columns: Porapak Q and Haysep Q, molecular sieve 5A. Porapak Q was used to separate organics and carbon dioxide with He as

carrier gas while the later two columns with Ar carrier gas were used for the separation of hydrogen, carbon monoxide and methane. Conversion of ethanol (X_{EtOH}) and selectivity to carbon containing species (S_{Ci}) were calculated based on Eqns. 3.5 and 3.6, respectively.

$$X_{EtOH} = (1 - \frac{2 \times mol_{EtOH_{out}}}{\sum_i^N mol\ C_i + 2 \times mol_{EtOH_{out}}}) \times 100\% \quad (3.5)$$

$$S_{Ci} = \frac{molC_i}{\sum_i^n molC_i} \times 100\% \quad (3.6)$$

where C_i represents a C-containing product. The selectivity S_{Ci} was calculated based on detected carbon numbers only, assuming that no coke was formed during the reaction. The yield of C-containing product was calculated by $X_{EtOH} \times S_{Ci}$. H_2 yield (Y_{H2}) was evaluated in terms of the number of moles of H_2 produced per mole of fed ethanol.

3.4. References

[1] C.H. Bartholomew, R.B. Pannell, J.L. Butler, J. Catal. 65 (1980) 335-347.

[2] J. Ryczkowski, Catal. Today 68 (2001) 263-381.

[3] B.H. Stuart, Infrared Spectroscopy: Fundamentals and Applications, John Wiley & Sons, Ltd, 2005, pp. 1-13.

[4] B.H. Stuart, Infrared Spectroscopy: Fundamentals and Applications, John Wiley & Sons, Ltd, 2005, pp. 15-44.

[5] B.M. Weckhuysen, R.A. Schoonheydt, Catal. Today 49 (1999) 441-451.

[6] D. Chen, E. Bjorgum, K.O. Christensen, A. Holmen, R. Lodeng, C.G. Bruce, K.z. Helmut, Advances in Catalysis, Academic Press, 2007, pp. 351-382.

Chapter 4

Investigation of Ethanol Steam Reforming Catalysis over Ca-Al_2O_3

Graphical Abstract

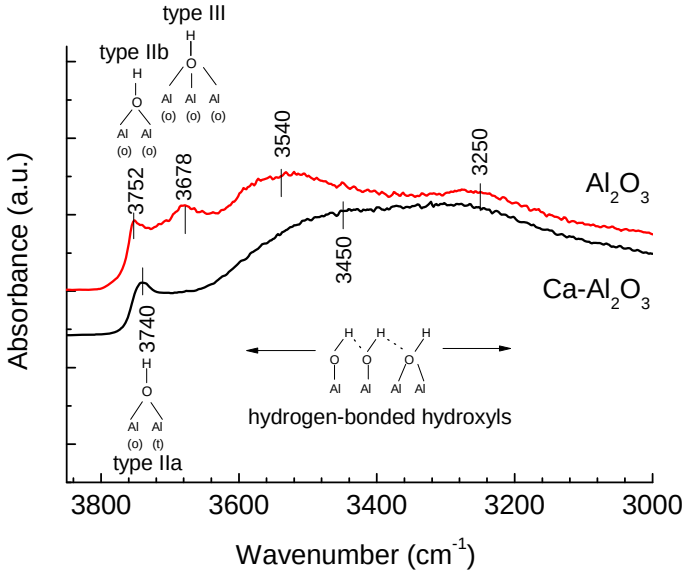

The effect of Ca modification to Al_2O_3 support in ethanol steam reforming was studied by using a 5-channel micro-reactor, *in situ* diffuse reflectance infrared Fourier transform spectroscopy (DRIFTS), temperature-programmed desorption (TPD) of probe molecules H_2O, NH_3, CO_2 and ethanol and X-ray photoemission spectroscopy (XPS). Both Al_2O_3 and Ca-modified Al_2O_3 supports are not catalytically active for the ethanol reforming. The introduction of Ca greatly reduces the acidity of Al_2O_3, depressing ethanol dehydration and ethylene formation. It brings about positive attributes such as increasing water adsorption,

providing the abundance of adsorbed OH groups. The involvement of OH groups in the reactions in turn enhances the ethanol adsorption, stabilizes its adsorbate intermediates for further conversions to H_2, CH_4 and CO_2 at relatively low temperatures. This paper therefore serves to illustrate the importance of acidity and steam adsorption capacity in the design of the catalysts for ethanol steam reforming.

4.1. Introduction

To date, gamma-alumina (γ-Al_2O_3) is one of the many important catalytic supports for catalysis applications because of its high surface area, thermal, mechanical stabilities and its acid/base characteristics [1]. γ-Al_2O_3 is widely use as a catalysts support for ESR [2, 3]. Gamma-alumina has a defect cubic spinel structure almost similar to magnesium spinel ($MgAl_2O_4$). Aluminum atoms occupy both the tetrahedral and octahedral cation positions among the cubic close-packed stacking of oxygen layers [4]. In order to fulfill the stoichiometry of Al_2O_3, some of the lattice positions remain empty as vacancies. The interaction of water vapor with Al_2O_3, resulting in surface hydroxyls, helps to achieve valency saturation and to a large extent governs the chemistry of the oxide surface. Indeed, the surface of γ-Al_2O_3 is characterized by a variety of surface hydroxyls which are often identified using infrared spectroscopy.

Five different types of OH groups as shown in Fig. 4.1 can be found on (1 1 1), (1 1 0) and (1 0 0) faces of γ-Al_2O_3 [5]. Type Ia hydroxyl anion is made up of a tetrahedrally coordinated Al^{3+} (Al^{IV}) while type Ib consists of an octahedral Al^{3+} group (Al^{VI}). On type II hydroxyl groups, OH group forms a bridged between one Al^{IV} and one Al^{VI} (type IIa) or between two Al^{VI} (type IIb). Type III surface hydroxyls are bounded to three Al^{VI}. Krözinger and Ratnasamy have determined the order of increasing positive charge at the hydroxyl group by estimating the net charges at the hydroxyl group and the oxygen atom of the group after proton removal. It is shown that the order of increasing positive charge is the following

order: Ib < Ia < IIb < IIa < III. Based on such interpretation, type III hydroxyls will have the largest Brönsted acidity while type Ib has the greatest basicity. This model, however, works based on some assumptions which neglect factors such as local chemical environment (hydroxylation/dehydroxylation) and hence has some deficiencies in the interpretation.

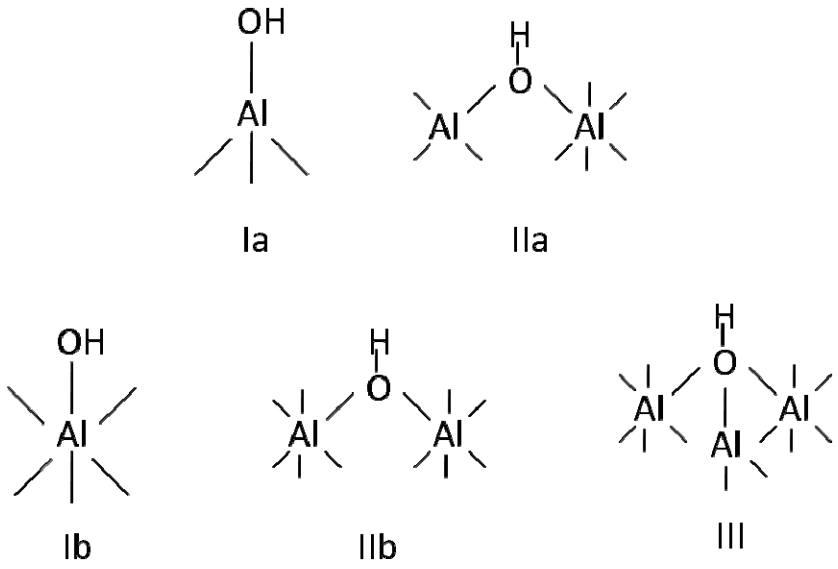

Figure 4.1. Different types of OH groups.

Alumina can under dehydroxylation to remove OH groups during high temperature treatment. During the process, coordinatively unsaturated suface (*cus*) cations such as Al^{IV} and Al^{VI} are created. This is accompanied by the formation of oxide anions. These partly uncoordinated metal cations and oxide anions are known as Lewis-acid sites and Lewis-base sites respectively. Rehydroxylation of the surface leads to the conversion of Lewis sites on a

dehydrated surface to creation of Brönsted sites. The above dehydroxylation/rehydroxylation process is illustrated simply in Fig. 4.2.

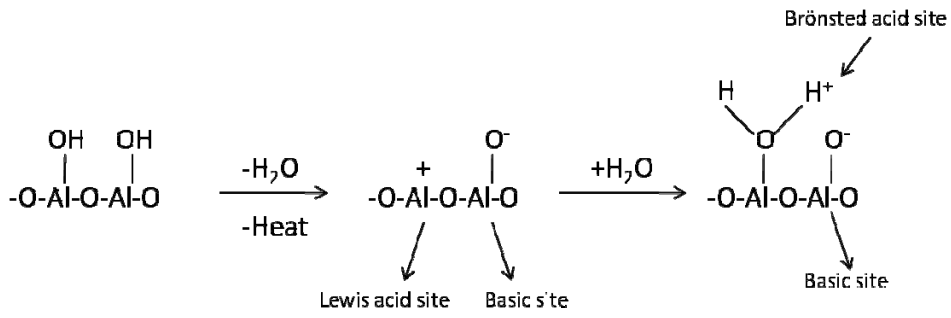

Figure 4.2. Dehydroxylation and rehydroxylation process on alumina.

The acid-basic nature of alumina is responsible for the chemistry of the oxide, especially during ethanol steam reforming whereby ethanol and steam react to produce CO_2 and H_2 (ESR, Eqn. 4.1). During ESR, ethanol can dehydrate (Eqn. 4.2) and dehydrogenate (Eqn. 4.3) rapidly to ethylene and acetaldehyde respectively.

$$C_2H_5OH + 3H_2O \rightarrow 2CO_2 + 6H_2 \quad (4.1)$$

$$C_2H_5OH \rightarrow C_2H_4 + H_2O \quad (4.2)$$

$$C_2H_5OH \rightarrow CH_3CHO + H_2 \quad (4.3)$$

Dehydration of ethanol to ethylene via a E_{1cB} mechanism and an E_2 concerted mechanism (Fig. 4.3) [6]. The difference of the two mechanisms lies in the distribution of acid and basic sites. The E_{1cB} mechanism in Fig. 4.3(a) requires

both strongly basic sites and weak Lewis acid sites where adsorption of ethanol and the rupturing of the O-H bond will take place, resulting in ethoxides. Following this, the most acidic proton in the ethoxide is abstracted on the basic site and finally producing the olefin, An E_2 mechanism involves the participation of both acidic and basic sites (Fig. 4.3(b)). In a concerted fashion, OH groups are extracted by Al acidic sites while the β-hydrogen of the alcohol will bind to the surface oxide basic anion site. A weak Lewis acid site and a strong Brönsted basic site, similar to those required for E_{1cB} mechanism, are needed for the dehydrogenation of ethanol to acetaldehyde (Fig. 4.4). The mechanism involves the abstraction of H from the OH by the strong Brönsted basic site, leaving behind the ethoxy group on the weak Lewis acid site. Further abstraction of H on α-C by the strong Brönsted basic site, will lead to the formation of acetaldehyde. Due to the acid sites (either Lewis or Brönsted) on alumina, ethanol adsorption often leads to the formation ethylene [7, 8]. During ESR, such intermediate is undesirable due to its propensity to form coke deposits [2, 9] . Modification of alumina using different metal oxides such as La_2O_3, MgO and ZrO_2 is aimed at increasing reaction stability and improving product selectivity during ESR [10]. Sánchez-Sánchez et al. investigated the catalytic activity of nickel catalysts supported on Al_2O_3 with different lanthanum loading [11]. It was found that the addition of La neutralizes part of the acidity of Al_2O_3, resulting in the decrease in ethylene formation while favoring of dehydrogenation. Enhanced stability was also observed over La doped catalysts, due to lower coke formation.

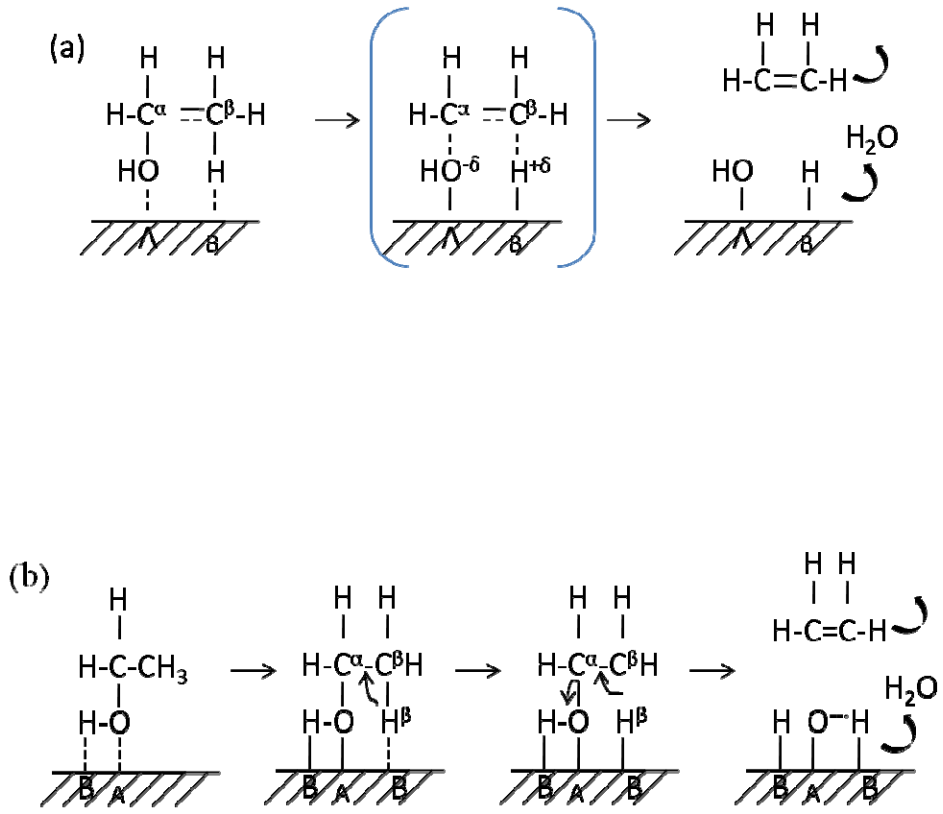

Figure 4.3. Schematic illustration of ethanol dehydration via (a) E_{1cB} and (b) E_2 mechanism.

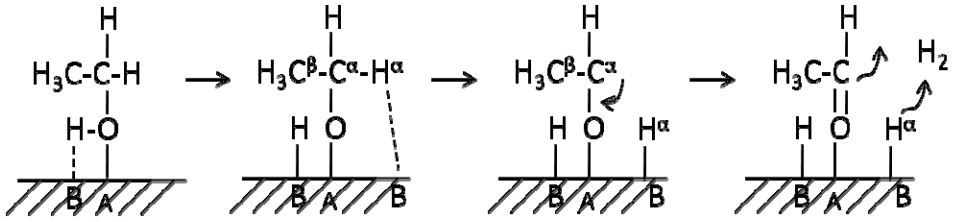

Figure 4.4. Schematic illustration of ethanol dehydrogenation via E_{1cB} mechanism.

In this study, the goal is to design a suitable catalyst support for ESR which promises excellent catalytic stability and product selectivity, particularly at low reaction temperature. Central to this idea, calcium emerges as a suitable candidate for further exploration. Calcium is a well known alkaline earth metal with basic property and has been used as a catalyst promoter by various research groups in different kinds of reactions, such as methane dry reforming [12], Fischer–Tropsch synthesis [13], propane dehydrogenation [14] and dehydrosulfurization of petroleum feedstocks [15]. Its basic property improves catalysts performance by reducing the acidic sites of the support and thus decreases coke formation [16]. Vizcaíno et al. found that coke deposition during ESR was reduced to almost one third of the amount with CuNi/SBA when the catalyst was modified with Ca [16]. Apart from the modification of acid/basic property by the alkali rare earth metal, Ca was also found to reduce the reactivity of coke deposits. Zhang and Verykios reported that the addition of CaO in the support improves the stability of the Ni/Al_2O_3 catalysts [12]. This is due to enhanced reactivity of carbon species which are easier to be removed during reaction conditions. Hence, the addition of calcium has led to positive catalytic effect in terms of higher activity and coke resistance. However, the information on the effect of CaO modification on Al_2O_3 and its use as a catalyst support for ESR is limited. In this chapter, a detailed study on the properties of Ca-modified Al_2O_3 support is reported. Careful investigation using various techniques such as temperature programmed desorption (TPD) of NH_3, CO_2, ethanol, *in situ* diffuse

reflectance infrared spectroscopy (DRIFTS) and X-ray photoemission spectroscopy (XPS) were performed. Fixed bed catalytic experiments performed under ESR conditions were conducted to evaluate the effect of Ca addition in this reaction.

4.2. Experimental

4.2.1. Catalyst Support Synthesis and Pretreatment

$Ca(NO_3)_2 \cdot 4H_2O$ (Riedel-deHaën) dissolved in deionised water was introduced onto activated, basic γ-Al_2O_3 (Arcōs Organics) support using incipient wetness impregnation technique. The resulting mixture was calcined in air at 1123 K for 8 h to obtain Ca-modified Al_2O_3, denoted as *x* Ca-Al_2O_3 where *x* varies between 0 and 7 wt% for Ca.

The samples for temperature-programmed adsorption/desorptions (NH_3-, CO_2-, H_2O-, EtOH-TPD) experiments were preheated in 50 ml/min of Ar stream from 298 K to 773 K for 1 h to remove any moisture, surface contaminants such as carbonates. Heating rate was maintained at 10 K/min.

4.2.2. Physicochemical Properties

Powder X-ray diffraction (XRD) patterns of the samples after calcination were analyzed with Bruker AXS XRD system equipped with Cu Kα radiation (λ = 0.154 nm). The profiles were collected at a step width of 0.02° in the (2θ) range from 20° to 90°. BET specific surface areas were measured by nitrogen

adsorption at 77 K using Autosorb-IC, Quantachrome Instruments. Prior to the measurement, the catalysts were outgassed and heated at 473 K overnight. The average pore diameters and the volume of pores were calculated from the desorption data using the Barret–Joyner–Halenda (BJH) method.

4.2.3. Temperature Programmed Desorption (TPD) of NH_3, CO_2, H_2O and Ethanol

NH_3-TPD profiles were collected using Thermo Scientific TPROD 1100 instrument. 100 mg of ***x***Ca-Al_2O_3 support (***x*** varies between 0 and 7) without Ni was loaded in a quartz tube and pretreated in Ar. After cooling, 30 ml/min of 10% NH_3/He was passed through the sample for 1 h at a constant temperature of 303 K. Finally, the gaseous and weakly adsorbed ammonia were removed by a steady flow of He for another 1 h. The sample was then heated in 50 ml min^{-1} of He with a heating rate of 20 K min^{-1} up to 873 K. The amount of NH_3 desorbed was measured by the TCD which was previously calibrated. CO_2-TPD profiles were analyzed using mass spectroscopy (HIDEN Analytical). 150 mg of ***x***Ca-Al_2O_3 support was used in the adsorption of CO_2 at 323 K for 30 min. The samples were purged in Ar for 30 min. Desorption of CO_2 took place while heating the sample from 298 K to 1023 K with a ramp rate of 15 K min^{-1}.

H_2O-TPD was performed to evaluate the water adsorption capacity of bare Al_2O_3 and Ca-modified Al_2O_3. After pretreatment, steam was introduced into the system via a bubbler saturator at 333 K for 40 min. After adsorption, the system

was purged with Ar for 1.5 h. The H_2O-TPD profiles were continuously analyzed using mass spectroscopy as it was heated from 303 K to 1023 K with a rate of 15 K min^{-1}.

EtOH-TPD profiles were collected for mechanism study. Prior to adsorption, 50 mg of the sample was reduced at 837 K for 2 h in H_2. They were purged in 50 ml min^{-1} of Ar for 15 min to remove residual H_2 before the adsorption of ethanol/He through a bubbler for 20 min at room temperature. Subsequently, Ar was flown for 30 min to remove physically adsorbed ethanol. The sample was heated up with a ramp rate of 15 K min^{-1} and the desorbed species were detected using mass spectroscopy. The species were characterized using ***m*/z** values = 2, 15, 18, 27, 28, 29, 31 and 44 for H_2, CH_4, H_2O, C_2H_4, CO, CH_3CHO, C_2H_5OH and CO_2, respectively.

4.2.4. Diffuse Reflectance Infrared Fourier Transformed Spectroscopy (DRIFTS)

The type of surface hydroxyl groups present on the supports or catalysts was determined using DRIFTS. All spectra were recorded at 303 K, based on 128 scans of measurements at a point resolution of 4 cm^{-1} on a Bio-Rad FT-IR 3000 MX with mercury–cadmium–telluride (MCT) detector. The DRIFTS spectrum from power KBr was used as a reference background. The support sample was placed in the reaction cell and pretreated at 673 K in He to remove surface moisture and contaminants while the catalyst sample was first reduced at 873 K

for 2 h. The sample was then cooled to 303 K in flowing He. For the ethanol adsorption and decomposition studies IR background spectrum from the support/catalyst sample was recorded at 303 K under He. Ethanol vapor was then introduced through a bubbler and a thermally insulated tube using He carrier. The adsorption took place at 303 K for 20 min on the reduced catalysts and IR spectra were taken after purging the sample for 30 min. The catalysts were heated and IR spectra were taken at variable temperatures between 303 K and 673 K. All the spectra shown in this study were obtained after background subtraction.

4.2.5. X-ray Photoemission Spectroscopy (XPS)

X-ray photoelectron spectra were obtained on Themo ESCALAB 250, using MgKα ($h\upsilon$ = 1253.6 eV) as photon source. The instrument was calibrated with respect to graphitic C 1s at 284.5 eV.

4.2.6. Catalysts Activity and Selectivity

The catalytic evaluation experiments were performed in customized 5-channels quartz micro-reactor (BEL, Japan), each of which was loaded with 100 mg of the catalyst. Temperatures of the samples were individually monitored with thermocouples located just on top of the catalyst samples.

The metal-free Ca-Al_2O_3 catalysts were heated up to 673 K. Then 40 ml min^{-1} of Ar was flown in, along with 0.005 ml min^{-1} of ethanol-water mixture (1:10 molar ratio) which was injected by a Shimadzu Liquid Pump and vaporized

at 443 K within the reactor. The total gas hourly space velocity (GHSV) was kept constant at 34,000 h^{-1}, monitored by mass flow controller. The reaction products were analyzed online using a gas chromatograph (GC) (Varian CP-3800) with three columns: Porapak Q and Haysep Q, molecular sieve 5A. Porapak Q was used to separate organics and carbon dioxide with He as carrier gas while the later two columns with Ar carrier gas were used for the separation of hydrogen, carbon monoxide and methane. Conversion of ethanol (X_{EtOH}) and selectivity to carbon containing species (S_{Ci}) were calculated based on Eqns. 3.5 and 3.6 in Chapter 3, respectively.

4.3. Results and Discussions

4.3.1. BET

In Table 4.1, the BET surface areas of the supports are shown. A decrease in the specific surface areas is observed with progressive increase in Ca content impregnated onto Al_2O_3. The surface area of 7Ca-Al_2O_3 (S_{BET} = 53.3 m^2/g) is nearly half in comparison to Al_2O_3 (S_{BET} = 116 m^2/g). This decrease is likely due to plugging of the pores by Ca. The average pore diameters of all the supports are determined by BJH method (Table 4.1). The average pore diameters are in the range of 6-10 nm, suggesting the mesoporous nature of the supports. The pore diameters of all the Ca modified Al_2O_3 are bigger than Al_2O_3, therefore giving lower surface area.

Table 4.1. BET surface area of Ca-modified Al_2O3 supports.

Catalyst Support	$S_{BET}(m^2/g)$	$V_p\,(cm^3/g)$	$D_p\,(nm)$
Al_2O_3	116	0.30	6.60
3Ca-Al_2O_3	75.5	0.27	7.92
5Ca-Al_2O_3	61.3	0.24	9.49
7Ca-Al_2O_3	53.3	0.23	9.58

4.3.2. X-ray Diffraction (XRD)

The XRD patterns of Al_2O_3 and modified Ca-Al_2O_3 after calcination at 1123 K are shown in Fig. 4.5. The XRD patterns of Ca-Al_2O_3 show similar diffraction peaks characteristic of amphorous γ-Al_2O_3 (JCPDS file card number 47-1308). No new species can be observed when Ca loading is less than 3 wt. %, suggesting that CaO is well dispersed on the alumina surface. At higher Ca loading (> 5 wt. %), traces of $CaCO_3$ can be observed. The presence of surface carbonates is a result of the interaction between atmospheric CO_2 and the CaO during calcination of catalyst. In order to eliminate the influence of the carbonates in our experiments, all catalysts are pretreated with inert gas or hydrogen at T ≥ 773 K prior to the analysis.

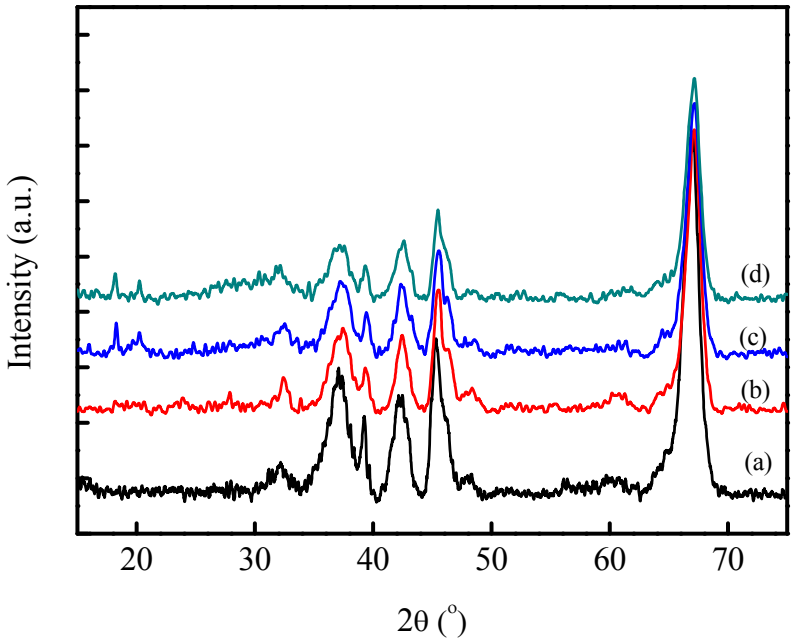

Figure 4.5. XRD patterns of Al_2O_3 and Ca-modified Al_2O_3 after calcination at 1123 K. (a) Al_2O_3; (b) 3Ca-Al_2O_3 ; (c) 5Ca-Al_2O_3 and (d) 7Ca-Al_2O_3.

4.3.3. X-ray Photoemission Spectroscopy (XPS)

XPS analysis is used to investigate the surface properties of the Ca-modified Al_2O_3 supports. The binding energies of Al 2p, O1s and Ca $2p_{3/2}$ are shown in Table. 1.2. No significant variation in the core binding energies of Al 2p (BE = 73.6±0.2 eV) and O1s (BE = 531.0±0.3 eV) can be observed in the presence of Ca. The Ca $2p_{3/2}$ spectrum of the samples demonstrated a principle peak at 347.0eV characteristic of CaO [17]. This peak is largely unchanged under different conditions.

Table 4.2. Binding energies (eV) from Al 2p, O1s and Ca $2p_{3/2}$ core-level.

	Al 2p BE(eV)	O 1s BE(eV)	Ca $2p_{3/2}$ BE(eV)
Al_2O_3	73.8	531.0	
3Ca-Al_2O_3	73.4	530.8	347.0
7Ca-Al_2O_3	73.8	531.3	347.1

Electronic interactions between the alkali/alkali earth atoms and active metals are often discussed to account for the catalytic effect in such system [18]. In fact, catalysts doped with small amount of alkali compounds usually change the product selectivity and activity in a favorable way, as in the case of potassium promotion in cobalt catalyst for Fischer-Tropsch synthesis [19]. As such, measurement of the valence band by XPS was conducted to evaluate the electron density of states (DOS) of the Ca-modified Al_2O_3. Valence-band photoelectron spectra of bare Al_2O_3 and Ca-Al_2O_3 supports are shown in Fig. 4.6. The valence band obtained for Al_2O_3 in Fig. 4.6(a) indicates the presence of both Al-O bonding and nonbonding states. This is in good agreement with the literatures which state that the bonding states are mainly derived from O 2p at ~13 eV and Al-O nonbonding states are contributed by weakly hybridized with Al 3s, 3p and 3d orbitals at ~9 eV [20, 21]. The addition of Ca results in the change in valence band spectrum. As observed in Fig 4.6 (b)-(c), the addition of Ca enhances the valence band intensity in the 6–8 eV binding energy regions. This can be

attributed to electronic donation from Ca 4s orbital. The electronic promotion effect induced by the addition of Ca will be discussed in the preceding chapter.

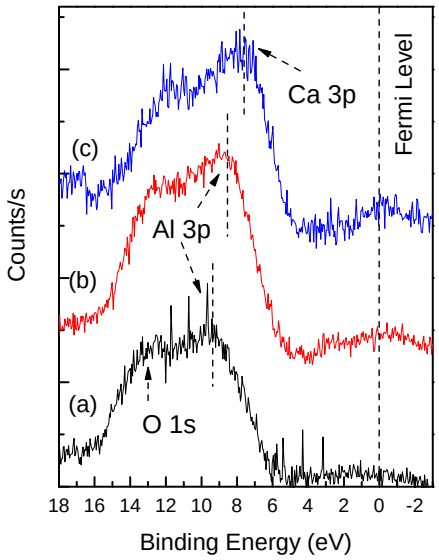

Figure 4.6. XPS valence band of (a) Al_2O_3; (b) 3Ca-Al_2O_3 and (d) 7Ca-Al_2O_3.

4.3.4. Diffuse Reflectance Infrared Fourier Transformed Spectroscopy (DRIFTS)

DRIFTS is an important spectroscopic tool to study and identify the type of surface hydroxyls of Al_2O_3 and Ca-modified Al_2O_3. DRIFTS spectra of the Al_2O_3 and Ca-Al_2O_3 supports are shown in Fig. 4.7. A clear difference in the IR spectra of γ-Al_2O_3 and Ca-Al_2O_3 supports is recognized in the 3200–3550 cm^{-1} region. Two distinct infrared absorption bands at 3752 and 3678 cm^{-1} and two broad bands centering at 3540 and 3250 cm^{-1} are registered on Al_2O_3 support. Al_2O_3 surface has a diverse surface hydroxyl groups as determined by means of

IR spectroscopy [22] and [23]. Knözinger and Ratnasamy [5] have mapped out the five different types of OH groups on the surface of γ- Al_2O_3 which have different ν_{OH} frequencies in 3800–3600 cm^{-1} region. They are generally known as isolated Al–OH groups which differ in the degree of coordination of the Al^{3+} ions [22] and [24]. According to the assignment proposed by Knözinger and Ratnasamy [5], the peak at 3678 cm^{-1} in Fig. 4.7(a), can be assigned as type III hydroxyls involving three octahedrally coordinated Al^{3+} ions while the peak at 3752 cm^{-1} may correspond to type IIb hydroxyls which form a bridge between two octahedrally coordinated Al^{3+} ions. Type III hydroxyls are acidic while type IIb hydroxyls are neutral in nature.

On Ca-Al_2O_3 support (Fig. 4.7(b)), a single hydroxyl band is observed at 3740 cm^{-1}. This marks the disappearance of acidic surface hydroxyl group (3678 cm^{-1}) upon the addition of calcium. In fact, the 3740 cm^{-1} band can be attributed to type IIa hydroxyls whose acidity lies somewhat between type III and type IIb hydroxyls. Morterra et al. [25] also reported the presence of 3740 cm^{-1} on their Ca-doped alumina system and proposed that this peak is a result of surface elimination of tetrahedrally coordinated Al^{3+} ions due to the presence of Ca^{2+}. On the surface of dehydrated γ-Al_2O_3, coordinatively unsaturated surface (*cus*) Al^{3+} ions are considered to be the strongest acid sites. Hence the CaO addition reduces the density of acidic sites on the Al_2O_3 surface, including isolated acidic surface hydroxyls and Lewis acidic sites.

The broad absorption bands centered at 3540 and 3250 cm^{-1} on Al_2O_3 support are attributed to associated hydroxyl groups which are hydrogen bonded.

On Ca-Al_2O_3 support, the IR intensity in the region, particularly at 3450 cm^{-1}, increases greatly, forming a strong rounded absorption arc span. This feature suggests that hydrogen-bonded hydroxyls predominate on Ca-Al_2O_3 support due to its affinity to adsorb water molecules [25]. These findings are further supported by H_2O-TPD profiles of Al_2O_3 and Ca-Al_2O_3 supports (Fig. 4.8). The profiles are characterized by a single H_2O desorption peak that shifts from 533 K to 478 K as the Ca loading increases from 0 to 7 wt%. Distinctly, the amount of water adsorbed increases from Fig. 4.8(a)-(d) with the increase in Ca loading. These results show that bare Al_2O_3 has less affinity for H_2O molecules whereas the hydrophilicity of the support increases with increasing Ca loading.

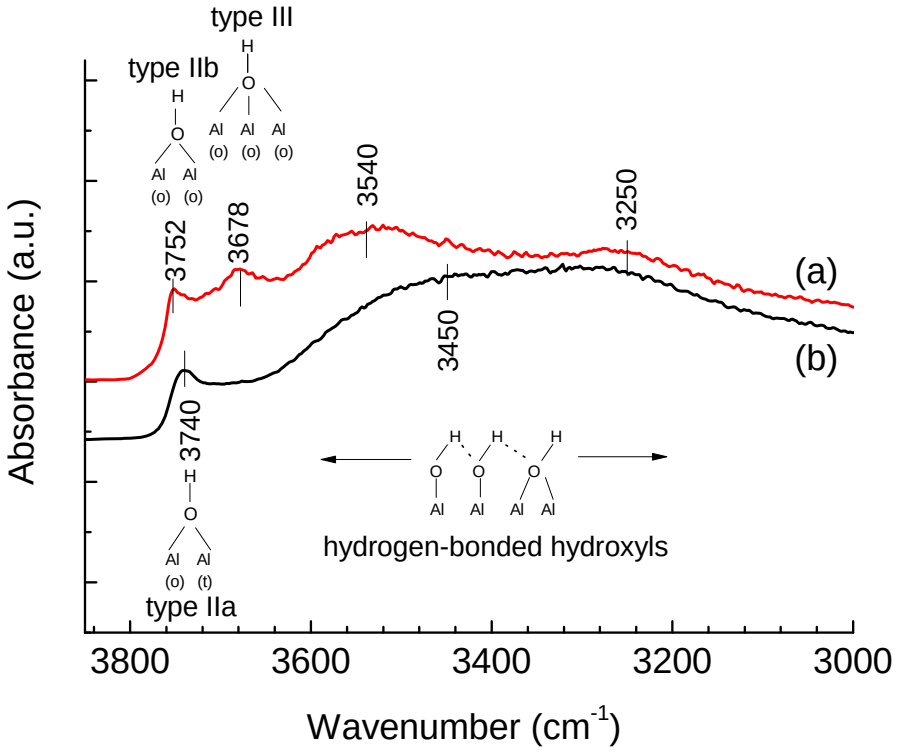

Figure 4.7. The DRIFTS spectra in the region between 3000 and 3800 cm^{-1} of the catalyst supports: (a) Al_2O_3 and (b) Ca-Al_2O_3. In the figure labeling Al(o) stands for octahedrally coordinated Al^{3+} ions while Al(*t*) for tetrahedrally Al^{3+} ions.

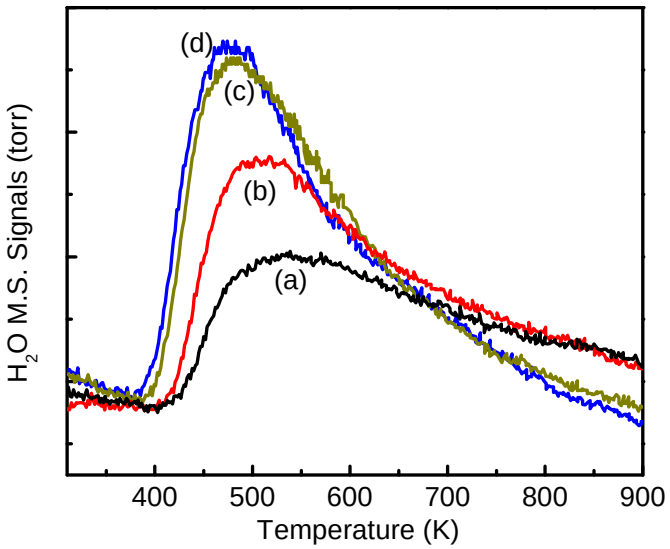

Figure 4.8. H_2O-TPD of (a) Al_2O_3; (b) 3Ca-Al_2O_3; (c) 5Ca-Al_2O_3 and (d) 7Ca-Al_2O_3.

4.3.5. Temperature Programmed Desorption of NH_3 (NH_3-TPD)

The amount and the strength of the acidic sites of the supports were studied by temperature programmed desorption (TPD) of NH_3. NH_3-TPD was used to examine the acidic property of the Ca-modified supports. On bare Al_2O_3, the NH_3-TPD profile (Fig. 4.9(a)) shows a strong peak around 423 K and a broad desorption shoulder tailing to 773 K, which are assigned to the desorption of adsorbed NH_3 molecules from Lewis-acid sites of various strength. According to the literature [26], there are 3 ranges of NH_3 desorption temperatures; (1) 293-473

K, (2) 473-623 K and (3) 623-823 K corresponding to weak, intermediate and strong acidic sites respectively. Hence, the surface of Al_2O_3 has large densities of weak acidic sites as well as strong acidic sites. On Ca-Al_2O_3 supports, symmetrical desorption peaks without high temperature tail are observed in Fig. 4.9(b)-(d), suggesting the elimination of high-acidity sites of Al_2O_3. Moreover, the low temperature peak around 423 K in Fig. 4.9(b)-(d) decays significantly, suggesting the disappearance of weak acidic sites. The amount of adsorbed NH_3 reduces from 439.4 μmol/g for bare Al_2O_3 to 164.8 μmol/g for 3Ca-Al_2O_3 and finally decreases to 63.9 μmol/g for 7Ca-Al_2O_3. This indicates that CaO is effective in reducing the density and the strength of acidic sites of the Al_2O_3 support.

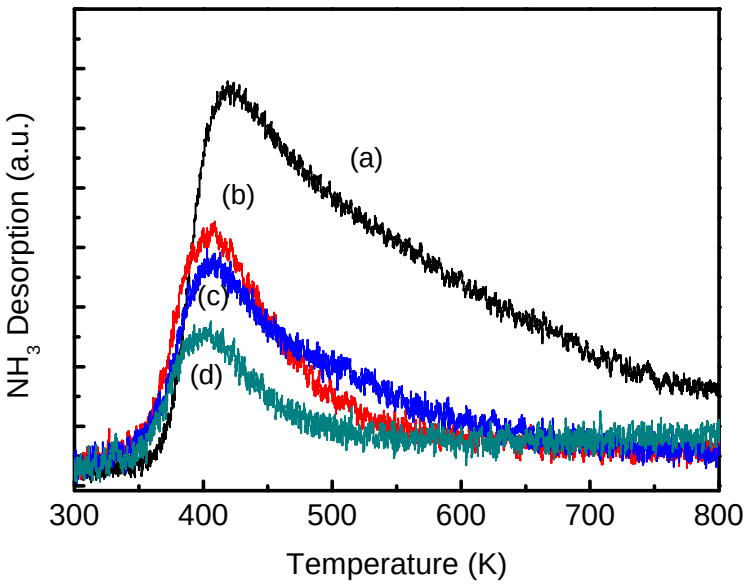

Figure 4.9. NH_3-TPD of (a) Al_2O_3; (b) 3Ca-Al_2O_3; (c) 5Ca-Al_2O_3 and (d) 7Ca-Al_2O_3.

4.3.6. Temperature Programmed Desorption of CO_2 (CO_2-TPD)

The basicity of the Al_2O_3 and Ca-modified supports was measured using CO_2-TPD. In Fig. 4.10, Al_2O_3 support demonstrates the least capacity to adsorb CO_2 with a single desorption peak centered at 399 K. This desorption peak is assigned to the low-strength basic sites such as bicarbonates, which results from the interaction between CO_2 and the weak basic surface hydroxyl groups [25]. Ca-loading expands CO_2 adsorption capacity and strengthens the basic character of the support, leading to the significant increase of the peak intensity and the shift of desorption temperature from 398 K to > 413 K. 7Ca-Al_2O_3 further enhances these effects and demonstrates an extra desorption peaks at 883 K (Fig. 4.10(d)). The latter peak is probably due to high-strength basic sites such as unidentate carbonates [27, 28]. The fact that the high temperature (873 K) CO_2-TPD peak can be observed only from 7Ca-Al_2O_3 may mean that over-saturated Ca loading exists as a separate CaO phase which adsorbs CO_2 much stronger than those Ca ions dispersed in the Al_2O_3 matrix.

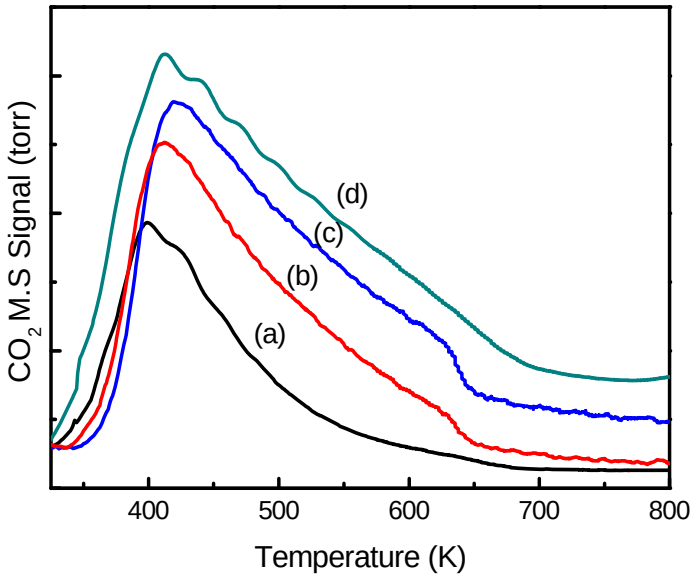

Figure 4.10. CO_2-TPD of (a) Al_2O_3, (b) 3Ca-Al_2O_3, (c) 5Ca-Al_2O_3 and (d) 7Ca-Al_2O_3.

4.3.7. Fixed Bed Reaction Testing

The ethanol steam reforming on the Al_2O_3 and Ca-Al_2O_3 supports were evaluated in a high-throughput micro-channel reactor at 673 K. The product distributions are presented in Fig. 4.11. Ethanol conversion on bare Al_2O_3 support is 59%, with the majority of the products being ethylene ($\boldsymbol{S}_{C2H4}$=89%). Other products include acetaldehyde ($\boldsymbol{S}_{CH3CHO}$=11%) and hydrogen ($\boldsymbol{S}_{H2}$=2%). On Ca-Al_2O_3 supports, ethanol conversion drops drastically to 7.6% and 4.5% on 3Ca-Al_2O_3 and 7Ca-Al_2O_3 respectively. The product distributions also varied with the addition of CaO. Formation of C_2H_4 is greatly suppressed ($\boldsymbol{S}_{C2H4}$=8%) on Ca-Al_2O_3 supports. The reduction in the ethylene selectivity of Ca-Al_2O_3 during ethanol steam reforming is attributed to the elimination of Lewis-acid centers

which otherwise favor the dehydration of ethanol to C_2H_4 through E_2 elimination mechanism [29, 30]. As shown in NH_3-TPD and CO_2-TPD, CaO modification greatly depresses the surface acidity while enhances the basicity of the Al_2O_3 support. Dehydrogenation of a primary alcohol to corresponding acetaldehyde (Eqn 4.3) is usually faster than alcohol dehydration (Eqn 4.4) on basic oxides. This reaction usually requires large polarizable cations, such as alkaline earths ions [6]. Pure Al_2O_3 catalyzes the dehydrogenation of ethanol to acetaldehyde at a very low rate. The presence of high-strength basic sites on Ca-modified Al_2O_3 thus promotes the dehydrogenation of ethanol via E_{1cB} elimination mechanism [6]. These results conclude that both Al_2O_3 and Ca-Al_2O_3 supports are not active for ethanol steam reforming and the Ca addition on Al_2O_3 support greatly suppresses dehydration of ethanol to C_2H_4. Similar observation was reported by Llorca et al. [31].

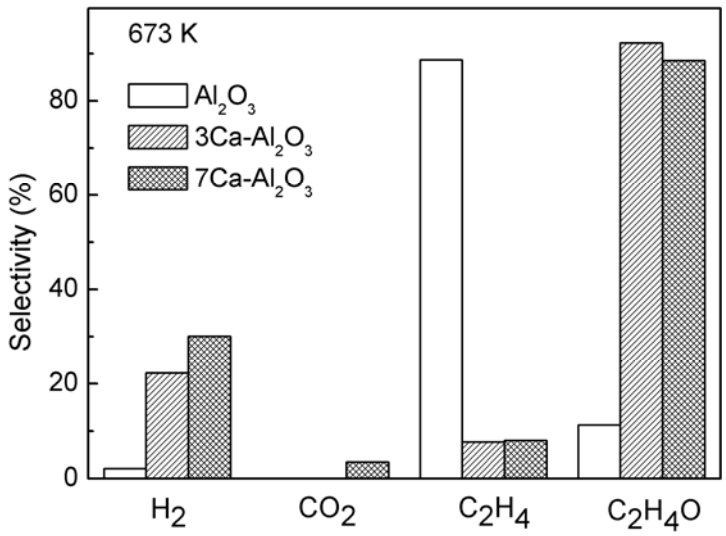

Figure 4.11. Product distribution of Al_2O_3, 3Ca-Al_2O_3 and 7Ca-Al_2O_3 for ethanol steam reforming at 673 K.

4.3.8. DRIFTS Study of Adsorbed Ethanol on Supports

DRIFTS spectra of ethanol adsorption on Al_2O_3 and Ca-Al_2O_3 supports at various temperatures are displayed in Fig. 4.12. Upon adsorption of ethanol on Al_2O_3 the IR bands at 2966, 2926 and 2875 cm^{-1}, which are ascribed to ν_a (CH_3), ν_a (CH_2) and ν_s (CH_3) respectively, are observed, implying the existence of surface ethoxide species due to the ethanol adsorption. At the same spectrum the OH bands at 3752 cm^{-1} and 3689 cm^{-1} decrease in intensity upon the ethanol adsorption, indicating that the ethoxide species are attached to the support at the expenses of type II and Type III OH groups, which is consistent with the results in literature [32]. The band at 2735 cm^{-1} which is clearly observable in the spectra after the adsorption is usually attributed to acetaldehyde C-H vibration. Hence its appearance may indicate the dehydrogenation of some adsorbed ethoxide via the C^{α}-H bond scission [33] . The ethoxide and acetaldehyde bands are stable upon heating up to 573 K. They completely disappear from Al_2O_3 at 673 K while the OH bands at 3689 and 3752 cm^{-1} re-appear. As ethylene could be observed as the main product from EtOH-TPD on pure Al_2O_3 at this temperature range (which will be presented later), it is likely that the desorption of ethylene from adsorbed ethanol on bare Al_2O_3 surface may proceed, as DFT calculation predicted, via the C-O and C^{β}-H bond scissions [33]. Nevertheless at 673 K, new IR bands at 1575 and 1456 cm^{-1} which are attributed to acetate species are also noted (Fig. 4.12(a)) [34]. Formation of acetates has been widely reported over various oxides, i.e. Al_2O_3 [35, 36], MgO [37] and CeO_2 [38]. Studies of the mechanisms of ethanol adsorption on Al_2O_3 suggest that a structural change from an ethoxide to an

acetate occurs through the attachment of carboxyl carbon to the oxygen atoms of the alumina surface, illustrating the importance of surface oxygen atoms in acetate formation [35]. Consistent with this hypothesis, spectroscopic observations from the work of Yee et al. on ethanol adsorption over unreduced CeO_2 and reduced CeO_2 also shows that surface oxygen atoms on unreduced CeO_2 is responsible for acetate formation while a reduced CeO_2 depletes the surface of oxygen atoms, leading to the absence of acetate [38]. Hence, the appearance of acetate on Al_2O_3 may suggest an alternative reaction pathway at 673 K, in which the ethoxides are converted to surface acetates via the interactions with surface oxygen atoms.

On Ca-Al_2O_3 support ethoxide and acetaldehyde adsorbed species are similarly observable (Fig. 4.12(b)). Interestingly the adsorbed ethoxide remains stable at 673 K, even more stable than that on pure Al_2O_3. In addition, no acetate species are detectable. These indicate that Ca modification can stabilize the ethanol adsorption intermediates, ethoxide and acetaldehyde species. The stabilizing of the ethoxide species is most probably due to the stronger hydrogen bonding between the alcohol and Ca-modified aluminum ion. The increased electronic density of Ca-modified Al_2O_3 as observed from the XPS valence band (Fig. 4.6), increases the availability of electrons on the aluminum ion for hydrogen bonding [37]. Consequently, the ethoxide species are more strongly adsorbed on Ca-Al_2O_3. In addition, the stabilizing effect could be attributed to the presence of adsorbed water as reported by several authors [34, 39, 40]. DFT study also showed the reduction of ethanol adsorption energy, from 31 kcal/mol without water to 21 kcal/mol in the presence of water on Al_2O_3 surface [41]. As discussed

above (Fig. 4.8), it is clear that Ca-Al_2O_3 supports interact with water molecules more readily than Al_2O_3. Water molecules interact with CaO by forming a hydrogen bond with a surface basic site [42], producing a reservoir of hydrogen bonded surface hydroxyls on Ca-Al_2O_3, so that more hydrogen bonded surface hydroxyls are observed at ca. 3350 cm^{-1}. Besides the stabilizing effect of ethoxide species by the surface hydroxyls, these surface hydroxyls also prevent the conversion of ethoxide species to acetates as they occupy the surface oxygen atoms required for the formation of acetate, as previously mentioned [35]. Based on these observations and previous discussions, the poor catalytic ESR activity of Ca-Al_2O_3 support can thus be attributed to: (1) the loss of Lewis acid centers (Al^{IV} *cus* ions) due to presence of Ca^{2+}, discouraging dehydration and (2) the increase in electronic density on the aluminum ion which stabilizes the ethoxide species and (3) the presence of associated hydrogen bonded surface hydroxyls on Ca-Al_2O_3 support, which denies the stabilized ethoxide of further conversion.

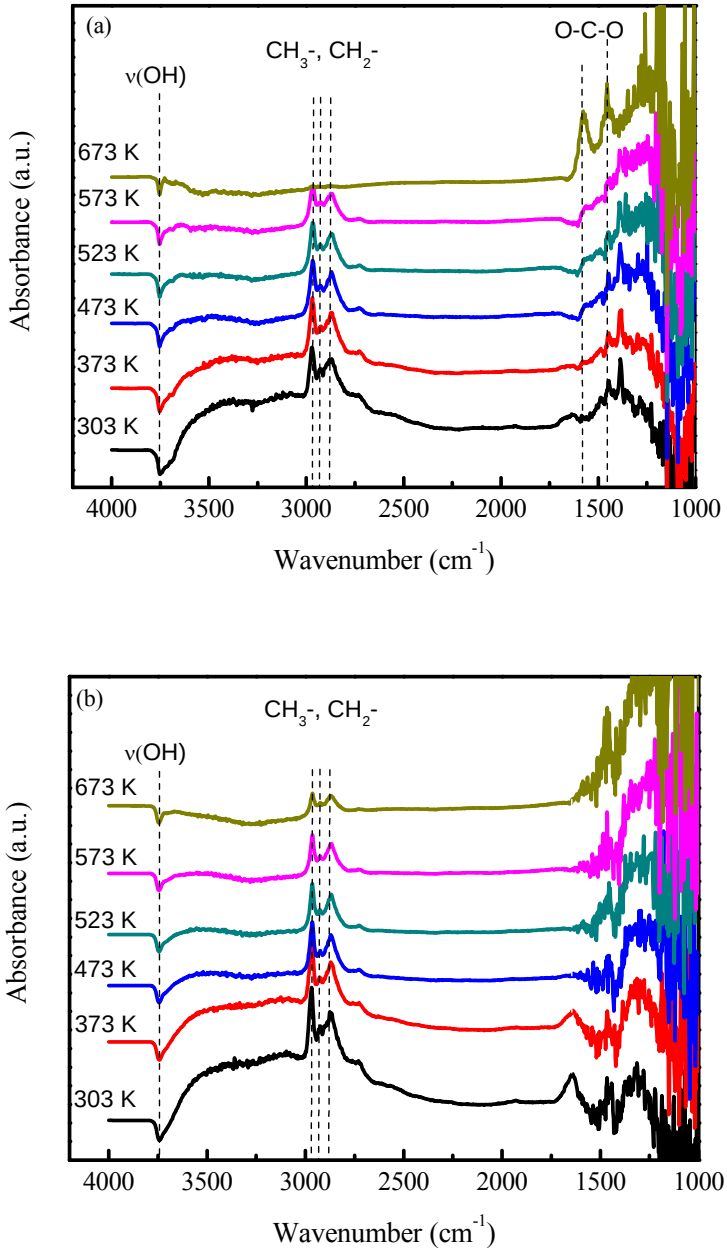

Figure 4.12. Variable temperature DRIFTS spectra for (a) Al_2O_3 and (b) Ca-Al_2O_3 after C_2H_5OH adsorption. Spectra of the samples were recorded at (i) 303 K after ethanol adsorption followed by He purge, (ii)-(vi) 373, 473, 523, 573 and 673 K.

4.3.9. Temperature Programmed Desorption of Ethanol (EtOH-TPD)

EtOH-TPD study was conducted on Al_2O_3 and Ca-Al_2O_3 supports which were prior exposed to ethanol at room temperature (Fig. 4.13). On Al_2O_3 (Fig. 4.13(a)), there is a big water desorption peak at 373–473 K, with slight desorption of adsorbed ethanol, acetaldehyde, ethylene and hydrogen. More CO and C_2H_4 are detected at 639 K, forming the majority of the ethanol decomposition products from Al_2O_3. On Ca-Al_2O_3 (Fig. 4.13(b)), more profound and broad desorbed water peak are observed while CO and C_2H_4 as the major ethanol decomposition products are detected at a higher temperature ($\boldsymbol{T}_{max}$ = 742 K). The peak intensity of CO and C_2H_4 is significantly lower in comparison with Al_2O_3, confirming that Ca addition promote water adsorption and stabilize ethoxide adsorbate, in good agreement to the above IR studies.

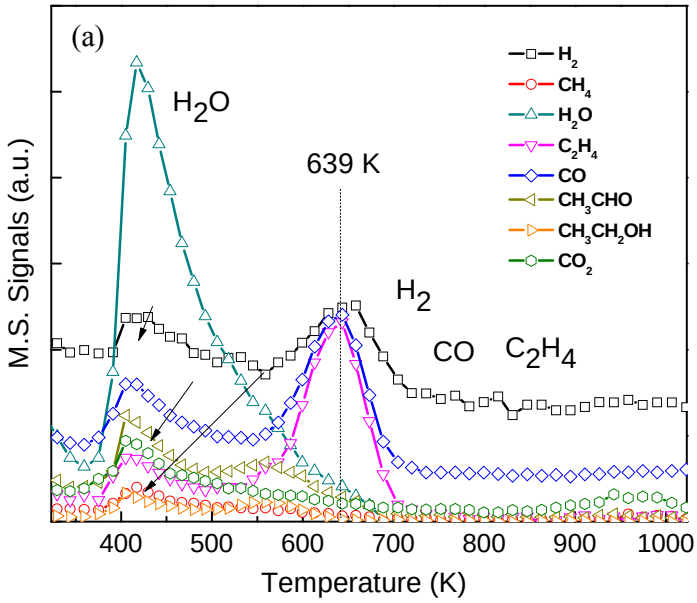

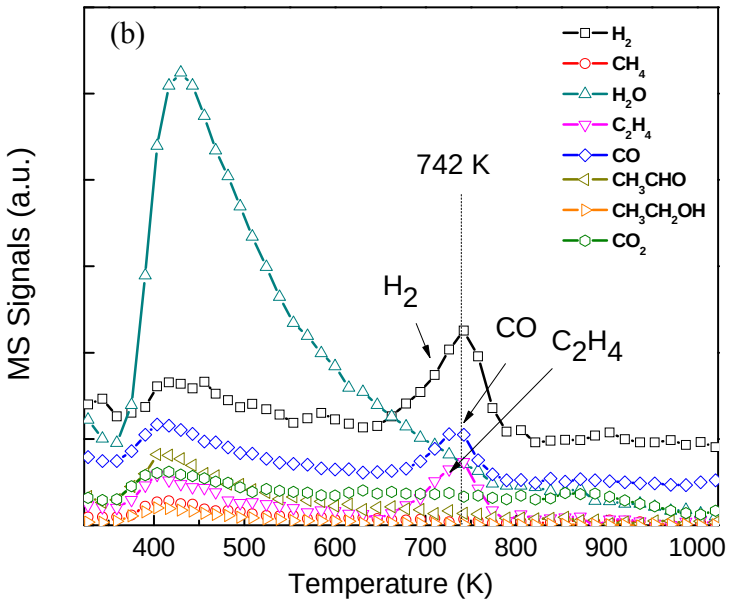

Figure 4.13. EtOH-TPD of (a) Al_2O_3 and (b) Ca-Al_2O_3.

4.4. Conclusions

Both Al_2O_3 and Ca-Al_2O_3 are not active catalysts for ESR in the absence of an active metal. Over Al_2O_3, C_2H_4, produced via E_2 elimination mechanism, is the main product at 673 K. The presence of Ca successfully reduces the formation of C_2H_4 – a coke precursor. Rather, the addition of Ca promotes dehydrogenation of ethanol, tilting the product distribution towards CH_3CHO. NH_3 and CO_2- TPD reveal the suppression of acidic sites and increase in basic sites of on the Ca-Al_2O_3, promote dehydrogenation. However, the poor conversion of Ca-Al_2O_3 is attributed to the stabilizing effect of ethoxide species as observed from DRIFTS of adsorbed ethanol. The promotion in DOS on Ca-Al_2O_3 increases the number of

electrons available for hydrogen bonding, strengthening the ethanol and support interaction. In addition, the abundance of surface hydroxyls on Ca-Al_2O_3 reduces the surface oxygen atoms required for conversion of ethoxide species to acetates.

4.5. References

[1] C. Márquez-Alvarez, N. Žilková, J. Pérez-Pariente, J. Čejka, Catalysis Reviews. 50 (2008) 222-286.

[2] S. Cavallaro, Energy & Fuels. 14 (2000) 1195-1199.

[3] A. Alberton, M. Souza, M. Schmal, Catal. Today 123 (2007) 257-264.

[4] R. Wyckoff (Ed.), Crystal Structures, Interscience: New York, New York, 1963.

[5] H. Knözinger, P. Ratnasamy, Catalysis Reviews. 17 (1978) 31-70.

[6] J. Di Cosimo, V. Díez, M. Xu, E. Iglesia, C. Apesteguía, J. Catal. 178 (1998) 499-510.

[7] H. Arai, Y. Saito, Y. Yoneda, J. Catal. 10 (1968) 128-133.

[8] L. Martins, D. Cardoso, P. Hammer, T. Garetto, S.H. Pulcinelli, C.V. Santilli, Appl. Catal. A: Gen. 398 (2011) 59-65.

[9] A. Vizcaíno, A. Carrero, J. Calles, Int. J. Hydrogen Energy. 32 (2007) 1450-1461.

[10] M. Sánchez-Sánchez, R. Navarro, J. Fierro, Int. J. Hydrogen Energy. 32 (2007) 1462-1471.

[11] M. Sánchez-Sánchez, R. Navarro, J. Fierro, Catal. Today 129 (2007) 336-345.

[12] Z. Zhang, X. Verykios, Catal. Today 21 (1994) 589-595.

[13] A. Bao, K. Liew, J. Li, J. Mol. Catal. A: Chem. 304 (2009) 47-51.

[14] L. Bai, Y. Zhou, Y. Zhang, H. Liu, M. Tang, Catal. Lett. 129 (2009) 449-456.

[15] S. Andonova, C. Vladov, B. Pawelec, I. Shtereva, G. Tyuliev, S. Damyanova, L. Petrov, Appl. Catal. A: Gen. 328 (2007) 201-209.

[16] A. Vizcaíno, A. Carrero, J. Calles, Catal. Today 146 (2009) 63-70.

[17] H. Van Doveren, J.A.T.H. Verhoeven, Journal of Electron Spectroscopy and Related Phenomena. 21 (1980) 265-273.

[18] C. Pedrero, T. Waku, E. Iglesia, J. Catal. 233 (2005) 242-255.

[19] S. Hussain, M. Nadeem, M. Mazhar, Catal. Comm. 9 (2008) 2048-2052.

[20] I. Oleinik, E. Tsymbal, D. Pettifor, Physical Review B. 62 (2000) 3952-3959.

[21] S. Mo, W. Ching, Physical Review B. 57 (1998) 15219-15228.

[22] J. Peri, R. Hannan, J. Phys. Chem. 64 (1960) 1526-1530.

[23] G. Busca, Catal. Today 41 (1998) 191-206.

[24] T. Ballinger, J. Yates, Langmuir. 7 (1991) 3041-3045.

[25] C. Morterra, A. Zecchina, S. Coluccia, A. Chiorino, Journal of the Chemical Society, Faraday Transactions 1: Physical Chemistry in Condensed Phases. 73 (1977) 1544-1560.

[26] P. Berteau, B. Delmon, Catal. Today 5 (1989) 121-137.

[27] T. Horiuchi, H. Hidaka, T. Fukui, Y. Kubo, M. Horio, K. Suzuki, T. Mori, Appl. Catal. A: Gen. 167 (1998) 195-202.

[28] A. Auroux, A. Gervasini, J. Phys. Chem. 94 (1990) 6371-6379.

[29] H. Pines, J. Manassen, H.P. D.D. Eley, B.W. Paul, Advances in Catalysis, Academic Press, 1966, pp. 49-93.

[30] A. Gervasini, J. Fenyvesi, A. Auroux, Catal. Lett. 43 (1997) 219-228.

[31] J. Llorca, P. de la Piscina, J. Sales, N. Homs, Chem. Comm. (2001) 641-642.

[32] H. Knoezinger, B. Stuebner, J. Phys. Chem. 82 (1978) 1526-1532.

[33] Y. Cheng, Density Functional Theory Study of Ethanol Decomposition Reaction Over Ni/α-Al_2O_3 (0 0 0 1) surface. Master Dissertation, National Taiwan University of Science and Technology, 2008.

[34] J. Raskó, M. Dömök, K. Baán, A. Erdőhelyi, Appl. Catal. A: Gen. 299 (2006) 202-211.

[35] R. Greenler, J. Chem. Phys. 37 (1962) 2094-2100.

[36] R. Kagel, J. Phys. Chem. 71 (1967) 844-850.

[37] R. Kagel, R. Greenler, J. Chem. Phys. 49 (1968) 1638-1647.

[38] A. Yee, S.J. Morrison, H. Idriss, J. Catal. 186 (1999) 279-295.

[39] M. Dömök, M. Tóth, J. Raskó, A. Erdőhelyi, Appl. Catal. B: Environ. 69 (2007) 262-272.

[40] A. Erdőhelyi, J. Raskó, T. Kecskés, M. Tóth, M. Dömök, K. Baán, Catal. Today 116 (2006) 367-376.

[41] S. Wu, Y. Lia, J. Ho, H. Hsieh, J. Phys. Chem. C 113 (2009) 16181-16187.

[42] N. Zhanpeisov, H. Nakatsuji, M. Hada, J. Mol. Catal. A: Chem. 112 (1996) 63-67.

Chapter 5

Influence of Ca loading for Ethanol Steam Reforming over Ni/Al_2O_3 Catalyst

Graphical Abstract

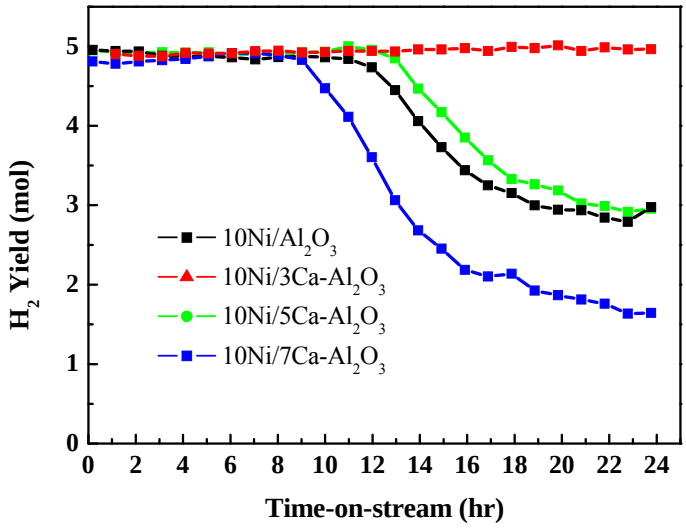

Ca-modified Ni/Al_2O_3 catalysts with various Ca loadings of 0, 3 and 7 wt% were studied for low temperature catalytic ethanol steam reforming (ESR). Catalyst with 3 wt% of Ca remains stable at 673 K for at least 24 h, while 0 wt% and 7 wt% Ca modified catalysts deactivate easily. The addition of Ca increases the particle size of active Ni which promotes the formation of un-reactive and encapsulating carbons, undermining the stability of highly loaded (7 wt%) Ca-modified Ni catalyst. XPS valence band shows that the presence of Ca increases

the density of Ni 3d band valence electrons which helps in dissociation of methane and deactivates the catalysts, as in the case of nickel catalysts supported on 7 wt% of Ca on Al_2O_3. Excellent catalytic performance of $10Ni/3Ca\text{-}Al_2O_3$ is due to the effective coke removal and the amorphous nature of coke deposition. Optimized Ca loading was found to play a critical role in coke removal, through its effect on Ni particle size, valence band of catalyst and steam gasification of coke.

5.1. Introduction

Thermodynamic calculations have proved and accounted for the feasibility of ethanol steam reforming (ESR, Eqn. 5.1) [1]. The reaction pathway of ESR is very much dependent on the reaction conditions and the catalytic material [2] and [3]. Some important side reactions are listed in Eqn. 5.2-5.9. Undesirable side reactions often give rise to CH_4, CO, C_2H_4 and C_2H_4O. For example, at low *S*/*E* ratios, the formation of methane is more favorable at low temperatures whereas carbon monoxide is favored at higher temperatures through decomposition of ethanol (Eqns. 5.2 and 5.3) and reversed water gas shift reaction (RWGSR). Dehydration of ethanol to ethylene and dehydrogenation of ethanol to acetaldehyde are believed to proceed via the acidic and basic sites of support (Eqns. 5.4 and 5.5) [4]. Fundamental mechanism study is required for optimization of catalytic material in ESR.

$$C_2H_5OH + 3H_2O \rightarrow 2CO_2 + 6H_2 \quad (5.1)$$

$$C_2H_5OH \rightarrow \frac{3}{2}CH_4 + \frac{1}{2}CO_2 \quad (5.2)$$

$$C_2H_5OH \rightarrow CH_4 + CO + H_2 \quad (5.3)$$

$$C_2H_5OH \rightarrow C_2H_4 + H_2O \quad (5.4)$$

$$C_2H_5OH \rightarrow C_2H_4O + H_2 \quad (5.5)$$

$$C_2H_4O + H_2O \rightarrow CO + CO_2 + H_2 \quad (5.6)$$

$$C_2H_4O \rightarrow CO + CH_4 \quad (5.7)$$

$$CH_4 + H_2O \rightarrow 3H_2 + CO \quad (5.8)$$

$$CO + H_2O \rightarrow H_2 + CO_2 \quad (5.9)$$

To date, the use of Ni-based catalysts supported on Al_2O_3 seems to be a popular and excellent material for ethanol steam reforming. This is because, both Ni and Al_2O_3 are cheaper alternatives to their expensive counterparts such as the noble metals as well as CeO_2, ZnO and ZrO_2 supports [3]. Furthermore, the catalytic performance of Ni is comparable to that of the noble metals such as Rh, Ru and Pt, making it an attractive choice as the active metal. Nickel-based catalysts have been studied in great details and have proven to be highly active in breaking of the C–C bond [4, 5]. However, poor stability caused by severe carbon deposition is often reported on Ni-based catalyst [6, 7]. Suppressing carbon formation to improve the Ni catalyst stability is urgently needed for the wide application of Ni catalysts in ESR.

In ESR, the reaction products or intermediates such as CO, CH_4, C_2H_4, CH_3CHO and their fragments may react via various pathways and form coke deposition [8]. Polymerization of unsaturated hydrocarbons C_2H_4 (Eqn. 5.10) is highly possible, leading to gummy carbonaceous deposits which may contain certain amount of hydrogen and oxygen. Methane undergoes decomposition, producing carbon and hydrogen (Eqn. 5.11). At relatively low temperatures CO disproportionate reaction (Eqn. 5.12), also known as Bourdard reaction, and CO de-oxygenation reaction (Eqn. 5.13) may occur, both forming carbon.

$$\gamma C_nH_{2m} \rightarrow C_{n\gamma} + m\gamma H_2 \quad (5.10)$$

$$CH_4 \rightarrow C + 2H_2 \quad (5.11)$$

$$2CO \rightarrow C + CO_2 \quad (5.12)$$

$$CO + H_2 \rightarrow C + H_2O \quad (5.13)$$

To improve catalyst stability, coke deposition arising from complicated processes and several reaction possibilities as listed in Eqns. 5.10-5.14 has to be suppressed. It has been proposed recently by Liberatori et al. [9] that the addition of Ag on Ni/Al_2O_3 has a negative effect on the suppression of carbonaceous compound deposition for ESR through the reduction of Ni sites with low coordination. They proposed that the activation of ethanol does not depend significantly on the coordination of Ni sites since the activation of ethanol molecule on the metal surface is easier than that of methane. This leads to the abundance of CH_x species on the Ag modified Ni surface which results in coke formation. However, the activation of water via Ni can be depressed since the water activation barrier on Ni planner surface is 53 kJ/mol higher than step sites [10]. Therefore, the suppression of low coordination Ni sites by Ag does not decrease CH_x species on Ni surface significantly, but decrease OH* species from activation of water, hence resulting in a negative effect on the overall control of carbon deposition. Modification of Al_2O_3 support by La has a positive effect on decreasing coking on Ni catalysts [9], [11] and [12]. Similarly, coke depression can be achieved by introducing Ce, Zr and Mg to Al_2O_3 [13] which decreases the acidity of Al_2O_3, thus minimizing dehydration of ethanol to ethylene. However, there is lack of detailed study on how these additives affect the carbon deposition.

In the previous Chapter, we have shown that the addition of calcium led to positive catalytic effect in terms of reducing the formation of coke precursor such as C_2H_4. However, the ethanol conversion on $Ca\text{-}Al_2O_3$ support is relatively poor.

In this Chapter, Ni active metal is impregnated over $Ca\text{-}Al_2O_3$ support to catalyze the reaction and a detailed study on the effect of CaO modified Ni/Al_2O_3 catalyst for ESR is reported. Careful investigations using various techniques of XRD, XPS, TPO, TEOM, SEM, TEM and catalytic reaction evaluation on the Ni/Al_2O_3 catalysts with and without Ca addition were performed in an attempt to understand the mechanism of coke formation in the ESR. The effect of Ca addition on the mitigation of coke formation was investigated. We also optimized the Ca-loading on the Ni/Al_2O_3 catalyst to develop a stable and active catalyst for ESR.

5.2. Experiment

5.2.1. Preparation of catalysts

$Ni(NO_3)_2{\cdot}6H_2O$ (Arcōs Organics) aqueous solution was wet-impregnated onto the $Ca\text{-}Al_2O_3$ support previously synthesized in Chapter 1. The mixture was dried in air for 2 h at 373 K before the temperature was up to 723 K and held constant for another 5 h. 1 wt% and 10 wt% of Ni were also impregnated in the similar fashion on bare $\gamma\text{-}Al_2O_3$ Al_2O_3 (Arcōs Organics) support. In this article, our samples are denoted as *y*Ni/*x*$Ca\text{-}Al_2O_3$, where *y* is either 1 wt% or 10 wt% for Ni and *x* varies between 0 and 7 wt% for Ca.

5.2.2. Catalyst characterization

Powder X-ray diffraction (XRD) patterns of the samples after calcination were analyzed with Bruker AXS XRD system equipped with Cu Kα radiation (λ = 0.154 nm). The profiles were collected at a step width of 0.02° in the (2θ) range from 20° to 90°.

H_2 temperature-programmed reduction (H_2-TPR) measurements were carried out on Thermo Scientific TPROD 1100. 50 mg of calcined catalysts, which had been thermally treated under Ar stream at 773 K to remove water and other contaminants, were heated from 303 K to 1123 K at a rate of 10 K min^{-1} in 50 ml min^{-1} of 5% H_2/Ar and maintained at 1123 K for 15 min while the hydrogen consumption was monitored.

In determining the metal dispersion of our catalysts, 500 mg of the catalyst was first reduced for 2 h at 873 K. After Ar purge the sample at room temperature was exposed to H_2 flow at a constant rate of 50 ml min^{-1} for 45 min. The catalyst was then purged with 30 ml min^{-1} of Ar for another 30 min, heated from 303 K to 873 K with a ramp rate of 20 K min^{-1} in 50 ml min^{-1} of Ar, and held at 873 K for 30 min. The hydrogen desorbed from the sample was detected by a TCD. In order to determine the fraction of nickel reduced to metallic state, O_2 chemisorption was performed at 723 K. The metal dispersion can be calculated using the equation employed by Bartholomew et al., assuming adsorption stoichiometry of H/Ni = 1[14].

X-ray photoelectron spectra were obtained on Themo ESCALAB 250, using MgKα ($h\upsilon$ = 1253.6 eV) as photon source. The instrument was calibrated

with respect to graphitic C 1s at 284.5 eV. To study the reduced catalysts, samples were reduced ex situ using the standard reduction conditions and transferred into the XPS chamber under Ar protection.

The morphology of the carbon deposition on spent catalysts was investigated using both scanning electron microscopy (SEM) (JEOL JSM-6700F) and transmission electron microscopy (TEM) (Tecnai G^2 TF20 S-twin, FEI Company). Raman analysis was conducted using LabRAM HR Raman spectrometer at an excitation wavelength of 514.5 nm at a power of approximately 1 mW, using a 50× objective.

The type and the quantity of the carbon deposition on spent catalysts were determined by temperature-programmed oxidation (TPO) in which the sample was heated in 50 ml min^{-1} of 5% O_2/He at a rate of 15 K min^{-1} up to 1023 K and held at this temperature for 15 min. CO_2 emission versus the sample temperature was recorded.

5.2.3. Fixed Bed Catalytic Testing

The catalytic evaluation experiments were performed in customized 5-channel quartz micro-reactor (BEL, Japan), each of which was loaded with 100 mg of the catalyst. Temperatures of the samples were individually monitored with thermocouples located just on top of the catalyst samples.

The catalysts were reduced by hydrogen at 873 K for 2 h. Then 40 ml min^{-1} of Ar was flown in, along with 0.005 ml min^{-1} of ethanol–water mixture (1:10

molar ratio) which was injected by a Shimadzu Liquid Pump and vaporized at 443 K within the reactor. The total gas hourly space velocity was kept constant at 27,000 ml (g-cat h)$^{-1}$, monitored by mass flow controller. The reaction products were analyzed online using a gas chromatograph (GC) (Varian CP-3800) with three columns: Porapak Q and Haysep Q, molecular sieve 5A. Porapak Q was used to separate organics and carbon dioxide with He as carrier gas while the later two columns with Ar carrier gas were used for the separation of hydrogen, carbon monoxide and methane. Conversion of ethanol (X_{EtOH}) and selectivity to carbon containing species (S_{Ci}) were calculated based on Eqns. 3.5 and 3.6 in Chapter 3, respectively.

5.2.4. Catalytic methane decomposition over Ni/*x*Ca-Al_2O_3 catalysts

Tapered element oscillating microbalance (TEOM), which is a mass sensitive reactor, was used to investigate the coke formation due to methane decomposition over Ni catalysts. 50 mg of the Ni catalyst was loaded between two layers of quartz wool on the top of the sample carrier. The catalyst was reduced by H_2 at 873 K for at least 2 h. After 1 h of helium flush, 50 ml min^{-1} of 10% CH_4/Ar was introduced into the reactor, passing through the reduced nickel catalyst at 773 K for 20 min. The mass change as a result of methane decomposition was monitored.

To study the steam gasification of the coke deposition, the coke-deposited catalyst was cooled to 423 K and steam was introduced by Ar at a rate of 0.002 ml min^{-1}. The catalyst was heated to 1023 K in the presence of steam with a ramp

rate of 10 K min^{-1}. The steam gasification products such H_2, CO and CO_2 were detected versus temperature, using mass spectroscopy.

5.3. Results

5.3.1. Catalytic Performance of $10Ni/Al_2O_3$ and Ca-modified $10Ni/Al_2O_3$

ESR was performed at 673 K for 24 h over $10Ni/Al_2O_3$, $10Ni/3Ca\text{-}Al_2O_3$, $10Ni/5Ca\text{-}Al_2O_3$ and $10Ni/7Ca\text{-}Al_2O_3$. The yield of H_2, ethanol conversion and product selectivities is shown in Fig. 5.1. In Fig. 5.1(a), the deactivation occurs after 12 h operation over $10Ni/Al_2O_3$. Upon the deactivation, ethanol conversion declines, S_{CO2} and S_{CH4} decrease while S_{CH3CHO} and S_{CO} increase. $10Ni/3Ca\text{-}Al_2O_3$ remains active during the whole test period, with 100% ethanol conversion, 90% S_{H2}, 80% S_{CO2} and 19% S_{CH4} (Fig. 5.1(b)). However, further increase in Ca loading in $10Ni/5Ca\text{-}Al_2O_3$ and $10Ni/7Ca\text{-}Al_2O_3$ leads to a severe loss of in catalytic life span and a catalytic performance (Fig. 5.1(c) and (d)). The deactivation starts at 10 h and 11 h for $10Ni/5Ca\text{-}Al_2O_3$ and $10Ni/7Ca\text{-}Al_2O_3$, respectively. The ethanol conversion drops to 30% and S_{CH3CHO} increases to ~40% on $10Ni/7Ca\text{-}Al_2O_3$. Obviously the Ca addition plays a role in the enhancement of the catalytic stability of ESR at 673 K and there is an optimum loading of Ca, above which Ca overloading may lead to the catalytic deactivation. Therefore, it is worth to perform detailed studies to investigate the role of Ca for ESR.

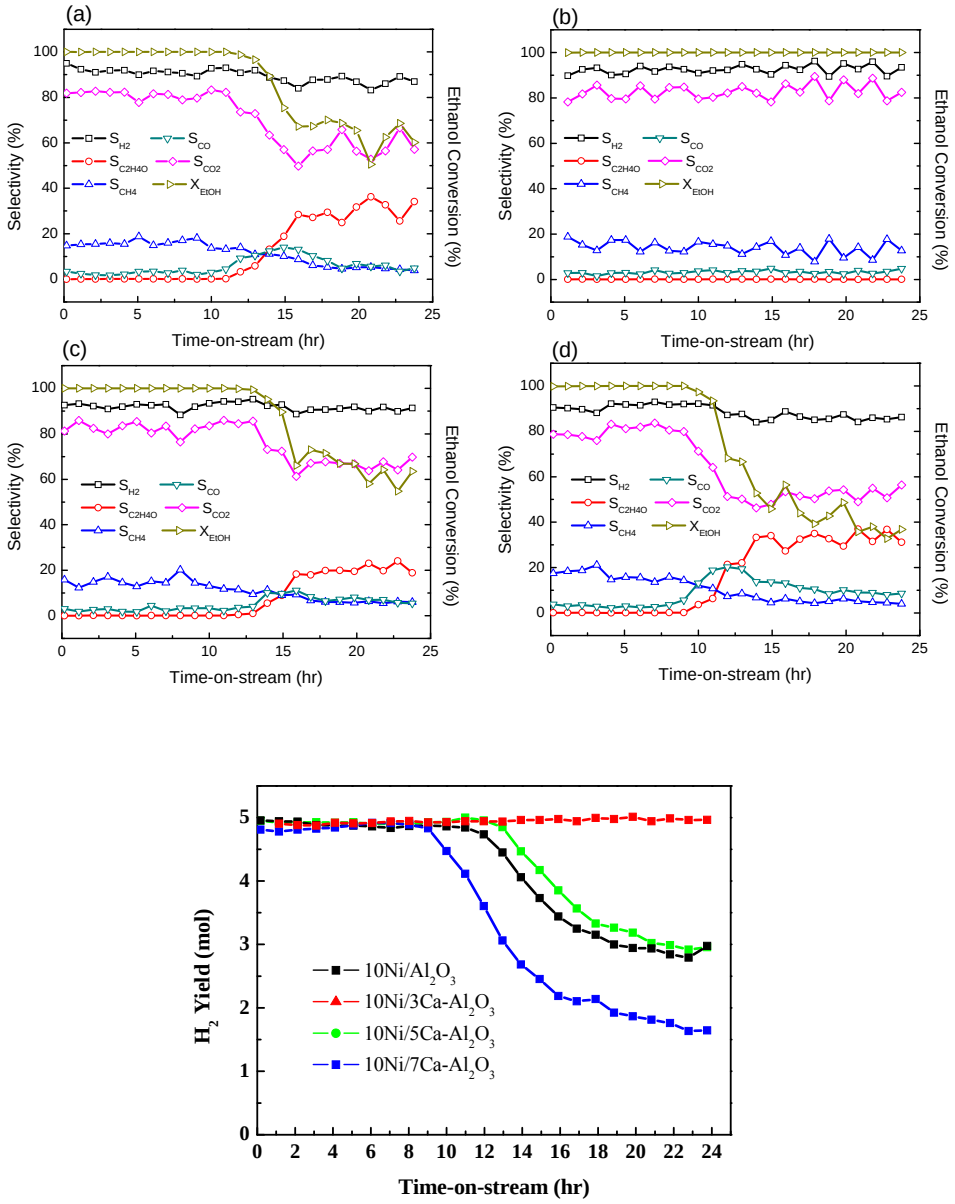

Figure 5.1. Catalytic performance of (a) $10Ni/Al_2O_3$; (b) $10Ni/3Ca\text{-}Al_2O_3$; (c) $10Ni/5Ca\text{-}Al_2O_3$; (d) $10Ni/7Ca\text{-}Al_2O_3$ as well as in (e) H_2 yield of the above catalysts. Reaction at 673 K with ethanol/water ratio at 1:3 by volume.

5.3.2 Metal Dispersion of $10Ni/xCa\text{-}Al_2O_3$

The H_2-TPD and O_2 pulse chemisorption were used to evaluate the nickel dispersion of the reduced catalysts. The degree of reduction of the nickel catalysts calculated using O_2 pulse chemisorption is shown in Table 5.1. On bare Al_2O_3 support, 55% of the NiO are reduced to metallic nickel. The addition of Ca elevates the degree reduction to 60% for 10Ni/3Ca-Al_2O_3 and 66% for 10Ni/7Ca-Al_2O_3. Considering these calculated values, the metal dispersion for 10Ni/7Ca-Al_2O_3 is determined to be 15.1% poorer in comparison to that of $10Ni/Al_2O_3$ which has a metal dispersion of 39.7%. Using the metallic crystallite sizes tabulated in Table 5.1 again verify that the addition of Ca over alumina increases the crystallite size of nickel.

Table 5.1. Ni particle size, Catalyst Dispersion and Degree of Reduction of Ni Catalysts.

Sample	**NiO Crystallite* Size (nm)**	**H_2 uptake** (µmol/g-cat)**	**Degree of Reduction** (%)**	**Percentage Dispersion** (%)**	**Ni Crystallite Diameter** (nm)**
$10Ni/Al_2O_3$	6.0	187.5	55.2	39.7	2.4
10Ni/3Ca-Al_2O_3	7.9	86.1	59.8	16.8	5.8
10Ni/7Ca-Al_2O_3	8.6	85.8	66.5	15.1	6.4

* Crystallite size obtained from XRD data calculated from Scherrer formula.

** Data obtained from metal dispersion experiment as described in Section 5.2.

TOF_{H2} of the reaction is obtained at 673 K and is calculated according to Eqn. (5.16):

$$TOF_{H_2}\ (s^{-1}) = \frac{Rate\ of\ H_2\ production\ (umols/g \cdot s)}{Amount\ of\ active\ sites\ (umols/g)} \tag{5.16}$$

TOF_{H2} of all catalysts at 573–873K are tabulated in Table 5.2. At 673 K, the TOF_{H2} is 0.091 s^{-1}, 0.205 s^{-1}, 0.207 s^{-1} for $10Ni/Al_2O_3$, $10Ni/3Ca\text{-}Al_2O_3$ and $10Ni/7Ca\text{-}Al_2O_3$ respectively. The presence of Ca increases the TOF_{H2} of ESR and is prevalent at all temperatures. Increasing Ca loading (>3 wt%) does not necessarily lead to further enhancement in TOF_{H2} as clearly shown in Table 5.2. The increase in TOF will be discussed in terms of Ni particle size, valence band Ni 3d density of catalyst in (in the discussion section).

Table 5.2. TOF_{H2} of catalysts at 573 K, 673 K, 773 K and 873 K.

Temperature (K)	Catalyst	TOF_{H2} (s^{-1})
573	$10Ni/Al_2O_3$	0.046
	$10Ni/3Ca\text{-}Al_2O_3$	0.114
	$10Ni/7Ca\text{-}Al_2O_3$	0.103
673	$10Ni/Al_2O_3$	0.091
	$10Ni/3Ca\text{-}Al_2O_3$	0.205
	$10Ni/7Ca\text{-}Al_2O_3$	0.207
773	$10Ni/Al_2O_3$	0.112
	$10Ni/3Ca\text{-}Al_2O_3$	0.245
	$10Ni/7Ca\text{-}Al_2O_3$	0.246
873	$10Ni/Al_2O_3$	0.115
	$10Ni/3Ca\text{-}Al_2O_3$	0.249
	$10Ni/7Ca\text{-}Al_2O_3$	0.250

5.3.3. X-ray Diffraction (XRD) and Particle Size of the Catalysts

Powder XRD analysis were performed on the calcined, reduced and spent catalysts to identify the species present in the catalysts. Fig. 5.2 shows the XRD patterns of $10Ni/Al_2O_3$, $10Ni/3Ca\text{-}Al_2O_3$ and $10Ni/7Ca\text{-}Al_2O_3$ at the various statuses (calcined, reduced and spent). XRD patterns of calcined catalysts exhibit characteristic diffraction peaks corresponding to nickel oxide (NiO, $2\theta = 37.1^o$, 43.1^o, 62.8^o) and alumina (Al_2O_3, $2\theta = 37.2^o$, 45.3^o, 66.9^o). The NiO crystallite size is calculated using Scherrer's formula, based on NiO (2 0 0) diffraction peak at 43.1^o. NiO particle sizes are found to increase with increasing Ca-loading (Table 5.1). Larger NiO particles are observed on $7Ca\text{-}Al_2O_3$ support, with crystal size of 8.6 nm. The characteristic XRD peaks of calcium oxide (CaO) and calcium-alumina spinels (Ca-Al-O) are not observed on Ca-modified catalysts. As CaO is likely to form after decomposition of calcium nitrate during the calcination, the absence of CaO peaks may suggest that CaO is amorphous in nature. Ca-Al-O spinel phases are absent since they can be formed only at high temperatures (> 1173 K). Diffraction peaks belonging to Ni metal ($2\theta = 44.4^o$, and 51.8^o) on all three reduced catalysts are identified. The peak intensity and hence the particle size are increased with increasing Ca loading as listed in Table 5.1. On spent catalysts, Ni metal peaks decay greatly in intensity and can be clearly observed only on $Ni/3Ca\text{-}Al_2O_3$. This is true particularly for the peak at 51.8^o. The Ni peak at 44.4^o which is the strongest one is overlapped with NiO peaks and cannot be easily distinguished from NiO peaks.

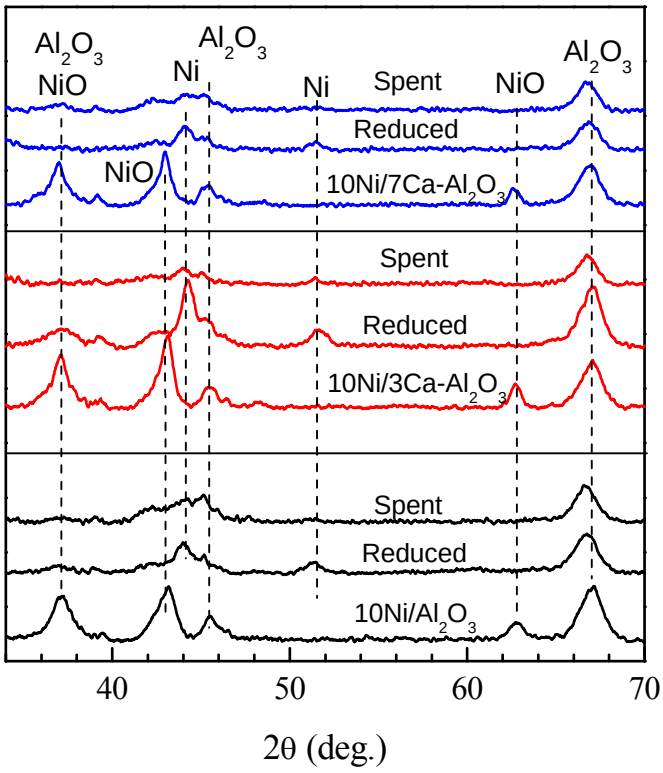

Figure 5.2. X-ray diffraction patterns of 10Ni/*x*Ca-Al_2O_3 catalysts.

5.3.4. H_2-temperature programmed Reduction (H_2-TPR) and the Reducibility of 10Ni/Ca-Al_2O_3 Catalysts

H_2-TPR gives important information on the reducibility and the type of reducible species present on the surface of the catalyst. The reduction profiles of bare and Ca-modified 10Ni/Al_2O_3 catalysts are presented in Fig. 5.3. The H_2-TPR profile of bare Ni/Al_2O_3 shows a broad H_2 consumption peak which centers at 826 K. This can be assigned to the reduction of bulk phase NiO, otherwise known

as "fixed nickel" which interacts intimately with the alumina support [15]. In contrast to bare $10Ni/Al_2O_3$, the addition of calcium shifts the maximum peak to a lower temperature ($T = 795$ K). The TPR profiles of $Ni/3Ca\text{-}Al_2O_3$ and $Ni/7Ca\text{-}Al_2O_3$ also present an additional shoulder peak located at 688 K and 713 K, respectively. These shoulder peaks are ascribed to the reduction of weakly bound NiO species, commonly known as "free nickel" [15]. Evidently, the addition of calcium promotes the reducibility of NiO species by weakening the interactions between support and metal. This observation is in agreement with [16], in which the reduction of $Ni/CaO/Al_2O_3$ catalyst is initiated at lower temperatures as compared to Ni/Al_2O_3 catalyst. The ease of NiO reduction indicates the presence of larger metallic Ni particles on $Ca\text{-}Al_2O_3$ supported Ni catalysts, which is in agreement with the metal dispersion analysis shown in Table 5.1.

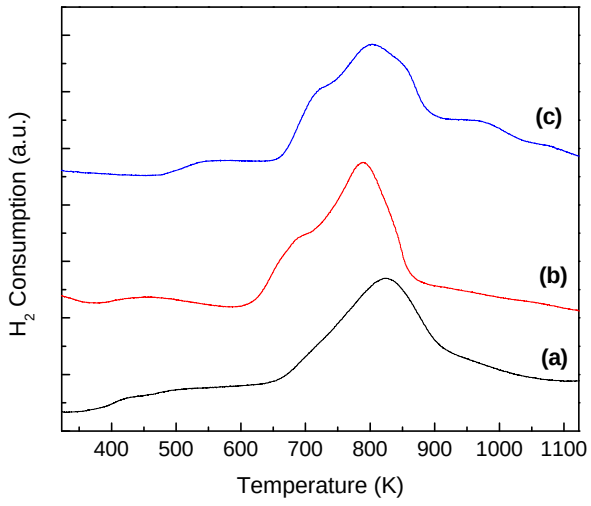

Figure 5.3. H_2-TPR of alumina and Ca-modified alumina nickel supported catalyst: (a) $10Ni/Al_2O_3$; (b) $10Ni/3Ca\text{-}Al_2O_3$ and (c) $10Ni/7Ca\text{-}Al_2O_3$.

5.3.5. XPS study of Ni/*x*Ca-Al_2O_3 catalysts

XPS wide scans and narrow scans of the Ca 2p, O 1s, Al 2p, Ni $2p_{3/2}$ and C 1s core levels were measured on the reduced and spent 10Ni/*x*Ca-Al_2O_3 catalysts (Fig. 5.4 and 5.5). Ca 2p spectra of all the samples demonstrated a principle peak at 347.0 eV which is characteristic of CaO and which is largely unchanged under different conditions. Al 2p peak at 73.7 eV is attributed to Al ions in Al_2O_3. O 1s spectra centered at binding energy of ~531 eV are related to the oxygen derived from Al_2O_3 (531.3 eV) though NiO (529.6 eV) and CaO (528.5 eV) might also contribute some intensity at lower binding energies.

The Ni 2p signals of reduced $10Ni/Al_2O_3$ catalyst in Fig. 5.4 are weak, but do indicate the presence of metallic Ni (852.5 eV), NiO (855.5 eV) and possibly some $NiAl_2O_4$ (856.5 eV) [17]. Since $NiAl_2O_4$ diffraction peaks are absent from XRD characterization, its formation may be restricted to the surface and the composition was insignificant. The Ni 2p signal is greatly enhanced in reduced Ni/3Ca-Al_2O_3 and Ni/7Ca-Al_2O_3 catalysts due to the addition of Ca. The atomic ratio of Ni/Al derived from XPS analysis increases from 0.14 on $10Ni/Al_2O_3$ to 0.37–0.38 on 10Ni/3Ca-Al_2O_3 and 10Ni/7Ca-Al_2O_3. Both Ni^0 and Ni^{2+} peaks as well as their shake-up satellites are evidently observable in Ca-modified catalysts. The presence of characteristic Ni^{2+} component indicates that the NiO are not completely reduced in all the samples. However, stronger metallic Ni peaks are found on Ca-modified catalysts. The extent of reduction as calculated using area ratio of $Ni^0/(Ni^0 + Ni^{2+})$ increases from 0.38 to 0.45 upon the introduction of

calcium. The increase in calcium loading does not further enhance the reducibility as the extent of reduction remains at 0.45 on $10Ni/7Ca\text{-}Al_2O_3$. This result differs from the degree of reduction data obtained from metal dispersion measurements where we observe a continuous increase in degree of reduction on $10Ni/7Ca\text{-}Al_2O_3$. The discrepancy arises because XPS is a surface sensitive tool while O_2 chemisorption of metallic particles analysis focuses more or less on the bulk characteristic of the material. Nevertheless it can be concluded that the presence of Ca on the Al_2O_3 support helps to enrich Ni on the catalyst surface and enhance the reducibility of NiO to metallic Ni under reduction conditions.

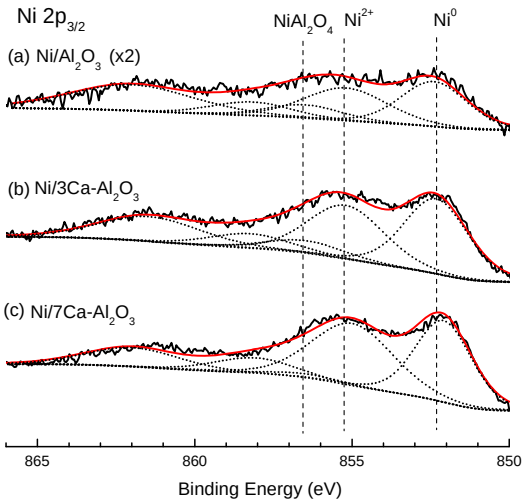

Figure 5.4. XPS spectra of Ni $2p_{3/2}$ on reduced (a) $10Ni/Al_2O_3$; (b) $10Ni/3Ca\text{-}Al_2O_3$ and (c) $10Ni/7Ca\text{-}Al_2O_3$ catalysts.

On the spent catalysts (Fig. 5.5(a)), the C 1s spectra are very strong. They exhibit principle peaks that are assigned to graphite, methyl fragments and carbonate/acetate at binding energies of 284.5 eV, 285.6 eV and 288.8 eV,

respectively [18]. The intensity of the graphite peak is extremely strong for all samples. An additional weak shoulder located at low binding energy of 282.6 eV is observed from spent $10Ni/7Ca\text{-}Al_2O_3$ sample. This binding energy is lower than the normal nickel carbide species (BE = 283.9 eV), thus suggesting the presence of NiC_x species. These different forms of carbon species can result in deactivation. The XPS Ni $2p_{3/2}$ signals of the spent catalysts in Fig. 5.5(b) are reasonably weak. Nevertheless, the spectrum can be deconvoluted into three nickel species including metallic nickel, unreduced nickel oxide and nickel aluminates. The percentage of metallic nickel that remains on the surface after 24 h of reaction is 10.9%, 23.4% and 8.9% for $10Ni/Al_2O_3$, $10Ni/3Ca\text{-}Al_2O_3$ and $10Ni/7Ca\text{-}Al_2O_3$, respectively. X-ray excited Auger electron spectroscopy (XAES), being more sensitive than XPS, is used to further probe the chemical state of Ni. The kinetic energy position of XAES of Ni LVV Auger transition is shown in Fig. 5.6. The Ni (LVV) Auger line is recorded at kinetic energy of 852.7 eV and is only observable on spent $Ni/3Ca\text{-}Al_2O_3$, but not on other two spent catalysts (Fig. 5.6). The high-energy electron ejects the inner electron from the L shell of Ni during an Auger process. The inner L shell vacancy is filled by a second electron at a higher V shell, and together with a third electron at the V shell, the Auger electron, leaves the Ni atom. The excess energy is transferred to the Auger electron in the form of kinetic energy. These results are consistent with our XRD observations which indicate that metallic nickel diffraction XRD peaks are only observable on spent $10Ni/3Ca\text{-}Al_2O_3$. The weakening of metallic nickel signals from XPS and XRD could be due to the presence of coke deposits after

ESR at 673 K for 24 h. The existence of nickel carbide species is observable by the appearance of a weak shoulder peak at BE = 852.0 eV on $10Ni/7Ca\text{-}Al_2O_3$ catalyst (Fig. 5.5(b-iii)).

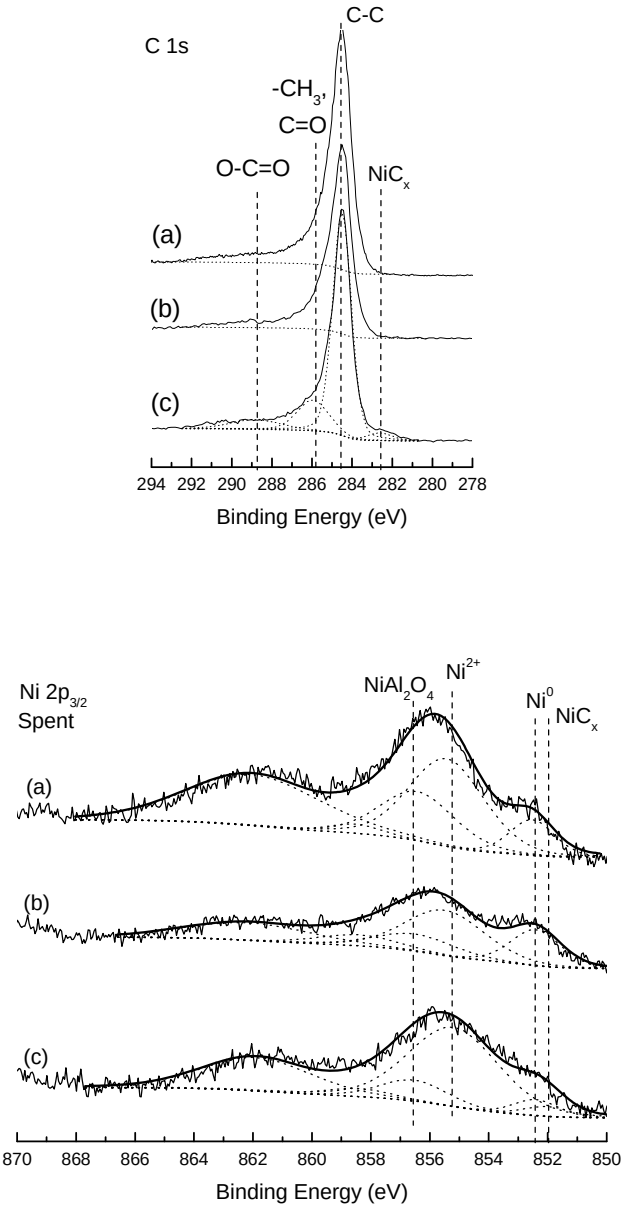

Figure 5.5. XPS spectra of (a) C 1s and (b) Ni $2p_{3/2}$ on spent (i) $10Ni/Al_2O_3$, (ii) $10Ni/3Ca\text{-}Al_2O_3$ and (iii) $10Ni/7Ca\text{-}Al_2O_3$ catalysts.

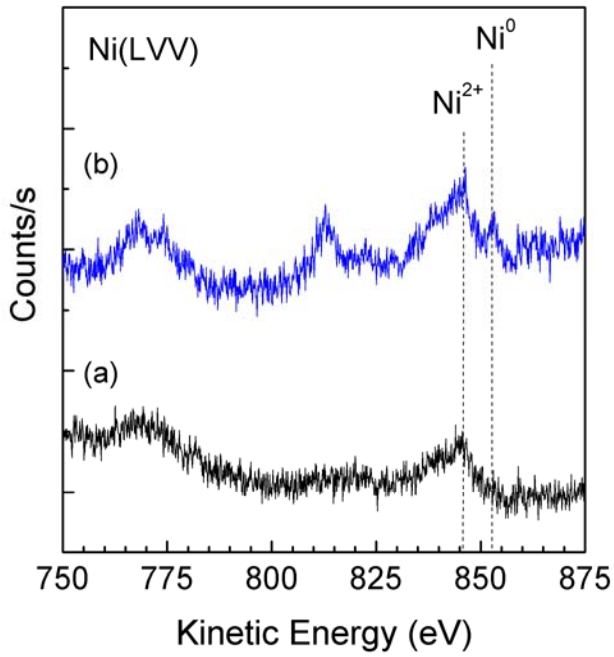

Figure 5.6. Auger electron spectra of Ni on spent (a) $10Ni/Al_2O_3$ and (b) $10Ni/3Ca\text{-}Al_2O_3$.

In the Chapter 4, we have compared the valence-band photoelectron spectra of bare Al_2O_3 and $7Ca\text{-}Al_2O_3$ (Fig. 4.6) and shown that the addition of Ca enhances the valence band intensity in the 6–8 eV binding energy region, which can be attributed to Ca 4s orbital. In Fig. 5.7, the valence band spectra of the reduced $10Ni/Al_2O_3$ catalyst and bare Al_2O_3 support are compare, demonstrating an enrichment of DOS at 0–5 eV which is due to Ni 3d orbitals. Based on these results, the valence band spectra of reduced $10Ni/Al_2O_3$, $10Ni/3Ca\text{-}Al_2O_3$ and $10Ni/7Ca\text{-}Al_2O_3$ in Fig. 5.7 clearly show that the addition of Ca promotes the reducibility of nickel oxide particles, resulting in stronger metallic Ni character.

The donating nature of both Ni 3d and Ca 3p may play a significant role in the activation of the adsorbate molecules bonded to Ni sites or CaO, such as ethanol, water and their fragments. Such valence electronic enhancement due to the addition of Ca is likely to affect the catalytic performance of the system.

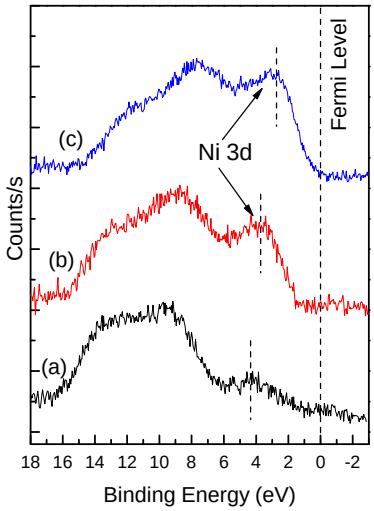

Figure 5.7. Valence band of Ni-supported catalysts on (a) Al_2O_3; (b) 3Ca-Al_2O_3 and (c) 7Ca-Al_2O_3.

5.3.6. Study of the spent catalysts with thermal gravimetric analysis (TGA), temperature-programmed oxidation (TPO), Raman spectroscopy, SEM and TEM

The spent catalysts with carbon deposition after ESR at 673 K for 24 h were characterized by TGA, TPO, SEM and TEM. TGA and TPO were both performed on the spent catalysts in oxygen stream to quantify the amount of coke deposited on the spent catalysts. TGA results indicate that 10Ni/7Ca-Al_2O_3

accumulated the largest amount of coke, accounting for a coking rate of 0.023 g $(g\ cat\ h)^{-1}$. $10Ni/Al_2O_3$ had the 2nd highest coking rate of 0.019 g $(g\ cat\ h)^{-1}$ while coking on $10Ni/3Ca\text{-}Al_2O_3$ is the least with a rate of 0.012 g $(g\ cat\ h)^{-1}$.

The TPO profiles in Fig. 5.8 display the CO_2 emission as a function of the oxidation temperature of carbon deposition on spent catalysts after ESR. The CO_2 peaks for all the catalysts are asymmetrical in shape, implying the presence of a few different carbonaceous species. It is generally accepted that saturated C–C bond such as paraffinic or amorphous carbon tends to oxidize at lower temperatures than unsaturated hydrocarbon such as olefins, graphitic and filamentous carbon [19, 20]. From the profiles, both amorphous ($T_{oxidation}$ = 673–823 K) and graphitic/filamentous ($T_{oxidation}$ = 823–923 K) carbon depositions can be found in all the spent catalysts. About 50% of the carbon deposition is in the filamentous form on $10Ni/Al_2O_3$ while most of it is amorphous on $10Ni/3Ca\text{-}Al_2O_3$. Further increase of the Ca content to 7% leads to more amorphous carbon on $Ni/7Ca\text{-}Al_2O_3$. This shows that the high Ca loading favors the formation of amorphous carbon (Fig. 5.8(c)). This is in agreement with our measured Raman I_D/I_G ratios which show that the degree of disordering of carbon deposition increased with increasing Ca loading (Table 5.3).

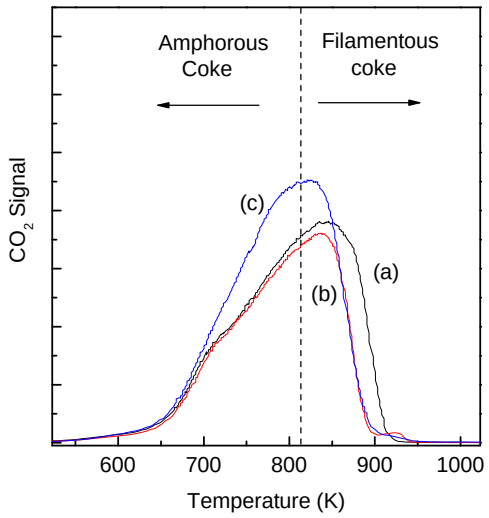

Figure 5.8. TPO profiles of spent catalysts: (a) $10Ni/Al_2O_3$; (b) $10Ni/3Ca\text{-}Al_2O_3$ and (c) $10Ni/7Ca\text{-}Al_2O_3$.

Table 5.3. Intensity Ratio of the *D* and *G* bands (I_D/I_G) of Spent ESR Catalysts.

Catalysts	**I_D/I_G**
$10Ni/Al_2O_3$	0.88
$10Ni/3Ca\text{-}Al_2O_3$	0.98
$10Ni/7Ca\text{-}Al_2O_3$	1.09

SEM images of the spent catalysts are shown in Fig. 5.9. Filamentous carbons are easily observed in $10Ni/3Ca\text{-}Al_2O_3$ and $10Ni/7Ca\text{-}Al_2O_3$ spent catalysts. The size of the carbon filaments, however, varies depending on the Ca loading. Larger filaments are found on higher Ca-loading catalysts such as $10Ni/7Ca\text{-}Al_2O_3$. The carbon filaments on $10Ni/Al_2O_3$ are small in size and not

easily observed by SEM (Fig. 5.9(a)). Fortunately they can be seen in the TEM image attached in Fig. 5.9(a) panel. Ni particle size of less than 10 nm can be observed on $10Ni/Al_2O_3$ by TEM in Fig. 5.10(a). Core–shell type encapsulating carbon with Ni particles around 20 nm as core can be found on spent $10Ni/7Ca\text{-}Al_2O_3$ (Fig. 5.10(b)).

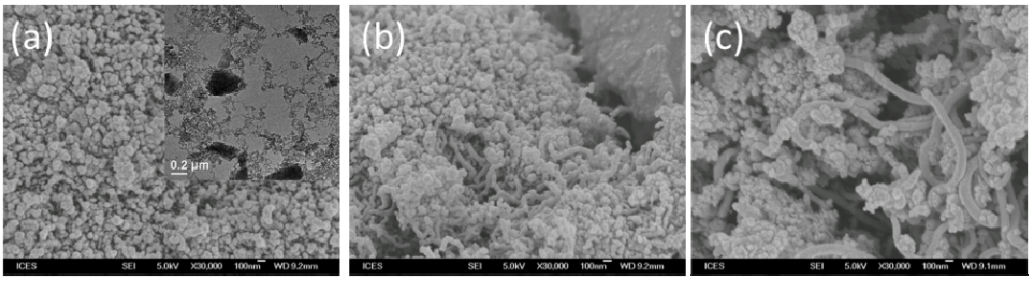

Figure 5.9. SEM images of spent catalysts after 24 h of ESR at 673 K: (a) $10Ni/Al_2O_3$; (b) $10Ni/3Ca\text{-}Al_2O_3$ and (c) $10Ni/7Ca\text{-}Al_2O_3$. Insert in (a): TEM image of spent $10Ni/Al_2O_3$.

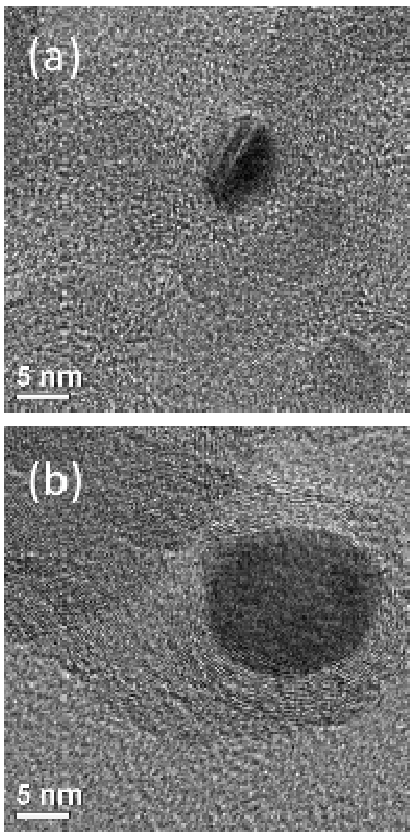

Figure 5.10. TEM images of spent (a) $10Ni/Al_2O_3$ and (b) $10Ni/7Ca\text{-}Al_2O_3$.

5.3.7. CH_4 decomposition and steam coke gasification

The carbon deposition on spent catalysts for ethanol steam reforming may derive from three different sources, namely, CH_4 decomposition (Eqn. 5.11), CO disproportionation (Eqn. 5.12) and the polymerization of unsaturated carbonaceous species such as C_2H_4, C_2H_4O and their fragments (Eqn. 5.10). Since the product distribution of ethanol steam reforming over 10 wt% Ni catalysts at 673 K (and 623 K) shows the absence of CH_3CHO, C_2H_4 and CO, it is likely that the deactivation is mainly due to the decomposition of CH_4, giving rise to C, CH_n and H_2. We therefore studied the catalytic decomposition of CH_4 using tapered

element oscillating microbalance (TEOM). The mass change due to the formation of carbon from the decomposition of CH_4 at 773 K over three different catalysts is shown in Fig. 5.11. The rate of carbon deposition from CH_4 decomposition is about 2.34 $atom_C$ $(atom_{Ni}\ min)^{-1}$, 5.90 $atom_C$ $(atom_{Ni}\ min)^{-1}$ and 6.02 $atom_C$ $(atom_{Ni}\ min)^{-1}$ for $10Ni/Al_2O_3$, $10Ni/3Ca\text{-}Al_2O_3$ and $10Ni/7Ca\text{-}Al_2O_3$, respectively. It is well known that metallic Ni can catalyze the CH_4 decomposition. The present results show that the presence of Ca can enhance the CH_4 decomposition, resulting in a higher coking rate. This should be related to the enhanced electron density near the Fermi level on the Ca-modified Ni catalysts, and will be discussed later.

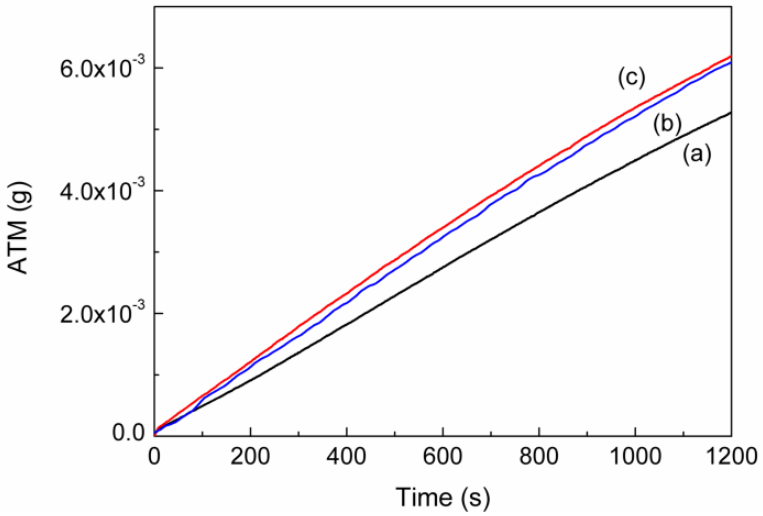

Figure 5.11. Carbon formation from CH_4 decomposition at 1 atm and 773 K catalyzed by: (a) $10Ni/Al_2O_3$; (b) $10Ni/3Ca\text{-}Al_2O_3$ and (c) $10Ni/7Ca\text{-}Al_2O_3$.

Choudhary and Goodman have shown that the surface carbon and/or carbonaceous species generated from methane cracking on Ni surface at 673 K or

below can be removed via reaction with water [21]. To study the effect of Ca addition on the steam gasification of coke deposition, we performed steam gasification tests on the three $10Ni/xCa\text{-}Al_2O_3$ catalysts which were covered with coke generated from the CH_4 decomposition. The samples were exposed to steam and heated from 423 K to 1023 K. The steam gasification products such H_2, CO and CO_2 were detected and monitored using mass spectroscopy. As plotted in Fig. 5.12, steam gasification of carbon deposition begins at $T = 675$ K on $10Ni/Al_2O_3$. The set-on temperature shifts to $T = 595$ K on the $Ni/Ca\text{-}Al_2O_3$ catalysts. At 675 K it proceeds at remarkable rates, indicating that the presence of Ca is able to effectively accelerate the steam gasification of coke deposition and remove it from the catalyst surface. This is due to the increased in water adsorption ability in the presence of Ca as previous demonstrated in Chapter 4. This may well explain the absence of deactivation of $10Ni/3Ca\text{-}Al_2O_3$.

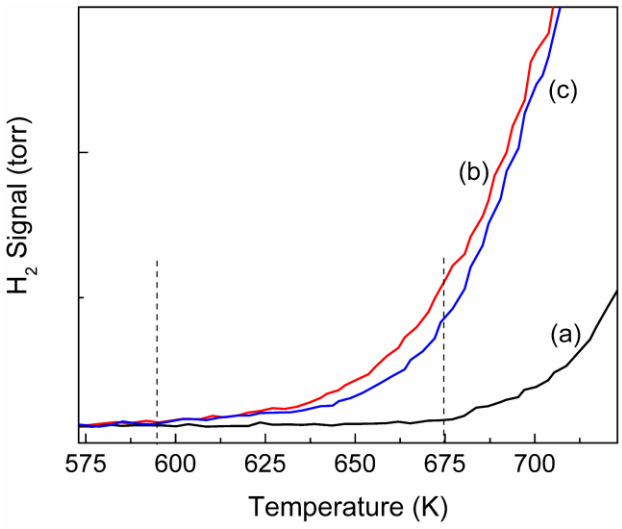

Figure 5.12. Steam Gasification of coke produced from CH_4 decomposition on (a) $10Ni/Al_2O_3$; (b) $10Ni/3Ca\text{-}Al_2O_3$ and (c) $10Ni/7Ca\text{-}Al_2O_3$.

5.4. Discussions

As presented above, the addition of Ca reduces the surface area of Al_2O_3, weakens the interaction between Ni and Al_2O_3 support, leading to a lower Ni dispersion as there are less surface sites for the Ni particles to anchor upon. This results in larger Ni particle size. However, a suitable amount (3 wt%) of Ca addition improves the Ni catalyst stability significantly, while catalyst without Ca or with high content of Ca (7 wt%) deactivates easily (Fig. 5.1(e)). The stability of catalysts decreases in the order of $10Ni/3Ca\text{-}Al_2O_3 > 10Ni/Al_2O_3 > 10Ni/7Ca\text{-}Al_2O_3$ with reversed coking rate during ESR.

The catalyst deactivation may result from the loss of active metallic Ni on the surface. From XPS study of Ni 2p on spent catalysts, there is only less than half of metallic Ni left on the surfaces of spent $10Ni/Al_2O_3$ and $10Ni/7Ca\text{-}Al_2O_3$ catalysts than that on $10Ni/3Ca\text{-}Al_2O_3$. Since the densities of Ni^0 particles detected on the surface of all three spent catalysts by XPS Ni 2p are small and that peak deconvolution is often subjective, it would be better to observe Ni^0 using XAES. The higher density of Ni^0 on the surface of $10Ni/3Ca\text{-}Al_2O_3$ can be observed from Ni XAES (Fig. 5.6) at about 852.7 eV on the kinetic energy scale while only Auger peak of Ni in oxide form is detected on the surface of $10Ni/Al_2O_3$ (K.E. = 845.9 eV) [22, 23]. These results are consistent with our XRD observations which indicate that metallic nickel diffraction XRD peaks are only observable on spent $10Ni/3Ca\text{-}Al_2O_3$. This may suggest that the Ni^0 on

$10Ni/Al_2O_3$ and $10Ni/7Ca\text{-}Al_2O_3$ has been covered, most probably by coke since more coke has been burned off on the spent $10Ni/Al_2O_3$ and $10Ni/7Ca\text{-}Al_2O_3$ than $10Ni/3Ca\text{-}Al_2O_3$ as measured by TGA.

The carbon deposition from ethanol steam reforming may derive from reaction products/intermediates, such as CH_4, CO, C_2H_4, CH_3CHO or/and their molecular fragments. Since the product distribution of ethanol steam reforming over $10Ni/x Ca\text{-}Al_2O_3$ catalysts shows an absence of C_2H_4O, C_2H_4 and CO at 673 K (and 623 K), it is likely that the carbon deposition at low temperature region is mainly due to the decomposition of CH_4. However, it is interesting to note that coking rates of CH_4 decomposition recorded by TEOM (Fig. 5.11) follow the sequence of $10Ni/7Ca\text{-}Al_2O_3 > 10Ni/3Ca\text{-}Al_2O_3 > 10Ni/Al_2O_3$, while the overall coking rates during ESR reaction follow the sequence of $10Ni/7Ca\text{-}Al_2O_3 > 10Ni/Al_2O_3 > 10Ni/3Ca\text{-}Al_2O_3$.

It is well known that Ni catalyzes CH_4 decomposition, and the dissociation of CH_4 was found to be able to occur at low temperatures such as 673 K, forming H_2, C or/and CH_x [21] and the coking rate is proportional to Ni particle size [24]. For example, Chen et al. found that the yield of carbon nanofiber (CNF) is extremely sensitive to Ni (NiO) crystal size and the yield of the CNF increases with Ni crystal size at a certain range. Ni crystals that are too large or too small yield low growth rates and low yield of CNF. This phenomenon was explained by the saturation concentration in Ni crystal which serves as a dominating factor [24]. In our investigation, the addition of Ca clearly increases the nickel particle size (Table 5.1), and larger coking rate was measured by TEOM on Ca promoted

catalysts (Fig. 5.11), which is consistent with Chen et al.'s findings [24]. Furthermore, the higher coking rate of CH_4 decomposition on Ca promoted catalysts could be well explained by our XPS study. Kratzer et al. postulated that the dissociation of CH_4 is more likely to occur when the empty anti-bonding orbital of C–H bond σ* of CH_4 interacts with the high density of nickel *d* states which are close to the Fermi level [25]. When Ni atoms are alloyed by neighbor Au atoms, the *d* band states are lowered and the interaction of σ* and the d states is weaken. This explains why coking on Ni atom can be reduced by alloying with Au [25]. The valence band spectra of reduced Ni catalysts in Fig. 5.6 shows that the addition of Ca in $10Ni/Al_2O_3$ enriches the surface metallic nickel and enhanced electron density near Fermi level due to the contribution of Ni 3d which is in favor of the C-H bond scission according to Kratzer et al. [25]. At this point, the higher coking rate on $10Ni/Ca\text{-}Al_2O_3$ catalysts than that of non-Ca promoted catalyst and the fact that the coking rate increases with Ca loading are well supported by both our experiment and literatures [24, 25]. It is therefore worthwhile to investigate why the coking rate during ESR on these catalysts does not follow the trend of coking rates during CH_4 decomposition.

Under ESR reaction conditions, the involvement of H_2O in the reaction will help to remove some coke via gasification. As shown in Fig. 5.12, the gasification of coke on Ni/Al_2O_3 begins at 675 K, the on-set temperature dramatically reduces 80–595 K for Ca promoted catalysts. This result indicates that the coke on Ca promoted catalyst is either more crystalline (or less stable) than that on $10Ni/Al_2O_3$ or Ca promoted catalysts is more active for H_2O

adsorption/activation and as a result the gasification is promoted or both factors take place simultaneously.

Several reports have shown that the crystalline structures of the carbon species are dependent on catalyst particle size, reaction temperature and aging time [21, 24, 26]. They can accumulate and deactivate the catalysts. In our experiment, since all the coked catalysts have been tested under identical conditions, the only parameter which results in the difference of crystalline structure of carbon would be the Ni particle size. Indeed, from the Raman I_D/I_G ratios shown in Table 5.3, the I_D/I_G ratio increases with increasing Ni particle size (with increase in Ca loading). Since the intensity ratio of the D line to the G line (I_D/I_G) is a measure of the degree of graphitization of the CNTs, a smaller I_D/I_G value will represent a well crystalline carbon structure. Hence, the results indicate that the crystallinity of coke is higher on $10Ni/Al_2O_3$ which has smaller Ni particles while the bigger Ni particles of $10Ni/7Ca\text{-}Al_2O_3$ produces CNF of poor crystallinity. The coke gasification by H_2O in Fig. 5.12 also shows lower on-set gasification temperature for $10Ni/7Ca\text{-}Al_2O_3$ which agrees well with the above discussion.

As discussed above, there are advantages and disadvantages to Ca addition. Coking rate is higher on Ca-modified catalysts, but the coke generated via fast coking rate is less crystalline and less stable, and hence can be gasified by steam easily. Ca may increase the H_2O adsorption/activation for gasification as well as discussed in Chapter 1. In this situation, it is therefore not surprising that there would be a suitable Ca loading which can balance these two factors. The

excellent stability achieved on $10Ni/3Ca\text{-}Al_2O_3$ can be attributed to the less crystalline nature and fast steam gasification of carbon deposition derived from CH_4 decomposition on the catalyst (Fig. 5.8 and Fig. 5.12). Our ESR experiments are mainly conducted at relatively low temperatures, 673 K or below. 673 K is a marginal temperature below which the amorphous to graphitic carbon transition will not occur [26]. Under such reaction conditions, the transition of amorphous carbon to graphite is largely dependent on the accumulation level of carbon deposition [26]. In the meantime, the addition of suitable amount (3 wt%) of Ca promotes the steam gasification of carbon deposition via the enhanced water adsorption and activation (Fig. 3.8). Hence it is expected that the steam gasification proceeds fast enough on $10Ni/3Ca\text{-}Al_2O_3$ to maintain more amorphous nature of carbon deposition on it, which in turn facilitates the carbon removal and keep the Ni sites active for ESR.

On bare Al_2O_3 support, the Ni catalyst is less active in methane decomposition due to lower d band density of the catalyst. However, smaller Ni particle size favored the saturation of amorphous carbon and its transition to graphite/filament (Fig. 5.9(a)). The well graphitic carbon is more difficult to remove compare to the less crystalline carbons on Ca promoted catalysts under the same reaction condition. The filamentous/graphitic carbon species is less reactive and more difficult to remove via oxidation or steam gasification than amorphous carbon species. Hence we did not observe the steam gasification from spent methane decomposition $10Ni/Al_2O_3$ catalyst at 673 K (Fig. 5.12) whereas at

the same temperature the steam gasification occurred evidently on $10Ni/Ca\text{-}Al_2O_3$ catalysts, in particular on $10Ni/3Ca\text{-}Al_2O_3$.

On $10Ni/7Ca\text{-}Al_2O_3$ the high Ca loading weakens the metal–support interaction and enhances the reducibility of NiO. As a result, larger Ni particles with enhanced Ni 3d valence electron density are observed on the $10Ni/7Ca\text{-}Al_2O_3$ catalyst. Larger methane decomposition rate and C–C bond formation rate (to form carbon network from surface C atoms) as well as higher accumulation level of carbon deposition are therefore expected, all of which lead to the transition of amorphous to graphite/filamentous carbon. Thus bigger carbon fibers are clearly observed on $10Ni/7Ca\text{-}Al_2O_3$ by SEM (Fig. 5.9(c)). Large Ni particle size may also favor the core/shell like encapsulating carbon deposition, because of larger ensemble size and lower bulk diffusion rate (as compare to the faster surface decomposition rate) according to Chen et al. [24], and indeed, it is not difficult to find the encapsulated Ni particles on $10Ni/7Ca\text{-}Al_2O_3$ as shown in the high resolution TEM image in Fig. 5.10. Both the encapsulating and filamentous carbons on $10Ni/7Ca\text{-}Al_2O_3$ are difficult to remove under the reaction condition. They block the active Ni sites, leading to the catalytic deactivation when the increase in the selectivity of acetaldehyde and the drop in the CH_4, H_2 and CO_2 selectivities are observed.

Of course, the function of oxide supports on the water adsorption/activation for coke gasification is another important factor which cannot be excluded since oxide supports are found to be the principle sites for water adsorption and activation [27]. The presence of alkaline earth or alkali

metals as promoter is found to create large number of water adsorption sites as shown previously in Chapter 4.

5.5. Conclusions

The catalytic performance and stability of Ni/Al_2O_3 ethanol steam reforming catalyst can be manipulated by the addition of Ca. There are advantages and disadvantages to Ca addition. Ca addition reduces the surface area of Al_2O_3 and weakens the interaction between Ni and Al_2O_3, as a result Ni particle becomes bigger. Electronic enrichment in Ni 3d band electrons was found on Ca-modified catalysts and increased with Ca loading. As a result, methane, a byproduct of ethanol steam reforming and the main source of coke precursor, was promoted to dissociate on Ca modified catalyst, and the coking rate increases following the sequence of $10Ni/7Ca\text{-}Al_2O_3 > 10Ni/3Ca\text{-}Al_2O_3 > 10Ni/Ca\text{-}Al_2O_3$. On the other hand, less crystalline carbon was formed on Ca modified catalysts which were easier to be gasified during ESR, leaving more active Ni particles exposed for reaction on $10Ni/3Ca\text{-}Al_2O_3$ catalyst. Therefore, the excellent stability of nickel supported catalysts on $3Ca\text{-}Al_2O_3$ is due to the optimization of Ca-loading such that coke deposition via CH_4 decomposition is minimized while maintaining a steady gasification of coke deposits by steam.

5.6. References

[1] M. Ball, M. Wietschel, Int. J. Hydrogen Energy. 34 (2009) 615-627.

[2] P. de la Piscina, N. Homs, Chem. Soc. Rev. 37 (2008) 2459-2467.

[3] E. Wanat, K. Venkataraman, L. Schmidt, Appl. Catal. A: Gen. 276 (2004) 155-162.

[4] S. Freni, S. Cavallaro, N. Mondello, L. Spadaro, F. Frusteri, J. Power Sources. 108 (2002) 53-57.

[5] N. Homs, J. Llorca, P. de la Piscina, Catal. Today 116 (2006) 361-366.

[6] K. Urasaki, K. Tokunaga, Y. Sekine, M. Matsukata, E. Kikuchi, Catal. Comm. 9 (2008) 600-604.

[7] J. Sehested, Catal. Today 111 (2006) 103-110.

[8] D. Trimm, Catal. Today 49 (1999) 3-10.

[9] J. Liberatori, R. Ribeiro, D. Zanchet, F. Noronha, J. Bueno, Appl. Catal. A: Gen. 327 (2007) 197-204.

[10] H. Bengaard, J. Nørskov, J. Sehested, B. Clausen, L. Nielsen, A.M. Molenbroek, J.R. Rostrup-Nielsen, J. Catal. 209 (2002) 365-384.

[11] A. Fatsikostas, X. Verykios, J. Catal. 225 (2004) 439-452.

[12] A. Lucrédio, J. Bellido, E. Assaf, Appl. Catal. A: Gen. 388 (2010) 77-85.

[13] M. Sánchez-Sánchez, R. Navarro, J. Fierro, Int. J. Hydrogen Energy. 32 (2007) 1462-1471.

[14] C. Bartholomew, R. Pannell, J. Catal. 65 (1980) 390-401.

[15] J. Zieliński, J. Catal. 76 (1982) 157-163.

[16] Z. Zhang, X. Verykios, Catal. Today 21 (1994) 589-595.

[17] P. Salagre, J.L.G. Fierro, F. Medina, J.E. Sueiras, J. Mol. Catal. A: Chem. 106 (1996) 125-134.

[18] J. Shabaker, D. Simonetti, R. Cortright, J. Dumesic, J. Catal. 231 (2005) 67-76.

[19] B. Kitiyanan, W. Alvarez, J. Harwell, D. Resasco, Chem. Phys. Lett. 317 (2000) 497-503.

[20] J. Herrera, D. Resasco, Chem. Phys. Lett. 376 (2003) 302-309.

[21] T. Choudhary, D. Goodman, J. Catal. 192 (2000) 316-321.

[22] C. Powell, N. Erickson, T. Jach, J. Vac. Sci. Technol.. 20 (1982) 625-625.

[23] E. Khawaja, M. Salim, M. Khan, F. Al-Adel, G. Khattak, Z. Hussain, J. Non-Cryst. Solids 110 (1989) 33-43.

[24] D. Chen, K.O. Christensen, E. Ochoa-Fernández, Z. Yu, B. Tøtdal, N. Latorre, A. Monzón, A. Holmen, J. Catal. 229 (2005) 82-96.

[25] P. Kratzer, B. Hammer, J.K. Nørskov, J. Chem. Phys. 105 (1996) 5595-5604.

[26] D. Goodman, R. Kelley, T. Madey, J. White, J. Catal. 64 (1980) 479-481.

[27] J. Rostrup-Nielsen, Catalysis: Science and Technology. 5 (1984) 1-117.

Chapter 6

Study of Ethanol Steam Reforming Mechanism over Ca-Al_2O_3 supported Noble Metal Catalysts

Graphical Abstract

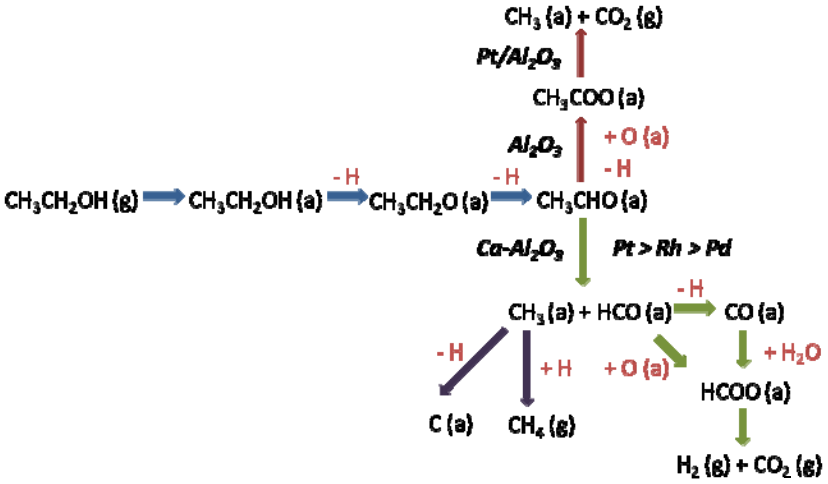

In situ diffuse reflectance infrared Fourier transformed spectrocopy study of ethanol adsorption/desorption was performed on Pt (Rh, Pd)/Ca-Al_2O_3. Contrary to the well-known *acetate-driven* reaction mechanism observed on Ca-free metal/Al_2O_3 catalysts, formate species are exclusively observed on Pt (Rh, Pd)/Ca-Al_2O_3, offering a new mechanism denoted as *formate-driven*. The key factor in determining the change in mechanism is the reduced availability of surface oxygen atoms and enhanced C-C bond breaking ability of the metal catalyst upon Ca modification. The *formate-driven* mechanism is more active on the noble metals in the order of Pt>Rh>Pd.

6.1. Introduction

One of the major problems in ethanol steam reforming (ESR, Eqn. 6.1) is the formation of carboneous species on the catalyst surface [1]. Non-noble metals like Ni and Co which are susceptible to coke formation, often result in rapid deactivation and a subsequent time and energy consuming catalyst regeneration process [1]. Noble metals are known to have lower carbon solubility and higher coking resistance, thus making them attractive active metals for ethanol steam reforming [2, 3]. Noble metals catalysts supported on different metal oxides have been studied for ESR. Auprêtre et al. studied the effects of both active metals and the supports [4]. It was found that the activity based on hydrogen yield over γ-alumina supported metal catalysts decreases in the following order: 9.7% Ni > 1% Rh > 0.5% Pd > 1% Pt > 0.67% Ru. They suggested that metals which are highly active in steam reforming but poor in water-gas-shift reaction (WGSR) (Eqn. 6.2), would give active and selective catalysts in ESR.

$$C_2H_5OH + 3H_2O \leftrightarrow 2CO_2 + 6H_2 \quad (6.1)$$

$$CO + H_2O \leftrightarrow CO_2 + H_2 \quad (6.2)$$

Liguras et al. reported that, for the same metal loading of 1 wt%, the performance of the noble metals for ESR at 873-1123 K is in the order of decreasing ethanol conversion Rh >> Pt > Pd > Ru [5]. In contrast to Auprêtre et al., Rh was found, not only to have good reforming capability over ethanol and ethylene, but also the ability to participate in WGSR. In another study, Basagiannis et al. concluded that the catalytic performance varies in the order of Pt > Pd > Rh > Ru at low temperature of 573-723 K, with Pt being the most active and stable catalyst

among the noble metals supported on γ-alumina [6]. Investigation showed that ESR occurs in a bifunctional manner where both the dispersed metallic phase and the support participate in effective reformation of ethanol. While many other literatures have suggested that noble metals are promising catalysts for ESR [7, 8], the high cost of noble metals is an impediment for industrial usage. Based on the price report recently published by Johnson Mattey in March 2012, the prices of Pt, Rh, Pd and Ru are $1658, $1400, $685 and $120 (in dollars) per ounce respectively [9]. In spite of the high cost of most noble metals, these noble catalysts have outstanding catalytic performance in terms of stability and selectivity and thus demand detailed investigations in ESR process. We should study the mechanism of ESR over supported noble metal catalysts, such that their full catalytic potentials can be exploited based on proper catalyst formulations and reaction conditions.

One generally accepted mechanism for the production of H_2 via ESR over noble metals catalysts envisions the participation of acetates via dehydrogenation and subsequent oxidation from ethoxides (Eqns. 6.3-6.8). This proposed pathway was supported by IR spectra, indicating the presence of ethoxides and acetates at different temperatures after ethanol adsorption. Ethoxides decompose into H_2, CO and CH_4 or undergo dehydrogenation (Eqn. 6.4), producing acetaldehyde and acetyl which may decompose to CO and CH_4 (Eqn. 6.5). The reaction of acetaldehyde and acetyl groups with lattice oxygen (Eqn. 6.6) or surface hydroxyls (Eqn. 6.7) leads to the formation of acetate intermediates and the final products (Eqn. 6.8) [10]. The role of active metals on the acetate formation is still

intriguing and remains elusive. Erdöhelyi et al. observed the formation of surface acetates over Al_2O_3 supported Rh, Ir, Ru, Pd and Pt catalysts and concluded that the acetate formation is independent of the nature of active metal [10]. On the other hand, the presence of surface oxygen on supports was found to play an important role. While surface acetates were detected on metal-free, unreduced CeO_2 at room temperature after ethanol adsorption [11], they were not found on both reduced CeO_2 and Pd/CeO_2 at a wide range of temperatures, probably due to the depletion of mobile oxygen since the presence of Pd promotes the reduction of CeO_2. Hence, on as-prepared Pd/CeO_2, no acetate was observed after the ethanol adsorption. Instead, ethoxides were dehydrogenated to acetaldehyde which can then be decomposed forming carbonate species [11]. These observations indicate that the catalyst support may also affect the reaction pathways. Herein, we denote the reaction pathway shown below as *acetate-driven* pathway.

$CH_3CH_2OH + OH\ (a) \rightarrow CH_3CH_2O\ (a) + H_2O$ and/or

$CH_3CH_2OH \rightarrow CH_3CH_2O\ (a) + H\ (a)$ (6.3)

$CH_3CH_2O\ (a) \rightarrow CH_3CHO\ (a) + H\ (a) \rightarrow CH_3CO\ (a) + H_2$ (6.4)

$CH_3CO\ (a) + H\ (a) \rightarrow CH_4 + CO$ (6.5)

$CH_3CO\ (a) + O\ (a) \rightarrow CH_3COO\ (a)$ (6.6)

$CH_3CHO\ (a) + OH\ (a) \rightarrow CH_3COO\ (a) + H_2$ (6.7)

$CH_3COO\ (a) + H\ (a) \rightarrow CH_4 + CO_2$ (6.8)

Recently, the coexistence of formate and acetate species on Al_2O_3 supported Pt catalysts was reported both by Panagiotopoulou et al. and Sanchez-

Sanchez et al. [12, 13]. Very weak IR bands of formate species were also reported over unreduced Pt/CeO_2 by Yee et al. [14]. In our study on Fe promoted Rh/Ca-Al_2O_3 catalyst, formate species were detected by diffuse reflectance infrared spectroscopy (DRIFTS) as an important intermediate of water-gas-shift reaction (WGSR) [15]. This work clearly showed that the formation of formate species not only enhanced the H_2 selectivity via WGSR but also stabilized the Rh catalyst by removing adsorbed CO from Rh active sites via low temperature (623-673 K) ESR. Therefore, an alternative mechanism to the *acetate-driven* pathway may exist over these catalysts, which we would be denoted as *formate-driven* mechanism.

Previously in Chapter 4, we have shown via spectroscopic means that no acetates are formed on Ca-modified Al_2O_3 – a contrast to adsorption of ethanol over clean Al_2O_3. Rather, only ethoxides which are stabilized by hydrogen bonding between the alcohol and the support are observed. The abundance of surface hydroxyls also depletes the surface oxygen atoms required for acetate formation. This offers a head-start towards a more stable carrier for ESR since the formation of acetates which tend to inhibit the activity of the active metals is minimized. In the present paper, we examined three noble metals catalysts (Pt, Rh and Pd, 1 wt. % loading) supported on Ca-Al_2O_3 and Ca-free Al_2O_3 carriers respectively. While formate species were exclusively observable on the Ca-Al_2O_3 supported catalysts, they were hardly observable on Ca-free catalysts. Hence, it is clear that the effect of Ca modification plays a key role on the ESR reaction mechanism over noble metals. In this contribution, we report an *in situ* DRIFTS

study and temperature-programmed desorption of ethanol (TPD-EtOH) on Ca-modified catalysts, providing new insights into the role of the support and metal on the ESR reaction pathway.

6.2. Experimental

6.2.1. Catalysts Synthesis

$Ca(NO_3)_2 \cdot 4H_2O$ (Riedel-deHaën) dissolved in deionised water was introduced onto activated γ-Al_2O_3 (Arcōs Organics) support using incipient wetness impregnation technique. The resulting mixture was calcined in air at 1123 K for 5 hr to obtain Ca-modified Al_2O_3, denoted as Ca-Al_2O_3. The Ca-Al_2O_3 supports were impregnated with respective aqueous solution of noble metals ($Rh(NO_3)_3$ (Aldrich), $H_2PtCl_6.6H_2O$ (Alfa Aesar) and $Pd(NO_3)_2.xH_2O$ (Aldrich)) to give a metal loading of 1 wt%. The resulting sample was dried in air for 2 hr at 373 K before ramping up to 723 K and held constant at this temperature for another 5 hr. The catalysts were denoted as Pt/Ca-Al_2O_3, Rh/Ca-Al_2O_3 and Pd/Ca-Al_2O_3.

6.2.2. Catalysts Activity and Selectivity

The catalytic evaluation experiments were performed in customized 5-channels quartz micro-reactor (BEL, Japan), each of which was loaded with 100 mg of the catalyst. Temperatures of the samples were individually monitored with thermocouples located just on top of the catalyst samples.

The Pt (Rh, Pd)/Ca-Al_2O_3 catalysts were reduced by hydrogen at 473 K for 0.5 hr. Then 40 ml min^{-1} of Ar was flown in, along with 0.005 ml min^{-1} of ethanol-water mixture (1:10 molar ratio) which was injected by a Shimadzu Liquid Pump and vaporized at 443 K within the reactor. The total gas hourly space velocity (GHSV) was kept constant at 34,000 h^{-1}, monitored by mass flow controller. The reaction products were analyzed online using a gas chromatograph (GC) (Varian CP-3800) with three columns: Porapak Q and Haysep Q, molecular sieve 5A. Porapak Q was used to separate organics and carbon dioxide with He as carrier gas while the later two columns with Ar carrier gas were used for the separation of hydrogen, carbon monoxide and methane. Conversion of ethanol (X_{EtOH}) and selectivity to carbon containing species (S_{Ci}) were calculated based on Eqns. 3.5 and 3.6 in Chapter 3, respectively.

6.2.3. Catalysts Characterization

6.2.3.1. DRIFTS-Ethanol

In situ DRIFTS experiments were performed using a Bio-Rad FT-IT 3000 MX equipped with a high temperature cell fitted with KBr windows and a mercury-cadmium-telluride (MCT-A) detector cooled with liquid nitrogen. Spectra were acquired at a resolution of 4 cm^{-1} and typically over 256 scans. The catalyst sample was first reduced with in flowing H_2 (20 ml min^{-1}) at 473 K for 2 hr and cooled in flowing He (20 ml min^{-1}) to 303 K. Subsequently, ethanol was introduced into the cell with a He flow (50 ml min^{-1}) through a saturator for 20 min. Following this, the sample was flushed with He flow (50 ml min^{-1}) to

remove physically adsorbed ethanol. Then, the sample was heated up to different temperatures in He (50 ml min^{-1}). Spectra were recorded at 303, 373, 473, 523, 573 and 673 K. The spectrum of the freshly reduced sample was used as a reference.

6.2.3.2. Temperature Programmed Desorption of Ethanol (TPD)

TPD-EtOH profiles were collected for mechanism study. Prior to adsorption, 50 mg of the catalysts was reduced at 473 K for 0.5 h in H_2. They were purged in 50 ml min^{-1} of Ar for 15 min to remove residual H_2 before the adsorption of ethanol/He through a saturator for 20 min at 303 K. Subsequently, Ar was flown for 30 min to remove physically adsorbed ethanol. The sample was heated up with a ramp rate of 15 K min^{-1} and the desorbed species were detected using mass spectroscopy. The species were characterized using m/z values = 2, 15, 18, 27, 28, 29, 31 and 44 for H_2, CH_4, H_2O, C_2H_4, CO, CH_3CHO, C_2H_5OH and CO_2 respectively.

TPD-EtOH-H_2O profiles were also collected after the adsorption of water on the samples preadsorbed with EtOH based on the above conditions. Water vapor was adsorbed on the sample via a saturator maintained at 333 K for 30 min. This is followed by purging the sample with Ar for 30 min. Subsequently, the sample was heated up with a ramp rate of 15 K min^{-1} and the desorbed species were detected using mass spectroscopy.

6.2.3.3. Temperature Programmed Surface Reaction (TPSR)

Similar to TPD, 50 mg the sample was reduced at 473 K for 0.5 h in H_2 prior to the experiment. Two sets of TPSR experiments were conducted. In the premier, ethanol carried by Ar through a saturator was first adsorbed on the sample at 303 K for 20 min. After saturation, the sample was purged with Ar for 30 min. Following this treatment, water vapor which was maintained by a water bath at 333 K was carried by Ar through a saturator and adsorbed over the sample for 10 min. Subsequently, the water vapor continued to pass over the sample surface in a temperature-programmed manner with a ramp rate of 15 K min^{-1}. The desorbing species were analyzed using mass-spectroscopy. In the second experiment, the order of the adsorption was reversed (water vapor was first adsorbed followed by passing ethanol vapor continuously) while maintaining the same adsorption conditions and ramping rate.

6.2.3.4. XPS

X-ray photoelectron spectra were obtained on Themo ESCALAB 250, using MgKα (hυ =1253.6 eV) as photon source. The instrument was calibrated with respect to graphitic C 1s at 284.5 eV. To study the reduced catalysts, samples were reduced *in situ* at 473 K for 2 h in H_2 prior to analysis.

6.3. Results and Discussions

6.3.1. DRIFTS Study of Adsorbed Ethanol

In situ DRIFTS studies were conducted to identify the formation of surface species upon ethanol adsorption and after treatment at various temperatures. Spectra of adsorbed ethanol on Pt/Al_2O_3 and $Pt/Ca\text{-}Al_2O_3$ at different temperatures are presented in Fig. 6.1.

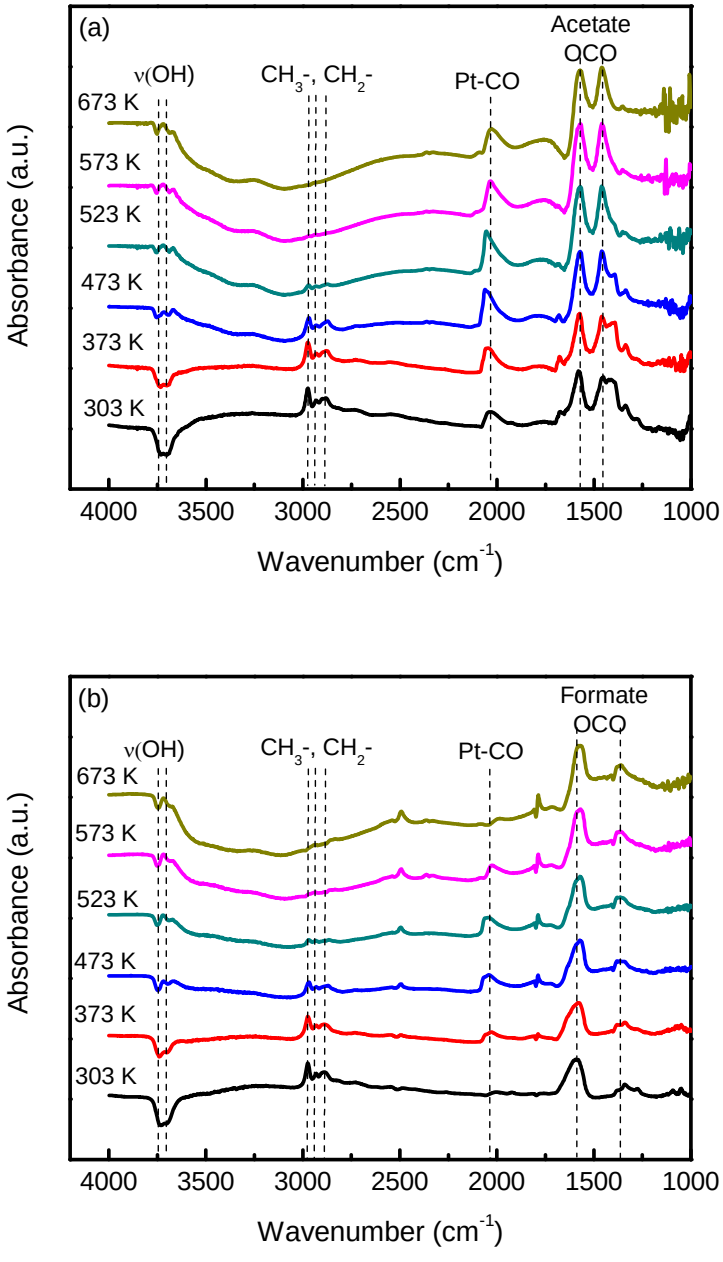

Figure 6.1. DRIFTS spectra at various temperatures after C_2H_5OH adsorption. (a) Pt/Al_2O_3 and (b) $Pt/Ca\text{-}Al_2O_3$. The spectra were recorded at (i) 303 K after ethanol adsorption followed by He purge, (ii)-(vi) 373, 473, 523, 573 and 673 K respectively.

Fig. 6.1(a) shows DRIFTS spectra of ethanol adsorption on Pt/Al_2O_3 during progressive heating. The C-H stretching bands at 2971 cm^{-1}($\nu_a(CH_3)$), 2935 cm^{-1}($\nu_a(CH_2)$) and 2880 cm^{-1} ($\nu_s(CH_3)$) are visible at 303 K, indicating the presence of ethoxide species from the dissociative adsorption of ethanol. Negative spectral peaks located at 3742 cm^{-1} and 3700 cm^{-1} reveal the loss of surface OH groups over the Al_2O_3 support, which may interact with the molecularly adsorbed ethanol as indicated in Eqn. 6.3. Further decomposition and oxidation of adsorbed ethoxide lead to the detection of strong CO band (Eqn. 6.5) at 2036 cm^{-1}. The predominant bands at 1575 cm^{-1} and 1460 cm^{-1} with intensity ratio of 1:1 can be assigned to asymmetric and symmetric O-C-O stretching respectively due to the presence of acetate resulting from the dehydrogenation of ethoxide and the subsequent oxidation by lattice O or OH groups (Eqns 3.6 and 3.7). Three shoulders are observable at the lower frequency region. The peaks at 1386 cm^{-1} ($\delta(CH_3)$ in ethanol) and 1277 cm^{-1} (δ(OH) in ethanol) correspond to molecularly adsorbed ethanol, which may bond to surface OH groups via H-bonding or/and to Lewis acid sites (Al^{3+}) on the oxidic support [16]. The peak at 1340 cm^{-1}, which is noticeable between 303-473 K, may be assigned to formate species.

The molecular ethanol signals remain observable until 473 K and disappear at 523 K, an observation consistent with the literature [10]. Similarly,

the intensities of ethoxide peaks decrease their intensities with increasing temperature up to 523 K, at which they are scarcely detectable. On the other hand, the intensities of the CO and acetate bands grow as temperature increases (up to 673 K), progressively. The intensity decreases in the region between 2750 and 3600 cm^{-1} is indicative of the dissociation and consumption of adsorbed water. As a result the negative OH peaks diminish. The above DRIFTS results of Pt/Al_2O_3 are in good agreement with the literature on Pt/Al_2O_3, suggesting the *acetate-driven* mechanism [17].

The DRIFTS spectrum of adsorbed ethanol over Pt/Ca-Al_2O_3 at 303 K is shown in Fig. 6.1(b). The appearance of adsorbed ethanol, ethoxides and the negative OH peaks on Pt/Ca-Al_2O_3 are similar to those on Pt/Al_2O_3. However, we note two significant differences between Pt/Ca-Al_2O_3 (Fig. 6.1(b)) and Pt/Al_2O_3 (Fig. 6.1(a)). First, the characteristic acetate peak at 1460 cm^{-1} band is not observable in Fig. 6.1(b). Instead, two predominant peaks appear at 1588 cm^{-1} and 1340 cm^{-1} respectively, with relative intensity ratio of 3:1. They are characteristic peaks of the asymmetric and symmetric O-C-O stretches of formate species and both peaks grow with increasing temperature [18]. This is the first time that formate species are so clearly identified without the coexistence of acetate, in constrast to the observations of Panagiotopoulou et al. [12] and Sanchez-Sanchez et al. [13]. Secondly, the CO band is not evident at 303 K. Progressive heating of the sample, leads to the loss of molecularly adsorbed ethanol as well as ethoxide species, as witnessed from the decrease in the intensity of the corresponding bands at 1384 and1270 cm^{-1} and 2971, 2935 and 2880 cm^{-1}

respectively (Fig. 6.1(b)). It is observed that the loss of ethoxide occurs with the increase in CO adsorption on Pt/Ca-Al_2O_3 at 373 K ≤ T ≤ 523 K. The adsorbed CO, hence, stems from the decomposition of ethoxide. Two vibration modes of linearly adsorbed CO are observed: CO adsorbed on partially oxidized $Pt^{\delta+}$ (υ(CO) = 2065 cm^{-1}) and CO adsorbed on reduced Pt^0 particles (υ(CO) = 2035 cm^{-1}) [12]. The intensity of υ (CO) bands starts to decrease at T ≥ 573 K, leaving a weak band at 2000 cm^{-1}. Similar to Fig. 6.1(a), the intensity decreases in the region between 2750 and 3600 cm^{-1} is also observed in the temperature range between 573-673 K, indicating the dissociation and consumption of adsorbed water. As a result the negative OH peaks diminish. At the same time, as temperature increased from 473 K up to 673 K, the bands at 2500 and 1786 cm^{-1} grow together. These two bands are not observed in Fig. 6.1(a), clearly indicating that these bands are associated with the presence of Ca species. They can be attributed to the H-OC and HO=C stretches of adsorbed HCO species, respectively [19, 20]. It is worth to note that, the intensity of the formate bands becomes stronger as the CO bands diminish, which may indicate that adsorbed CO species have been converted into formate species.

At this instance, spectroscopic evidences clearly show that the modification of alumina by calcium has altered the reaction pathway of ESR from one mediated by acetates (*acetate-driven*) over Pt/Al_2O_3 to one aided by formate species (*formate-driven*) over Pt/Ca-Al_2O_3. In fact, in our previous study [21], we have already shown that Ca promotion could alter the reaction pathway of ethanol over metal-free Al_2O_3. Over Al_2O_3, ethoxide bands disappeared at 673 K while

asymmetric and symmetric O-C-O bands of acetates of similar intensities were observed at 1586 cm^{-1} and 1484 cm^{-1} over Al_2O_3 at the same temperature. In contrast, ethoxide species with C-H stretching bands of 2966 cm^{-1}, 2924 cm^{-1} and 2870 cm^{-1} remained detectable over ethanol/Ca-Al_2O_3 at 673 K, without observable bands attributed to either acetate or formate species. Hence, it is clear that the formation of formate on Pt/Ca-Al_2O_3 results from the simultaneous presence of both Ca and Pt. Therefore, the properties induced by the presence of Ca are crucial to unravel the reason behind the change in the reaction mechanism.

Formation of acetates from the ethanol adsorption has been widely reported over various oxides, such as Al_2O_3 [22, 23], MgO [24] and CeO_2 [11]. Mechanistic studies of ethanol adsorption on these supports and their corresponding metal catalysts suggest that a structural change from an ethoxide to an acetate species occurs via dehydrogenation to form an acyl group and subsequent oxidation to acetate. The availability of oxygen atoms on the support or metal surfaces for the attachment (of oxygen) to carboxyl carbon is important in acetate formation [22]. Yee et al. studied ethanol adsorption over unreduced CeO_2, reduced CeO_2 and Pd/CeO_2. Their results show that surface oxygen atoms on unreduced CeO_2 are responsible for acetate formation while on reduced CeO_2 the depletion of surface oxygen atoms leads to the absence of acetate [11]. The presence of Pd helps in the reduction of CeO_2, and also leads to the absence of acetate over Pd/CeO_2. By analogy, on Ca-free Al_2O_3 and Pt/Al_2O_3 catalyst surfaces, there is abundance of surface oxide ions which are in close interaction with the adsorbed ethoxide/acetaldehyde (which are located at Al^{3+} Lewis acidic

centers or Pt sites at metal/oxide interface), favoring the formation of acetate species as evidenced in Fig. 6.1(a) as well as reported in literatures [10, 23, 25]. In contrast, our previous DRIFTS characterization of Ca-Al_2O_3 surface showed large amount of adsorbed water on the surface of the sample [21]. These species as well as Ca additives might block surface oxygen sites which are close to the active sites and therefore hindering the formation of acetate species [25]. In addition to the structural effect reported above, Ca doping was shown to donate valence electron and increase the electronic density of metals on the Ca-modified alumina-supported metal catalysts. Similar effect was reported for K-promoted metal catalysts [26]. The increased pool of valence electrons on Pt/Ca-Al_2O_3 is evidenced by the red shift of the IR bands for adsorbed CO on Pt/Ca-Al_2O_3 as compared to that on Pt/Al_2O_3 (2002 cm^{-1} vs. 2035 cm^{-1} due to a stronger Pt valence electron back donation effect). The enriched valence electrons favor Pt active sites with hydrogen bonding and/or carbon bonding, causing the alcohol to be more strongly bonded to the Ca-modified Al_2O_3 and to the active metal, hence increasing the stability of the ethoxides as observed from DRIFTS [24]. Surface science study of ethanol adsorption on Ni(111) and Pt surfaces revealed that ethanol adsorption on Ni(111) or Pt surfaces [27, 28] was dissociative following the bond scission sequence (i) O-H, (ii) C_α-H and (iii) C-C and (iv) C_β-H bond. Since Ca doping enhances the valence electron density of the metal and promotes C-C bond scission as compared to Ca-free catalysts [29], one would expect that, on Ca-Al_2O_3 supported Pt catalysts, ethanol adsorption and reaction may follow the above mentioned bond breaking sequence, forming HCO (see Eqn. 6.11

below) and finally adsorbed CO species on the catalyst surface (Eqn. 6.12, in which * denotes vacancy sites on the surface), both of which can react with adjacent OH and generate formate species HCOO on the surface (Eqn. 6.13). HCOO intermediate may undergo dehydration and be converted back to adsorbed CO or gaseous CO. On the other hand, it may dehydrogenate producing H_2 and CO_2 (Eqns. 6.14-6.16), which is more favorable on a basic oxide such as CaO. Therefore our results unravel a new mechanism for ethanol reforming over Ca-Al_2O_3 supported Pt catalysts, the *formate-driven* reaction pathway:

$$CH_3CH_2O\ (a) \rightarrow CH_3CHO\ (a) \rightarrow CH_3\ (a) + HCO\ (a) \quad (6.11)$$

$$HCO\ (a) + * \leftrightarrow CO\ (a) + H\ (a) \text{ or } HCO\ (a) + OH\ (a) \rightarrow CO\ (a) + H_2O \quad (6.12)$$

$$OH\ (a) + CO\ (a) \leftrightarrow HCOO\ (a) + * \text{ or } O\ (a) + HCO\ (a) \rightarrow HCOO\ (a) \quad (6.13)$$

$$HCOO\ (a) + * \leftrightarrow CO_2\ (a) + H\ (a) \quad (6.14)$$

$$CO_2\ (a) \leftrightarrow CO_2 + * \quad (6.15)$$

$$2H\ (a) \leftrightarrow H_2 + 2* \quad (6.16)$$

In brief, the *acetate-driven* mechanism occurs over Al_2O_3 due to availability of surface oxygen atoms. The strong Lewis acid (electron withdrawing) nature of aluminum ion in Al_2O_3 favors alcohol adsorption, facilitates its conversion to acetates via dehydrogenation and undergoes oxidation in the presence of adjacent oxygen atoms. In contrast, on Ca-Al_2O_3, the lack/blockage of surface oxygen atoms significantly hinders the formation of acetate. It is worth noting that the *formate-driven* pathway over Ca-Al_2O_3 has to be assisted by an active metal site since no formate species were detected over metal-free Ca-Al_2O_3. Ca additives donate valence electrons to metal active sites

and hence promote the dehydrogenation and C-C bond breaking of adsorbed ethoxide species, favoring the formate formation and the *formate-driven* reaction pathway.

The effect of Ca resulting in the change of mechanism from *acetate-driven* to *formate-driven* is also observed on Rh catalyst. In Fig. 6.2(a) shows the DRIFTS spectra of ethanol over Rh/Ca-Al_2O_3 after treatment at various temperatures. At 303 K, the appearance of adsorbed ethanol and ethoxides are similar to that observed in Fig.3.1. However, no formate species or acetates are seen at this temperature. At 373 K, ethoxide bands at 2975, 2930 and 2889 cm^{-1} begin to reduce the intensity and eventually disappear at 573 K. At 373 K, two IR bands are observed at 2030 cm^{-1} and 1830 cm^{-1}, corresponding to linear and bridge-bonded Rh-CO respectively. The formation of formate species (υ_a (O-C-O) = 1572 cm^{-1} and υ_s (O-C-O) = 1380 cm^{-1}) is not observed until 473 K and the intensities of these bands gradually increase as the temperature increases. At high temperatures (> 573 K), water depletion and HCO species (H-CO and HC=O stretches at 2495 and 1784 cm^{-1}) are similarly observed as in Fig. 6.1(b). The formate bands over Rh are weaker than those on Pt. This suggests that the reaction pathway on Rh/Ca-Al_2O_3 follows the *formate-driven* route as in the case of Pt/Ca-Al_2O_3. Thus, it is expected that Rh participates in WGSR via formate formation but probably less effective than Pt. DRIFTS analysis of adsorbed ethanol over Rh/Al_2O_3 in Fig. 6.2(b), again reveals the formation of acetates. With all other bands identified and located at similar wavenumbers as Pt catalysts, acetates were observed at 303 K over Ca free Rh/Al_2O_3 catalysts.

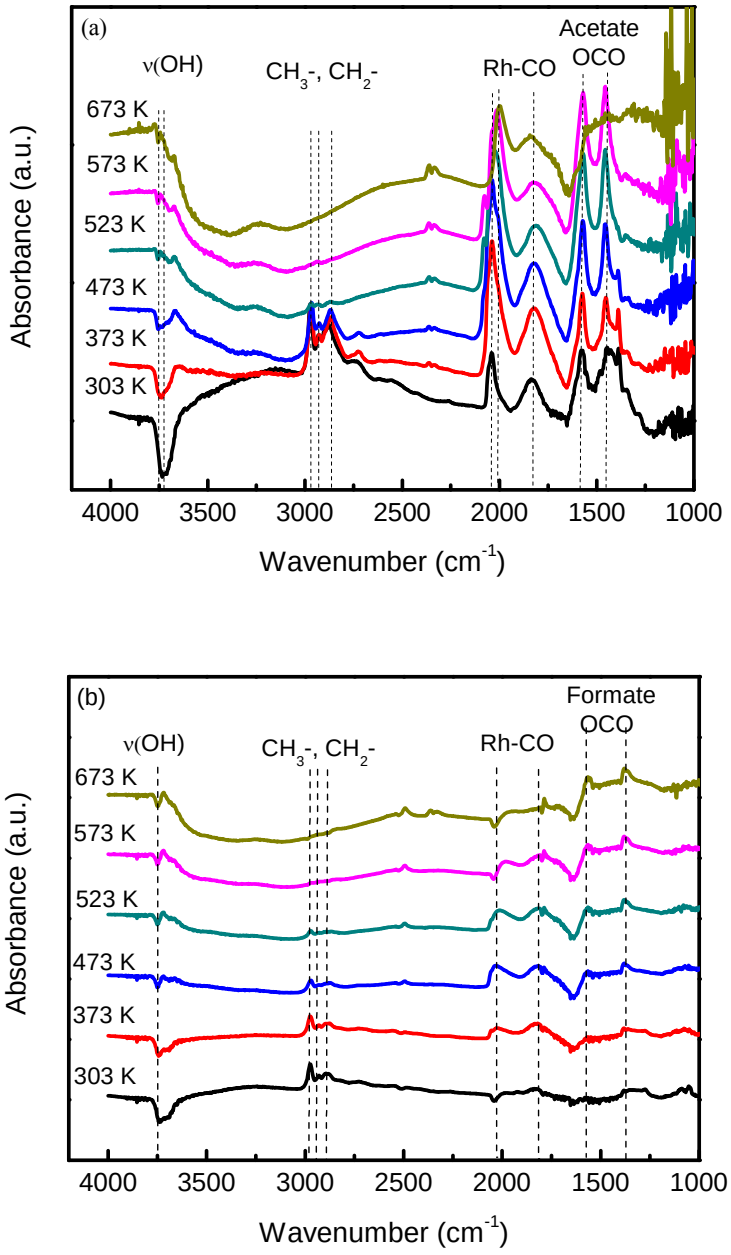

Figure 6.2. DRIFTS spectra at various temperatures after C_2H_5OH adsorption. (a) Rh/Al_2O_3 and (b) $Rh/Ca\text{-}Al_2O_3$. The spectra were recorded at (i) 303 K after ethanol adsorption followed by He purge, (ii)-(vi) 373, 473, 523, 573 and 673 K respectively.

The *formate-driven* reaction pathway is also observed over Pd/Ca-Al_2O_3 as illustrated in Fig. 6.3. At 303 K, bands corresponding to ethoxide species are seen at 2980, 2924, 2874 cm^{-1}, indicating ethanol dissociation. Ethanol molecular adsorption bands at 1390 and 1272 cm^{-1} corresponding to $\delta(CH_3)$ and $\delta(OH)$ of ethanol respectively, are detected but weaker than those observed on Pt and Rh catalysts, implying weaker Pd-ethanol interaction. The IR band at 1930 cm^{-1} which can be attributed to bridge-bonded CO, is rather weak on Pd [30]. An intense band at 1609 cm^{-1} along with a band located at 1339 cm^{-1} indicates the presence of formate species [31]. Progressive heating of the Pd catalyst leads to the disappearance of ethoxides and Pd-CO at 523 K. The formate bands increase in intensity gradually and remain visible up to 673 K. Hence, the reaction mechanism over Pd/Ca-Al_2O_3 seems to be similar to the one of Pt/Ca-Al_2O_3 and Rh/Ca-Al_2O_3. However the IR band intensity of reaction intermediates such as formate and adsorbed CO is much weaker than those on Pt and Rh catalysts. Temperature-programmed desorption (TPD) of ethanol over Pd/Ca-Al_2O_3 shows the desorptions of CO and H_2 at 657 K, whereas CO is essentially converted to CO_2 over Pt and Rh catalysts (Section 6.3.2). Indeed DFT calculations showed that the ability of Pd to adsorb CO is not as good as other noble metals such as Pt, Rh, Ru, Os and Ir [32], which could probably explain why Pd is less active for the catalytic ESR reaction in this study (Section 6.3.5).

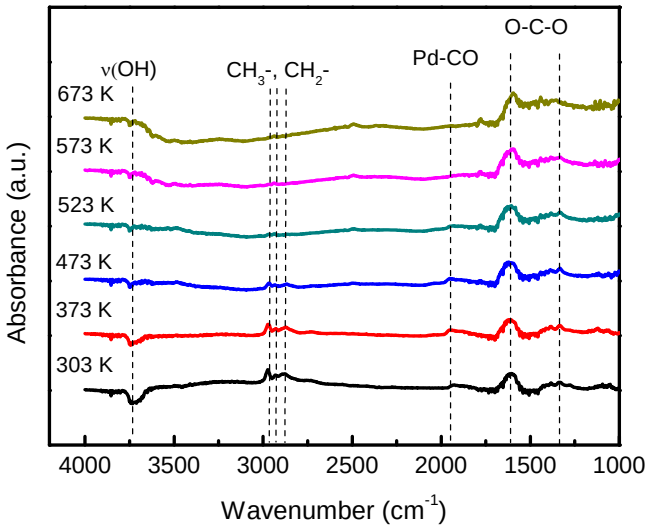

Figure 6.3. DRIFTS spectra of Pd/Ca-Al_2O_3 at various temperatures after C_2H_5OH adsorption. The spectra were recorded at (i) 303 K after ethanol adsorption followed by He purge, (ii)-(vi) 373, 473, 523, 573 and 673 K respectively.

6.3.2. Temperature Programmed Desorption of Ethanol

6.3.2.1. TPD of Adsorbed Ethanol

The interaction of ethanol with the noble metals supported on Ca-modified alumina supported was studied with temperature programmed desorption of adsorbed ethanol (TPD-C_2H_5OH). In Fig. 6.4(a) shows the TPD spectrum obtained over Pt/Ca-Al_2O_3. At the low temperature (T= 416 K), desorbed molecular ethanol is detected. In addition, acetaldehyde and ethylene which are products from dehydrogenation and dehydration of ethanol respectively are also detected at the same temperature [33]. At 525 K, the formation of H_2, CO and CH_4 suggests the occurrence of decomposition of ethoxides, which is in good agreement with the DRIFTS analysis. Ethanol is first adsorbed on the oxide

surface, forming ethoxide species which decompose in the presence active metals supported on the oxide surface. It is also observed that H_2 concentration is higher than CH_4 and CO, thus it is highly possible that H_2 which is previously formed during ethanol dehydrogenation and dehydration starts to desorb at this temperature. The formation of H_2 and CO_2 at higher temperature (T=658 K) is believed to derive from WGSR, a reaction clearly taking place as observed from the presence of formate species in DRIFTS analysis. At higher temperature (723 K $\leq$ T $\leq$ 1023 K), CO_2 is continuously desorbing, providing evidence of the presence of carboneous species which are previously adsorbed. Rather similar spectrum is obtained over Rh/Ca-Al_2O_3 (Fig. 6.4(b)). Ethanol decomposition occurs at 513 K, which is lower than that over Pt/Ca-Al_2O_3. This demonstrates that Rh is a more active catalyst in breaking the C-C bond than Pt. Similar to Pt/Ca-Al_2O_3, WGSR occurs over Rh/Ca-Al_2O_3 at 618 K. In contrast to Pt/Ca-Al_2O_3, less CO_2 is desorbed at higher temperature.

The TPD spectrum over Pd/Ca-Al_2O_3 is shown in Fig. 6.4(c). Molecularly adsorbed ethanol, acetaldehyde and ethane are seen desorbing at 373-523 K. Ethanol decomposition occurs at 493 K, producing H_2, CO and CH_4. At 658 K, H_2 together with CO and CO_2 desorption peaks are observed. It is worth noting that the amount of H_2 desorption peak at 658 K is significantly larger than all the other noble metals studied. This could be contributed by the release of hydrogen previously adsorbed on Pd as palladium hydride during the pretreatment process or during ethoxides decomposition. Evidence has showed that PdH can be formed at room temperature in the presence of H_2 of low partial pressure [34]. The

appearance of CO again verifies that WGSR is not active on Pd/Ca-Al_2O_3 due to little formate species formation (Fig. 6.3). The occurrence of large CO_2 desorption peak at 929 K, may be assigned to decomposition of carbonates.

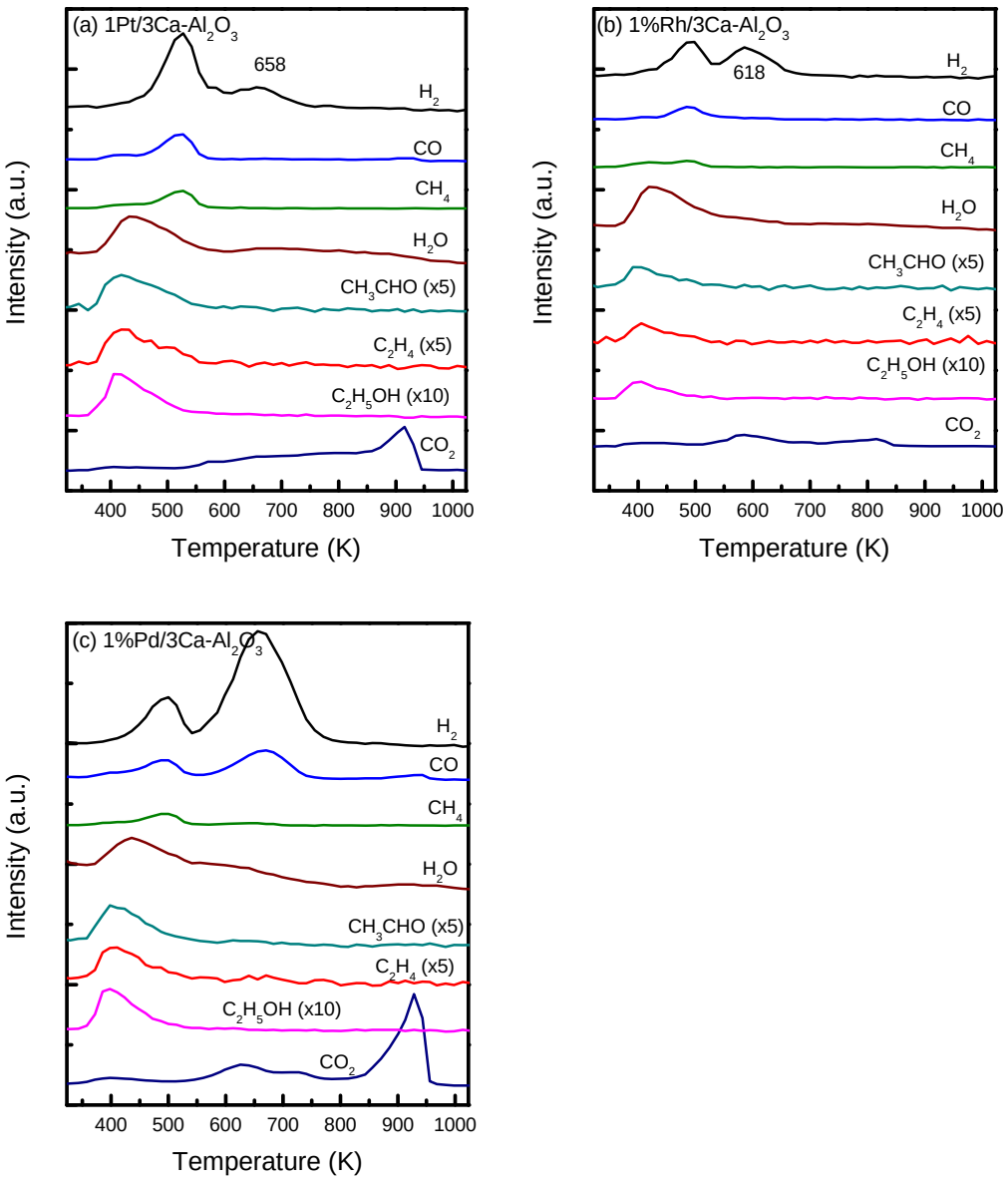

Figure 6.4. Temperature programmed desorption of adsorbed ethanol over (a) Pt/Ca-Al_2O_3, (b) Rh/Ca-Al_2O_3 and (c) Pd/Ca-Al_2O_3.

Temperature-programmed oxidation (TPO) was performed over the spent catalysts following TPD of ethanol to study the nature of the coke deposits adsorbed on different noble metals. Fig. 6.5 shows the CO_2 desorption profiles in the presence of oxygen with a linear ramp rate of 15 K min-1. In general, CO_2 desorption occurs over two temperature region; low temperature of 373-673 K and high temperature of 673-1023 K. It is generally accepted that a high temperature is required for the oxidation of carbon species with higher crystallinity such as graphitic and filamentous carbon, while the lower oxidation temperature is required to oxidize paraffinic or amorphous carbon. As shown in Fig. 6.5, CO_2 desorbs between 350 K and 700 K with T_{max} at 445 K and 645 K over Rh/Ca-Al_2O_3, suggesting poorer carbon crystallinity. Such carbon species are easier to remove via gasification by steam. CO_2 desorption occurs at T_{max} = 658 K and 774 K over Pt/Ca-Al_2O_3. The oxidization temperature indicates that the nature of coke deposits over Pt/Ca-Al_2O_3 has a balanced mixed of carbon species of low and high crystallinity. Considerable amount of CO_2 is desorbed over Pd/Ca-Al_2O_3. The high oxidation temperature of T > 620 K over Pd/Ca-Al_2O_3 is attributed to the oxidization of carbonates of greater strength. The larger amount of coke deposits and the higher carbon crystallinity are likely to be responsible for the poor ESR activity and it is anticipated that deactivation over Pd/Ca-Al_2O_3 would be faster than other catalysts in long catalytic run [35].

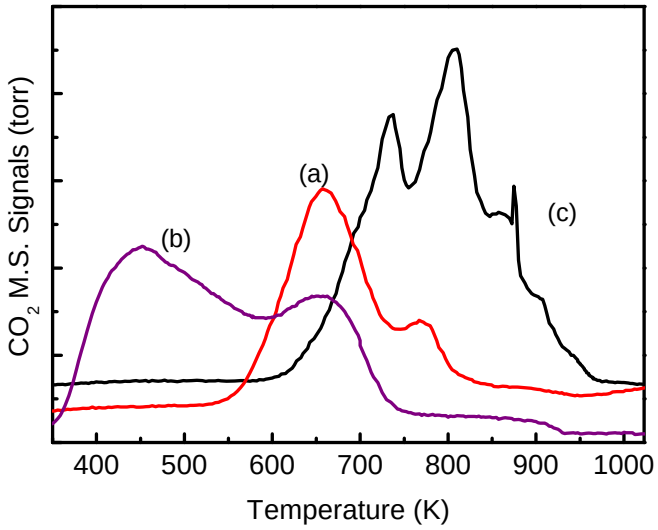

Figure 6.5. Temperature programmed oxidation of (a) Pt/Ca-Al_2O_3; (b) Rh/Ca-Al_2O_3 and (c) Pd/Ca-Al_2O_3 following TPD-EtOH.

6.3.2.2. TPD of Adsorbed Ethanol + Water

The reaction network of ESR over noble metals is further probed by temperature programmed desorption of pre-adsorbed ethanol and water. Ethanol was first preadsorbed over the catalyst for 20 min at 298 K. After purging in Ar for 30 min, steam was adsorbed for another 30 min. This was followed by continuous purging of Ar for another 30 min. A linear temperature ramp from 298 to 1023 K at 15 K min^{-1} was then employed.

The TPD spectra of pre-adsorbed ethanol and water over Pt, Rh and Pd catalysts are presented in Fig. 6.6. In comparison to the TPD-EtOH spectra, the desorptions of molecular ethanol, acetaldehyde, ethylene at $T < 473$ K were unfound. In addition, the lower H_2 desorption peak ($473 K < T < 573$ K) which is

largely due to decomposition of ethanol was also undetected. Based on the above observations, it is likely that presence of steam displaces the weakly adsorbed ethanol, which is easily displaced during Ar purging. Fatsikostas et al. indicated that adsorption sites of the La_2O_3-Al_2O_3 support for both ethanol and steam are the same and resulting in competitive adsorption [36].

On the other hand, the presence of steam appears to have less influence on the WGSR, as the second H_2 and CO_2 peaks remain detectable. This shows that the formate species are promoted in the presence of Ca and they are stabilized in presence of steam. This also substantiated from the observations that the second H_2 desorption peak is recorded at higher temperature in the presence of steam for Pt/Ca-Al_2O_3 and Rh/Ca-Al_2O_3 at 681 K and 628 K respectively.

The CO_2 desorption profiles are similar to those obtained from TPD-EtOH. This implies that the carboneous species are largely contributed during WGSR, rather than the decomposition of ethoxides.

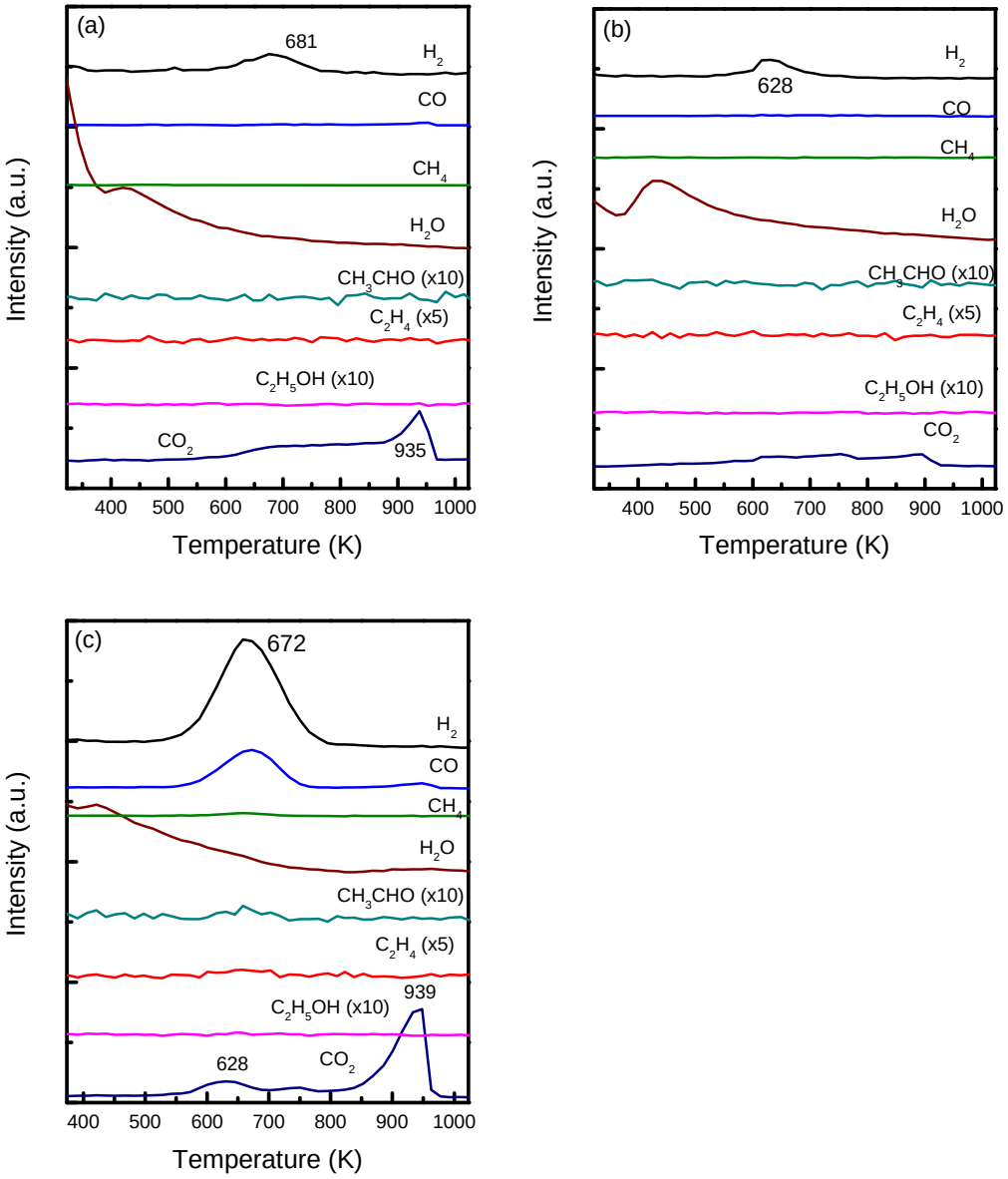

Figure 6.6. Temperature programmed desorption of adsorbed ethanol and steam over (a) Pt/Ca-Al_2O_3; (b) Rh/Ca-Al_2O_3 and (c) Pd/Ca-Al_2O_3.

6.3.3. Temperature Programmed Surface Reaction (TPSR)

TPSRs were performed by first the pre-adsorption of one of the reactants and followed a continuous feed of the second reactant via a saturator. A linear heating of 15 K min^{-1} was applied during the continuous feed and the desorbed products were monitored using a mass spectroscopy. TPSR-EtOH-H_2O refers the temperature programmed desorption over sample which are first pre-adsorption with ethanol at 303 K followed by continuous feeding of steam. TPSR-H_2O-EtOH would indicate an experiment of the reverse order.

TPSR-EtOH-H_2O over Pt/Ca-Al_2O_3 and Rh/Ca-Al_2O_3 are given in Fig. 6.7. The desorption of ethanol, acetaldehyde and ethylene occurs almost instantly as the temperature increases, an evidence that the adsorbed species are weakened and are easily removed in the presence of steam over the two noble metals. One broad H_2 desorption peak is identified at 669 K over Pt/Ca-Al_2O_3 whereas two H_2 desorption peaks are noted at 613 K and 708 K over Rh/Ca-Al_2O_3. All H_2 peaks are accompanied by the release of CO_2, thus suggesting the occurrence of WGSR. While it was noted that the presence of surface adsorbed steam (likely to be monolayer coverage) does not contribute to enhancement in WGSR during TPD-EtOH-H_2O, higher partial pressure of steam through continuous feeding leads to a significant increase in the production of H_2 and CO_2.

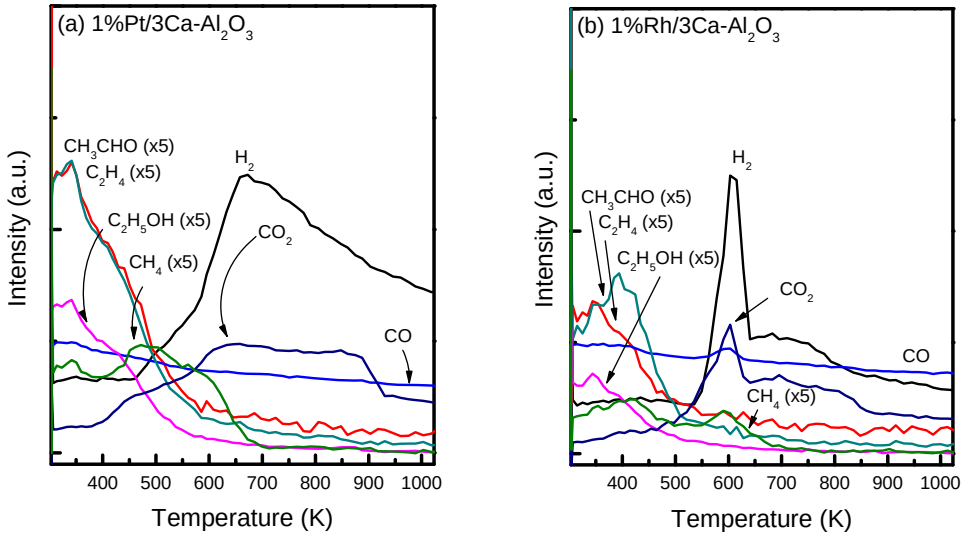

Figure 6.7. Temperature-programmed surface reaction with preadsorbed of ethanol followed by continuously flow of steam and a heating ramp of 15 K min^{-1} over (a) Pt/Ca-Al_2O_3 and (b) Rh/Ca-Al_2O_3.

TPSR-H_2O-EtOH spectra of the two catalysts in Fig. 6.8 depict markedly different desorption profiles as compared to TPSR-EtOH-H_2O. Previously, it has been established that ethoxides and steam competes for the same active sites on the support carrier. Steam is preferentially adsorbed on the active sites in comparison to ethanol since the ethoxides initially formed during pre-adsorption of ethanol can be easily removed during purging. In this set of experiment, whereby steam is first pre-adsorbed on the surface, shows that the pre-adsorbed steam promotes the dehydrogenation and dehydration, as seen from the higher acetaldehyde and ethylene signals at low temperature ($T < 623$ K). Higher intensities of the mentioned species are recorded over Pt/Ca-Al_2O_3 than Rh/Ca-Al_2O_3, implying that Pt is more active over Rh for dehydrogenation and

dehydration. At temperature higher than 473 K, H_2, CH_4 and CO are observed, likely due to the decomposition of ethanol. At this point, it is noted that Rh is more effective in breaking the C-C bond than Pt as the H_2 produced is much higher. However, the better WGS ability over Pt is witnessed by the increased concentration of CO_2. CH_4 concentration decreases at c.a. 723 K, an indication of methane dissociation into H_2 and C (Eqn. 6.17).

$$CH_4 \rightarrow 2H_2 + C \qquad (6.17)$$

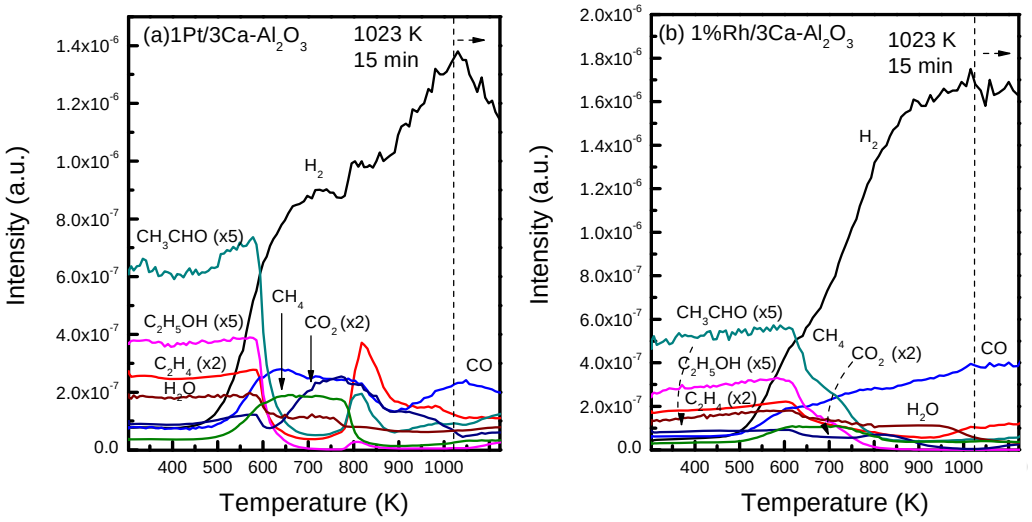

Figure 6.8. Temperature-programmed surface reaction with preadsorbed of steam followed by continuously flow of ethanol and a heating ramp of 15 K min^{-1} over (a) Pt/Ca-Al_2O_3 and (b) Rh/Ca-Al_2O_3.

6.3.4. Fixed-bed Reaction Testing

The catalytic performances of the noble metals as a function of temperature (573 K ≤ T ≤ 873 K) for ESR are shown in Fig. 6.9. In general, the activity of the catalysts increased with temperature. Water gas shift activities are observed between 623 K and 673 K. At 673 K, H_2, CO_2, CH_4 and CO are the

main products observed over Pt/Ca-Al_2O_3 with selectivities of 60.9%, 51.4%, 44.1% and 2.7%, respectively. A hydrogen yield of 3.6 mol is attained. Over Rh/Ca-Al_2O_3, at 673 K, a product stream of H_2 (S_{H2} = 73.7%), CO_2 (S_{CO2} = 47.2%), CO (S_{CO} = 19.3%), CH_4 (S_{CH4} = 32.3%) and trace amount of CH_3CHO (S_{CH3CHO} = 1.2%) is reported. This is accompanied by 4.2 mol of hydrogen yield at 673 K. ESR of Pd/Ca-Al_2O_3 catalyst at 673 K yields a product distribution which consists of 56.6% S_{H2}, 29.9% S_{CO2}, 44.4% S_{CH4} and 24.8% S_{CO}. This gives rise to 3.4 mol of hydrogen yield. In terms of hydrogen production, the catalysts are ranked in the following order at 673 K (Fig. 6.10): Rh/Ca-Al_2O_3 > Pt/Ca-Al_2O_3 > Pd/Ca-Al_2O_3. However, WGSR is more evident in the following order: Pt/Ca-Al_2O_3 > Rh/Ca-Al_2O_3 > Pd/Ca-Al_2O_3, a result consistent with our DRIFTS investigations.

Table 6.1. ESR catalytic performance of different noble metals at 673 K. Reaction conditions: catalyst mass = 100 mg; EtOH/H_2O = 1:3 (v:v); EtOH/H_2O flow rate = 0.005 ml min^{-1} ; Ar flow rate = 40 ml min^{-1}; GHSV = 34,000 h^{-1}.

Catalyst	X_{EtOH} (%)	Y_{H2} (mol)	S_{H2} (%)	S_{CO2} (%)	S_{CO} (%)	S_{CH4} (%)	S_{CH3CHO} (%)
Pt/Ca-Al_2O_3	98.8	3.6	60.9	51.4	2.70	44.1	0.45
Rh/Ca-Al_2O_3	95.0	4.2	73.7	47.2	19.3	32.3	1.24
Pd/Ca-Al_2O_3	100	3.4	56.6	29.9	24.8	44.4	0

The product distribution as a function of temperature over Rh/Ca-Al_2O_3 is shown in Fig. 6.9(b). At low temperature of 573 K, besides the formation of trace amount of CH_3CHO, H_2, CO and CH_4 are predominant products. This indicates

that ethanol decomposition (Eqn. 6.3) is the governing reaction at such low temperature. Complete conversion of ethanol is achieved at 723 K. Ethanol steam reforming becomes more favorable as the temperature increases as observed from the simultaneous increase in H_2 and CO_2 selectivities. Concurrently, selectivity towards methane decreases since CH_4 reforming (Eqn. 6.18) is thermodynamically enhanced at higher temperature.

$$CH_4 + H_2O \leftrightarrow CO + 3H_2 \quad (6.18)$$

The presence of CO during ESR over Rh/Ca-Al_2O_3 suggests that Rh is not as active as a WGSR catalyst. In contrast, Pt/Ca-Al_2O_3 displays WGSR at 623 K $\leq$ T $\leq$ 723 K where $S_{CO} \approx 3\%$ (Fig. 6.9(a)). However, Pt/Al_2O_3 is not known to be an active catalyst for ESR despite being an efficient catalyst in WGSR [4]. This is again verified from our results where S_{H2} and S_{CO2} over Pt/Ca-Al_2O_3 are much lower than Rh/Ca-Al_2O_3 at T $\geq$ 673 K. Complete conversion of ethanol is achieved over Pd/Ca-Al_2O_3 at temperature as low as 573 K (Fig. 6.9(c)). Similar to Rh/Ca-Al_2O_3, ESR is only favorable as higher temperature. Palladium does not possess WGS capability and thus has a lower H_2 and CO_2 selectivities than Pt/Ca-Al_2O_3. Pd is less active among the noble metals. Frusteri et al. has similarly noted the poor catalytic performance of MgO-supported Pd catalyst for ESR among catalysts such as Rh, Ni and Co [35]. The poor performance is attributed to metal sintering and coke formation.

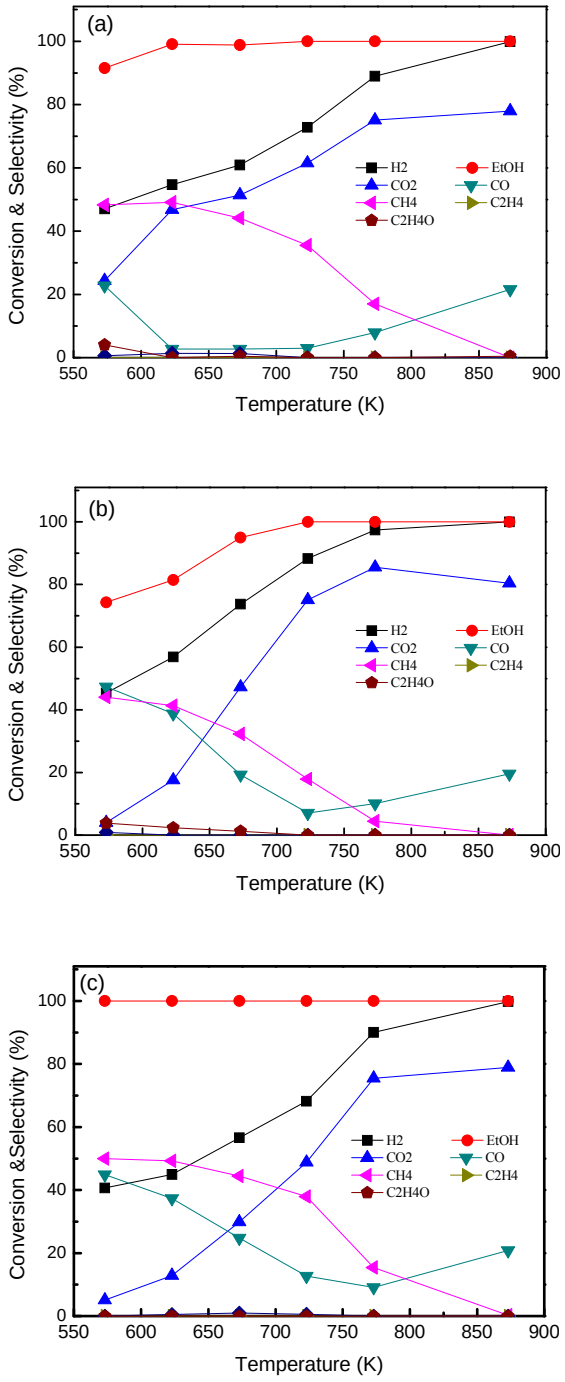

Figure 6.9. Product distribution of ethanol steam reforming over (a) Pt/Ca-Al_2O_3; (b) Rh/Ca-Al_2O_3, and (c) Pd/Ca-Al_2O_3.

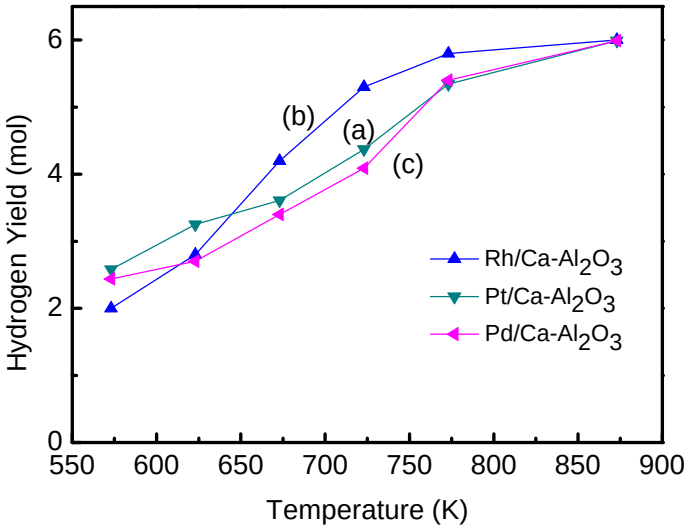

Figure 6.10. Hydrogen yield of (a) Pt/Ca-Al_2O_3; (b) Rh/Ca-Al_2O_3 and (c) Pd/Ca-Al_2O_3.

6.3.5. Electronic Properties – Valence Band

Valence bands (VB) which are occupied by electrons of low binding energy (BE < 20 eV) are often involved in the bonding orbitals. Electronic structure of the surface at valence level influences the catalytic performance through the variation of adsorption energy between the adsorbates and the metal d-states. It is generally accepted the higher degree of interaction with the adsorbate states occurs when the d-states are of higher energy relative to the Fermi energy. This is because the antibonding states are emptied as they shift above the Fermi level when the d-states are around the Fermi energy and as such

results in increasing bond strength. Hence, the VB provides valuable information on the electronic structure of the catalysts.

The VB spectra of the different noble metals supported on Ca-Al_2O_3 in the present study are shown in Fig. 6.11. Prior to the analysis, the samples were reduced in-situ in the XPS chamber at 473 K for 2 hr. For all spectra, it can be seen that the VB spectra of the catalysts exhibit broad features at ~ 13 eV and ~9 eV which are attributed to O 2p orbital and Al 3s, 3p and 3d orbitals respectively. Electronic density of states (DOS) are observed in the 6-8 eV region due to electronic donation from Ca 4s orbital, is consistent with the valence band spectrum obtained on Ca-Al_2O_3 support as shown in Chapter 4.

Interestingly, the VB for Rh/Ca-Al_2O_3 has a higher DOS around the Fermi level (-1 to +4 eV). This observation is similar to Wong et al. who reported that Rh (111), among other surfaces such as Pt (111) and Pd (111), has the highest DOS distribution near Fermi level using density functional theory analysis [37]. The higher DOS near Fermi level is likely to be contributed from Rh 4d orbitals which have proven to be useful in ESR as observed from our catalytic activity results. Rh has demonstrated the best catalytic activity in terms of hydrogen yield at 673 K. Wang et al. suggested that the higher DOS distribution near the Fermi level enhances the redox reactions in ESR.

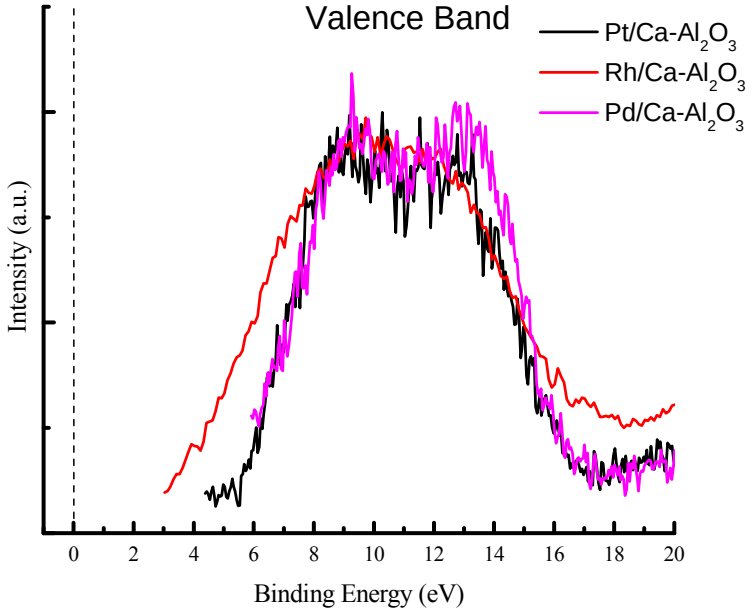

Figure 6.11. Valence band spectra of reduced catalysts.

6.4. Conclusions

The reaction mechanisms of ESR on noble metals (Pt, Rh and Pd) supported on Al_2O_3 and Ca-Al_2O_3 were thoroughly investigated using *in situ* DRIFTS, temperature-programmed desorption of ethanol and steady-state catalytic testing. The ESR pathway over Pt/Al_2O_3 involves the formation of acetates. In contrast, the presence of Ca in Pt/Ca-Al_2O_3 catalyst alters the reaction pathway, shifting from *acetate-driven* to *formate-driven*. This is the first time that the *formate-driven* reaction pathway was clearly demonstrated for ESR.

The availability of surface oxygen determines the reaction pathway. While the *acetate-driven* route is preferred over catalyst supports, such as CeO_2 and dehydrated Al_2O_3 where surface oxygen is readily available, enriched surface

hydroxyls and adsorbed water on catalyst surfaces such as Pt/Ca-Al_2O_3 facilitate the formation of formate species which are responsible for the *formate-driven* route. The noble metals play three different roles in the formation of formate species formation: (1) breaking of C-C bond; (2) holding of adsorbed CO, and (3) promoting the decomposition of formate species. The activity of the catalysts in WGSR during ethanol steam reforming decreases in the following order Pt > Rh > Pd. Scheme 1 illustrates the proposed reaction pathways.

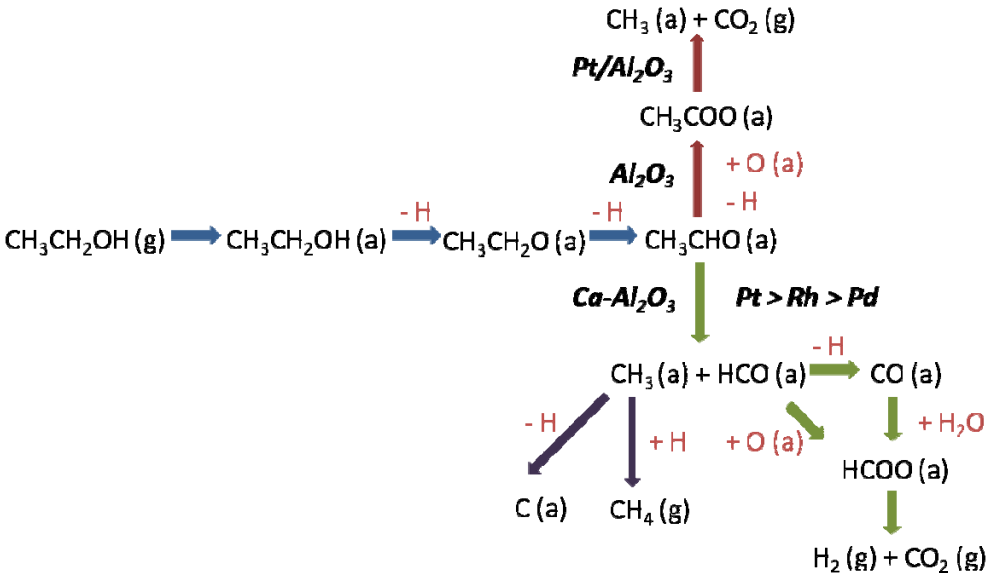

Scheme 1. Reaction pathways of ethanol over Al_2O_3, Ca-Al_2O_3 and Pt, Rh and Pd supported Ca- Al_2O_3.

6.5. References

[1] P. Bichon, G. Haugom, H. Venvik, A. Holmen, E. Blekkan, Top. Catal. 49 (2008) 38-45.

[2] J. Rostrupnielsen, J. Hansen, J. Catal. 144 (1993) 38-49.

[3] J. Richardson, S. Paripatyadar, Applied Catalysis. 61 (1990) 293-309.

[4] F. Auprêtre, C. Descorme, D. Duprez, Catal. Commun. 3 (2002) 263-267.

[5] D.K. Liguras, D.I. Kondarides, X.E. Verykios, Appl. Catal. B: Environ. 43 (2003) 345-354.

[6] A. Basagiannis, P. Panagiotopoulou, X. Verykios, Top. Catal. 51 (2008) 2-

[7] S. Cavallaro, Energy & Fuels. 14 (2000) 1195-1199.

[8] M. Goula, S. Kontou, P. Tsiakaras, Appl. Catal. B: Environ. 49 (2004) 135-144.

[9] J.M. Inc., Platinum Group Metals, Monthly Price Report, Johnson Mattey Inc., 2012.

[10] A. Erdőhelyi, J. Raskó, T. Kecskés, M. Tóth, M. Dömök, K. Baán, Catal. Today 116 (2006) 367-376.

[11] A. Yee, S. Morrison, H. Idriss, J. Catal. 186 (1999) 279-295.

[12] P. Panagiotopoulou, X. Verykios, Int. J. Hydrogen Energy.

[13] M. Sanchez-Sanchez, R. Navarro Yerga, D. Kondarides, X. Verykios, J. Fierro, J. Phys. Chem. A. 114 (2009) 3873-3882.

[14] A. Yee, S.J. Morrison, H. Idriss, J. Catal. 191 (2000) 30-45.

[15] L. Chen, C.K.S. Choong, Z. Zhong, L. Huang, T.P. Ang, L. Hong, J. Lin, J. Catal. 276 197-200.

[16] J. Raskó, M. Dömök, K. Baán, A. Erdőhelyi, Appl. Catal. A: Gen. 299 (2006) 202-211.

[17] M. Dömök, M. Tóth, J. Raskó, A. Erdőhelyi, Appl. Catal. B: Environ. 69 (2007) 262-272.

[18] J. Benítez, I. Carrizosa, J. Odriozola, Appl.Surf. Sci. 84 (1995) 391-399.

[19] J. Raskó, J. Kiss, Appl. Catal., A. 287 (2005) 252-260.

[20] G.C. Cabilla, A.L. Bonivardi, M.A. Baltanás, Appl. Catal. A: Gen. 255 (2003) 181-195.

[21] C. Choong, L. Huang, Z. Zhong, J. Lin, L. Hong, L. Chen, Appl. Catal. A: Gen. 407 (2011) 155-162.

[22] R. Greenler, J. Chem. Phys. 37 (1962) 2094-2100.

[23] R. Kagel, J. Phys. Chem. 71 (1967) 844-850.

[24] R. Kagel, R. Greenler, J. Chem. Phys. 49 (1968) 1638-1647.

[25] H. Evans, W. Weinberg, J. Chem. Phys. 71 (1979) 1537-1542.

[26] M. Dömök, K. Baán, T. Kecskés, A. Erdőhelyi, Catal. Lett. 126 (2008) 49-57.

[27] S. Gates, J. Russell J. Yates Jr, Surf. Sci. 171 (1986) 111-134.

[28] M. Mavrikakis, M.A. Barteau, J. Mol. Catal. A: Chem. 131 (1998) 135-147.

[29] C. Choong, Z. Zhong, L. Huang, Z. Wang, T.P. Ang, A. Borgna, J. Lin, L. Hong, L. Chen, Appl. Catal. A: Gen. 407 145-154.

[30] A. Maroto-Valiente, I. Rodríguez-Ramos, A. Guerrero-Ruiz, Thermochim. Acta. 379 (2001) 195-199.

[31] H. Borchert, B. Jürgens, V. Zielasek, G. Rupprechter, S. Giorgio, C.R. Henry, M. Bäumer, J. Catal. 247 (2007) 145-154.

[32] W. Liu, Y.F. Zhu, J.S. Lian, Q. Jiang, J. Phys. Chem. C 111 (2006) 1005-1009.

[33] A. Erdőhelyi, J. Raskó, T. Kecskés, M. Tóth, M. Dömök, K. Baán, Catal. Today 116 (2006) 367-376.

[34] J. Benson, H. Hwang, M. Boudart, J. Catal. 30 (1973) 146-153.

[35] F. Frusteri, S. Freni, L. Spadaro, V. Chiodo, G. Bonura, S. Donato, S. Cavallaro, Catal. Comm. 5 (2004) 611-615.

[36] A. Fatsikostas, X.Verykios, J. Catal. 225 (2004) 439-452.

[37] J. Wang, C. Lee, M. Lin, J. Phys. Chem. C 113 (2009) 6681-6688.

Chapter 7

CO-free Ethanol Steam Reforming over Fe promoted Rh/Ca-Al_2O_3 Catalyst

Graphical Abstract

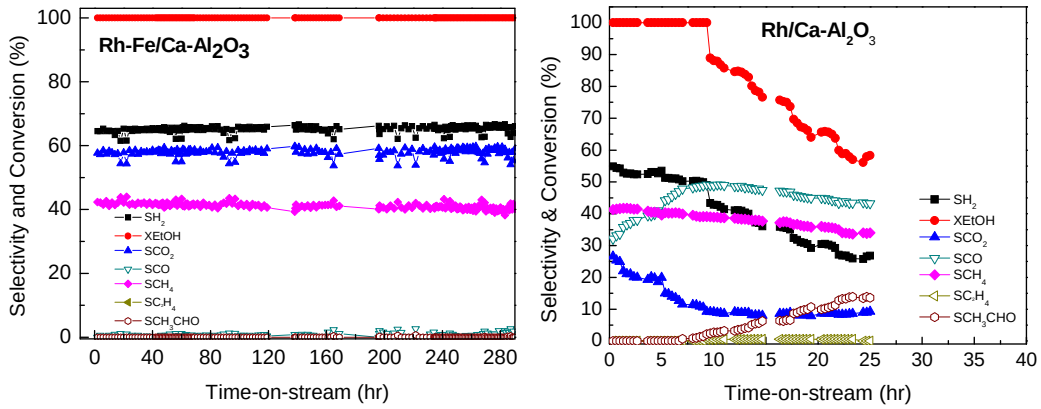

Building on the good performance of Rh catalyst in ethanol steam reforming, the loading of Fe promotion on the activity and selectivity of Rh catalyst was explored. The performances of catalysts using different catalyst bed configurations were also investigated. Promotion of 10 wt% of Fe on Rh/Ca-Al_2O_3 catalyst reduced CO selectivity to negligible amount at low temperature of 623 K, due to an increase in water-gas shift reaction (WGSR). Furthermore, the Fe-modified catalyst was stable for at least 280 h with little coke formation. Transmission electron microscopy image indicated that rhodium and iron oxides are in close proximity. The iron oxides in the vicinity of Rh sites reduce the CO

adsorption on Rh sites and transfer the adsorbed CO from Rh to COO-formate species on Fe_xO_y for the subsequent WGSR.

7.1. Introduction

The technological advancement of fuel cells is instrumental in harnessing clean energy for the future. Polymer electrolyte membrane (PEMFC) and phosphoric acid fuel cells (PAFC) use hydrogen as a fuel which can be produced via internal reforming within the fuel cell stack. While this may appear as an effortless task, challenges such as durability, cost and system size hinder the commercialization of fuel cells in reality [1-3]. For example, the Pt catalyst, which is an electrolyte for both PEMFC and PAFC, is susceptible to CO poisoning. This results in the loss of durability and money. It is also extremely difficult to meet the packing requirements of fuel cells for automobiles as it is limited not solely by the fuel cell stack but also to its auxiliary components such as the fuel processors. A fuel processor consists of reformers, compressors/expanders, heat exchangers and low and high temperature water-gas shift (WGS) reactors and CO removal units. The latter units are essential for CO cleanup in order to prevent CO poisoning of the Pt electrodes. However, these units occupy the main bulk of the system. Hence, in order to realize the commercialization of fuel cells, it will be ideal if hydrogen can be produced in the absence of CO. A fuel reformer which can produce CO free hydrogen is thus desirable.

A promising alternative to coal and natural gas derived hydrogen is the reforming of alcohols. Ethanol steam reforming (ESR, Eqn. 7.1) is a favorable reaction as ethanol has low toxicity and high energy density. Also, ethanol can be produced from lignocellulosic biomass such as wood chips, grass and agricultural

waste. ESR is also a carbon-neutral process since carbon dioxide released by the reforming process is offset by the CO_2 captured by plants through photosynthesis. The reaction pathway of ESR is complex and is dependent on the catalyst formulation and reaction conditions. Some of the reactions are described in Eqns 7.2-7.7.

$$C_2H_5OH + 3H_2O \leftrightarrow 2CO_2 + 6H_2 \quad (7.1)$$

$$C_2H_5OH \rightarrow CH_3CHO + H_2 \quad (7.2)$$

$$C_2H_5OH \rightarrow C_2H_4 + H_2O \quad (7.3)$$

$$CH_3CHO \rightarrow CH_4 + CO \quad (7.4)$$

$$CH_3CHO + H_2O \rightarrow 2CO + 3H_2 \quad (7.5)$$

$$CO + H_2O \leftrightarrow CO_2 + H_2 \quad (7.6)$$

$$CH_4 + H_2O \leftrightarrow CO + 3H_2 \quad (7.7)$$

ESR is thermodynamically favored at high reaction temperature (823-1073 K) to achieve high hydrogen yield [4-6]. In addition, coke accumulation is also significantly reduced at high temperature. However, high temperature ESR is not practical in reality due to high operating cost and long start-up time. Furthermore, WGSR (Eqn. 7.6) is a reversible reaction whereby the equilibrium shifts to the left at high temperature and limits CO conversion. Thus, in order to facilitate WGSR, low reaction temperature is required. However, low temperature ESR

reaction is limited by low hydrogen yield and severe coking due to the following reactions:

$$2CO \leftrightarrow CO_2 + C \quad (7.8)$$

$$CH_4 \leftrightarrow 2H_2 + C \quad (7.9)$$

$$C_2H_4 \rightarrow polymers \rightarrow coke \quad (7.10)$$

In view of this, the development of a carbon resistance catalyst which can facilitate both ESR and WGSR at low temperature condition is of primary importance.

A survey through literature shows the scarcity of reports based on low temperature ESR using noble metals based catalysts. Basagiannis et al. concluded that the catalytic performance varies in the order of Pt > Pd > Rh > Ru at low temperature of 573-723 K, with Pt being the most active and stable catalyst among the noble metals supported on γ-alumina [7]. However, selectivity to CO was as high as 30% at 623 K. In a recent study, CO selectivity of 1 wt. % Pt/Al_2O_3 and 1 wt. % Pt/CeO_2 was reported to be 45% and 21% respectively at 573 K [8]. On Rh catalysts, Zhong et al. reported a CO selectivity of about 30% over 1% Rh supported on hydrothermally synthesized ZrO_2 in the temperature range 573-673 K [9]. A 2% $Rh/Ce_{0.8}Zr_{0.2}O_2$ catalyst was found to have a lower CO selectivity of 10%, with a hydrogen yield of 4.3 mol H_2/mol EtOH at 723 K [10]. In Chapter 6, we have compared the performance of various noble metals (1 wt%) supported on Ca-Al_2O_3 at low temperature ESR. Results showed that the in

terms of hydrogen production, the catalysts are ranked in the following order at 673 K: Rh/Ca-Al_2O_3 > Pt/Ca-Al_2O_3 > Pd/Ca-Al_2O_3. While Rh catalyst is selective towards hydrogen production (4.2 mol H_2/mol EtOH), CO with S_{CO} =19.3% is evident over Rh/Ca-Al_2O_3. Hence, the presence of CO in the reformate stream seems inevitable over noble metal based catalysts, especially at low temperature reforming.

In order to remove CO from the reformate stream, one has to consider the importance of WGSR during reforming. This process is thermodynamically favored at a low temperature range between 573 K and 723 K. Iron-based catalysts have been industrially utilized for high temperature shift (623 K-723 K) where magnetite, Fe_3O_4, is the active phase for WGSR. On bulk iron oxide, the regenerative redox mechanism, which involves the oxidation of oxygen vacant sites by H_2O to form H_2 and the reduction of CO to CO_2, is dominant [11]. The associative formate mechanism has been observed on supported iron oxides such as Fe/Al_2O_3 and Fe/TiO_2 but their activities are lower than unsupported iron oxide [11]. Associative formate mechanism proceeds via the decomposition of formate species which are formed when CO reacts with surface hydroxyls. In either case, iron oxide based materials have proven to be a good WGSR catalyst [12, 13]. In view of this, iron oxide may be a suitable dopant during formulation of ESR catalysts.

Building on the good activity of Rh/Ca-Al_2O_3 catalyst from our previous findings, in this chapter, supported Rh catalysts with various loading of iron oxide

promoters were prepared via wet-incipient impregnation method. The ESR catalytic activities of the Fe promoted Rh catalysts were compared with Fe-free Rh/Ca-Al_2O_3 at different temperatures, with emphasis placed on CO selectivity. The catalytic evaluations were complemented with X-ray diffraction (XRD), temperature-programmed reduction (TPR), *in situ* diffuse reflectance infrared Fourier transformed spectroscopy (DRIFTS), X-ray photoelectron spectroscopy (XPS) and X-ray absorption near edge structure (XANES) characterizations. Our experimental results show that high hydrogen yield and extremely low CO selectivity can be achieved using Rh-Fe/Ca-Al_2O_3 during ESR. It was shown through a plausible mechanism that Fe_xO_y species play an essential role in enhancing the WGSR during ESR.

7.2. Experimental

7.2.1. Catalysts Synthesis

The Rh–Fe/Ca–Al_2O_3 catalyst was prepared by a sequential incipient wetness impregnation method in the following steps: (1) Ca-modified alumina, denoted as Ca-Al_2O_3, was prepared by the calcination of a paste of γ-Al_2O_3 (Merck, 103 m^2/g) impregnated with $Ca(NO_3)_2 \cdot 4H_2O$ (Riedel–deHaën) solution. (2) The obtained Ca-Al_2O_3 powder was impregnated with an appropriate amount of $Fe(NO_3)_3$ solution to get a precursor with Fe loading of 10 wt. %. The precursor was dried at 393 K for 10 h and heated to 723 K in air and then held for 5 h. (3) By impregnation with a $RhCl_3$ solution (Alfa Aesar), 1 wt. % of Rh was

introduced into the powder obtained in step (2). The obtained catalyst was dried and calcined in the same manner as in step (2) and is denoted as Rh–Fe/Ca–Al_2O_3. For comparison, a Fe-free 1 wt. % Rh catalyst, denoted as Rh/Ca–Al_2O_3, was also prepared, following steps (1) and (3).

7.2.2. Fixed Bed Catalytic Testing

The catalytic evaluation was performed in a customized 5-channels quartz micro-reactor (BEL, Japan), each of which was loaded with 100 mg of the catalyst. The temperature of the samples was individually monitored with thermocouples located just on top of the catalyst samples.

The Rh based catalysts were reduced in hydrogen at 473 K for 0.5 h. Then 40 ml min^{-1} of Ar was flown in, along with 0.005 ml min^{-1} of ethanol-water mixture (1:10 molar ratio) which was injected using a Shimadzu Liquid Pump and vaporized at 443 K within the reactor. The total gas hourly space velocity (GHSV) was kept constant at 34,000 h^{-1}, using a mass flow controller. The reaction products were analyzed online by a gas chromatograph (Varian CP-3800) with three columns: Porapak Q, Haysep Q and molecular sieve 5A. Porapak Q was used to separate organics and carbon dioxide with He as carrier gas while the later two columns were used for the separation of hydrogen, carbon monoxide and methane with Ar as carrier gas. The conversion of ethanol (X_{EtOH}) and selectivity to carbon containing species (S_{Ci}) were calculated based on Eqns. 3.5 and 3.6 in Chapter 3, respectively.

7.2.3. Catalysts Characterization

Powder X-ray diffraction (XRD) patterns were collected with a Bruker D8 X-ray diffraction system equipped with Cu Kα radiation ($\lambda = 0.154$ nm). The profiles were collected at a step width of 0.02° in the (2θ) range from 20° to 90°. X-ray photoelectron spectroscopy (XPS) was performed on a VG ESCALAB 250 spectrometer using an Mg Kα radiation source. The XPS data were processed with respect to the adventitious carbon C1*s* peak at 284.5 eV.

XANES spectra were measured on references and catalyst samples at Shanghai Synchrotron Radiation Facility (SSRF) using BL14W1 beamline. The X-ray ring has a flux of 2 x 1E12 photons per second at 200 mA and 3.5 GeV, and the energy range capability is 4-22.5 keV. Si(111) double crystals were used as monochromator. The energy resolution is about 2 x 10E-4 at 10 keV. The catalysts were reduced under reaction conditions before collection of spectra at room temperature.

In situ DRIFTS experiments were performed using a Bio-Rad FT-IT 3000 MX equipped with a high temperature cell fitted with KBr windows and a mercury-cadmium-telluride (MCT-A) detector cooled with liquid nitrogen. Spectra were acquired at a resolution of 4 cm^{-1} and typically over 256 scans. A powder sample was put into a reaction cell (Harricks HV-DR2) and reduced under the same conditions as for the activity test. A flow of 1% CO/He was introduced at room temperature after the sample has been purged by He for 0.5 h after the

reduction. Spectra were taken after CO had been adsorbed for 0.1 h and purged for 1 h. The spectrum of the freshly reduced sample was used as a reference.

Temperature programmed reduction (TPR) measurements were carried out on Thermo Scientific TPROD 1100. 100 mg of calcined catalysts, which had been thermally treated under Ar stream at 773 K to remove water and other contaminants, were heated from 303 K to 1123 K at a rate of 10 K min^{-1} in 50 ml min^{-1} of 5% H_2/Ar and maintained at 1023 K for 15 min while the hydrogen consumption was monitored. The type and the quantity of the carbon deposition on spent catalysts were determined by temperature-programmed oxidation (TPO) in which the sample was heated in 50 ml min^{-1} of 5% O_2/He at a rate of 15 K min^{-1} up to 1023 K and held at this temperature for 15 min. CO_2 emission versus the sample temperature was recorded using mass spectroscopy (HIDEN Analytical).

7.3. Results

7.3.1. Catalytic Performance

7.3.1.1. Influence of Fe loading on Rh/Ca-Al_2O_3

The effect of Fe loading on Rh/Ca-Al_2O_3 which varies between 2.5 wt. % to 10 wt. %, unpromoted Rh/Ca-Al_2O_3 and Rh-free Fe/Ca-Al_2O_3 are evaluated at 623 K. The results are summarized in Table 7.1. At 623 K, products such as H_2, CO_2 CO and CH_4 are observed without any detection of CH_3CHO over Rh/Ca-Al_2O_3. Ethanol conversion (X_{EtOH}) is 93.4 % at 623 K, giving a hydrogen yield of

3.6 mol. The production of CO and CH_4 is derived from the decarbonylation of CH_3CHO (Eqn. 7.4). Given that stoichiometry of the reaction, the CO and CH_4 should be of equal quantities. The lower S_{CH4} (S_{CH4} = 36.4%) and higher S_{CO} (S_{CO} = 47.0%) suggest that rate of methane decomposition (Eqn. 7.9) is high while WGSR (Eqn. 7.6) proceeds at a lower rate over Rh/Ca-Al_2O_3. On Rh-free 5.0 wt% Fe/Ca-Al_2O_3, X_{EtOH} is 6.1%, giving a hydrogen yield of 0.08 mol at 623 K. Acetaldehyde selectivity is found to be 100%, suggesting that dehydrogenation is dominant and that iron oxides is not active for ESR at this temperature.

The addition of small amount of Fe to Rh/Ca-Al_2O_3, i.e. Rh-2.5%Fe/Ca-Al_2O_3, leads to a decrease in CO selectivity from 47.0% (Fe-free) to 22.6% while CO_2 selectivity increases from 16.7% (Fe-free) to 37.1% at 623 K. CH_4 selectivity remains almost unchanged at 36.7 % as compared to Rh/Ca-Al_2O_3, suggesting that the reaction mechanism remains largely unchanged for Fe-promoted Rh/Ca-Al_2O_3 catalyst. Increasing Fe loading from 2.5 wt. % to 10 wt. % leads to a progressive decrease in S_{CO} from 22.6% to 0%, with a corresponding S_{CO2} increase from 37.1% to 60.3% Ethanol conversion also increases from 95.3% to a complete conversion using Rh/Ca-Al_2O_3 promoted with 10 wt. % Fe, eventually giving a hydrogen yield of 4.1 mol.

The role of iron oxide in reducing the S_{CO} in the product stream using Rh/Ca-Al_2O_3 catalyst during ESR is clearly evident from Table 7.1. There are three possibilities where CO can be converted to other products through (1) WGSR (Eqn. 7.6), (2) methanation (Eqn. 7.7) and (3) Boudouard reaction (Eqn. 7.8). The latter two possibilities can be ruled out. It has been pointed out that the

selectivity of CH_4 remains at a rather constant value over Rh/Ca-Al_2O_3 and Fe-promoted Rh/Ca-Al_2O_3 catalysts, a clear indication that methanation does not occur at 623 K. In addition, Boudouard reaction can only take over metallic Fe particles which are not prevalent from our reduced Fe-promoted catalysts, as shown in the later part of the chapter. Hence, WGSR appears to be the reason behind the CO reduction in the presence of iron oxides. It has been observed in Table 7.1 that increasing Fe loading, leads to a progressive decrease in S_{CO} along with an increase in S_{CO2} and Y_{H2}, which are the products from WGSR. In order to verify, WGSR was conducted between 573 K-673 K using Rh-10 wt. % Fe/Ca-Al_2O_3 and Fe-free Rh/Ca-Al_2O_3 catalysts. The results in Fig. 7.1 show that Rh-Fe catalyst is able to reach CO conversion at thermodynamic equilibrium level within the experimented temperature range. Higher CO conversion than thermodynamic equilibrium is due to the co-existence of CO methanation reaction at $T > 623$ K. In contrast, Rh/Ca-Al_2O_3 catalyst is less active catalyst for WGSR at lower temperature ($T < 653$ K) where CO conversion falls way below thermodynamic equilibrium. At $T \geq 653$ K, WGSR and methanation reaction are observed over Rh/Ca-Al_2O_3 catalyst. Therefore, it is shown experimentally that the presence of iron oxides over Rh/Ca-Al_2O_3 enhances the WGSR during ESR. This is also in line with the fact that iron oxides are excellent WGSR catalyst.

Table 7.1. Effect of Fe loading on Rh-Fe/Ca-Al_2O_3 catalysts for ethanol steam reforming at 623 K.

Catalyst	X_{EtOH} (%)	Y_{H_2} (mol)	Product distribution (%)			
			S_{CO2}	S_{CO}	S_{CH4}	S_{CH3CHO}
Rh/Ca-Al_2O_3	93.4	3.6	16.7	47.0	36.4	0.0
Rh-2.5 wt. % Fe/Ca-Al_2O_3	95.3	3.3	37.1	22.6	36.7	3.0
Rh-5.0 wt. % Fe/Ca-Al_2O_3	95.7	3.4	50.0	9.5	37.1	3.2
Rh-7.5 wt. % Fe/Ca-Al_2O_3	100.0	3.7	59.1	2.2	37.7	0.0
Rh-10% wt. % Fe/Ca-Al_2O_3	100.0	4.1	60.3	0.0	39.7	0.0
5.0 wt. % Fe/Ca-Al_2O_3	6.1	0.08	0.0	0.0	0.0	100.0

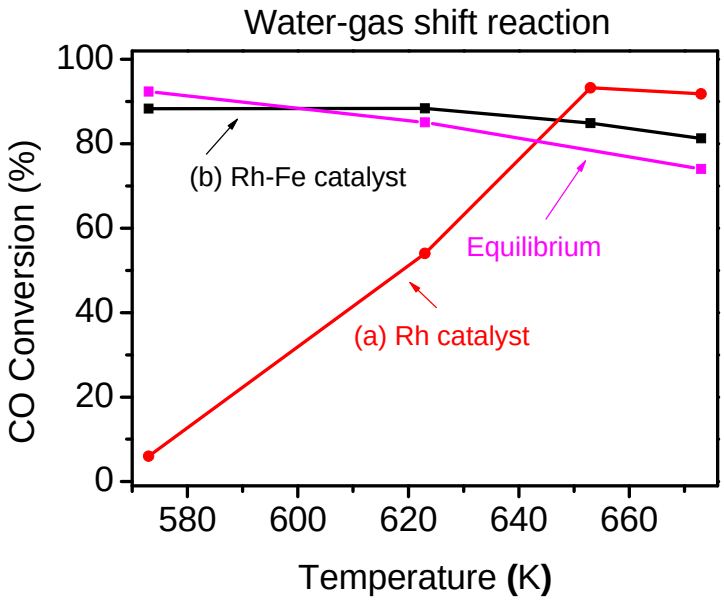

Figure 7.1. Water-gas shift reaction over (a) Rh/Ca-Al_2O_3 and (b) Rh-Fe/Ca-Al_2O_3. (Catalyst pre-reduced at 473 K for 0.5 h. Gas compositions: CO 2.1%, H_2O 36.0%, CO_2 8.0%, H_2 18.6%, He make up to 100%. Total flow 24.5 $mlmin^{-1}$, GHSV=1176 h^{-1}).

7.3.1.2. Catalytic Performance of Rh-Fe_2O_3-Ca-Al_2O_3 catalysts under different configurations

Rh/Ca-Al_2O_3 modified with 10 wt. % of Fe effectively reduces the CO content to negligible quantities. For simplicity, we will denote Rh-10 wt. % Fe/Ca-Al_2O_3 as Rh-Fe/Ca-Al_2O_3 for the rest of the section. In order to evaluate the importance of Rh-Fe interactions as well as surface hydroxyls in promoting WGSR in the presence of Fe, Rh/Fe_2O_3, Fe/Ca-Al_2O_3, Rh/Ca-Al_2O_3 and Ca-Al_2O_3 catalysts were packed in three different catalytic bed configurations and their catalytic activites were examined for ESR at 623 K (Table 7.2). The first

configuration is a double layer configuration with Rh/Ca-Al_2O_3 on top and Fe/Ca-Al_2O_3 below, separated by a thin layer of quartz wool. In the second configuration, Fe_2O_3 supported Rh catalyst is physically mixed with Ca-Al_2O_3 support. The third configuration is comprised of physically mixed Rh/Ca-Al_2O_3 and Fe/Ca-Al_2O_3.

In all the three configurations, CO_2, CO, CH_4, CH_3CHO products are observed together with trace amount of C_2H_4 at 623 K. In the double layer configuration previously described, a high S_{CO} of 48.1% and a low S_{CO2} of 6.8% suggests the lack of WGSR in such system. The CO concentration falls to 38.5% when a mixture of Rh/Ca-Al_2O_3 and 10%Fe/Ca-Al_2O_3 catalysts is being evaluated. Further improvement in the WGSR, resulting in S_{CO} of 21.8%, is made by using a mixture of physically mixed Rh/Fe_2O_3 and Ca-Al_2O. In this system, a product distribution of S_{CO2} = 35.2%, S_{CO}=21.8%, S_{CH4}=35.2 and S_{CH3CHO} = 7.0% is attained. Ethanol conversion is best achieved using physically mixed Rh/Fe_2O_3 and Ca-Al_2O_3, giving rise to Y_{H2} of 3.5 mol.

The results in Table 7.2 outline two important observations. First, Rh and Fe are required to be close proximity to achieve an enhanced WGSR during ESR. This is demonstrated in the two physically mixed configurations whereby there is direct contact between Rh and Fe which leads to an improvement in S_{CO} reduction. In contrast, in the double layer configuration, where Rh and Fe are separated, no occurrence of WGSR is observed. These results substantiate our previous reasoning that close proximity of Rh and Fe (i.e. Rh-Fe/Ca-Al_2O_3) is required to generate coordinatively unsaturated ferrous (CUF) sites necessary for

the promotion effect. The second observation which is clearly outlined in these experiments is the need for surface hydroxyls and/or water activation sites to initiate WGSR in ESR. While Rh/Fe_2O_3 should have the highest degree of Rh-Fe proximity, the mixture of Rh/Fe_2O_3 and Ca-Al_2O_3 fails to convert CO completely, giving a S_{CO} of 21.8%. The replacement of Ca-Al_2O_3 by Fe_2O_3 depletes the catalyst of surface hydroxyls and hence fails to attain full CO conversion via WGSR. This effect will be further discussed in Chapter 8.

Table 7.2. Effect of catalytic bed configuration on Rh-Fe/Ca-Al_2O_3 catalysts for ethanol steam reforming at 623 K.

Catalyst	X_{EtOH} (%)	Y_{H2} (mol)	Product distribution (%)				
			S_{CO2}	S_{CO}	S_{CH4}	S_{C2H4}	S_{CH3CHO}
Double layers: (1) Rh/Ca-Al_2O_3 and (2)10%Fe/Ca-Al_2O_3	73.2	2.1	6.8	48.1	40. 5	0.9	3.8
Mixture of Rh/Fe_2O_3 and Ca-Al_2O_3	100.0	3.5	35.2	21.8	35.2	0.8	7.0
Mixture of Rh/Ca-Al_2O_3 and 10%Fe/Ca-Al_2O_3	60.2	1.8	17.0	38.5	37.1	0.2	7.1

7.3.1.3. Influence of reaction temperature

The effect of reaction temperature (573 K ≤ T ≤673 K) on the activities of Rh/Ca-Al_2O_3 and Rh-Fe/Ca-Al_2O_3 catalysts is compared in Table 7.3. The WGSR promoted by the presence of Fe is noted at a temperature as low as 573 K. At 573 K, S_{CO} decreases from 50.2% (Fe-free) to 12.3% when the catalyst is promoted by Fe. The presence of Fe leads to an almost complete ethanol conversion at 99.3%, with Y_{H2} = 3.5 mol. At higher temperature of 623 K and 673 K, significant CO clean-up takes place with S_{CO} going so low that is undetectable by gas chromatography. Ethanol conversion is complete at both temperatures, with Y_{H2} = ~ 4.2 mol. At 673 K, it is however noted that the hydrogen yield of Rh/Ca-Al_2O_3 (Y_{H2} = ~ 4.7 mol) is higher that Rh-Fe/Ca-Al_2O_3 (Y_{H2} = 4.3 mol). The higher CH_4 selectivity from Rh-Fe/Ca-Al_2O_3 than Rh/Ca-Al_2O_3 would thus suggest that methanation process which consumes CO and H_2 to produce CH_4 occurs over Rh-Fe/Ca-Al_2O_3 catalyst at 673 K. This is in consistent with our results from WGSR measurements.

Hence, the addition of iron oxide in the formulation of Rh catalyst is a significant research milestone whereby the possibility of elimination of CO reactors in a fuel processor can be a reality. Furthermore, Fe-promoted Rh/Ca-Al_2O_3 can function at low ESR reforming temperature of 623 K, increasing its potential use for on-site hydrogen production for fuel cells in portable and mobile applications.

Table 7.3. Catalytic Activity of Rh/Ca-Al_2O_3 and Rh-Fe/Ca-Al_2O_3 at 573, 623 and 673 K.

T(K)	Catalyst	X_{EtOH} (%)	Y_{H_2} (mol)	Product distribution (%)				
				S_{CO_2}	S_{CO}	S_{CH_4}	$S_{C_2H_4}$	S_{CH_3CHO}
573	Rh/Ca-Al_2O_3	63.5	1.8	2.5	50.2	40.0	0.19	7.1
	Rh-Fe/Ca-Al_2O_3	99.3	3.5	43.0	12.3	44.7	0.0	0.0
623	Rh/Ca-Al_2O_3	93.4	3.6	16.7	47.0	36.4	0.0	0.0
	Rh-Fe/Ca-Al_2O_3	100	4.1	60.3	0.0	39.7	0.0	0.0
673	Rh/Ca-Al_2O_3	100	4.7	55.5	15.7	28.8	0.0	0.0
	Rh-Fe/Ca-Al_2O_3	100	4.3	63.8	0.0	36.2	0.0	0.0

7.3.1.4. Stability Catalytic Test

The stabilities and product distributions of Fe promoted and unpromoted Rh/Ca-Al_2O_3 catalysts at 623 K are compared in Fig. 7.2. The promotion effect of iron oxides on Rh/Ca-Al_2O_3 is not only limited to its ability to remove CO

effectively from the product stream but also increases the catalyst life span significantly. No significant deactivation is observed for at least 288 h at 623 K. This is in contrast to the stability of Rh/Ca-Al_2O_3 whereby deactivation is observed after 7.5 h under the same reaction conditions. During deactivation, S_{CH3CHO} and S_{CO} increase. Based on our previous study, Rh catalysts undergo dehydrogenation to produce CH_3CHO. This compound will decarbonylate into CO and CH_4, breaking the C-C bond. Carbon monoxide will proceed via WGSR to produce CO_2 and H_2O while CH_4 can either reform or decompose to form H_2, CO and CO_2. The progressive increase in S_{CH3CHO} is an indication that the ability for Rh to rupture the C-C bond is weakened. This may be attributed to the blockage of Rh active sites due to CO poisoning which will be discussed later.

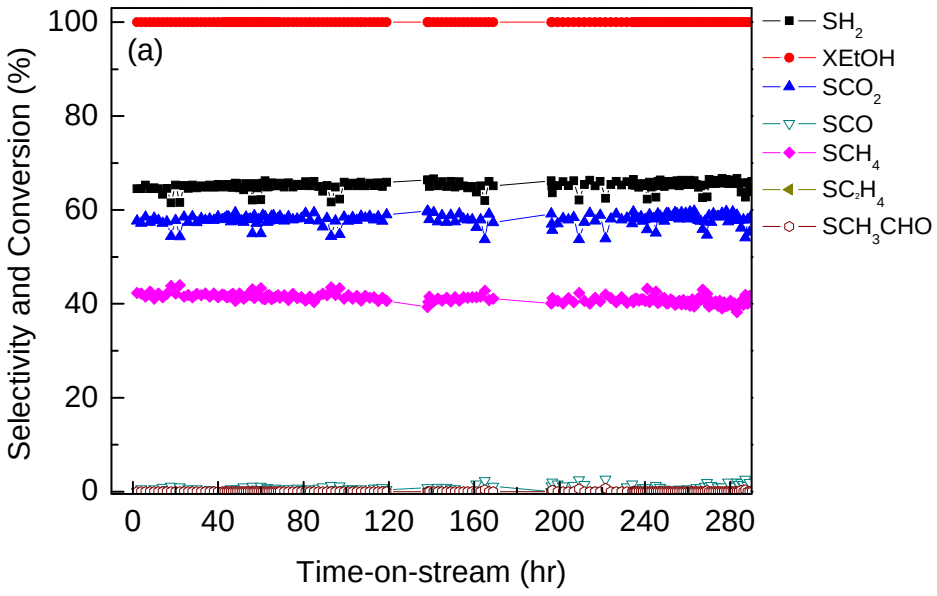

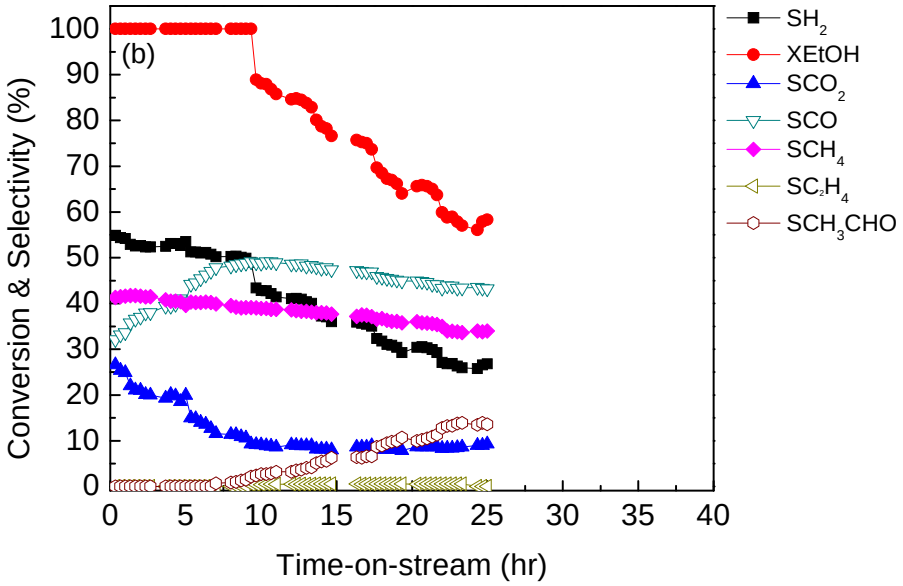

Figure 7.2. Catalytic stability of (a) Rh-Fe/Ca-Al_2O_3 and (b) Rh/Ca-Al_2O_3 for ethanol steam reforming at 623 K.

7.3.2. Catalyst Characterization

7.3.2.1. XRD

In order to investigate and verify the state of the iron oxides during reaction, XRD was performed on as calcined Rh-Fe/Ca-Al_2O_3 catalyst and spent catalysts of Rh-Fe/Ca-Al_2O_3 after 40 h of ESR reaction. In Fig. 7.3(a), XRD of as calcined Rh-Fe/Ca-Al_2O_3 catalyst shows the presence of Fe_2O_3, haematite phase, in addition of the characteristic peaks of Al_2O_3 at 39.4°, 45.6° and 67.1°. The diffraction peaks of the Fe_2O_3 species are located at 24.2°, 33.2°, 35.6°, 49.7°, 54.1°, 62.6° and 64.1°. The XRD of spent catalysts of Rh-Fe/Ca-Al_2O_3 after 40 h

of ESR reaction at 623 K (Fig 7.3(b)) shows most of the Fe_2O_3 phase are being reduced to Fe_3O_4. This is the most stable oxide in most of the WGSR feeds.

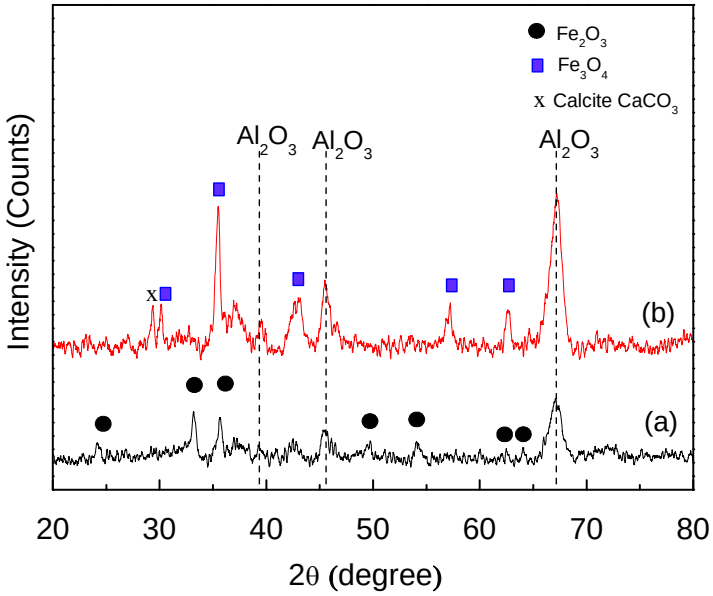

Figure 7.3. XRD of (a) as calcined Rh-Fe/Ca-Al_2O_3 and (b) spent Rh-Fe/Ca-Al_2O_3 catalyst after 40 h of reaction.

7.3.2.2. Temperature-programmed Reduction (TPR)

TPR profiles of the Rh/Ca-Al_2O_3, Fe/Ca-Al_2O_3 and Rh-Fe/Ca-Al_2O_3 are illustrated in Fig. 7.4. Theoretical consumptions of hydrogen per mole of metal based on the reduction of rhodium oxides and iron oxides are given in Table 7.4. Values of hydrogen consumption per mole of metal based on TPR profiles deconvolution of the above catalysts are tabulated in Table 7.5. The TPR profile of Rh/Ca-Al_2O_3 shows weak reduction peaks at 369 K and 463 K which are

attributed to the reduction of Rh_2O_3 to Rh metal ($Rh_2O_3 + H_2 \rightarrow 2Rh + H_2O$). The presence of two peaks is attributed to the particle size effect [14]. The reduction peak at lower temperature corresponds to the reduction of well dispersed Rh_2O_3 whereas the higher temperature peak is assigned to the reduction of bulk Rh_2O_3. The molar ratio of H_2 consumption to Rh (mol H_2/ mol Rh) which is determined to be 1.48 is close to the theoretical value ((mol H_2/ mol Fe)$_{theo}$) = 1.5. This indicates the complete reduction of oxides to metallic Rh by 530 K. The reduction of Fe/Ca-Al_2O_3 catalyst begins at 470 K with Tmax = 657 K. Another broad peak at 885 K is also observed on Fe/Ca-Al_2O_3 catalyst. In general, reduction of iron oxide proceeds in the following manner, i.e. $Fe_2O_3 \rightarrow Fe_3O_4 \rightarrow Fe$ [15]. The peak at 657 K can be attributed to the reduction of $Fe_2O_3 \rightarrow Fe_3O_4$, based on the molar ratio of H_2 consumption to Fe (mol H_2/ mol Fe) of 0.22. The molar ratio of H_2 consumption per mol of Fe (mol H_2/ mol Fe) of 0.19 corresponds to the broad peak of at 855 K. This value is smaller than the theoretical value of $Fe_3O_4 \rightarrow Fe$ ((mol H_2/ mol Fe)$_{theo}$ = 1.33) which indicates that Fe_3O_4 is reduced to FeO instead of Fe. FeO is a thermodynamically unstable phase in air but its presence has been observable during reduction [16]. Four reduction peaks are observed on Rh-Fe/Ca-Al_2O_3 catalyst. At 416 K, the sharp reduction peak is assigned to both the reduction of Rh_2O_3 to Rh metallic with a mol H_2/ mol Rh of 1.46 and the reduction of iron oxide. Together with the peaks at 510 K and 595 K, the hydrogen consumption is tabulated to be mol H_2/ mol Fe = 0.17 and is assigned to the reduction of $Fe_2O_3 \rightarrow Fe_3O_4$. The latter peak at 798 K (mol H_2/ mol Fe = 0.28) corresponds to the reduction of $Fe_3O_4 \rightarrow FeO$ (mol H_2/ mol Fe = 0.33). TPR of

Rh-Fe/Ca-Al_2O_3 shows that the presence of Rh shifts the whole reduction of iron oxides to a lower temperature range. Therefore, the presence of Rh increases the reducibility of iron oxides, an observation consistent with the literature [17]. The spillover effect of H_2 from Rh to iron oxide facilitates the reduction of the promoter oxide. The reduction process ends with FeO phase instead of metallic Fe. This can be attributed to the metal-support interaction between iron oxide and Ca-Al_2O_3 [18, 19].

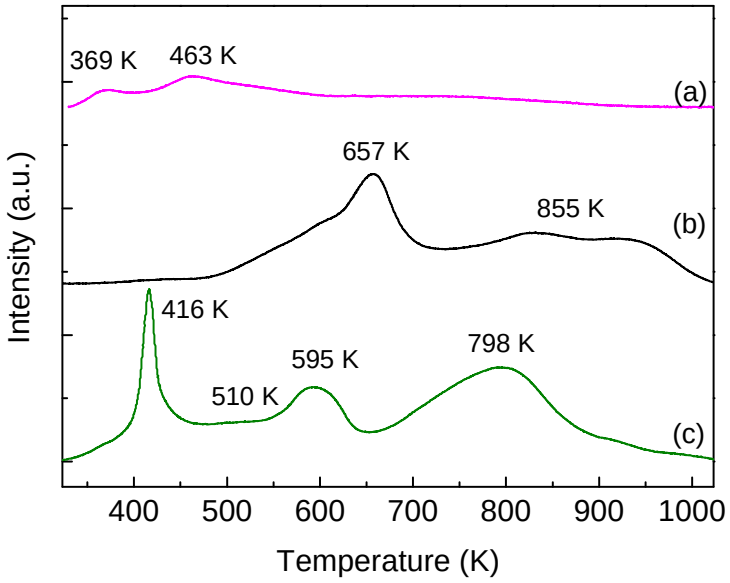

Figure 7.4. TPR profiles of (a) Rh/Ca-Al_2O_3; (b) Fe/Ca-Al_2O_3 and (c) Rh-Fe/Ca-Al_2O_3.

Table 7.4. Theoretical consumption of H_2 per mole of metal (mol/mol).

	mol H_2/ mol Rh	mol H_2/ mol Fe
$Rh_2O_3 + 3H_2 \rightarrow 2Rh + 3H_2O$	1.5	-
$3Fe_2O_3 + H_2 \rightarrow 2Fe_3O_4 + H_2O$	-	0.17
$Fe_3O_4 + H_2 \rightarrow 3FeO + H_2O$	-	0.33
$FeO + H_2 \rightarrow Fe + H_2O$	-	1

Table 7.5. Tabulation of consumption of H_2 per mole of metal (mol/mol) over Rh/Ca-Al_2O_3, Fe/Ca-Al_2O_3 and Rh-Fe/Ca-Al_2O_3 catalysts.

Catalyst	Tmax (K)	mol H_2/ mol Rh	mol H_2/ mol Fe
Rh/Ca-Al_2O_3	369	0.24	
	463	1.24	
Fe/Ca-Al_2O_3	657		0.22
	855		0.19
Rh-Fe/Ca-Al_2O_3	416	1.37	0.03
	510		0.07
	595		0.07
	798		0.29

7.3.2.3. X-ray Spectroscopy (XPS) and X-ray absorption near edge structure (XANES)

The oxidation state of iron oxides was probed over the surface of reduced Rh-Fe/Ca-Al_2O_3 catalyst using XPS (Fig. 7.5). On the as-calcined Rh-Fe/Ca-Al_2O_3 catalysts, the peak positions of Fe $2p_{3/2}$ and Fe 2 $p_{1/2}$ are located at 711.2 eV and 724.5 eV respectively. They correspond to Fe^{3+} ions obtained from Fe_2O_3 [20], a phase identified from our XRD diffraction peaks. The presence of satellite peak at 719.2 eV, which is a distinct feature of Fe_2O_3, is also distinguishable from the as-calcined catalyst. The XPS of reduced Rh-Fe/Ca-Al_2O_3 catalyst by H_2 at 473 K for 0.5 h shows the disappearance of satellite peak which indicates the loss of Fe_2O_3 species upon reduction. Furthermore, an electronic shift towards the lower binding energy of 710.5 eV, which is characteristic of Fe^{2+} is clearly visible. The presence of Fe_xO_y species has gone unnoticed from the previous characterization techniques due to the lack of surface sensitivity, unlike XPS which is a surface sensitive tool. Fe K-edge XANES results also provide unambiguous evidence for the formation of FeO like species after reduction at 473 K in H_2 for 2 h. Fe K-edge XANES spectra of a series Fe reference compounds such as metallic Fe, Fe_2O_3 and Fe_3O_4 were compared with that of reduced Rh-Fe/Ca-Al_2O_3 catalyst (Fig. 7.6). Determination of the oxidation state of the compound can be compared using the absorption edge energy obtained XANES. The lower absorption edge energy of metallic Fe than the iron oxides is due to the zero valency of metallic Fe. Increasing valence state of Fe will shift the absorption edge energy towards higher energy. As observed from Fig. 7.6, the

absorption edge energy of reduced Rh-Fe/Ca-Al_2O_3 catalyst is somewhere metallic Fe and fully oxidized iron oxides with a composition of 12% Fe, 43% Fe_3O_4 and 45% of Fe_2O_3 after fitting (Table 7.6). This provides evidence of the presence of Fe_xO_y species as previously observed using XPS.

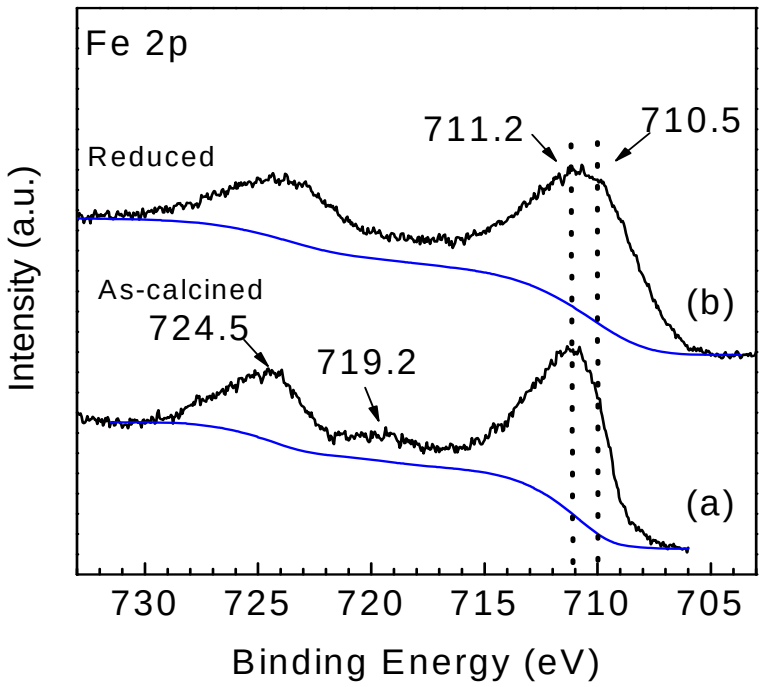

Figure 7.5. XPS of (a) as calcined Rh-Fe/Ca-Al_2O_3 and (b) reduced Rh-Fe/Ca-Al_2O_3 catalyst at 473 K for 0.5 h.

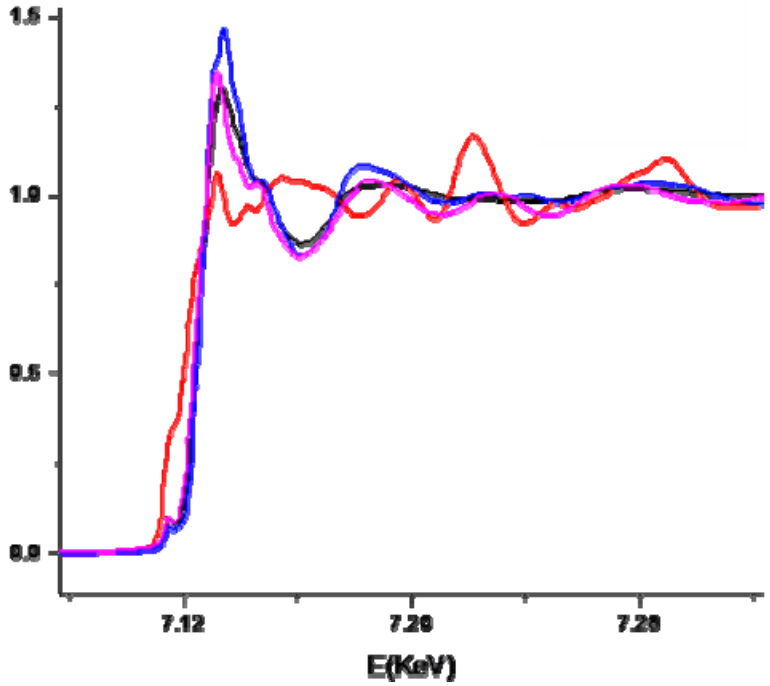

Figure 7.6. Fe K-edge XANES spectra of metallic Fe (red), Fe_3O_4 (pink), Fe_2O_3 (blue) and reduced Rh-Fe/Ca-Al_2O_3 (black).

Table 7.6. Composition of iron species on reduced Rh-Fe/Ca-Al_2O_3 determined using Fe K-edge.

	Concentration
Fe	0.12
Fe_3O_4	0.43
Fe_2O_3	0.45

7.3.2.4. *In situ* DRIFTS

In situ DRIFTS studies of CO adsorption are performed on Rh/Ca-Al_2O_3 and Rh-Fe/Ca-Al_2O_3. On Rh/Ca-Al_2O_3, peaks at 2093 and 2020 cm^{-1}, characteristic of symmetric and asymmetrical gem-dicarbonyl CO on Rh are observed. Linearly bonded and bridged bonded CO peaks and located at 2063 cm^{-1} and 1820 cm^{-1} are also noted. These assignments are in line with the literature by Yang et al [21]. It is generally accepted that gem-dicarbonyl CO are the result of the interaction of CO with Rh^+ species while linear and bridged CO are stemmed from Rh^0 metallic species. Fig. 7.7(a) shows the presence of a large concentration of gem-dicarbonyl CO adsorbed on Rh/Ca-Al_2O_3 species which are responsible for the catalyst deactivation. Krishanmurthy et al. found that the Rh-CO bond strength in gem-dicarbonyl CO to be 141 kJ/mol, which is higher than Rh-Rh bonds (121 kJ/mol) in metallic Rh. The high concentration and high bond strength of the gem-dicarbonyl CO on Rh over unpromoted catalyst block the Rh active sites available for ethanol adsorption and for the cleavage of C-C bond in acetaldehyde, resulting in deactivation. This phenomenon is described as CO poisoning.

In comparison, CO adsorption on Rh-Fe/Ca-Al_2O_3 catalysts reveals that the concentration of gem-dicarbonyls located at 2093 cm^{-1} and 2020 cm^{-1} are decreased, hence reducing the CO poisoning effect as previously mentioned. The lack of CO adsorption either in linearly or bridged forms on Rh^0 is noted. New adsorption peaks corresponding to ν_a(OCO) and ν_s(OCO) of formate species on iron oxides are registered at 1522 cm^{-1} and 1373 cm^{-1}. Therefore, in the presence

of iron oxide, which is close proximity to Rh as shown in TEM (Fig. 7.8), CO adsorption of Rh can be easily converted into formate species which are active intermediates for WGSR.

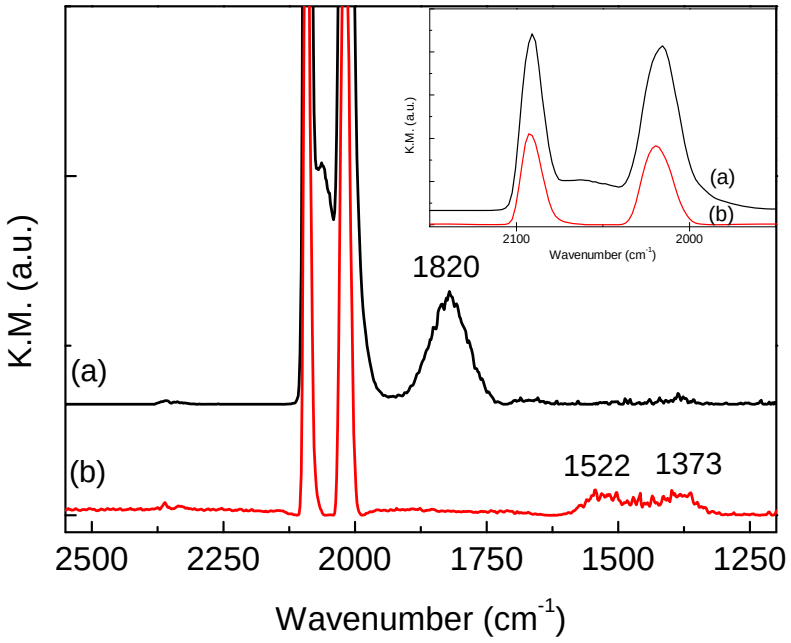

Figure 7.7. *In situ* DRIFTS spectrum of adsorbed CO at 303 K of reduced (a) Rh/Ca-Al_2O_3 and (b) Rh-Fe/Ca-Al_2O_3 catalysts.

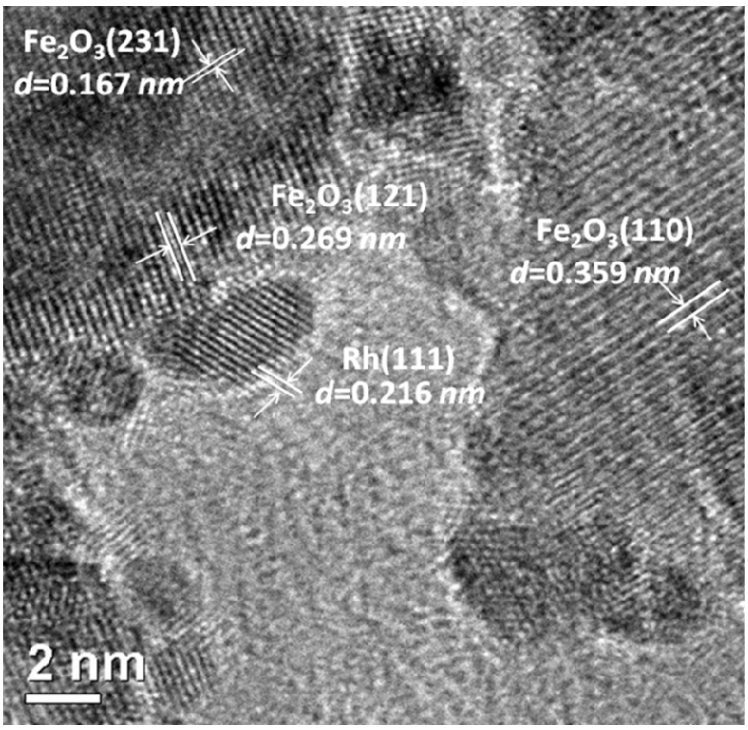

Figure 7.8. TEM image of pre-reduced Rh-Fe/Ca-Al_2O_3 catalyst by H_2 at 473 K for 0.5 h.

7.3.2.5. Temperature programmed oxidation (TPO)

Temperature programmed oxidation (TPO) was performed to determine the nature and the amount of coke deposits on spent catalysts. In Fig. 7.9 shows the TPO profiles of spent Rh/Ca-Al_2O_3 and Rh-Fe/Ca-Al_2O_3 catalysts after 24 h and 40 h of reaction respectively at 623 K. Over spent Rh/Ca-Al_2O_3, a big CO_2 desorption peak centered at 625 K is observed. Here, we may attribute this peak due to the oxidation of surface carbon deposited from the dissociation of CO on Rh. Rh can adsorb CO both dissociatively and non-dissociatively [22]. Solymosi and Erdöhelyi observed the dissociation of CO on highly dispersed Rh at temperatures above 473 K [23]. *In situ* DRIFTS (in section 7.3.4) shows that CO

populates and adsorbs strongly on Rh catalyst on Fe-free Ca-Al_2O_3. At ESR reaction temperature of 623 K, CO dissociates to give CO_2 and surface carbon (Eqn. 7.8). There is also likelihood that the carboneous species are derived from acetate-like species. During deactivation, concentration of CH_3CHO increases due to the absence of C-C bond rupture by the active metal. Consequently, the accumulation of CH_3CHO leads to the presence of acetate-like species which decomposes during TPO [24, 25].

In contrast, spent Rh-Fe/Ca-Al_2O_3 catalyst gives two CO_2 desorption peak with T_{max} at 375 K and 623 K. Taking into consideration that the TPO profile of Rh-Fe/Ca-Al_2O_3 was collected after 40 h of reaction, the amount of coke deposited is significantly smaller than that on Rh/Ca-Al_2O_3 which was only reacted for 24 h. This shows that the addition of Fe is able to lower the rate of coke deposition by converting the adsorbed CO to formate species. Given that the CO adsorb on Rh are weaker and unstable, dissociation of CO into surface carbon is deterred. This extends the catalyst lifespan and also minimizes the accumulation of acetaldehydes which will otherwise result in significant coke deposition.

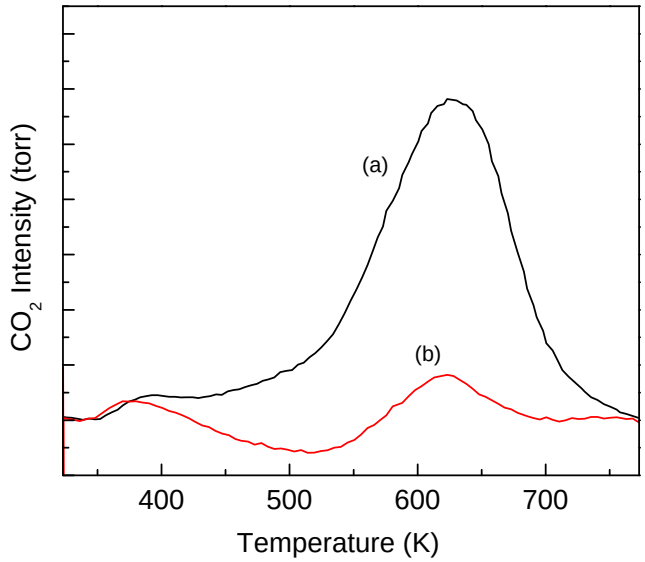

Figure 7.9. Temperature-programmed oxidation (TPO) of spent (a) Rh/Ca-Al_2O_3 and (b) Rh-Fe/Ca-Al_2O_3 catalysts after reaction for 24 h and 40 h, respectively.

7.4. Discussions

Rh-Fe/Ca-Al_2O_3 catalyst with 10 wt% iron loading shows high, stable catalytic activity with negligible CO selectivity for ESR at a low temperature of 623 K. This is attributed to WGSR which converts CO and H_2O to CO_2 and H_2. *In situ* DRIFTS study of adsorbed CO over Rh-Fe/Ca-Al_2O_3 catalyst shows the presence of formate species which are intermediates for WGSR. Adsorbed CO species are constantly being converted either to formate species or gaseous CO_2, resulting in low CO selectivity over Rh-Fe/Ca-Al_2O_3 catalyst. This also leaves Rh active sites available for ethanol activation and hence increasing its catalytic lifespan. In contrast, infrared spectrum of adsorbed CO over Rh/Ca-Al_2O_3 catalyst

has provided evidence that Rh-CO bonding is very strong. Since, Rh atoms are active sites for ethanol adsorption and for ESR, these adsorbed CO on Rh will lead to poorer ESR catalytic performance and faster deactivation as shown in Fig. 7.2. Higher CO selectivity over Rh/Ca-Al_2O_3 is due to the lack of WGSR as the CO remains adsorbed on the active sites.

Experimentally proven, Rh and Fe are required to be in close proximity in order for WGSR to be effective. TPR profiles of Rh/Ca-Al_2O_3, Fe/Ca-Al_2O_3 and Rh-Fe/Ca-Al_2O_3 show that Rh facilitates the reduction of iron oxides at a lower temperature than Rh-free Fe/Ca-Al_2O_3. Fe_2O_3 is reduced to FeO within the reduction temperature range of 1023 K. It cannot be further reduced to metallic Fe due to the strong metal-support effect. This minimizes the likelihood of alloy formation between Rh and Fe and thus it is assumed that the catalytic activity of Rh in Rh-Fe/Ca-Al_2O_3 is unaffected. XRD indicates the presence of Fe_3O_4 species during ESR reaction at 623 K. Various characterization techniques at surface level such as XPS and XANES both reveal the presence of Fe_xO_y species after reduction. Therefore, it may be suggested that coordinatively unsaturated ferrous (CUF) species are formed along the interface of Rh and Fe_xO_y. The WGSR proceeds via the following mechanism in which water adsorbs and dissociates at a surface vacancy (*) which may be a CUF site (Eqn. 7.11). CO then adsorbs on the lattice oxide ion (O_{latt}) to give gaseous CO_2 (Eqn. 7.12). In the meantime, the CUF site is regenerated.

$$H_2O + * \rightarrow 2OH\ (a) \rightarrow 2O_{latt} + H_2\ (g) \qquad (7.11)$$

$$CO + O_{latt} \rightarrow CO_2\,(a) \rightarrow CO_2\,(g) + * \quad (7.12)$$

The enhanced catalytic activity promoted by Fe_xO_y has been reported by various research bodies especially for selective oxidation of CO using Pt-Fe/Al_2O_3 [26, 27]. It was said that the Fe_xO_y species provide additional oxygen adsorption sites for the oxygen and enhances the activity. Our findings can be drawn parallel to a recent report by Fu et al. who identified the coordinatively unsaturated ferrous (CUF) species formed at the boundaries between FeO_x and the Pt (111) surface as the active sites for CO oxidation [28]. In comparison to the un-promoted Pt active sites, the CO adsorption energy on the CUF sites is smaller such that CO poisoning on FeO/Pt is minimized. Instead, oxygen activation occurs easily at CUF sites, facilitating the reaction between the oxygen and the adsorbed CO on Pt.

7.5. Conclusions

It was shown in this study that Fe promoted Rh/Ca-Al_2O_3 increases the hydrogen yield and lowers CO selectivity. The iron oxide loading was optimized at 10 wt% with negligible CO selectivity at a low temperature of 623 K. Rh-Fe/Ca-Al_2O_3 catalyst promotes WGSR during low temperature ESR. In addition, the catalytic lifespan of Rh-Fe/Ca-Al_2O_3 is extended significantly in comparison to that of Rh/Ca-Al_2O_3. DRIFTS analysis of adsorbed CO shows that the addition of iron oxide minimizes CO poisoning on the Rh catalysts through the formation of formate species and thus prolongs its activity. Coke formation was also found

to be lower on Rh-Fe/Ca-Al_2O_3 catalyst. XPS and XANES measurements suggest the presence of Fe_xO_y species, which are responsible for the mitigation of CO poisoning of Rh.

7.6. References

[1] C. Song, Catal. Today 77 (2002) 17-49.

[2] S. Chalk, J. Miller, F. Wagner, J. Power Sources. 86 (2000) 40-51.

[3] M. Debe, Nature. 486 43-51.

[4] K. Vasudeva, N. Mitra, P. Umasankar, S.C. Dhingra, Int. J. Hydrogen Energy. 21 (1996) 13-18.

[5] I. Fishtik, A. Alexander, R. Datta, D. Geana, Int. J. Hydrogen Energy. 25 (2000) 31-45.

[6] V. Mas, R. Kipreos, N. Amadeo, M. Laborde, Int. J. Hydrogen Energy. 31 (2006) 21-28.

[7] A. Basagiannis, P. Panagiotopoulou, X. Verykios, Top. Catal. 51 (2008) 2-12.

[8] P. Ciambelli, V. Palma, A. Ruggiero, Appl. Catal. B: Environ. 96 18-27.

[9] Z. Zhong, H. Ang, C. Choong, L. Chen, L. Huang, J. Lin, Phys. Chem. Chem. Phys. 11 (2009) 872-880.

[10] H. Roh, Y. Wang, D. King, A. Platon, Y. Chin, Catal. Lett. 108 (2006) 15-19.

[11] D. Rethwisch, J. Dumesic, J. Catal. 101 (1986) 35-42.

[12] S. Natesakhawat, X. Wang, L. Zhang, U.S. Ozkan, J. Mol. Catal. A: Chem. 260 (2006) 82-94.

[13] D. Andreeva, V. Idakiev, T. Tabakova, A. Andreev, R. Giovanoli, Appl. Catal. A: Gen. 134 (1996) 275-283.

[14] P. Fornasiero, R. Dimonte, G.R. Rao, J. Kaspar, S. Meriani, A. Trovarelli, M. Graziani, J. Catal. 151 (1995) 168-177.

[15] H. Lin, Y. Chen, C. Li, Thermochim. Acta. 400 (2003) 61-67.

[16] A. Wielers, A. Kock, C. Hop, J. Geus, A. van Der Kraan, J. Catal. 117 (1989) 1-18.

[17] W. Chen, Y. Ding, X. Song, T. Wang, H. Luo, Appl. Catal. A: Gen. 407 231-237.

[18] A. Kock, H. Fortuin, J. Geus, J. Catal. 96 (1985) 261-275.

[19] H. Wan, B. Wu, C. Zhang, H. Xiang, Y. Li, B. Xu, F. Yi, Catal. Commun. 8 (2007) 1538-1545.

[20] T. Yamashita, P. Hayes, Appl. Surf. Sci. 254 (2008) 2441-2449.

[21] C. Yang, C.W. Garl, J. Phys. Chem. 61 (1957) 1504-1512.

[22] S. Chuang, R. Stevens, R. Khatri, Top. Catal. 32 (2005) 225-232.

[23] F. Solymosi, A. Erdöhelyi, Surface Science Letters. 110 (1981) L630-L633.

[24] M. Virginie, M. Araque, A.-C. Roger, J.C. Vargas, A. Kiennemann, Catal. Today 138 (2008) 21-27.

[25] Y. Li, M. Bowker, Surface Science. 285 (1993) 219-226.

[26] X. Liu, O. Korotkikh, R. Farrauto, Appl. Catal. A: Gen. 226 (2002) 293-303.

[27] A. Sirijaruphan, J.G. Goodwin Jr, R.W. Rice, J. Catal. 224 (2004) 304-313.

[28] Q. Fu, W. Li, Y. Yao, H. Liu, H. Su, D. Ma, X. Gu, L. Chen, Z. Wang, H. Zhang, B. Wang, X. Bao, Science. 328 1141-1144.

Chapter 8

Effect of Support over Rh-Fe Catalysts for Water Gas Shift Reaction in Ethanol Steam Reforming

Graphical Abstract

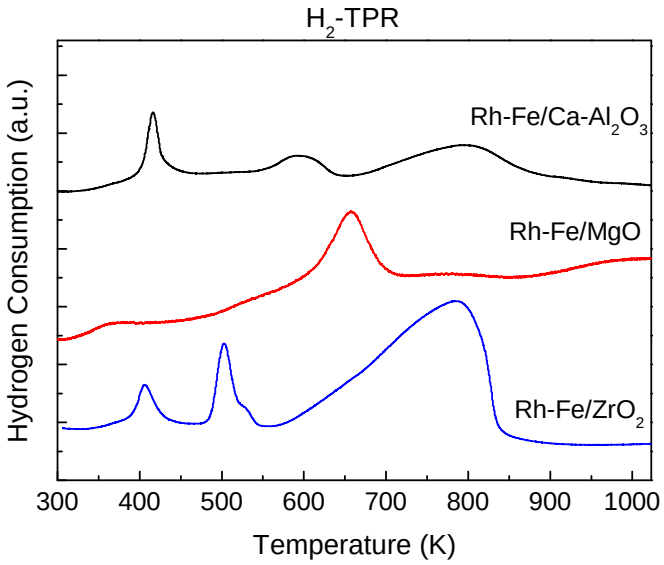

Iron modified Rh catalysts supported on different metal oxides (Ca-Al_2O_3, MgO and ZrO_2) were investigated for low temperature ethanol steam reforming (ESR). Comparative studies with their Fe-free counterparts were investigated at 623 K. The catalysts were characterized by X-ray diffraction, X-ray photoelectron spectroscopy, temperature programmed reduction and diffuse reflectance infrared Fourier transform spectroscopy. A support-dependent effect was found for the decreased selectivity to CO due to water-gas shift reaction during ESR. The difference could be attributed to the influence of metal-support interaction on the

chemical state of iron oxide which in turn determines the formation of coordinatively unsaturated ferrous (CUF) sites. These CUF sites facilitate the conversion of CO to CO_2 and promote water activation.

8.1. Introduction

Previously in Chapter 7, we have shown a synergistic effect between Rh, Fe and Ca-Al_2O_3 during ESR. Fe-promoted Rh catalyst supported on Ca-Al_2O_3 enhances the WGSR and decreases coke formation significantly. By changing the catalyst bed configuration, we confirmed that intimate interaction between Rh and Fe is required for high catalytic activity, low CO selectivity and good stability. The Rh-Fe interaction leads to the formation of coordinatively unsaturated ferrous (CUF) active sites which are responsible for the conversion of CO to CO_2 during low temperature ESR. The chemical states of iron are thus important in this catalytic system.

In catalysis, metal-support interaction plays an important role in governing the catalytic activity. For example, the metal-support effect has been studied using Fe promoted Rh catalysts for CO hydrogenation for ethanol production [1, 2]. The metal-support interaction influences the reduction behavior of the active metal. For supported iron oxide catalysts, investigations on the reduction behavior of iron oxides have shown that the nature of the catalyst support strongly affects the final chemical state of iron [3]. Wan et al. studied the effect of Al_2O_3 on the reducibility of iron oxide [4]. They found that the phase transformations of Al_2O_3 supported iron oxide catalyst during temperature programmed reduction (TPR) process are $Fe_2O_3 \rightarrow Fe_3O_4 \rightarrow FeO$. The formation of metallic Fe was retarded due to the strong Fe-Al_2O_3 interaction. With Fe/MgO system prepared by Boudart et al., solid solution $Fe_xMg_{1-x}O$ was detected and only half of the iron in iron oxide/MgO could be reduced to metallic Fe at 700 K

[5]. The formation of solid solution during calcination could possibly stabilize some of the iron in Fe^{2+} state, resulting in minimal metallic iron formation [6]. Investigation on the reduction behavior of zirconia supported iron oxide catalysts using TPR and *in situ* Mössbauer spectroscopy revealed that the reducibility of the iron oxide species depends on the type of iron oxide species on the surface and their interactions with the support [7].

Since iron has a profound effect on the selectivity of CO in ESR, in this chapter, we will study the important roles of support (Ca-Al_2O_3, MgO and ZrO_2) and Fe promotion on these Rh supported catalysts. Interaction between supports was discussed based on results from X-ray diffraction, X-ray photoelectron spectroscopy, temperature programmed reduction and diffuse reflectance infrared Fourier transform spectroscopy.

8.2. Experimental

8.2.1. Catalysts Synthesis

The Rh–Fe/Ca–Al_2O_3 catalyst was prepared by a sequential incipient wetness impregnation method, following the steps given below: (1) Ca-modified alumina, denoted as Ca-Al_2O_3, was prepared by the calcination of a paste of γ-Al_2O_3 (Merck, 103 m^2/g) impregnated with $Ca(NO_3)_2 \cdot 4H_2O$ (Riedel–deHaën) solution. (2) The obtained Ca-Al_2O_3 powder was impregnated with an appropriate amount of $Fe(NO_3)_3$ solution to get a precursor with Fe loading of 10 wt. %. The precursor was dried at 393 K for 10 h and heated to 723 K in air and then held for

5 h. (3) By impregnation with a $RhCl_3$ solution (Alfa Aesar), 1 wt. % of Rh was introduced into the powder obtained in step (2). The obtained catalyst was dried and calcined in the same manner as in step (2) and is denoted as Rh–Fe/Ca–Al_2O_3. Rh-Fe catalysts on different supports such as MgO (Sigma Aldrich), SiO_2(Sigma Aldrich)and ZrO_2 (Spectro), were also prepared, following steps (2) and (3).

8.2.2. Fixed Bed Catalytic Testing

The catalytic evaluation was performed in a customized 5-channels quartz micro-reactor (BEL, Japan), each of which was loaded with 100 mg of the catalyst. The temperature of the samples was individually monitored with thermocouples located just on top of the catalyst samples.

Prior to the reaction, catalysts were reduced in pure H_2 with a flow of 50 ml min^{-1} at 473 K for 0.5 h. Then, 40 ml min^{-1} of Ar was flown in, along with 0.005 ml min^{-1} of ethanol-water mixture (1:10 molar ratio) which was injected using a Shimadzu Liquid Pump and vaporized at 443 K within the reactor. The total gas hourly space velocity (GHSV) was kept constant at 34,000 h^{-1}, using a mass flow controller. The reaction products were analyzed online by a gas chromatograph (Varian CP-3800) with three columns: Porapak Q, Haysep Q and molecular sieve 5A. Porapak Q was used to separate organics and carbon dioxide with He as carrier gas while the later two columns were used for the separation of hydrogen, carbon monoxide and methane with Ar as carrier gas. Conversion of

ethanol (X_{EtOH}) and selectivity to carbon-containing species (S_{Ci}) were calculated Eqns. 3.5 and 3.6 in Chapter 3, respectively.

8.2.3. Catalysts Characterization

Powder X-ray diffraction (XRD) patterns were collected with a Bruker D8 X-ray diffraction system equipped with Cu Kα radiation ($\lambda = 0.154$ nm). The profiles were collected at a step width of 0.02° in the (2θ) range from 20° to 90°. X-ray photoelectron spectroscopy (XPS) was performed on a VG ESCALAB 250 spectrometer using an Mg Kα radiation source. The XPS data of the catalysts were obtained after *in situ* H_2 reduction inside the XPS chamber at 473 K for 0.5 h. The XPS data were processed with respect to the adventitious carbon C1*s* peak at 284.5 eV.

In situ diffuse reflectance infrared Fourier transform spectroscopy (DRIFTS) study of surface hydroxyls and CO adsorption was carried out in a Bio-Rad FT-IR 3000 MX with a mercury-cadmium-telluride (MCT) detector. A powder sample was put into a reaction cell (Harricks HV-DR2) and reduced under the same conditions as for the activity test. Spectra with a resolution of 4 cm^{-1} were taken after reduction and the resulting spectra were obtained after subtraction of KBR background. For DRIFTS study of CO adsorption, a flow of 1% CO/He was introduced at room temperature after the sample after the reduction. Spectra with a resolution of 4 cm^{-1} were taken after CO had been adsorbed for 20

min and purged for 1 h. The spectrum of the clean sample taken after reduction was used as reference.

Temperature programmed reduction (TPR) measurements were carried out on Thermo Scientific TPROD 1100. 100 mg of calcined catalysts, which had been thermally treated under Ar stream at 773 K to remove water and other contaminants, were heated from 303 K to 1123 K at a rate of 10 K min^{-1} in 50 ml min^{-1} of 5% H_2/Ar and maintained at 1023 K for 15 min while the hydrogen consumption was monitored.

8.3. Results

8.3.1. Catalytic Performance

8.3.1.1. Catalytic Performance of Rh-Fe/Ca-Al_2O_3, Rh-Fe/MgO and Rh-Fe/ZrO_2 catalysts

The effect of catalyst support on the enhanced WGSR during ESR is investigated using Rh-Fe catalyst supported on various oxides. In Table 8.1, the ESR activities of Rh and Rh-Fe supported on various supports are compared at 623 K. On Rh/Ca-Al_2O_3, major products include CO_2, CH_4 and CO with selectivity of 16.7%, 47.0% and 36.4% respectively. Ethanol conversion of 93.4% is attained with Y_{H2} of 3.6 mol at 623 K. On Fe promoted Rh/Ca-Al_2O_3 catalyst, S_{CO} is reduced to 0%, with CO_2 and CH_4 at 60.3% and 39.7% respectively. Previous results have concluded that the presence of Fe promotes the WGSR,

which reduces the S_{CO} considerably at low temperature ESR. Hydrogen yield of 4.1 mol also increases over Rh-Fe/Ca-Al_2O_3. The product distribution of Rh/MgO shows that ESR at 623 K produces S_{CO2} of 3.3%, S_{CH4} of 29.4%, S_{CO} of 41.7% and S_{CH3CHO} of 25.0%. Ethanol conversion is 38.2%, producing 1.1 mol of H_2. The poor activity over Rh/MgO can be attributed to the basic nature of MgO, resulting in the main reaction being dehydrogenation of ethanol in CH_3CHO [8]. In addition, the strong interaction between rhodium oxide and MgO makes the reduction of Rh_2O_3 to metallic Rh more difficult than Rh/Ca-Al_2O_3 [9]. This diminishes the number of Rh active sites for C-C bond break during ESR. Fe promoted Rh/MgO catalyst shows an improvement in the activity with X_{EtOH} of 88.8% and Y_{H2} of 3.5 mol. Selectivity of CO is reduced to 24.9% and accompanied by S_{CO2} of 36.0%, S_{CH4} of 32.7% and S_{CH3CHO} of 5.9%. Similar to Rh-Fe/Ca-Al_2O_3, the WGSR is promoted in the presence of Fe on MgO support but the effect is less obvious on MgO since S_{CO} is quite considerable at 623 K. On Rh/ZrO_2, major products are CO_2 (S_{CO2} = 55.2%) and CH_4 (S_{CH4} = 35.5%) with S_{CO} = 9.3%. A hydrogen yield of 4.3 mol is achieved with 100% X_{EtOH}. On Fe promoted Rh/ZrO_2 catalyst, selectivity is 47.2% to CO_2, 32.8% to CH_4 and 17.2% to CO and Y_{H2} is 4.2 mol. At this instance, it is interesting to note that the Fe promotion effect in reducing S_{CO} is not observable on Rh-Fe/ZrO_2. In fact, the presence of Fe seems to deteriorate the performance of Rh/ZrO_2, giving a higher S_{CO} and lower hydrogen yield than Rh/ZrO_2.

The results in Table 8.1 shows that the ESR activity of Fe-free Rh catalyst decreases in the following order: Rh/ZrO_2 > Rh/Ca-Al_2O_3 > Rh/MgO and CO

selectivities decrease in the order Rh/Ca-Al_2O_3 > Rh/MgO > Rh/ZrO_2 at 623 K. On Fe promoted catalysts, the performance of Rh-Fe catalyst is the similar descending order of Rh-Fe/ZrO_2 > Rh-Fe/Ca-Al_2O_3 > Rh-Fe/MgO. Water gas shift activity can be observed over Rh-Fe/Ca-Al_2O_3 and Rh-Fe/MgO where CO is significantly reduced and hydrogen yield is enhanced. The enhanced ESR is due to the WGSR in the presence of Fe, as previously discussed in Chapter 7.

Table 8.1. Catalytic performance of Rh and Rh-Fe catalysts on various supports for ethanol steam reforming at 623 K.

Catalyst	X_{EtOH} (%)	Y_{H2} (mol)	Product distribution (%)				
			S_{CO2}	S_{CO}	S_{CH4}	S_{C2H4}	S_{CH3CHO}
Rh/Ca-Al_2O_3	93.4	3.6	16.7	47.0	36.4	0.0	0.0
Rh-Fe/Ca-Al_2O_3	100	4.1	60.3	0.0	39.7	0.0	0.0
Rh/MgO	38.2	1.1	3.3	41.7	29.4	0.6	25.0
Rh-Fe/MgO	88.8	3.5	36.0	24.9	32.7	0.5	5.9
Rh/ZrO_2	100	4.3	55.2	9.3	35.5	0	0
Rh-Fe/ZrO_2	99.1	4.2	47.2	17.2	32.8	0	2.8

8.3.1.2. Influence of Steam/Ethanol (S/E) ratio

The effect of steam/ethanol (S/E) molar ratio (3:1 to 13:1) on the catalytic activity of ESR is investigated at 623 K using Rh-Fe/Ca-Al_2O_3 and Rh-Fe/MgO catalysts. Fig. 8.1(a) shows the product distribution of ESR at 623 K as a function S/E over Rh-Fe/Ca-Al_2O_3 catalysts. Several products such as H_2, CO, CO_2, CH_4 and C_2H_4 are observed. Increasing S/E from 3 to 13 shows a decrease in CO selectivity from 33.1% to 1.4%. An increase of CO_2 from 37.3% to 62.2% together with the increase of H_2 is observed concurrently as the partial pressure of steam increases. A plot of S_{CO}/S_{CO2} against temperature (573 K < T < 673 K) in Fig. 8.1(b) shows that the WGSR is most active between 623 K and 673 K, especially at higher S/E molar ratio. This illustrates that the presence of higher steam concentration is effective in promoting WGSR.

On Rh-Fe/MgO catalyst, ESR produces CH_3CHO in addition to the products observed from Rh-Fe/Ca-Al_2O_3 catalyst (Fig. 8.2(a)). This is due to the strong basic sites of MgO which promote dehydrogenation of ethanol to CH_3CHO. It is clear that while increasing S/E molar ratio from 3 to 13 reduces the CO selectivity from 41.4% to 33.8%, CO selectivity still remains relatively higher than Rh-Fe/Ca-Al_2O_3 catalyst at 623 K. Fig. 8.2(b) shows that S_{CO}/S_{CO2} of Rh-Fe/MgO is higher than Rh-Fe/Ca-Al_2O_3 for the same S/E used in the experiment. For example, at 623 K, S_{CO}/S_{CO2} of Rh-Fe/MgO is 1.6 whereas the value is 0.02 for Rh-Fe/Ca-Al_2O_3. This shows that even a high S/E molar ratio (i.e. S/E=13) is unable to remove CO from the product stream via WGSR over Rh-Fe/MgO catalysts. In another words, Rh-Fe/MgO has poorer water activation ability than

supported on Ca-Al_2O_3 catalyst. Rh-Fe/Ca-Al_2O_3 promotes water activation which facilitates the WGSR at low temperature.

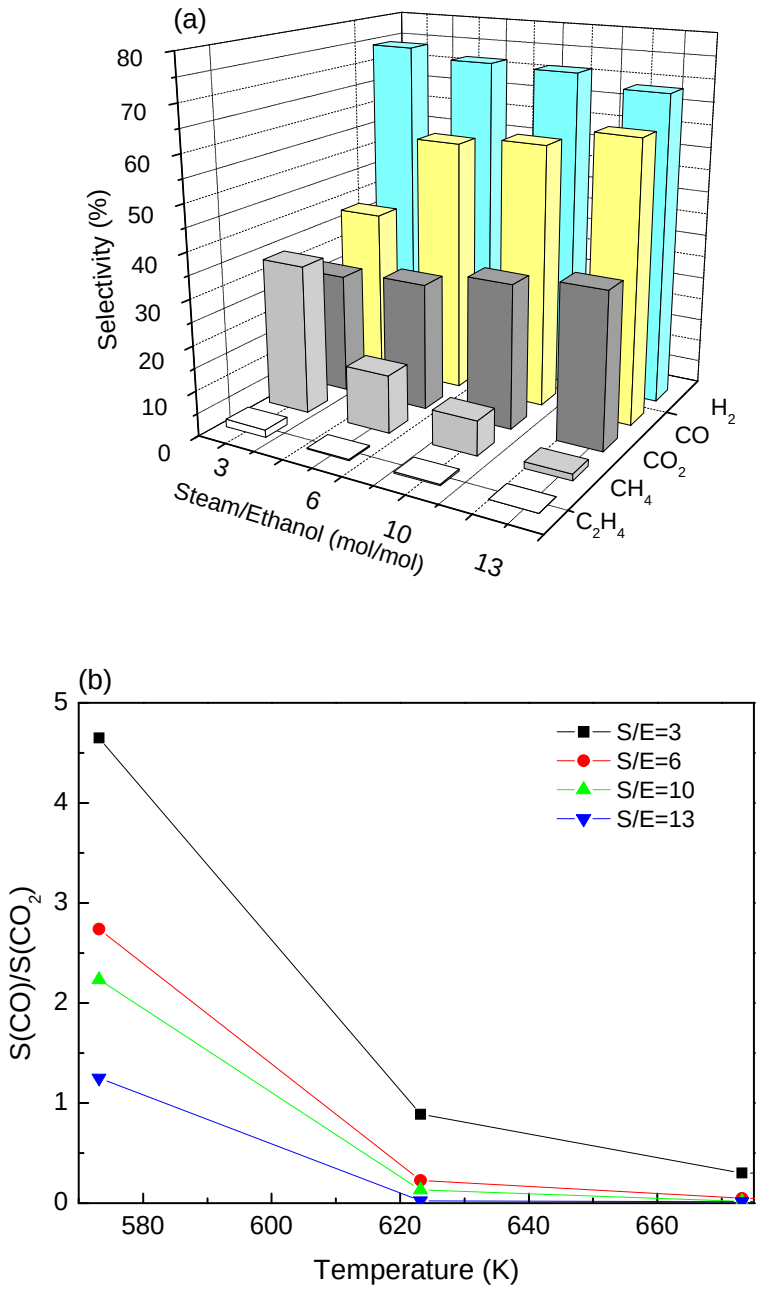

Figure 8.1. Plot of (a) ESR product distribution over Rh-Fe/Ca-Al_2O_3 as a function of steam/ethanol (S/E) molar ratio at 623 K and (b) S_{CO}/S_{CO2} as a function of S/E molar ratio and temperature.

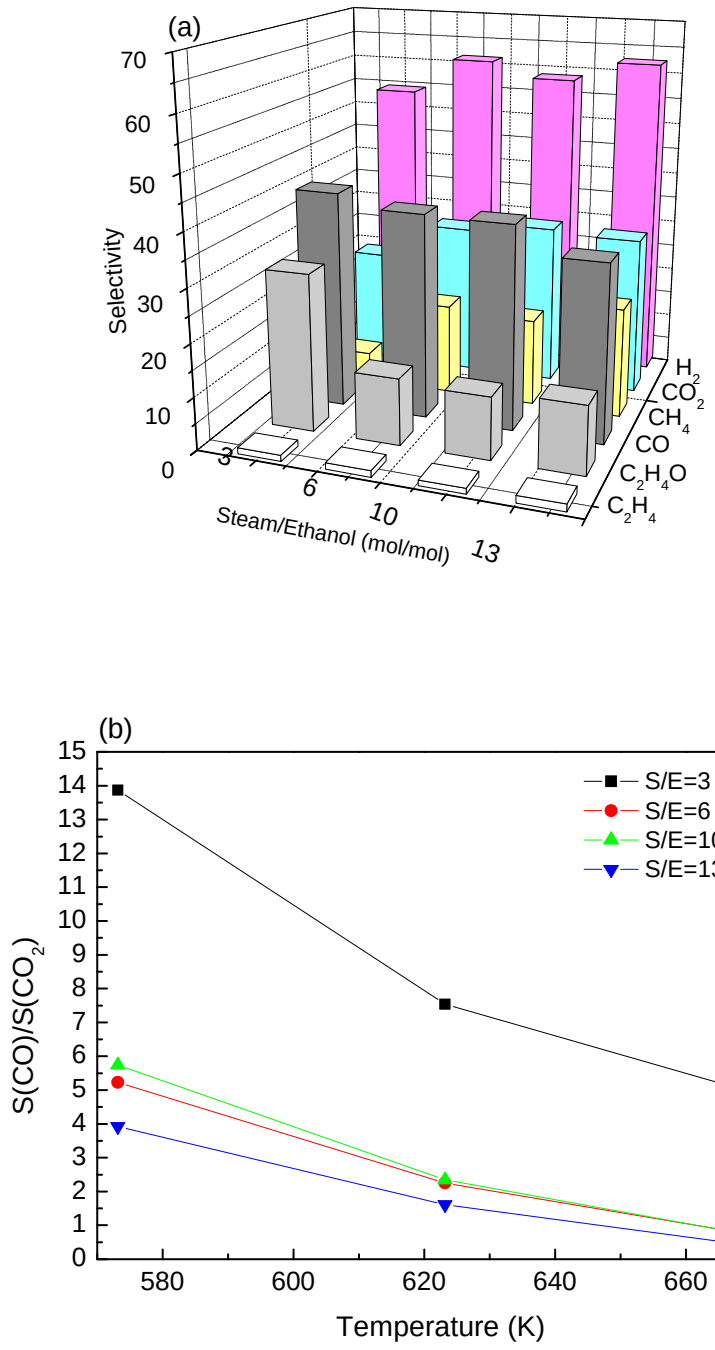

Figure 8.2. Plot of (a) ESR product distribution over Rh-Fe/MgO as a function of steam/ethanol (S/E) molar ratio at 623 K and (b) S_{CO}/S_{CO2} as a function of S/E molar ratio and temperature.

8.3.2. Catalysis Characterization

8.3.2.1. BET and XRD

The textural properties (S_{BET}, pore volume (V_p), pore diameter (D_p)) of the Rh and Rh-Fe catalysts on different supports are summarized in Table 8.2. In general, textural data in Table 8.2 shows that the surface area of Rh catalysts increase slightly after the addition Fe to the catalysts. This could be due to the formation of amorphous Fe oxide or Fe–Al (Mg or Zr) oxides on the surface of the support. The surface area of Rh-Fe catalysts decrease in the following order: Rh-Fe/Ca-Al_2O_3 > Rh-Fe/MgO > Rh-Fe/ZrO_2.

Table 8.2. BET surface area of Rh and Rh-Fe catalysts on various supports.

Catalyst	S_{BET} (m^2/g)	V_p (cm^3/g)	D_p (nm)
Rh/Ca-Al_2O_3	90.5	0.24	9.8
Rh-Fe/Ca-Al_2O_3	94.3	0.22	8.2
Rh/MgO	85.7	0.66	25.9
Rh-Fe/MgO	91.3	0.53	18.5
Rh/ZrO_2	7.6	0.05	26.0
Rh-Fe/ZrO_2	8.3	0.05	22.6

The XRD patterns of the prepared catalysts are shown in Fig. 8.3. Rh-Fe/Ca-Al_2O_3 showed the characteristic peaks of Al_2O_3 ($2\theta = 37.4^o, 45.6^o, 67.2^o$).

Crystalline phases of Fe_2O_3 are also observed (2θ = 24.2°, 33.2°, 35.7°, 49.6°, 54.2°). Similar Fe_2O_3 crystalline phases are detected along side with the diffraction peaks of monoclinic ZrO_2 (2θ = 28.2°, 31.4°, 34.1°) on Rh-Fe/ZrO_2. On Rh-Fe/MgO, only peaks characteristic of MgO (2θ = 37.0°, 41.8°, 60.6°, 72.6°, 76.4 °) phase were reflected. The absence of Fe_2O_3 diffraction peaks may suggest the formation of iron oxide-MgO solid solution. No Rh diffraction peaks are identified from the XRD patterns, due to the low concentration.

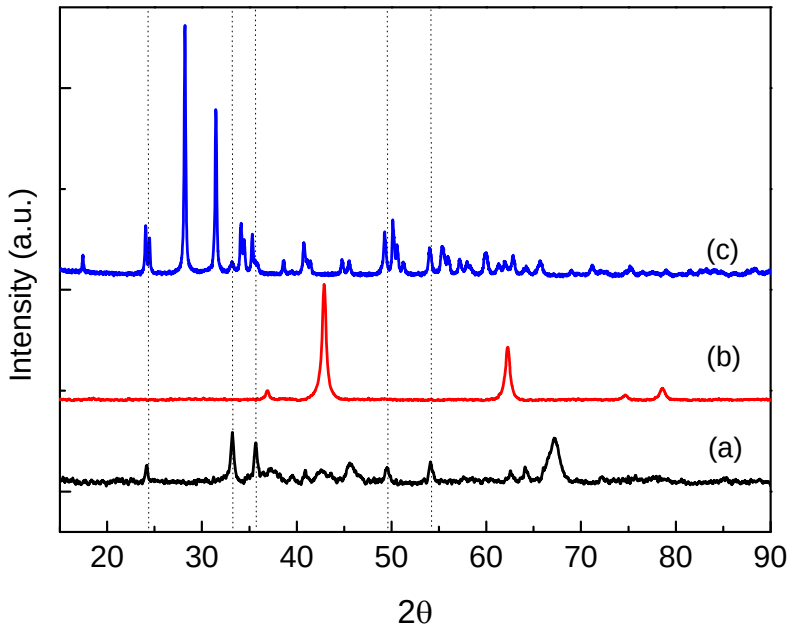

Figure 8.3. XRD patterns of (a) Rh-Fe/Ca-Al_2O_3; (b) Rh-Fe/MgO and (c) Rh-Fe/ZrO_2. Dotted lines correspond to the diffraction bands of Fe_2O_3.

8.3.2.2. Temperature-programmed reduction (TPR)

The TPR profiles of Rh-Fe catalysts supported on different metal oxides are shown in Fig. 8.4 and the H_2 consumptions per mol of metal were tabulated in

Table 8.3. As shown in Chapter 7, four reduction peaks at 416 K, 510 K, 595 K and 798 K are observed on Rh-Fe/Ca-Al_2O_3 catalyst. Based on the calculation of H_2 consumption, at 416 K, the sharp reduction peak is assigned to both the reduction of Rh_2O_3 to Rh metallic and reduction of iron oxide. Together with the peaks at 510 K and 595 K, they may be assigned to the reduction of Fe_2O_3 → Fe_3O_4 and the latter peak at 798 K corresponds to the reduction of Fe_3O_4 → FeO. Reduction beyond Fe^{2+} state is difficult probably due to the strong interaction of iron oxides with the Ca-Al_2O_3 support. The TPR profiles of Rh-Fe/MgO show three peaks at 365 K, 660 K and 972 K. The reduction peaks at 365K and 660 K mainly corresponds to the reduction of Rh_2O_3 to Rh based on hydrogen consumption. The higher reduction temperature of Rh_2O_3 can be attributed to the formation of $MgRh_2O_4$ compound as Rh interacts with MgO support during calcinations [10]. Fe_2O_3 starts reducing to Fe_3O_4 at 660 K and is fully reduced to Fe_3O_4 by 1023 K. This indicates that the interaction between iron oxide with MgO is even stronger than iron oxide and Ca-Al_2O_3 interaction since iron oxide on Rh-Fe/MgO can only be reduced to Fe_3O_4 within the experimental range. On Rh-Fe/ZrO_2, the reduction peaks are more defined. The first reduction peak occurs at 407 K and is assigned to reduction of Rh_2O_3. The second peak at 510 K involves the reduction of Fe^{3+} to Fe^{2+} while the broad peak at 785 K corresponds to the reduction of Fe_3O_4→ FeO → Fe. This signifies that the interaction of iron oxide on ZrO_2 is weaker, suggesting a poor dispersion of iron oxide on Rh-Fe/ZrO_2 catalyst.

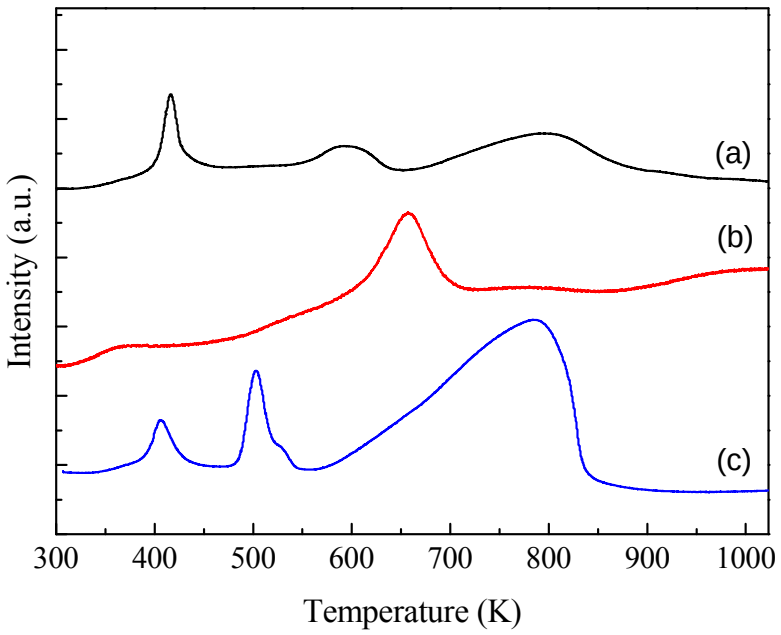

Figure 8.4. TPR profiles of (a) Rh-Fe/Ca-Al_2O_3; (b) Rh-Fe/MgO and (c) Rh-Fe/ZrO_2.

Table 8.3. Tabulation of consumption of H_2 per mole of metal (mol/mol) over Rh/Ca-Al_2O_3, Rh-Fe/MgO and Rh-Fe/ZrO_2 catalysts.

Catalyst	Tmax (K)	mol H_2/ mol Rh	mol H_2/ mol Fe
Rh-Fe/Ca-Al_2O_3	416	1.46	
	510		0.15
	595		0.17
	798		0.15
Rh-Fe/MgO	365	0.19	
	660	1.26	0.07
	972		0.08

Rh-Fe/ZrO_2	407	1.49	
	510		0.12
	785		0.79

8.3.2.3. X-ray spectroscopy (XPS)

The XPS spectra of Rh-Fe catalysts illustrate the oxidation state of iron oxides after reduction at 473 K for 0.5 h. XPS peaks of Fe $2p_{3/2}$ are typically located at 711.2, 709.8 and 706.8 eV for Fe^{3+}, Fe^{2+} and Fe^0, respectively [11]. Evidence from XPS Fe 2p spectra in Fig. 8.5(a) shows binding energies of 711.2 eV and 710.5 eV on reduced Rh-Fe/Ca-Al_2O_3. The premier corresponds to Fe^{3+} species. Since the binding energy of 710.5 eV is higher than that of Fe^{2+} species, it is likely Fe_xO_y species consisting of a mixture of Fe^{3+} and Fe^{2+} species are observed on the surface. Similar observations are noted for Rh-Fe/MgO where Fe^{3+} and Fe_xO_y species are detected at 711.2 eV and 710.5 eV, respectively. Given the poorer iron oxide and support interaction as observed from TPR (Fig. 8.4), one would expect that iron oxides are easier to be reduced on ZrO_2 than Ca-Al_2O_3 and MgO. Indeed, a lower Fe 2p binding energy of 710.0 eV Fig. 8.5(c)) is observed on Rh-Fe/ZrO_2 than on the other two catalysts. This can be assigned to the presence of Fe^{2+} species. However, it was determined in a recent study by Wu et al. that the binding energy of Fe $2p_{3/2}$ shift to a higher value than Fe^0 and was assigned to the formation of PdFe alloy like clusters [12] . RhFe alloy has also been observed on SiO_2 support using Mossbauer spectroscopy [13, 14]. Since, our XPS Rh 3d spectrum of reduced Rh-Fe/ZrO_2 shows that most of the Rh atoms are

in the reduced state, the formation of RhFe alloy can occur when part of the reduced Fe^0 comes into contact with Rh^0. Thus, the binding energy at 710.0 eV may be attributed to the formation of RhFe alloy on ZrO_2 support. TEM images may also suggest the formation of RhFe alloy. TEM image of reduced Rh/ZrO_2 in Fig. 8.6(a) shows that the Rh is deposited as dispersed particles on ZrO_2 while on TEM of reduced $Rh\text{-}Fe/ZrO_2$ (Fig. 8.6(b)) shows the lack of such individual Rh particles.

From XPS analysis, we may conclude that Fe_xO_y species consisting of a mixture of Fe^{3+} and Fe^{2+} species are observed on the surface of $Rh\text{-}Fe/Ca\text{-}Al_2O_3$ and Rh-Fe/MgO catalysts. Iron oxides, which are largely Fe_2O_3, are also present on the surface of $Rh\text{-}Fe/ZrO_2$. However, TPR suggests that the poor iron oxides and support interaction on $Rh\text{-}Fe/ZrO_2$ catalyst promotes the reducibility of iron oxide and favors the formation of RhFe alloy. These alloy clusters, however, are less preferred surface sites as opposed to Fe_xO_y species.

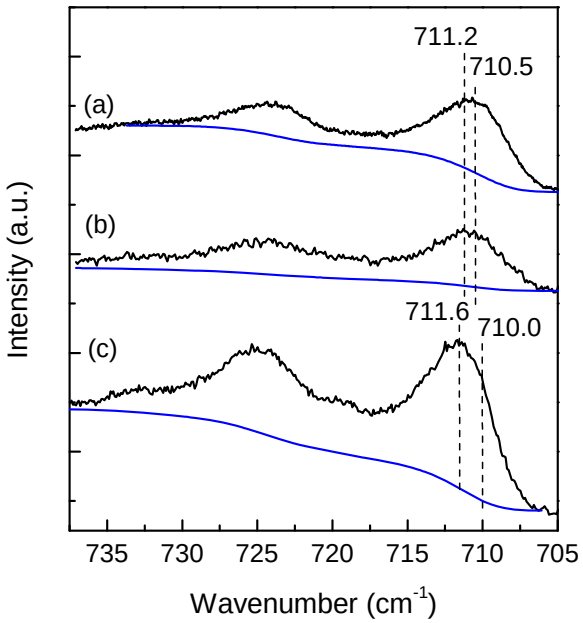

Figure 8.5. XPS Fe 2p spectra of reduced (a) Rh-Fe/Ca-Al_2O_3; (b) Rh-Fe/MgO and (c) Rh-Fe/ZrO_2.

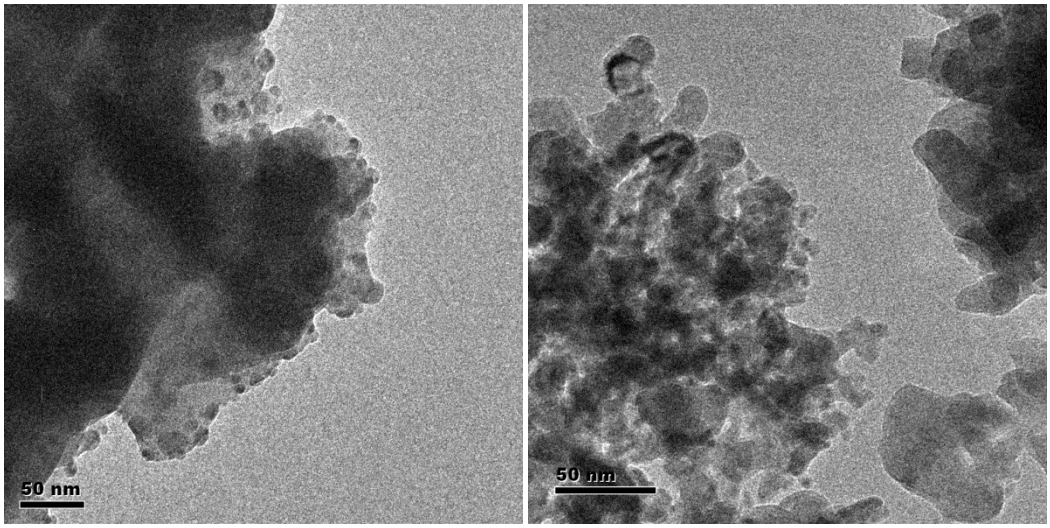

Figure 8.6. TEM images of reduced (a) Rh/ZrO_2 and (b) Rh-Fe/ZrO_2 catalysts.

8.3.2.4. DRIFTS measurements of surface hydroxyls

Catalytic results from varying S/E ratio (section 8.3.1.2) have shown that surface hydroxyls and/or water activation sites are necessary for promoting WGSR in the presence of Fe. Results in Chapter 7 have shown the importance of surface hydroxyls through different catalytic bed configuration. Diffuse reflectance infrared Fourier transformed spectroscopy (DRIFTS) is used to examine the stretching vibrations of surface hydroxyls and coordinated water molecules of Rh-Fe catalysts on different supports. In Fig. 8.7, after reduction of catalyst in H_2 for 2 h, the OH stretching region of Rh-Fe/Ca-Al_2O_3 shows an IR peak at 3680 cm^{-1} which can be assigned as type III hydroxyls involving three octahedrally coordinated Al^{3+} ions. Hydrogen-bonded surface hydroxyls are in abundance as seen from the broad IR peak centered at 3500 cm^{-1}. The OH stretching bands located at 3750 cm^{-1} and 3710 cm^{-1} observed on Rh-Fe/MgO catalysts corresponding to the presence of isolated surface hydroxyls. On reduced Rh-Fe/ZrO_2 catalyst, only one hydroxyl group with weak IR band of 3750 cm^{-1} is clearly visible. This may be assigned to OH group bonded to one Zr ion [15]. The lack of hydrogen bonded surface hydroxyls at 3480 cm^{-1} indicates the hydrophobic nature of ZrO_2, hinting towards poor water activation ability. DRIFTS measurements show that availability of the surface hydroxyls decreases in the order of Rh-Fe/Ca-Al_2O_3 > Rh-Fe/MgO > Rh-Fe/ZrO_2.

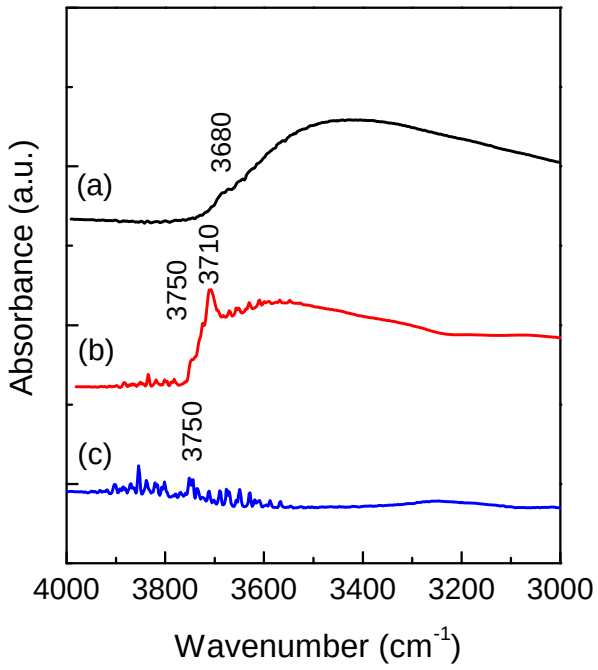

Figure 8.7. DRIFTS spectra of catalysts (a) Rh-Fe/Ca-Al_2O_3; (b) Rh-Fe/MgO and (c) Rh-Fe/ZrO_2.

8.3.2.5. DRIFTS of adsorbed CO

In situ DRIFTS analysis was conducted to observe the surface species after CO adsorption on Rh-Fe catalysts supported on different oxides. In particular, the presence of formate bands can be related to density of OH on the support [16]. The density of OH in turns depends on the water dissociation on vacant sites and thus the presence of formate species are also an indication of the availability of vacant sites on the catalyst surface. In Fig. 8.8(a), bands corresponding to ν_a(OCO) and ν_s(OCO) of formate species are registered at 1535 cm^{-1} and 1380 cm^{-1} over Rh-Fe/Ca-Al_2O_3. On Rh-Fe/MgO, formate species are

identified by absorbance bands at 1658 cm^{-1} and 1370 cm^{-1}. Absorbance peaks assigned to formate species located at 1590 cm^{-1} and 1350 cm^{-1} on Rh-Fe/ZrO_2 catalyst are barely visible. Various literatures have reported that the formate species are related to the density of OH on the support. Our results are in consistent with their argument as can be seen from Fig. 8.7 and Fig. 8.8. Formate species are seen on Rh-Fe/Ca-Al_2O_3 and Rh-Fe/MgO which have abundance of surface OH while limited concentration of surface OH on Rh-Fe/ZrO_2 restricts the formation of formate species on the catalyst. Since surface OH can also be formed from the dissociation of water at vacant sites and they react to give formate species, the results may also suggest that the oxygen vacancies are in larger quantities on Rh-Fe/Ca-Al_2O_3 and Rh-Fe/MgO than Rh-Fe/ZrO_2. These oxygen vacancies are likely to derive from the CUF sites found at the interface of Rh-Fe and their availability increases on the Rh-Fe catalysts in the order of: Rh-Fe/Ca-Al_2O_3 > Rh-Fe/MgO > Rh-Fe/ZrO_2.

On Rh-Fe/Ca-Al_2O_3 (Fig 8.8(a)), gem-dicarbonyl CO attached on single charged Rh^+ are observed with CO vibrations at 2095 and 2020 cm^{-1}. Similar gem-dicarbonyl species are observed on Rh-Fe/MgO with bands at 2080 and 2006 cm^{-1}. The spectrum also shows a bridge-bonded CO band at 1840 cm^{-1}. In the case of Rh-Fe/ZrO_2, gem-dicarbonyl species at 2086 and 2014 cm^{-1}, together with bridge-bonded CO at 1852 cm^{-1} are observed. In addition, a band at 2054 cm^{-1} is also noted. This band is attributed to linear-bonded CO on Rh. From the spectra, Rh^+ species are more readily available on Rh-Fe/Ca-Al_2O_3 > Rh-Fe/MgO > Rh-Fe/ZrO_2. The formation of Rh^+ species occurs via the oxidation of Rh^0 atoms.

Buchanan et al. reported that the presence of gem-dicarbonyl is the result of oxidation of Rh^0 by OH groups of the support [17]. This is consistent with our findings since Ca-Al_2O_3 possesses more surface hydroxyls than MgO and ZrO_2.

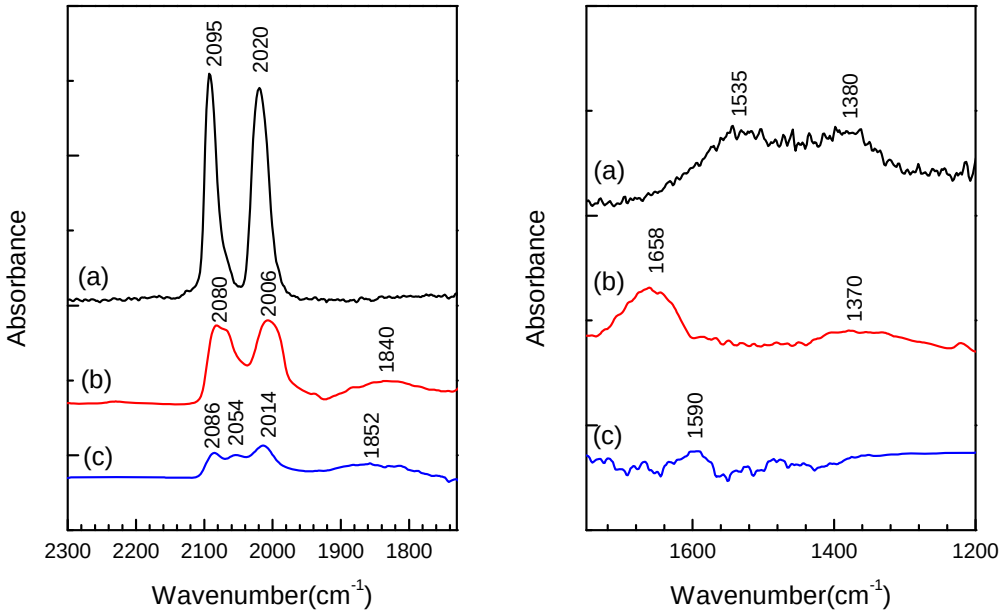

Figure 8.8. DRIFTS spectra after adsorption of CO on (a) Rh-Fe/Ca-Al_2O_3; (b) Rh-Fe/MgO and (c) Rh-Fe/ZrO_2.

8.4. Discussions

In this study, we probe the importance of support in facilitating this unprecedented removal of CO from ESR reformate stream, with emphasis placed on the chemical states of iron and their influence in water activation.

The results in Table 8.1 show that the ESR activity is enhanced in the presence of Fe over Rh/Ca-Al_2O_3 and Rh/MgO with Rh-Fe/Ca-Al_2O_3 being a

more superior catalyst. In comparison to the Fe-free Rh catalysts, CO selectivity is also depressed in the presence of Fe due to WGSR on both Ca-Al_2O_3 and MgO supports. This can be attributed to the formation of Fe_xO_y on these supports. TPR results suggest that strong iron oxide and support interaction occurs over Rh-Fe/Ca-Al_2O_3 and Rh-Fe/MgO as iron oxide can only be reduced to FeO and Fe_3O_4 on Rh-Fe/Ca-Al_2O_3 and Rh-Fe/MgO, respectively. As massive reduction of iron oxides to Fe^0 is hindered on Ca-Al_2O_3 and MgO supports, Fe_xO_y species are found on Ca-Al_2O_3 and MgO support, a conclusion also supported by *in situ* XPS results. The poorer catalytic performance of Rh-Fe/MgO may be attributed to the formation of $Fe_xMg_{1-x}O$ solid solution as suggested through TPR and XRD diffraction profiles. Furthermore, it is shown through TPR that the reduction of Rh_2O_3 to metallic Rh more difficult on than Rh-Fe/Ca-Al_2O_3, resulting in less available metallic Rh for C-C bond rupture.

Unlike Rh-Fe/Ca-Al_2O_3 and Rh-Fe/MgO catalysts, the activity of Rh-Fe/ZrO_2 is deteriorated with the addition of Fe and CO selectivity is higher than Rh/ZrO_2. Based TPR, iron oxides are easier to be reduced on ZrO_2 than the other two catalyst support which indicates that the interaction of iron oxide with ZrO_2 is weaker than Ca-Al_2O_3 and MgO. The surface area of ZrO_2 is relatively smaller than Ca-Al_2O_3 and MgO based on BET analysis, hence poorer dispersion of iron oxides is observed on ZrO_2 support. Given the increased reducibility of iron oxides observed from TPR as well as XPS analysis, part of the iron oxide can be reduced to Fe^0 and interacts with the Rh^0 atoms forming RhFe alloy clusters. The poorer ESR performance of Rh-Fe/ZrO_2 than Rh/ZrO_2 can be explained by the

formation of RhFe alloy clusters which is likely to proceed with Rh atoms diffusing into the iron oxide matrix [18]. This depletes the surface of active Rh sites for ESR.

Previously in Chapter 7, the catalytic performances of Rh and Fe catalysts placed in different configurations (Table 7.3) clearly indicate that, in order to achieve efficient CO removal via WGSR, the following rule-of thumb has to be followed: (1) Rh and Fe are required to be in close proximity and (2) surface hydroxyls and/or water activation sites are needed. This observation reinstates the importance of surface hydroxyls in this reaction. Intrinsically, decreasing density of surface hydroxyls on the different supports is observed from DRIFTS (Fig. 8.7) in the order of: Rh-Fe/Ca-Al_2O_3 > Rh-Fe/MgO > Rh-Fe/ZrO_2, which runs along with the diminishing WGSR during ESR. The lack of surface OH on ZrO_2 fails to provide the surface intermediate required for WGSR as seen from spectroscopic means (Fig. 8.7(c)). In addition to the intrinsic surface hydroxyls provided by the support, water activation is advantageous for ESR and WGSR as it further enhances the number of hydroxyl species on the support after dissociation. Surface water activation may occur on defect sites and on most metal oxides, the defects may be cation or anion vacancies [19-23]. CUF sites which are oxygen deficient may also act as defect sites for water activation. As previously discussed, CUF are found on Rh-Fe/Ca-Al_2O_3 and Rh-Fe/MgO and are almost negligible on Rh-Fe/ZrO_2. Thus it is expected that water activation occurs more readily in the following order: Rh-Fe/Ca-Al_2O_3 > Rh-Fe/MgO > Rh-Fe/ZrO_2. The surface hydroxyls produced from water activation on CUF sites can react with

adsorbed CO to form formate species through associative formate mechanism. Indeed, DRIFTS spectra of adsorbed CO in Fig. 8.8 indicate the formation of formate species with the intensities following the same decreasing order as above.

8.5. Conclusions

Ethanol steam reforming reactions were performed over Rh-Fe/Ca-Al_2O_3, Rh-Fe/MgO and Rh-Fe/ZrO_2 catalysts at 623 K. Comparing to the activities of their respective iron-free catalysts, catalytic performance is enhanced on Rh-Fe/Ca-Al_2O_3 and Rh-Fe/MgO with Rh-Fe/Ca-Al_2O_3 being more superior. CO selectivity was significantly reduced through WGSR over these catalysts, increasing hydrogen yield. Rh-Fe/ZrO_2 exhibited poorer catalytic activity than Rh/ZrO_2, with CO selectivity being higher than unpromoted catalyst. The support affects the chemical states of the iron oxide due to various degree of interaction between iron oxide, Rh and the support. The intimate metal-support interaction between iron oxides and MgO, led to formation of solid solution which reduces the amount of CUF sites and hence the WGSR promotion effect is weaker than the one over Rh-Fe/Ca-Al_2O_3 catalyst. WGSR promotion effect was not observed over Rh-Fe/ZrO_2 due to the formation of formation of RhFe alloy clusters instead of CUF sites. The alloy formation can be attributed to the poor metal-support interaction which increases the reducibility of Fe. These RhFe alloy clusters also reduce surface Rh atoms and thus result in poorer ESR activity than Rh/ZrO_2. Over Rh-Fe/Ca-Al_2O_3, the metal-support interaction was moderate, ensuring an ample supply of CUF sites for CO conversion to CO_2. In addition, CUF sites

assisted in water activation which increases the supply of surface hydroxyls. DRIFTS analyses have shown abundance of surface hydroxyls on the Ca-Al_2O_3 and MgO support which can react with adsorbed CO to form formate species. Water activation occurs more readily on Rh-Fe/Ca-Al_2O_3 and Rh-Fe/MgO due to presence of CUF sites. In contrast, promotion effect was not observed over Rh-Fe/ZrO_2 due to the lack of surface hydroxyls and water activation sites.

8.6. References

[1] W. Chen, Y. Ding, X. Song, T. Wang, H. Luo, Appl. Catal. A: Gen. 407 (2011) 231-237.

[2] M. Haider, M. Gogate, R. Davis, J. Catal. 261 (2009) 9-16.

[3] X. Gao, J. Shen, Y. Hsia, Y. Chen, J. Chem. Soc., Faraday Trans. 89 (1993) 1079-1084.

[4] H. Wan, B. Wu, C. Zhang, H. Xiang, Y. Li, B. Xu, F. Yi, Catal. Comm. 8 (2007) 1538-1545.

[5] M. Boudart, A. Delbouille, J.A. Dumesic, S. Khammouma, H. Topsøe, J. Catal. 37 (1975) 486-502.

[6] D. Stobbe, F. van Buren, A. Stobbe-Kreemers, A. van Dillen, J. Geus, J. Chem. Soc., Faraday Trans. 87 (1991) 1631-1637.

[7] K. Chen, Y. Fan, Z. Hu, Q. Yan, J. Solid State Chem. 121 (1996) 240-246.

[8] J. Llorca, N. Homs, J. Sales, P. de la. Piscina, J. Catal. 209 (2002) 306-317.

[9] H. Wang, E. Ruckenstein, J. Catal. 186 (1999) 181-187.

[10] E. Ruckenstein, H. Wang, J. Catal. 190 (2000) 32-38.

[11] P. Graat, M. Somers, Appl. Surf. Sci. 100/101 (1996) 36-40.

[12] C. Wu, K. Yu, F. Liao, N. Young, P. Nellist, A. Dent, A. Kroner, S. Tsang, Nat Commun. 3 (2012) 1050-.

[13] Y. Minai, T. Fukushima, M. Ichikawa, T. Tominaga, J. Radioanal. Nucl. Chem. 87 (1984) 189-201.

[14] J. Niemantsverdriet, J. van Kaam, C. Flipse, A. van der Kraan, J. Catal. 96 (1985) 58-71.

[15] P. Graf, D. de Vlieger, B. Mojet, L. Lefferts, J. Catal. 262 (2009) 181-187.

[16] T. Shido, Y. Iwasawa, J. Catal. 141 (1993) 71-81.

[17] D. Buchanan, M. Hernandez, F. Solymosi, J. White, J. Catal. 125 (1990) 456-466.

[18] J. Luo, M. Meng, Y. Zha, Y. Xie, T. Hu, J. Zhang, T. Liu, Appl. Catal. B: Environ. 78 (2008) 38-52.

[19] M. Barteau, Chem. Rev. 96 (1996) 1413-1430.

[20] G. Pacchioni, P. Pescarmona, Surf. Sci. 412/413 (1998) 657-671.

[21] S. Coluccia, S. Lavagnino, L. Marchese, Mater. Chem. Phys. 18 (1988) 445-464.

[22] X. Deng, T. Herranz, C. Weis, H. Bluhm, M. Salmeron, J. Phys. Chem. C 112 (2008) 9668-9672.

[23] A. Ignatchenko, D.G. Nealon, R. Dushane, K. Humphries, J. Mol. Catal. A: Chem. 256 (2006) 57-74.

Chapter 9

Summary and Future Work

9.1. General Conclusions

Hydrogen is a clean energy carrier which can be utilized in a fuel cell system to generate power. Among the different methods of hydrogen production, biomass-derived liquid fuels such as ethanol, is a potential feedstock for hydrogen production via steam reforming. This is because of its low toxicity and high hydrogen content. Ethanol can be derived from converting corn to sugars and from sugars to ethanol through fermentation. Alternatively, a less controversial method which involves conversion of lignocelluosic biomass such as wood chips and grasses has been developed. Thus, ESR not only relieves the demand on the use of fossil fuels but also achieve a near-zero net greenhouse gas emission due to the use of biomass.

For mobile fuel processor, there are major challenges in the development of catalyst for (1) efficient on-site or on-board hydrogen production at low temperature fuel reforming; (2) CO-free (< 10 ppm) hydrogen production via steam reforming in order to reduce CO poisoning on the fuel cell anode and (3) coke-free hydrogen production. Hence, the objective of this PhD research project was to develop a catalyst system which is active, stable and coke resistance for low temperature CO-free hydrogen production via ethanol steam reforming. In order to fulfill the objectives, several approaches were made towards the

formulation of catalysts, such as, (1) modification of Al_2O_3 by Ca; (2) use of various active metals (Ni, Pt, Rh, Pd) and (3) introduction of promoter (Fe) on Rh catalysts. Furthermore, mechanistic studies of the reaction pathways in ESR were studied using infrared spectroscopy over several catalytic systems. Deactivation mechanism was investigated as a guideline for better catalyst formulation in the future. Several conclusions are drawn from the study:

- Ca-modified alumina supports have been found to neutralize the acidic sites of Al_2O_3 and increase the basicity of the support. This led to a signification reduction in the formation of ethylene from dehydration of ethanol in the presence of Ca. Instead, dehydrogenation of ethanol to acetaldehyde was favored. Ca enhanced water adsorption and increased electronic density of states near the Fermi level.
- With optimized Ca loading of 3 wt%, Ni supported Ca-Al_2O_3 catalysts have shown high stability (of at least 24 h time of stream) and high hydrogen selectivity during ESR at 673 K. However, high Ca loading of 7 wt% have found to deactivate faster than unmodified Ni/ Al_2O_3. A combination of factors led to the improved stability over 10Ni/3Ca-Al_2O_3 catalyst. The introduction of Ca reduces the metal-support interaction between Ni and Al_2O_3 and as such enhances the availability of surface nickel. In this respect, higher electron density of states near the Fermi level, due to more surface nickel, promotes the rupturing of C-C bond. Since, coking rate is dependent on Ni particle size, this optimal amount of Ca also helps to keep Ni particle size within a comfortable range whereby

deactivation via coking is less severe. Furthermore, the coke deposits can be removed via gasification due to the presence of water adsorption sites in the presence of Ca.

- A new ESR reaction pathway denoted as *formate-driven* pathway have been proposed over Ca-modified Al_2O_3 supported noble metal catalysts. Using infrared spectroscopy, formate species, which are reaction intermediates for WGSR, were observed as opposed to traditionally observed acetate species. The addition of Ca reduces the availability of surface oxygen which is otherwise needed for the formation of acetate. Instead, Ca addition stabilizes the ethoxide species due to an increase in valence electrons. In the presence of an active metal such as Pt, the reaction proceeds via dehydrogenation and rupturing of C-C bond, resulting on the formation of CO. Carbon monoxide reacts with the surface hydroxyls found on Ca-Al_2O_3 to form formate intermediates which upon decomposition led to the formation of CO_2 and H_2. In this study, it was concluded that the activity of the catalysts in WGSR during ESR decreases in the following order: Pt> Rh> Pd.
- Fe promoted Rh/Ca-Al_2O_3 catalyst has been found to improve the hydrogen yield and lower CO selectivity during low temperature ESR. The iron oxide loading was optimized at 10 wt% with negligible CO selectivity at 623 K and this promotion effect is due to enhanced WGSR during ESR. In comparison to Rh/Ca-Al_2O_3, the catalytic lifespan of Rh-Fe/Ca-Al_2O_3 is extended significantly as the addition of iron oxide

minimizes CO poisoning on the Rh catalysts by converting adsorbed CO into formate species. The close interaction Rh-Fe on Ca-Al_2O_3 support favors the formation of Fe_xO_y species which produce coordinatively unsaturatured ferrous (CUF) ions.

- The catalytic performance of Rh-Fe catalysts supported on different oxides such as Ca-Al_2O_3, MgO and ZrO_2 have outlined the importance of metal-support interaction in generating the active sites for WGSR in ESR. CUF sites were observed on Rh-Fe catalysts supported on Ca-Al_2O_3 and MgO. Poorer enhanced WGSR in ESR over Rh-Fe/MgO was due to formation of iron oxide-MgO solid solution which hindered the development of CUF. Over Rh-Fe/ZrO_2, the poor iron oxide-ZrO_2 interaction favored the reduction of iron oxide to metallic iron, promoting the formation of RhFe alloy clusters instead of CUF. The loss of surface Rh active sites due to alloy formation over Rh-Fe/ZrO_2 resulted in slightly poorer ESR activity and higher CO selectivity than Rh/ZrO_2.

9.2. Future Directions

Among the different catalysts examined in this study, Rh-Fe/Ca-Al_2O_3 exhibited the best performance with excellent stability for at least 280 h at 623 K. Furthermore, CO selectivity was reduced to negligible amount with Fe promotion. Building on to the outstanding performance of Rh-Fe/Ca-Al_2O_3, some further directives are proposed.

9.2.1. EXAFS Characterization of Rh-Fe catalysts supported on Ca-Al_2O_3, MgO and ZrO_2

In Chapter 8, we have shown that Rh-Fe catalysts supported on Ca-Al_2O_3, MgO and ZrO_2 demonstrated different ESR catalytic performance. Water-gas shift reactions were dependent on the properties of the support and the presence of Fe_xO_y was important in promoting the WGSR. In this respect, extended X-ray absorption fine structure (EXAFS) techniques can be applied for the characterization of the state of Fe and Rh on various supports. Since, reduction temperature can vary the oxidation state of the iron oxides and Rh, EXAFS can also be conducted under different reducing conditions.

9.2.2. Kinetic Studies on Rh-Fe catalysts supported on Ca-Al_2O_3, MgO and ZrO_2

The kinetics of the reforming reaction is important in sizing the reactor. Power-law and Langmuir-Hinselwood rate expressions can be derived from the experimental data and a reaction mechanism maybe proposed based on the results. Rh-Fe/Ca-Al_2O_3 catalyst has delivered outstanding performance for low temperature CO-free hydrogen production via ESR. The kinetics for this catalyst can be compared with Fe-free Rh/Ca-Al_2O_3 catalyst. Similarly, kinetic studies can be performed on Rh-Fe catalysts on other supports such as MgO and ZrO_2.

9.2.3. Density functional theory (DFT) calculations

Computer simulations provide valuable information with regards to surface structure, physisorption and chemisorption of atoms and molecules on surface sites, lateral interactions between surface intermediates and activation barriers and reaction energies for the elementary surface reactions. Therefore, computation study using DFT calculations can be conducted on Rh-Fe catalysts with the objectives of (1) investigating activation of water and CO on Rh-Fe catalysts on different supports; (2) identifying the key step for ESR reaction on Rh-Fe/Ca-Al_2O_3 catalysts.